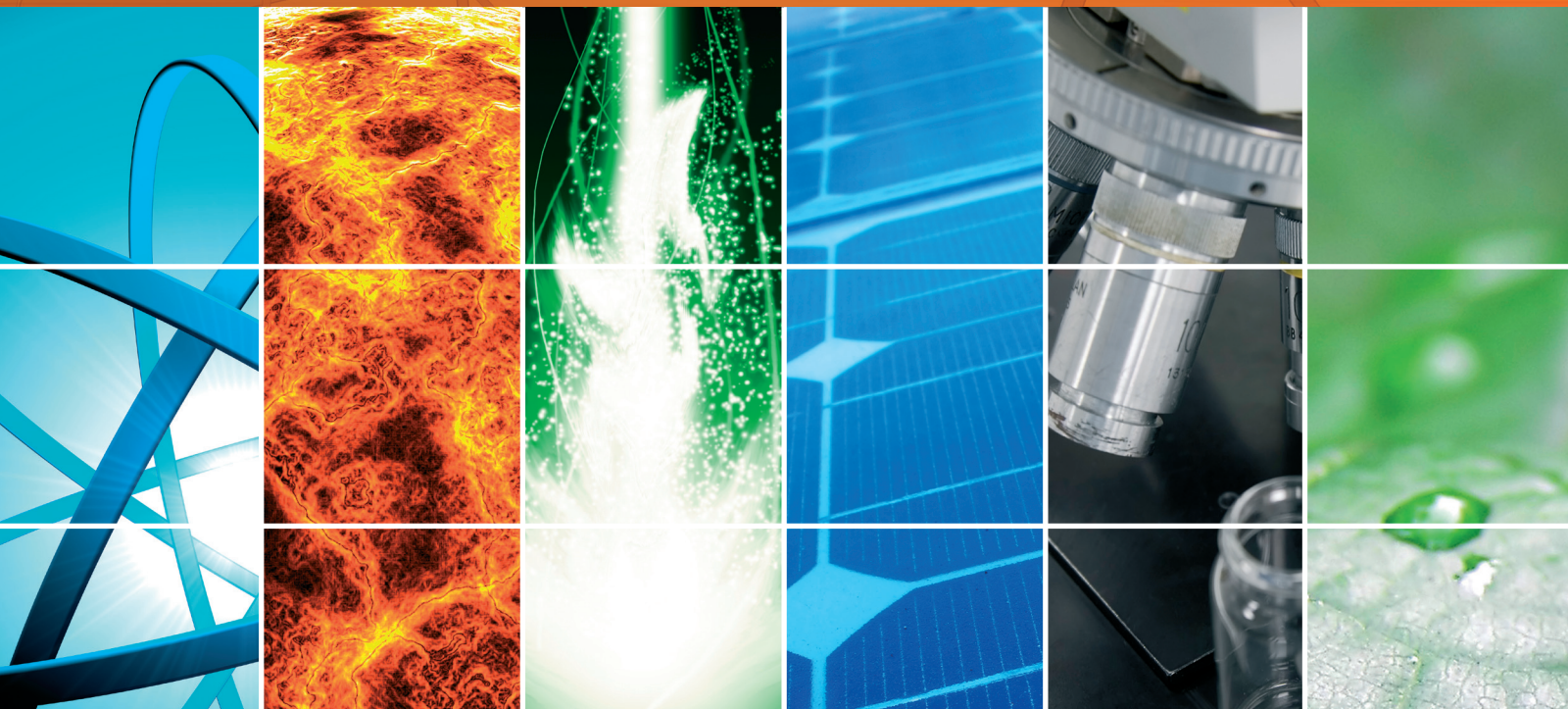


Solar Energy Conversion by Nanostructured TiO_2

Guest Editors: Jia Hong Pan, Detlef W. Bahnemann, Qing Wang, Chuanyi Wang, and Xiwang Zhang





Solar Energy Conversion by Nanostructured TiO₂

International Journal of Photoenergy

Solar Energy Conversion by Nanostructured TiO₂

Guest Editors: Jia Hong Pan, Detlef W. Bahnemann,
Qing Wang, Chuanyi Wang, and Xiwang Zhang



Copyright © 2014 Hindawi Publishing Corporation. All rights reserved.

This is a special issue published in "International Journal of Photoenergy." All articles are open access articles distributed under the Creative Commons Attribution License, which permits unrestricted use, distribution, and reproduction in any medium, provided the original work is properly cited.

Editorial Board

- M. S. A. Abdel-Mottaleb, Egypt
Xavier Allonas, France
Nicolas Alonso-Vante, France
Wayne A. Anderson, USA
Yanhui Ao, China
Raja S. Ashraf, UK
V. Augugliaro, Italy
Detlef W. Bahnemann, Germany
I. R. Bellobono, Italy
Raghu N. Bhattacharya, USA
Pramod H. Borse, India
Alessio Bosio, Italy
Stephan Buecheler, Switzerland
Gion Calzaferri, Switzerland
C. Chen, China
Sung Oh Cho, Republic of Korea
V. Cimrová, Czech Republic
Juan M. Coronado, Spain
Ying Dai, China
D. D. Dionysiou, USA
Pingwu Du, China
M. M. El-Nahass, Egypt
Polycarpos Falaras, Greece
Chris Ferekides, USA
Paolo Fornasiero, Italy
Hermenegildo García, Spain
Germà Garcia-Belmonte, Spain
E. I. Garcia-Lopez, Italy
Beverley Glass, Australia
M. A. Gondal, Saudi Arabia
Jr-Hau He, Taiwan
Shinya Higashimoto, Japan
Cheuk-Lam Ho, Hong Kong
Wing-Kei Ho, Hong Kong
Fuqiang Huang, China
Adel A. Ismail, Egypt
Chun-Sheng Jiang, USA
Misook Kang, Republic of Korea
Shahed Khan, USA
Sun-Jae Kim, Republic of Korea
Jong Hak Kim, Republic of Korea
Sungjee Kim, Republic of Korea
Cooper H. Langford, Canada
Tae-Woo Lee, Republic of Korea
Lecheng Lei, China
Xinjun Li, China
Zhaosheng Li, China
Yuexiang Li, China
Stefan Lis, Poland
Vittorio Loddo, Italy
Gongxuan Lu, China
Dongge Ma, China
N. M. Mahmoodi, Iran
Nai Ki Mak, Hong Kong
Rajaram S. Mane, India
D. Mantzavinos, Greece
Ugo Mazzucato, Italy
Sheng Meng, China
Jacek Miller, Poland
Claudio Minero, Italy
Antoni Morawski, Poland
Franca Morazzoni, Italy
F. Morlet-Savary, France
M. Muneer, India
Kun Na, Republic of Korea
Ebinazar B. Namdas, Australia
Maria Neves, Portugal
Tebello Nyokong, South Africa
Kei Ohkubo, Japan
Haridas Pal, India
Leonidas Palilis, Greece
Leonardo Palmisano, Italy
Ravindra K. Pandey, USA
H. Park, Republic of Korea
Pierre Pichat, France
Gianluca Li Puma, UK
Tijana Rajh, USA
Peter Robertson, UK
Avigdor Scherz, Israel
Elena Selli, Italy
Ganesh D. Sharma, India
Jinn Kong Sheu, Taiwan
Panagiotis Smirniotis, USA
Zofia Stasicka, Poland
Elias Stathatos, Greece
J. Subbiah, Australia
M. Swaminathan, India
Kazuhiro Takanabe, Saudi Arabia
Mohamad-Ali Tehfe, Canada
K. R. Justin Thomas, India
Yang Tian, China
Nikolai V. Tkachenko, Finland
Ahmad Umar, Saudi Arabia
Thomas Unold, Germany
Veronica Vaida, USA
Roel van De Krol, Germany
Mark van Der Auweraer, Belgium
Rienk Van Grondelle, The Netherlands
Wilfried Van Sark, The Netherlands
Sheng Wang, China
Xuxu Wang, China
Mingkui Wang, China
Ezequiel Wolcan, Argentina
Man Shing Wong, Hong Kong
David Worrall, UK
Jeffrey C. S. Wu, Taiwan
Yanfa Yan, USA
Jiannian Yao, China
Minjoong Yoon, Republic of Korea
Jiangbo Yu, USA
Hongtao Yu, USA
Ying Yu, China
Klaas Zachariasse, Germany
Juan Antonio Zapien, Hong Kong
Tianyou Zhai, China
Lizhi Zhang, China
Guijiang Zhou, China
Yong Zhou, China
Rui Zhu, China

Contents

Solar Energy Conversion by Nanostructured TiO₂, Jia Hong Pan, Detlef W. Bahnemann, Qing Wang, Chuanyi Wang, and Xiwang Zhang
Volume 2014, Article ID 704729, 2 pages

One-Dimensional Nanostructured TiO₂ for Photocatalytic Degradation of Organic Pollutants in Wastewater, Ting Feng, Gen Sheng Feng, Lei Yan, and Jia Hong Pan
Volume 2014, Article ID 563879, 14 pages

Effect of Mn Doping on Properties of CdS Quantum Dot-Sensitized Solar Cells, Tianxing Li, Xiaoping Zou, and Hongquan Zhou
Volume 2014, Article ID 569763, 6 pages

Photocatalytic Degradation of Anthracene in Closed System Reactor, Faiq F. Karam, Falah H. Hussein, Sadiq J. Baqir, Ahmed F. Halbus, Ralf Dillert, and Detlef Bahnemann
Volume 2014, Article ID 503825, 6 pages

Recent Progress in TiO₂-Mediated Solar Photocatalysis for Industrial Wastewater Treatment, Tong Zhang, Xiaoguang Wang, and Xiwang Zhang
Volume 2014, Article ID 607954, 12 pages

Sol-Gel to Prepare Nitrogen Doped TiO₂ Nanocrystals with Exposed {001} Facets and High Visible-Light Photocatalytic Performance, Hui-Ying Ai, Jian-Wen Shi, Rui-Xi Duan, Jian-Wei Chen, Hao-Jie Cui, and Ming-Lai Fu
Volume 2014, Article ID 724910, 9 pages

Layer-by-Layer Assembly and Photocatalytic Activity of Titania Nanosheets on Coal Fly Ash Microspheres, Xing Cui, Jianwen Shi, Zhilong Ye, Zhaoji Zhang, Bin Xu, and Shaohua Chen
Volume 2014, Article ID 823078, 10 pages

Theoretical Study of One-Intermediate Band Quantum Dot Solar Cell,
Abou El-Maaty Aly and Ashraf Nasr
Volume 2014, Article ID 904104, 10 pages

Steric and Solvent Effect in Dye-Sensitized Solar Cells Utilizing Phenothiazine-Based Dyes, Hany Kafafy, Hongwei Wu, Ming Peng, Hsienwei Hu, Kai Yan, Reda M. El-Shishtawy, and Dechun Zou
Volume 2014, Article ID 548914, 9 pages

Equilibrium and Kinetic Aspects in the Sensitization of Monolayer Transparent TiO₂ Thin Films with Porphyrin Dyes for DSSC Applications, Rita Giovannetti, Marco Zannotti, Leila Alibabaei, and Stefano Ferraro
Volume 2014, Article ID 834269, 9 pages

Editorial

Solar Energy Conversion by Nanostructured TiO₂

Jia Hong Pan,¹ Detlef W. Bahnemann,¹ Qing Wang,² Chuanyi Wang,³ and Xiwang Zhang⁴

¹ Institut für Technische Chemie, Leibniz Universität Hannover, Callinstrasse 3, 30167 Hannover, Germany

² Department of Materials Science & Engineering, Faculty of Engineering, National University of Singapore, 5 Engineering Drive 2, Singapore 117576

³ Laboratory of Eco-Materials and Sustainable Technology (LEMST), Xinjiang Technical Institute of Physics and Chemistry and Key Laboratory of Functional Materials and Devices for Special Environments, Chinese Academy of Sciences, Urumqi, Xinjiang 830011, China

⁴ Department of Chemical Engineering, Monash University, Clayton, VIC 3800, Australia

Correspondence should be addressed to Jia Hong Pan; pan@iftc.uni-hannover.de

Received 24 August 2014; Accepted 24 August 2014; Published 22 December 2014

Copyright © 2014 Jia Hong Pan et al. This is an open access article distributed under the Creative Commons Attribution License, which permits unrestricted use, distribution, and reproduction in any medium, provided the original work is properly cited.

Research in solar energy conversion and the associated photoactive materials has attracted continuous interest. Due to its proper electronic band structure, high quantum efficiency, and photonic and chemical innerness, TiO₂ has been demonstrated as a versatile oxide semiconductor capable of efficiently utilizing sunlight to produce electrical and chemical energy. Its outstanding physicochemical performances have led to an array of advanced photocatalytic and photoelectrochemical applications including environmental photocatalysis, dye/semiconductor-sensitized solar cell, and solar fuel productions.

Scientific papers in this special issue have covered this highly developing field. Authors have submitted review and original research articles in the following topics:

- (i) kinetics and mechanism of TiO₂-mediated environmental photocatalysis,
- (ii) TiO₂-based dye/semiconductor-sensitized solar cells,
- (iii) photocatalytic organic synthesis over TiO₂-mediated system,
- (iv) photocatalytic solar fuel production (water splitting and CO₂ reduction),
- (v) novel TiO₂-based nanomaterials for solar energy conversion.

We wish to express our sincere gratefulness to all the authors and referees whose contributions make this special

issue possible. A brief overview of all nine accepted papers is below.

In “Recent progress in TiO₂-mediated solar photocatalysis for industrial wastewater treatment,” the authors overview the major challenges in industrial wastewater treatment and analysed the merits of TiO₂ photocatalysis over conventional water treatment technologies. Then a brief but comprehensive review is carried out on the recent progress in their applications in several typical industrial wastewaters. The paper could advance the development of solar photocatalysis systems and promote their practical application.

In “Photocatalytic degradation of anthracene in closed system reactor,” the authors investigate the effect of operating parameters on the degradation efficiency of anthracene, one of the toxic persistent organic pollutants. The photodegradation products are identified by GC-MS to better understand the degradation path of anthracene on P25 TiO₂ nanoparticles under UV irradiation. Optimum parameters have been systematically investigated to obtain a high photocatalytic degradation rate. The research reported here gives an excellent example how to design proper photocatalytic process for organic pollutants removal.

In “Sol-gel to prepare nitrogen doped TiO₂ nanocrystals with exposed {001} facets and high visible-light photocatalytic performance,” a facile synthetic method based on sol-gel process is developed to synthesize anatase TiO₂ with dominant {001} facets and nitrogen doping by simply hydrolysing tetrabutyl titanate in NH₄F-containing alcoholic solution. NH₄F

not only acts as the N dopant source, but also guides the preferential growth along [001] direction. The synthesized N-doped TiO₂ nanoparticles outperform P25 referents in photocatalytic degradation of methylene blue under visible light irradiation.

In “*One-dimensional nanostructured TiO₂ for photocatalytic degradation of organic pollutants in wastewater*,” current progress in the synthetic methods for one-dimensional (1D) TiO₂ nanostructures including nanorods, nanotubes, nanowires/nanofibers, and nanobelts is reviewed. Modification of 1D TiO₂ with metal oxide, metal ions, and anions in order to enhance the photocatalytic activity is discussed. Furthermore, photocatalytic degradations of organic pollutants in wastewater over 1D TiO₂ are summarized, and the underlying mechanism is discussed. Finally, using 1D nanostructured TiO₂ as building blocks to construct film or membrane is highlighted.

In “*Layer-by-layer assembly and photocatalytic activity of titania nanosheets on coal fly ash microspheres*,” an attempt to address the problem with nanoparticulate TiO₂ distribution and recovery is made. Coal fly ash (CFA) microspheres are used as a substrate for the layer-by-layer assembly of Ti_{0.91}O₂ sheets. That is, the Ti_{0.91}O₂ nanosheets are immobilized on CFA by using sequential modification of cationic polyelectrolyte and Ti_{0.91}O₂ nanosheets. The resultant Ti_{0.91}O₂/CFA composites show considerable photocatalytic activity in degradation of methylene blue under UV irradiation. After photocatalysis, the Ti_{0.91}O₂/CFA can be easily separated and recycled from aqueous solution.

In “*Effect of Mn doping on properties of CdS quantum dot-sensitized solar cells*,” impurity Mn²⁺ ions are doped into the precursor solution for CdS deposition. By optimizing the experimental parameters, a significant improvement in photoelectric conversion efficiency can be achieved. After a successive ionic layer adsorption and reaction of a fixed number of six times, the photoelectric conversion efficiency shows the maximum value (1.51%) at the optimal doped ratio, which is much higher than that of the pure one (0.71%).

In “*Theoretical study of one-intermediate band quantum dot solar cell*,” the authors theoretically studied the influence of the new band on the power conversion efficiency for the structure of the quantum dots of intermediate band solar cell. The time-independent Schrödinger equation is used to determine the optimum width and location of the intermediate band. From their calculation results, the maximum power conversion efficiency is about 70.42% for simple cubic quantum dot crystal under full concentration light. It is strongly dependent on the width of quantum dots and barrier distances.

In “*Equilibrium and kinetic aspects in the sensitization of monolayer transparent TiO₂ thin films with porphyrin dyes for DSSC applications*,” the adsorption of free base and Cu(II) and Zn(II) complexes of the 2,7,12,17-tetrapropionic acid of 3,8,13,18-tetramethyl-21H,23H porphyrin (CPI) on transparent monolayer TiO₂ nanoparticle films was studied. The dye loading is found to be accordant with Langmuir isotherm, while kinetic data show significantly better fits to pseudo-first-order model and the evaluated rate constants linearly

increase with the grow of initial dye concentrations. The stoichiometry of the adsorption of CPI-dyes into TiO₂ and the influence of presence of coadsorbent (chenodeoxycholic acid) are established. This study paves a way for choosing the best experimental conditions for the adsorption of these dyes.

In “*Steric and solvent effect in dye-sensitized solar cells utilizing phenothiazine-based dyes*,” three novel phenothiazine-based dyes are prepared and utilized for dye-sensitized solar cells (DSSC). The dye-bath solvent presents a significant effect on the overall cell performance. The highest conversion efficiency of 3.78% is obtained using ethanol (EtOH) and 2.53% for tetrahydrofuran (THF) as solvent, respectively. The higher efficiency is related to the higher dye loading and coverage on the TiO₂ surface. Meanwhile, phenothiazine-based dyes with longer and branched aliphatic chain increase the steric hindered effect which is mainly responsible for increasing the electron lifetime and decreases the dye aggregation as well as increasing the electron recombination resistance rate at the TiO₂-dye-electrolyte interface, hence, enhancing the overall cell performance.

Jia Hong Pan
Detlef W. Bahnemann
Qing Wang
Chuanyi Wang
Xiwang Zhang

Review Article

One-Dimensional Nanostructured TiO₂ for Photocatalytic Degradation of Organic Pollutants in Wastewater

Ting Feng,¹ Gen Sheng Feng,¹ Lei Yan,² and Jia Hong Pan³

¹ School of Metallurgical and Ecological Engineering, University of Science and Technology Beijing, Beijing 100083, China

² College of Materials, Optoelectronics and Physics, Xiangtan University, Xiangtan, Hunan 411105, China

³ Department of Materials Science and Engineering, NUSNNI-NanoCore, National University of Singapore, Singapore 117576

Correspondence should be addressed to Ting Feng; fengting@ustb.edu.cn and Lei Yan; yanlei@xtu.edu.cn

Received 4 April 2014; Revised 12 June 2014; Accepted 23 June 2014; Published 5 August 2014

Academic Editor: Xiwang Zhang

Copyright © 2014 Ting Feng et al. This is an open access article distributed under the Creative Commons Attribution License, which permits unrestricted use, distribution, and reproduction in any medium, provided the original work is properly cited.

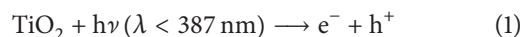
The present paper reviews the progress in the synthesis of one-dimensional (1D) TiO₂ nanostructures and their environmental applications in the removal of organic pollutants. According to the shape, 1D TiO₂ nanostructures can be divided into nanorods, nanotubes, nanowires/nanofibers, and nanobelts. Each of them can be synthesized via different technologies, such as sol-gel template method, chemical vapor deposition, and hydrothermal method. These methods are discussed in this paper, and the recent development of the synthesis technologies is also presented. Furthermore, the organic pollutants, degradation using the synthesized 1D TiO₂ nanostructures is studied as an important application of photocatalytic oxidation (PCO). The 1D nanostructured TiO₂ exhibited excellent photocatalytic activity in a PCO process, and the mechanism of photocatalytic degradation of organic pollutants is also discussed. Moreover, the modification of 1D TiO₂ nanostructures using metal ions, metal oxide, or inorganic element can further enhance the photocatalytic activity of the photocatalyst. This phenomenon can be explained by the suppression of e⁻-h⁺ pairs recombination rate, increased specific surface area, and reduction of band gap. In addition, 1D nanostructured TiO₂ can be further constructed as a film or membrane, which may extend its practical applications.

1. Introduction

Organic pollutants are widely presented in wastewater, which have negative effects on environment and human health. Even developing water treatment technology calls for efficient decontamination method for complete degradation of persistent organic pollutants (POPs) [1–3]. Conventional biological, physical, and chemical processes have been employed and have showed capability in degrading most organic pollutants, while for POPs, complete degradation is still a big challenge. Advanced oxidation process (AOP) has thus developed by oxidation with hydroxyl radicals (•OH), which are provided by introducing ozone, hydrogen peroxide, and UV irradiation. However, complete degradation of POPs is still difficult due to the ease in forming disinfection by-products.

TiO₂-mediated semiconductor photocatalysis has attracted considerable attention in view of their excellences in complete degradation of organic pollutants via photocatalytic oxidation (PCO) process. A general mechanism is illustrated

in Figure 1 [4]. Initially, PCO process is triggered by the excitation of TiO₂ under the irradiation of photons with energy greater than the band-gap energy of TiO₂. The photogenerated electron (e⁻) and holes (h⁺) pairs without recombination can migrate to TiO₂ surface to participate in redox reactions with adsorbed species with the possible formation of superoxide radical anion (•O₂⁻) and hydroxyl radical (•OH), respectively. These reactive oxygen species are mainly responsible for the degradation of organic pollutants in water. Furthermore, the excitation of TiO₂ by UV light can be displayed in the following equations [5–8]:



In an organic degradation process, the formed e⁻ and h⁺ act as reductant and oxidant, respectively. The reaction steps are represented as follows [6].

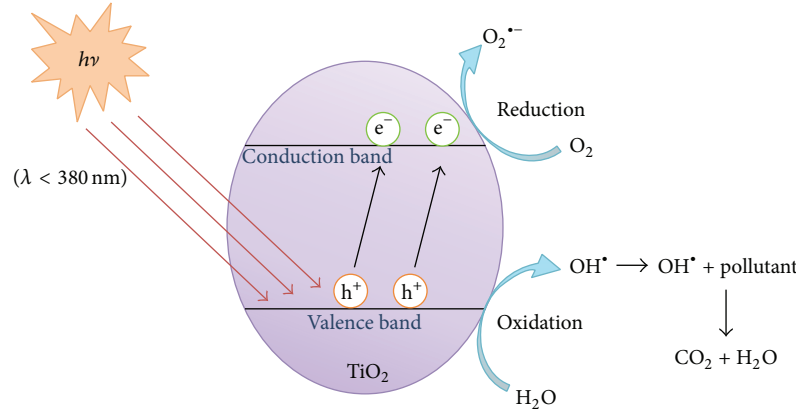
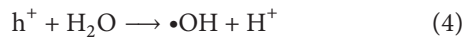
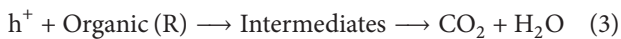
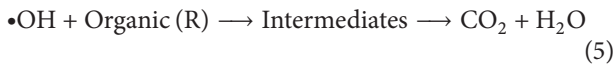


FIGURE 1: General mechanism of the photocatalysis [13].

TABLE 1: Typical synthetic methods of 1D TiO₂ nanostructures.

| TiO ₂ nanostructures | Synthesis methods | References |
|---------------------------------------|----------------------------|-------------|
| TiO ₂ nanorods | Sol-gel template method | [20] |
| | Hydrothermal method | [22] |
| | Chemical vapor deposition | [23] |
| TiO ₂ nanotubes | Electrochemical deposition | [37] |
| | Template method | [41, 42] |
| | Hydrothermal method | [39, 44–46] |
| TiO ₂ nanowires/nanofibers | Hydrothermal method | [5] |
| | Microwave | [75] |
| | Electrospinning | [76] |
| TiO ₂ nanobelts | Solvothermal method | [65] |
| | Chemical vapor deposition | [68] |
| | Hydrothermal method | [67] |

Oxidative Reaction:*Reductive Reaction:*

Current research progress has shown that TiO₂-based materials demonstrate highly active photocatalytic degradation of different organic pollutants [9–11]. For example, phenol, chlorinated aromatics, and aniline compounds are susceptible to oxidation by TiO₂, and they can form intermediate radicals that may subsequently trigger a series of radical reactions in this process. Due to the excellent oxidation ability, the resulting intermediates can be finally degraded into CO₂ and H₂O. Since the oxidation process is primarily driven by electron transfer reactions at the surface of TiO₂, the specific surface area of TiO₂ is an important factor which can affect the PCO efficiency.

To significantly boost the photoenergy conversion efficiency, tailing nanostructured TiO₂ has attracted continuous research interest, among which one-dimensional (1D)

nanostructures possessing large surface areas and unique physical and chemical specificities are of particular interest [12]. Various 1D nanostructures including nanorods, nanowires/nanofibers, nanotubes, and nanobelts have been successively synthesized during the past decades. Some typical synthetic methods of 1D TiO₂ nanostructures are summarized in Table 1. Nanorods have a low aspect ratio (length divided by width) ranging from 3 to 5. Nanotubes are a type of nanometer-scale tube-like structure, which have a similar size with nanorods. For the nanowires/nanofibers, they have a higher aspect ratio as compared to nanorods. Nanobelt is a nanostructure in a form of belt. The specific geometry with high aspect ratio renders dramatical enhancements in charge carrier generation, transport, and separation, boosting the photoenergy conversion efficiency [13, 14]. Up to now 1D TiO₂ has been comprehensively investigated for the degradation of organic pollutants, such as dyes, POPs (phenol and derivatives) and natural organic matters (NOMs) [15, 16].

2. TiO₂ Nanorods

TiO₂ nanorods have a relatively small amount of grain boundaries and can act as single crystal, which is able to reduce the grain boundary effect and provide fast

electron transport [17]. Previous reports indicated that TiO₂ nanorods exhibited higher photocatalytic activity than nanoparticle counterparts due to the increased numbers of active sites and crystal plane effects [18]. Furthermore, TiO₂ nanorods have lower recombination rate of e⁻ and h⁺ as compared with TiO₂ nanoparticles, which would enhance the photocatalytic activity of the photocatalyst [19].

Various synthetic strategies have been designed for the preparation of TiO₂ nanorods, which include sol-gel template method, chemical vapor deposition (CVD), and hydrothermal method [19–23].

Attar et al. [20] developed an improved sol-gel template method for the synthesis of TiO₂ nanorods, as shown in Figure 2(a). Anodic alumina membranes (Figure 2(a)) were applied as the template with pore sizes ranging from 50 to 300 nm. Owing to the adjustable membrane pore sizes, the diameter of the synthesized TiO₂ nanorods can be controlled. Figure 2(b) shows the synthesized TiO₂ nanorods with diameter of 160–250 nm, revealing that the nanorods synthesized via this method have a uniform diameter as well as a smooth surface. However, they found that the diameter of the synthesized TiO₂ nanorods was much smaller than the pore size of the template, which was attributed to the densification and lateral shrinkage of the template during the annealing process.

Wu and Yu synthesized a novel type of well-aligned rutile and anatase TiO₂ nanorods via a template-free metal-organic CVD method [21]. As shown in Figure 2(c), TiO₂ nanorods were grown directly on a silicon substrate at a temperature of 500–700°C. The single-crystalline rutile and anatase TiO₂ nanorods were formed at 630°C and 560°C, respectively, which indicated that the temperature was a key factor in the synthesis process. The disadvantage of this method is the complicated synthesis process, which is not suitable for production in large-scale.

Hydrothermal method is facile for the synthesis of 1D nanostructured TiO₂ [22]. Feng et al. [22] developed a new type of nanorod film on glass substrates via a low-temperature hydrothermal process. As shown in Figure 2(d), the nanorods have diameters of 30–60 nm and they have uniform orientation. Furthermore, the authors found that the surface of the synthesized film has switchable wettability which transferred from superhydrophobicity to superhydrophilicity under UV light irradiation. This phenomenon can be explained by the reaction between the photogenerated holes and the lattice oxygen, leading to the formation of surface oxygen vacancies.

TiO₂ nanorods have been widely used in PCO process for the degradation of organics [24]. For example, organic dyes and acetone can be effectively degraded into CO₂ and H₂O. Melghit and Al-Rabaniah [24] prepared rutile TiO₂ nanorods using a sol-gel method at room temperature, and the material exhibits excellent photodegradation of Congo red under sunlight. It can be explained by two aspects. (1) The Congo red is easily absorbed onto the synthesized TiO₂ nanorods, and, subsequently, the dye decomposed in a PCO process. (2) Organic dyes are capable of photosensitizing TiO₂ because of the absorption of visible light [25].

The photosensitization was considered as another way for the degradation of dyes in the presence of TiO₂ under sunlight irradiation. It was worth noting that the synthesized rutile TiO₂ nanorods which possess optimum size and shape are much more efficient for PCO process than the anatase TiO₂ [24]. Yu and coworkers [26] synthesized TiO₂ nanostructures using TiF₄ and H₃BO₃ as the precursors. The morphology characterization revealed that the synthesized material is a combination of TiO₂ nanorods and nanotubes. It is important to notice that the synthesized TiO₂ exhibited a higher PCO efficiency for the degradation of acetone than that of P25 due to the larger specific surface area and pore volume of the synthesized TiO₂. Moreover, compared with the nanosized powder photocatalysts, the prepared TiO₂ is easier to be separated from aqueous solutions after PCO process due to its long structure, and it also possesses higher photocatalytic activity. In addition, the photocatalytic activity of TiO₂ nanorods can be further improved via a thermal treatment because of the enhanced crystallization [27].

In order for facile recycling, TiO₂ nanorods have been coated onto substrates. A successful example is that well-aligned TiO₂ nanorod can be prepared on pretreated quartz substrate [28]. The quartz substrate was precoated with a thin rutile TiO₂ seed layer to facilitate the subsequent growth of the rutile TiO₂ nanorods. Owing to the excellent nucleation and growth properties, rutile TiO₂ crystal seeds are more preferable than anatase TiO₂. Thus, the pretreatment of substrates is important for the synthesized TiO₂ morphology, which would also affect the performance of the material in a PCO process. Based on the experimental results, the density of TiO₂ seeds can be controlled by the concentration of the coating colloid solution. Then the TiO₂ crystal seeds will affect the growth density, diameter distribution, and growth morphologies of TiO₂ nanorods. When the density of TiO₂ seeds is high, the seeds tend to merge together to form larger TiO₂ particles. It is shown that the degradation rates of methyl blue increased with large growth density and small diameter size of TiO₂ nanorods.

Pure TiO₂ is not an effective visible-light photocatalyst due to its wide band gap (>3.0 eV) and can be activated only by UV light at $\lambda \leq 380$ nm. Modification of TiO₂ has been explored to extend the absorption spectra of photocatalysts to visible light range [29]. Doping of TiO₂ with various metals or nonmetals has been considered as a valid way to lower the band gap of TiO₂ and thus make the photocatalyst more active under solar light. Doping of TiO₂ would introduce allowed energy states within the band gap but very close to the energy band. The gap between the energy states and the nearest energy band is usually reduced. Thus, the electrons and holes would be more easily excited under visible light irradiation. Kerkez and Boz [30] used Cu²⁺ as a dopant to modify TiO₂ nanorod array films (Figure 3(a)), and they found that the methylene blue degradation efficiency under visible light was increased 40% with respect to the efficiency of the unmodified sample. The notable improvement could be explained by the following factors. (1) Cu²⁺ acts as a trap

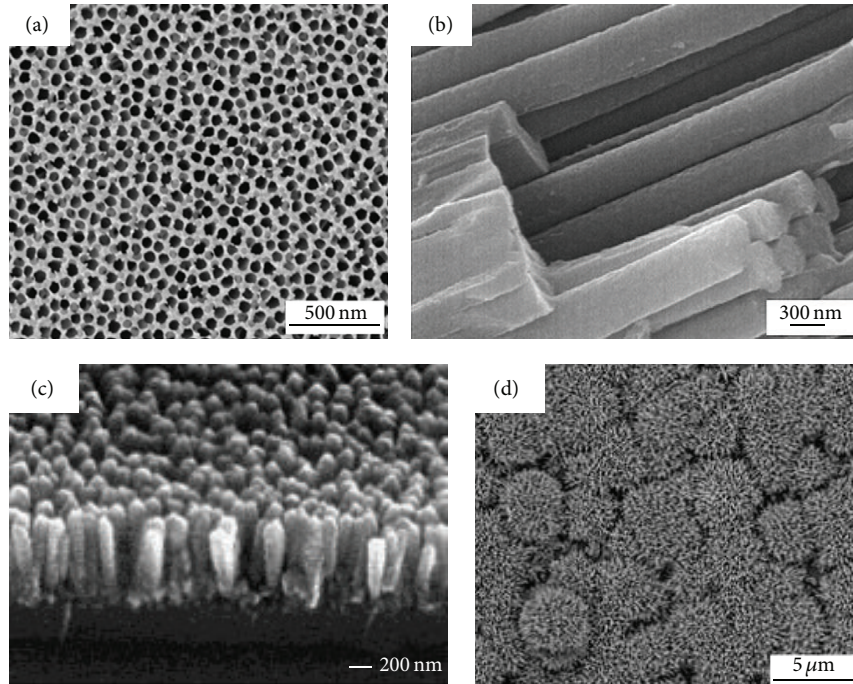


FIGURE 2: (a) FESEM image of the template (anodic alumina membrane) [20], (b) FESEM image of the synthesized TiO_2 nanorod arrays [20], (c) FESEM image of anatase TiO_2 nanorods [21], and (d) FESEM image of TiO_2 nanorod film [22].

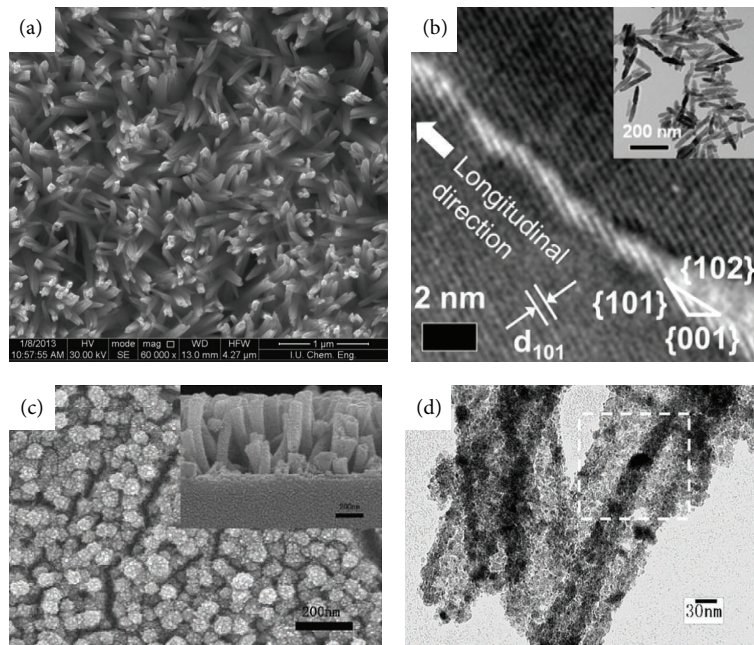


FIGURE 3: (a) SEM image of Cu^{2+} - TiO_2 nanorods, (b) TEM image of N- TiO_2 nanorods [31], (c) FESEM image of N-F- TiO_2 nanorods (inset: its cross section) [32], and (d) TEM image of Au-loaded TiO_2 hollow nanorods [33].

of photogenerated electrons. The electrons were transferred from TiO_2 to the conduction band of the CuO with little chance to return and thus increase the life time of e^- - h^+ . Thus, the presence of Cu^{2+} could retard the recombination rate of electrons and holes on the surface of the synthesized Cu^{2+} - TiO_2 . (2) The band gap of Cu^{2+} - TiO_2 nanorods is lower than

that of the original TiO_2 , which can extend the photoresponse of the photocatalyst and make the material utilizable under both UV light and visible light.

TiO_2 nanorods with 3% of nitrogen doping were prepared by Lee and coworkers, as shown in Figure 3(b) [31]. Although the N-doping process did no change the morphology of TiO_2

nanorods, it provides extra occupied states above its valence band which may enhance the photocatalytic activity. Lv et al. also reported the synthesis of N-F-doped visible light active TiO₂ nanorods via a liquid phase deposition process (Figure 3(c)) [32]. They firstly synthesized ZnO nanorod arrays on glass substrates and then combined the ZnO nanorod arrays and TiO₂ via an aqueous solution method to get the as-prepared TiO₂ nanorods. Their experimental results indicated that the doping quantity of N and F in the resultant material could be easily controlled by adjusting the calcination temperature, and the optimal temperature was found to be 450°C. Owing to the higher visible light photocatalytic activity, the obtained TiO₂ nanorods' films exhibited higher degradation rate for methylene blue as compared to P25 films [32].

Metals have been incorporated into TiO₂ nanorods to form nanocomposites with a heterojunction structure. For example, TiO₂ nanorods can be coated by Au nanoparticles to form a novel heterojunction, as shown in Figure 3(d) [33]. As a model organic pollutant, methylene blue can be used to characterize the photocatalytic activity of the synthesized photocatalysts. 35% of methylene blue was degraded in the presence of Au-TiO₂ nanorods, which is much more effective than that of 15% for pure nanorods. In addition, the other metals such as Ag and Cu can also be coated onto TiO₂ nanorods [34, 35]. The synthesized nanocomposites exhibited outstanding photocatalytic activity as compared to the pure TiO₂. The enhancement in photocatalytic activity is related with the slow recombination rate of charge carriers. During PCO process, the generated electrons from TiO₂ nanorods could transfer to Au nanoparticles, leading to the longer lifetime of the e⁻-h⁺ pairs and therefore more reactive oxygen species produced for the degradation of organic pollutants in water. The mechanism of photocatalytic degradation of organic pollutants over metal/TiO₂ under UV light irradiation is shown in Figure 4.

3. TiO₂ Nanotubes

Currently, TiO₂ nanotube structures have been successfully synthesized and applied for organic pollutants degradation [36]. Hoyer [37] firstly reported the synthesis of TiO₂ nanotubes via an electrochemical deposition in a porous aluminum oxide mold. Then, an electrochemical anodic oxidation method was developed by Zwilling et al. for the synthesis of TiO₂ nanotubes [38]. Although this method is very facile to synthesize TiO₂ nanotubes with controllable pore size, good uniformity, and conformability over large areas, the high cost of fabrication apparatus and complicated operation limited its further application [39, 40]. Templating method was considered as a suitable technology to construct materials with desirable morphology [41]. TiO₂ nanotubes can be synthesized in controlled sol-gel hydrolysis of solutions containing titanium compounds and templating agents followed by polymerization or deposition of TiO₂ on the template. For example, Peng and coworkers [42] fabricated TiO₂ nanotubes via a surfactant-mediated templating method, and the fabrication process can be summarized

in Figure 5. In the synthesis process, a sol-gel method was conducted for fabricating the material, and laurylamine hydrochloride (LAHC) was used as a template. Titanium alkoxide was first hydrolyzed with the addition of tetra-n-butyl-orthotitanate (TBOT), and then there is an interaction between partially charged hydrolytic species and laurylamine surfactant by H-bonding forces (Figure 5(a)). The edge part of the bilayer assemblies of LAHC was unstable and apt to combine with the interlayers, which lead to the enlargement of the layers (Figure 5(b)). Then the bilayer-like aggregates rearranged into lamellar-like liquid-crystal phases through the condensation reaction (Figure 5(c)). After the interlayer combination and crosslinking between adjacent hydrolyzed titanium alkoxide species, a mixed lamellar liquid-crystal phase membrane formed, and rodlike micelles were separated by bilayers of surfactant and water (Figure 5(d)). Upon the addition of TBOT, charge imbalance leads to the curvature of the membrane along one direction (Figure 5(e)) and then bends fully the membrane into tubules (Figure 5(f)). Moreover, the condensation of the hydrolyzed titanium species would lead to the rodlike micelles in a random arrangement (Figure 5(g)). The synthesized TiO₂ nanotubes possess a hierarchical tubules-within-tubules structure with cylindrical nanochannels walls. This structure is a combination structure of microtube and nanotube, causing the formation of porous structure. Moreover, the specific surface area of the material is also increased. The structure would be beneficial for catalysts and thus enhance the PCO efficiency. Furthermore, the scale of the synthesized TiO₂ nanotubes can be controlled by adjusting the morphology of the template [41]. However, the instability of the TiO₂ nanotubes synthesized by this method is a big issue, and the tube morphology is easily destroyed [39, 40, 43].

Recently, hydrothermal method has been widely used for the synthesis of high quality of TiO₂ nanotubes with diameter of about 10 nm [44]. Crystalline TiO₂ nanoparticles and highly concentrated NaOH are normally used as the precursors in a typical hydrothermal process [41]. As a necessary step, the drying or calcination process is generally conducted, leading to the transformation of titanate nanotubes to TiO₂ nanotubes. Based on previous reports [39, 45, 46], the advantages of hydrothermal process for TiO₂ nanotubes synthesis can be concluded as the following. (1) It is suitable for large scale production; (2) the modification process of TiO₂ nanotubes can be directly conducted in the synthetic system; (3) nanotubes with ultrahigh aspect ratio can be synthesized. However, hydrothermal process requires high temperature and pressure, as well as the long reaction time, which also cause a high cost. Figure 6 lists various TiO₂ nanotubes synthesized by different methods.

TiO₂ nanotubes can be used for the degradation of POPs such as benzene and acetaldehyde [47, 48]. Yuan et al. [49] studied the performance of TiO₂ nanotubes for water treatment. The synthesized TiO₂ nanotubes showed complete photodegradation of humic acid in comparison to the 97.7% removal efficiency of TiO₂ P25. Moreover, the TiO₂ nanotubes can be totally separated and recovered via a membrane filtration. The stability test presented that no catalyst deactivation was observed after five consecutive

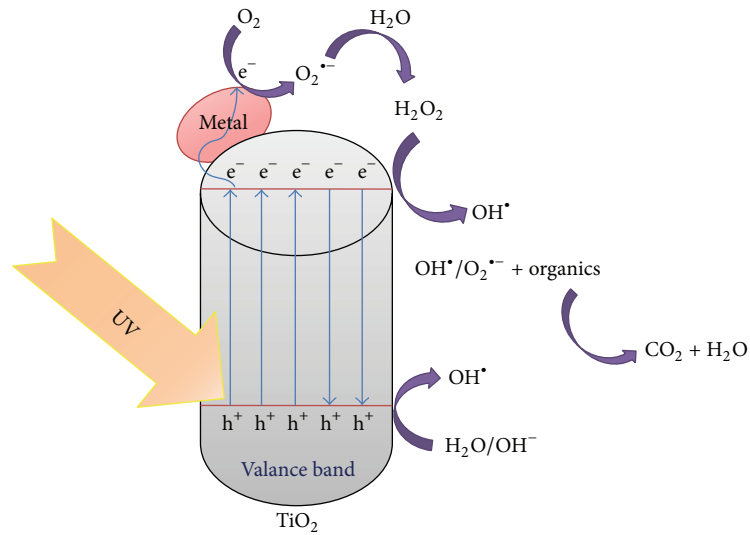


FIGURE 4: The mechanism of photodegradation of organic pollutants over metal/TiO₂ in water under UV light irradiation.

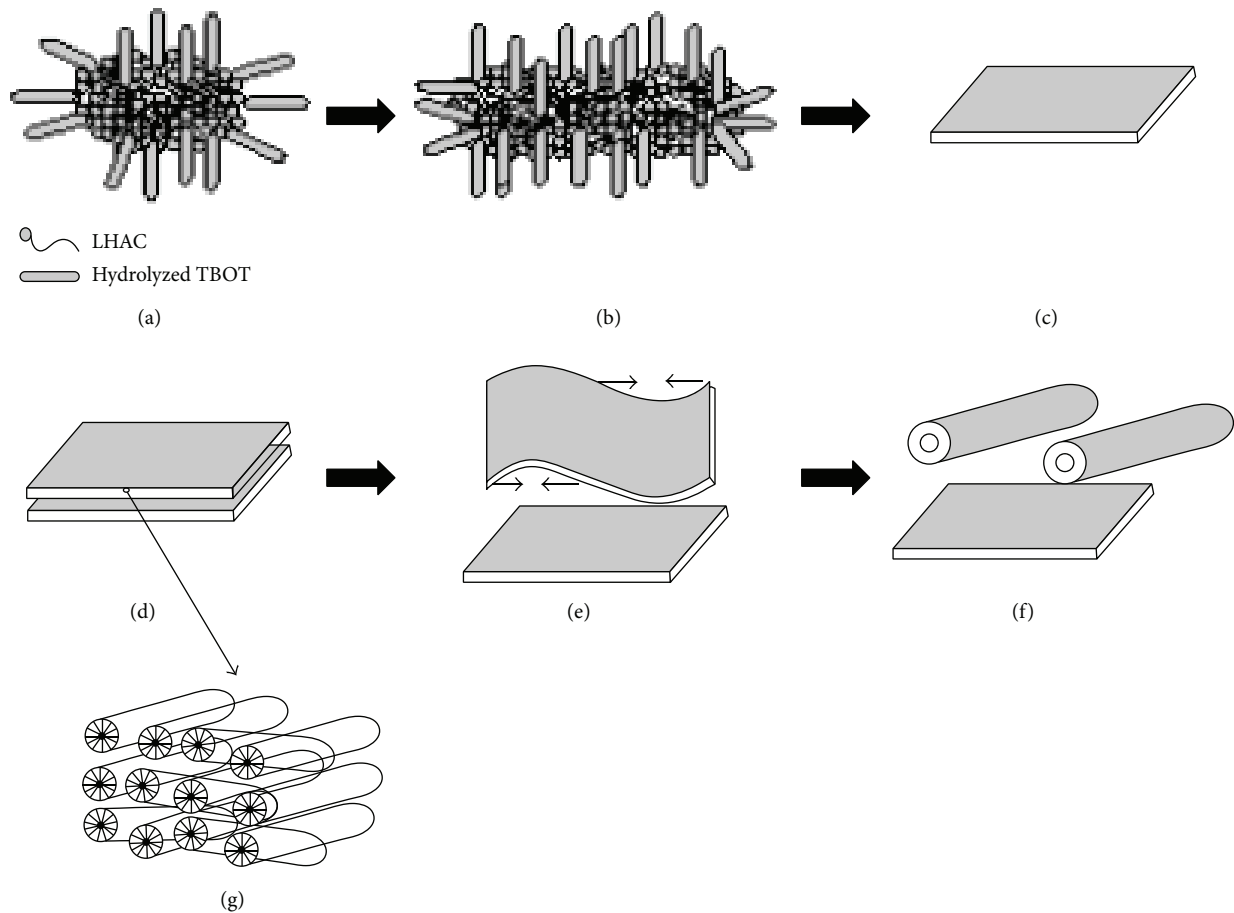


FIGURE 5: Proposed formation processes of the microtubules. (a) Globular aggregates containing LHAC and hydrolyzed TBOT. (b) Aggregates enlarged in size. (c) and (d) Mixed lamellar liquid-crystal phase membrane containing rodlike micelles. (e) Charge imbalance resulting in membrane curvature. (f) Further bending into tubules. (g) Random and segregated arrangement of rod micelle layers which are separated by bilayers of LHAC from bulk solution [42].

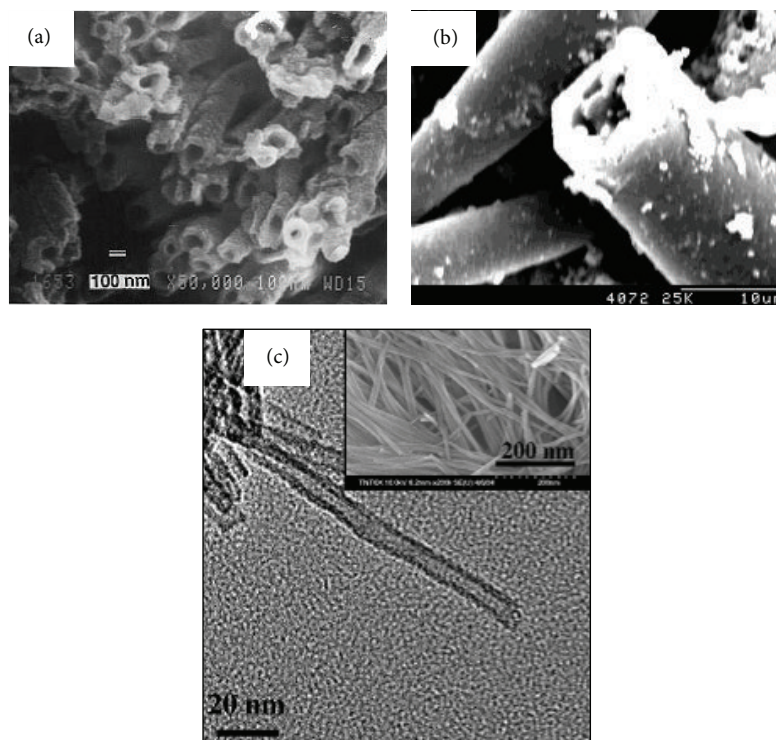


FIGURE 6: SEM image of TiO_2 nanotubes synthesized via an electrochemical deposition (a) [37] and templating methods (b) [42]; (c) FESEM (inset) and TEM images of TiO_2 nanotubes synthesized via a hydrothermal method [74].

PCO experiments of newly added humic acid. Yuan et al. [49] degraded humic acid using an enhanced photocatalytic process with Al and Fe codoped TiO_2 nanotubes as photocatalysts. They reported that calcination temperature, doping ions, and dosage of dopant would impact the PCO efficiency. Under an optimal condition of 1.0% codoped TiO_2 nanotubes containing 0.25:0.75 of Al: Fe, 79.4% of humic acid was degraded and a pseudo-first-order rate constant of 0.172 min^{-1} was achieved. Bisphenol A (BPA) is a pervasive chemical intermediate primarily from the production of polycarbonate plastics and epoxy resin [50]. Over the past few years, considerable effort has been devoted to the development of effective treatment technologies of the removal for bisphenol A (BPA), such as Fenton's reagent, ultrasonic cavitation, photocatalysis, and ozonation [51]. Recent research [52] displayed that a nearly complete removal of BPA was observed by Cu doped TiO_2 nanotubes. The pseudo-first-order rate constants for BPA photodegradation by Cu doped TiO_2 nanotubes at pH 7.0 were 2–5 times higher than that of pure Degussa P25. In a typical process, the generated electrons from TiO_2 with a lower conduction band could recombine with the holes in Cu, resulting in the reduction of recombination rate of electrons and holes. Then, the holes and electrons reacted with water and oxygen to form peroxy and hydroxyl radicals, respectively. In a supposed BPA degradation process, BPA radicals were generated via an electron transfer process. Subsequently, the BPA radicals triggered a suite of reactions of radical coupling, fragmentation, substitution, and elimination, which eventually

resulted in degradation of BPA [53]. However, further study is needed to prove this mechanism. BPA molecules were firstly photodegraded into some intermediates and products with smaller molecular weight, and these intermediates can be further oxidized to CO_2 and H_2O by the oxidative species produced in the PCO process. N-doped TiO_2 nanotubes also showed enhanced photocatalytic activity. Based on the research work of Chen and coworkers [54], 72.5% and 89.4% of methyl orange are photodegraded in the presence of TiO_2 nanotubes and N-doped TiO_2 nanotubes, respectively. In addition, the degradation rate of methyl orange over TiO_2 nanotubes without calcination is only 17.1%, which is lower than that (45.1%) of TiO_2 nanotubes calcined at 200°C . This is due to the narrow band gap and good crystallinity [55]. However, the photocatalytic activity of the TiO_2 nanotubes calcined at 400°C decreased, which can be attributed to the agglomeration and sintering damage of nanotubes caused by calcination at high temperature [56]. The specific surface area of the calcined material may also decrease due to the destruction of the nanotube structure.

4. TiO_2 Nanowires/Nanofibers

TiO_2 nanowires/nanofibers are common nanostructures of TiO_2 , as shown in Figure 7. Fujishima et al. [5] prepared two kinds of TiO_2 nanowires (TNW_{10} and TNW_{20}) for the degradation of humic acid. The investigation of photocatalytic activities of the synthesized materials showed that TNW_{10} performed better than TiO_2 P25 while TNW_{20}

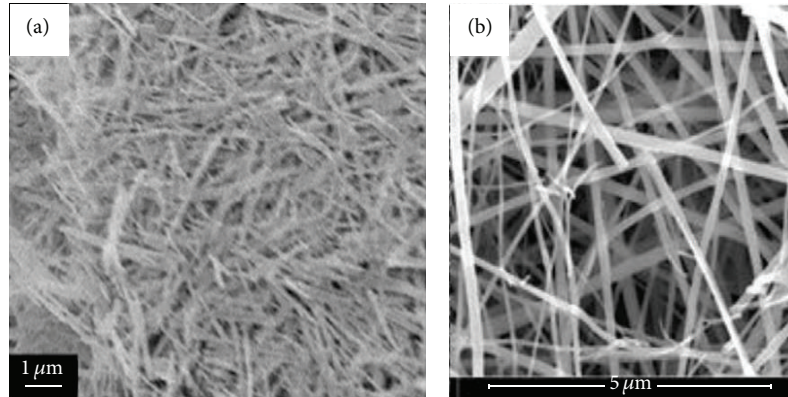
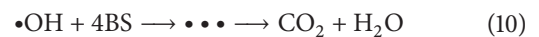
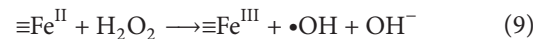
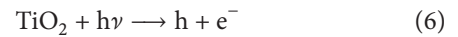


FIGURE 7: (a) FESEM of TiO_2 nanowires synthesized via a hydrothermal process [5], (b) FESEM of TiO_2 nanowires synthesized via an electrospun process [63].

was as good as P25. This is due to the high ratio aspect of the synthesized TiO_2 nanowires. Owing to the incomplete degradation, the degradation rates of total organic carbon content are lower than the removal rate of humic acid. This problem can be addressed by extending reaction time. Furthermore, the nanowires can be totally separated by a commercial microfiltration membrane with negligible membrane fouling. Pirilä and coworkers [57] studied the photocatalytic degradation of butanol in aqueous solutions using commercial TiO_2 , N-Pt-doped TiO_2 nanofibers, and N-Pd-doped TiO_2 nanofibers. The experimental results showed that the N-Pd-doped TiO_2 nanofibers had high efficiency in the degradation of butanol under UV irradiation as compared to the N-Pt-doped TiO_2 nanofibers and the commercial TiO_2 . It probably has relationship with the proton formation caused by better radical formation ability. GC-MS analysis revealed that butanol converted to some decomposition products such as aldehydes and ethanol [58]. Moreover, the synthesized materials had very similar BET surface area whereas they expressed relatively different reaction rate of the photocatalytic degradation, and it can be concluded that the specific surface area of the photocatalysts is not a key factor for the photocatalytic efficiency, while the doped metals played an important role in promoting the PCO reaction. In addition, Zn^{2+} doped TiO_2 nanofibers can be synthesized by electrospinning followed by calcination process [59]. The different dosage of Zn^{2+} would affect the photodegradation rate of methylene blue. For example, 96.1% of methylene blue was removed in the presence of TiO_2 nanofibers with 2 at. % Zn^{2+} , which was considered as an optimum doping dosage. Furthermore, the synthesized nanofibers were successfully recycled and reused for five times with little photocatalytic activity reduced. TiO_2 nanowires can also combine with other nanostructures, which can enhance the photocatalytic activity. Fe_2O_3 nanoparticles have been grafted onto TiO_2 nanowires by Qin and coworkers via a facile impregnation-solvothermal method [60]. The synthesized heterojunctions exhibited remarkable photocatalytic activity for photocatalytic oxidation of Direct Red 4BS in the presence of H_2O_2 . Moreover, the material showed good tolerance with respect

to organic matter poisoning due to the synergetic effect of TiO_2 nanowires and Fe_2O_3 nanoparticles. The size of Fe_2O_3 also affected the performance of the material, and it can be controlled by adjusting the impregnation duration time in the synthesis process. The possible reaction pathways are shown as follows [60]:



where the 4BS stands for the dye molecule and the $\bullet\bullet\bullet$ stands for the produced intermediates.

The heterojunction of TiO_2 nanofibers and Fe_2O_3 nanoparticles can promote the separation of photogenerated e^- and h^+ . The conduction band of Fe_2O_3 is more active as compared to that of TiO_2 , leading to the electrons transfer from TiO_2 to Fe^{III} and the further conversion to Fe^{II} . Since Fe^{II} promotes the decomposition of H_2O_2 to $\bullet\text{OH}$ [61], the photocatalytic activity was enhanced in this charge transfer process.

Liu and coworkers [62] prepared another kind of core-shell heterojunctions (TiO_2 -B nanowires and anatase nanocrystals) using a combination of hydrothermal and calcination methods. Similarly, the charge recombination rate was suppressed. The synthesized material tends to separate the e^- and h^+ into two different regions of the catalyst and thus enhances photocatalytic efficiency [63].

Recently, TiO_2 nanowire membranes were fabricated and applied for organics degradation in water purification process due to their photocatalytic activity, excellent chemical resistance, and thermal stability [64–66].

Microfiltration and ultrafiltration membranes have been successfully synthesized by Zhang and coworkers. The membranes were fabricated by TiO_2 nanowires with different

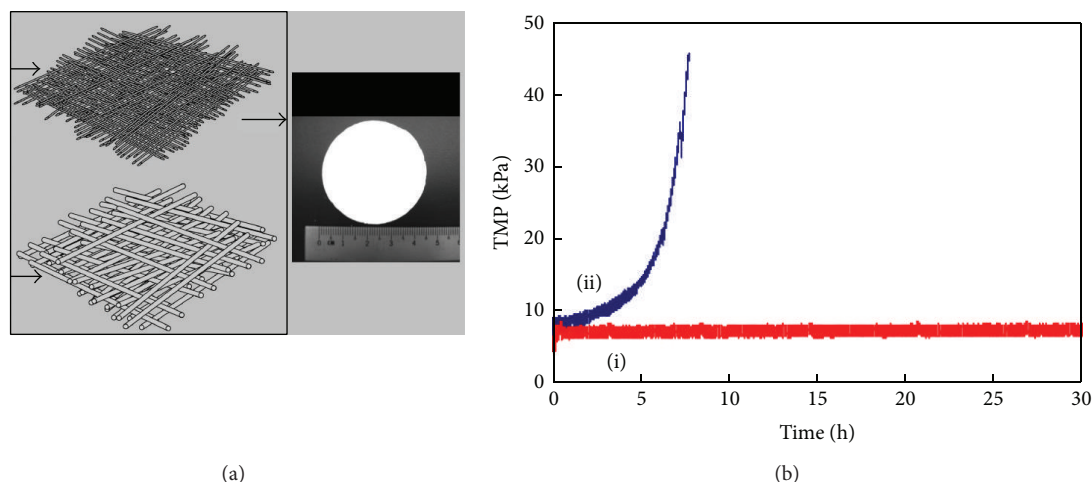


FIGURE 8: (a) TiO₂ nanowire membrane. (b) The transmembrane pressure change of TiO₂ nanowire membrane during filtration: (i) with UV irradiation and (ii) without UV irradiation.

diameters. In a typical synthesis process, the TiO₂ nanowires' suspension was first filtered via a vacuum filtration setup to form a porous functional layer. After drying at 105°C, a free-standing membrane can be peeled off from the filter. Finally, the membrane was pressurized under 5 bar at 120°C via a hot-press before being calcined at 550°C. As shown in Figure 8(a) [64], the synthesized membranes were robust and flexible and they possess multifunctions. In continuous experiments, the synthesized TiO₂ microfiltration nanowire membrane achieved near 100% and 93.6% removal rate of humic acid and total organic carbon, respectively. It is important to notice that the transmembrane pressure of the nanowire membrane did not change under UV light irradiation (Figure 8(b), [66]), indicating the antifouling and self-cleaning property of the synthesized TiO₂ nanowire membrane. The organic pollutants can be degraded concurrently during the filtration process. For a TiO₂ nanowire ultrafiltration membrane, the membrane showed a higher separation ability as well as excellent photocatalytic activity due to the enhanced selectivity. The rejection rate of humic acid by the ultrafiltration membrane can be achieved till 65% without UV irradiation, and even the bacteria (*E. coli*) can be intercepted by the membrane. In addition, the synthesized membranes were capable of overcoming the polymeric membrane problems such as membrane fouling and high-temperature applications. The antifouling property would facilitate the regeneration of the membrane and thus lower the cost for membrane cleaning.

TiO₂ nanowires membrane can also apply for the degradation of pharmaceuticals in water [65]. The membrane was directly fabricated by hydrothermal growth on Ti substrates at 180°C with the assistance of some organic solvents. Experimental details revealed that various pharmaceuticals such as norfluoxetine, atorvastatin, lincomycin, and fluoxetine were almost completely removed in a concurrent filtration and PCO process.

5. TiO₂ Nanobelts

TiO₂ nanobelts can be synthesized via CVD, solvothermal, and hydrothermal methods [67–69]. Gao and coworkers [69] reported the self-catalytic growth of codoped TiO₂ nanobelts via a metallorganic CVD method, and they found that rutile structure is dominant in the synthesized material. Furthermore, the material exhibited a magnetic anisotropy with a high coercive field value at room temperature. This property may facilitate the separation of the synthesized material after PCO process.

A solvothermal process was carried out to synthesize nitrogen-fluorine codoped TiO₂ (N-F-TiO₂) by He et al. [67]. Amorphous titania microspheres were used as precursors, which were prepared by the hydrolysis of Ti(OBu)₄. The synthesized N-F-TiO₂ nanobelts showed higher photocatalytic activity for the degradation of methyl orange as compared to that of TiO₂ P25. As shown in Figure 9, the codoped nanobelts photocatalyst exhibited the highest decrease in COD values for the degradation of organic compounds under both visible light and UV irradiation. This phenomenon can be attributed to the porous structures of the synthesized N-F-TiO₂, the increased specific surface area, and enhanced light adsorption. The N-F doping induced oxygen vacancy and led to the red shift in optical energy gap. Moreover, the nanobelt structure of the synthesized material would facilitate the capture of photogenerated photons and thus promote the formation of e⁻-h⁺.

Hydrothermal methods are more commonly used for TiO₂ nanobelts synthesis [70–72]. A commercial P25 TiO₂ can be used as a precursor, which is subsequently hydrothermally treated for nanobelts synthesis, as shown in Figure 10(a) [70]. However, the photocatalytic activity of the synthesized TiO₂ nanobelts was lower than that of P25. The degradation rates of methyl orange are 35% and 95% in the presence of

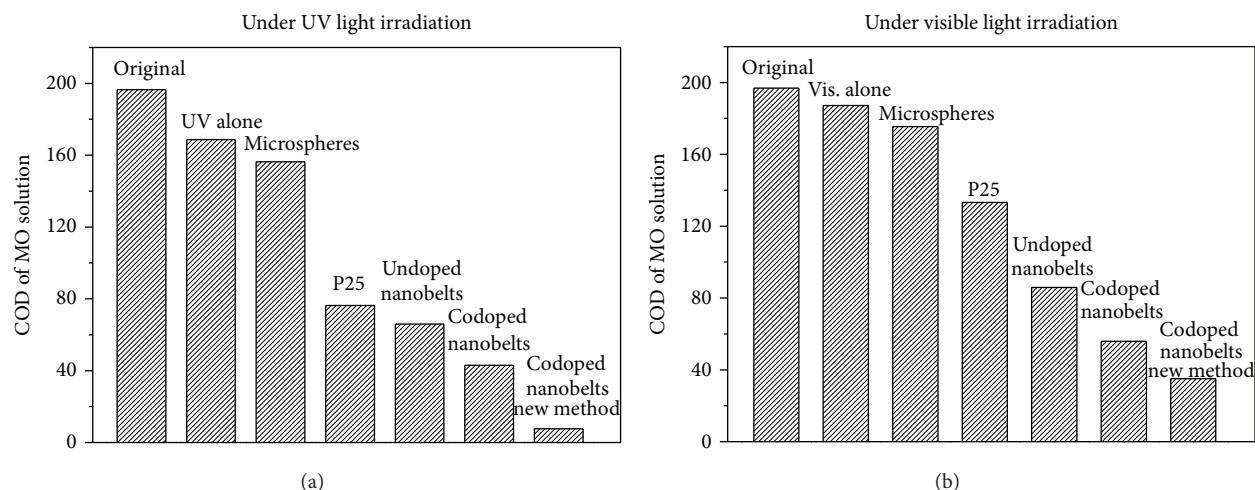


FIGURE 9: COD removal of the methyl orange solution after the photocatalytic degradation under UV and visible light irradiations [67].

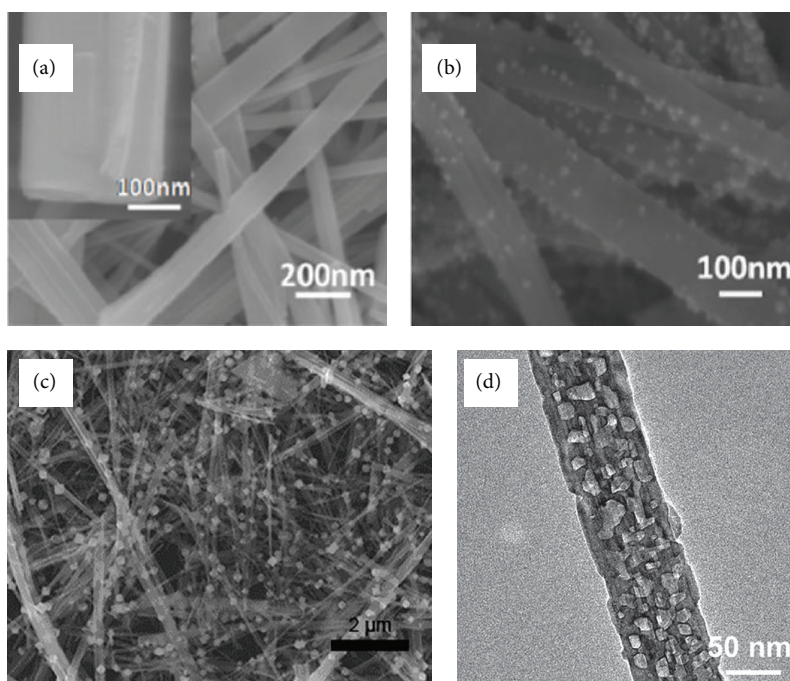


FIGURE 10: (a) SEM image of TiO₂ nanobelts synthesized via a hydrothermal process [70], (b) SEM image of NiO/TiO₂ heterojunctions [64], (c) SEM image of the Cu₂O/TiO₂ heterojunctions [71], and (d) TEM image of the synthesized CeO₂/TiO₂ nanobelt heterojunction [72].

TiO₂ nanobelts and P25, respectively. To further enhance the performance of the material for organics degradation, NiO nanoparticles were successfully deposited onto the nanobelts, as shown in Figure 10(b). The synthesized materials were applied for the decomposition of methyl orange under ultraviolet light irradiation. Experimental results indicated that heterojunction NiO-TiO₂ nanobelts showed better performance for the methyl orange removal as compared to both pure NiO nanoparticles and TiO₂ nanobelts. It can be attributed to the increased specific surface area and extended e⁻-h⁺ lifetime.

Similar with this kind of heterojunction, other metal oxides nanoparticles and TiO₂ nanobelts can also be combined together for the improvement of photocatalytic activity. Zhang et al. prepared Cu₂O/TiO₂ heterojunctions using a combination process of hydrothermal method and chemical precipitation method [71]. The TiO₂ nanobelt acted as a substrate, and the dosage of Cu₂O can be controlled by adjusting the concentration of the precursor (copper sulfate). Figure 10(c) shows that Cu₂O nanoparticles were evenly grafted onto the TiO₂ nanobelts. Moreover, the synthesized heterojunction possessed higher adsorbability as compared

to pure TiO₂ nanobelt. Although the photocatalytic activity of the synthesized material showed a little decrease, the decoloration activity of the material for organics was enhanced. This phenomenon is attributed to the strong adsorption of methyl orange molecules on the surface of Cu₂O with exposure of {1 1 1} facets.

Tian et al. synthesized novel CeO₂/TiO₂ nanobelt heterojunctions via a facile hydrothermal process, as shown in Figure 10(d) [72]. Compared with TiO₂, the synthesized CeO₂/TiO₂ exhibited enhanced photocatalytic performance for the degradation of methyl orange due to the proposed capture-photodegradation release mechanism. During PCO process, methyl orange molecules were captured by CeO₂ nanoparticles, then degraded by photogenerated radicals, and finally released to the solution. Since the PCO process is mainly conducted at the surface of photocatalysts, the adsorption capacity of CeO₂ nanoparticles was found to be important for the performance of PCO process. The synthesized CeO₂/TiO₂ nanobelt heterojunctions possessed good stability, high activity, and recyclable properties.

TiO₂ nanobelts have been applied to photocatalyze the oxidation of pharmaceutical contaminants in wastewater. Liang and coworkers [73] prepared anatase phase TiO₂ nanobelts with 30–100 nm in width and 10 μm in length via a high temperature hydrothermal method. Their results showed that persistent pharmaceuticals such as malachite green, naproxen, carbamazepine, and theophylline can be efficiently photodegraded in the presence of the synthesized TiO₂ nanobelts. The photogenerated active oxygen species such as hydroxyl radical, h⁺, and hydrogen peroxide were determined and it was proven that they played an important role in the PCO process. Investigation on operation parameters presented that photodegradation of the pharmaceuticals was evidently dependent on pH, illumination time, temperature, and concentrations of contaminants. This work heralds a pathway towards the photodegradation of organics in actual wastewater. TiO₂ nanobelts can have potential in applications of industrial wastewater.

6. Conclusions

This review paper overviews the recent development in synthesis of 1D TiO₂ nanostructures and their photocatalytic applications for organics degradation. Thanks to the development of nanotechnology, significant progress has been achieved in controllable synthesis of 1D TiO₂ materials with different aspect ratio and inner structure (solid nanowire, nanorod, nanobelt, and hollow nanotube). Various synthetic strategies have been developed, prompting the subsequent exploration of their photocatalytic properties and the practical environmental applications. Under the excitation of UV light, efficient degradation of organic pollutants, such as NOMs, POPs, dyes, phenols, and pharmaceuticals, has been achieved by numerous groups. On contrast, solar-light-active 1D TiO₂ material is still in its infant stage. Since solar energy is economical, solar photocatalysis using 1D TiO₂ nanostructures would be a promising pathway for the degradation of organic pollutants. It is important to note that

the application of 1D TiO₂ in industry cannot be successful without solar energy assistance. Thus, many future works should concentrate on the synthesis of solar-light-active TiO₂ materials. Doping of 1D TiO₂ is considered as a possible way to lower the band gap of TiO₂ and thus enhance the activity of TiO₂ under solar light. Moreover, sensitization of 1D TiO₂ nanostructures with other narrow-band-gap semiconductor and noble metals (e.g., Au or Ag) may further enhance the photocatalytic activity by suppressing the charge recombination rate.

Alternatively, 1D nanostructured TiO₂ materials can be used as building blocks to assemble active and integrated nanosystems, such as TiO₂ nanorod, nanotube, or nanowire membrane or film. The coupling of semiconductor photocatalysis of 1D nanomaterials and engineering design such as self-cleaning membrane filtration and microreactor construction might significantly broaden the application range of 1D TiO₂ photocatalysts. Rapid progress is expected and will mainly occur in developing economic and scalable synthetic strategy of 1D TiO₂ nanostructures and their industry-scale applications in water treatment process.

Conflict of Interests

The authors declare that there is no conflict of interests regarding the publication of this paper.

References

- [1] G. T. Daigger, B. E. Rittmann, S. Adham, and G. Andreottola, "Are membrane bioreactors ready for widespread application?" *Environmental Science and Technology*, vol. 39, no. 19, pp. 399A–406A, 2005.
- [2] M. A. Shannon, P. W. Bohn, M. Elimelech, J. G. Georgiadis, B. J. Marias, and A. M. Mayes, "Science and technology for water purification in the coming decades," *Nature*, vol. 452, no. 7185, pp. 301–310, 2008.
- [3] T. Zhang, X. Zhang, J. Ng, H. Yang, J. Liu, and D. D. Sun, "Fabrication of magnetic cryptomelane-type manganese oxide nanowires for water treatment," *Chemical Communications*, vol. 47, no. 6, pp. 1890–1892, 2011.
- [4] M. Y. Ghaly, T. S. Jamil, I. E. El-Seesy, E. R. Souaya, and R. A. Nasr, "Treatment of highly polluted paper mill wastewater by solar photocatalytic oxidation with synthesized nano TiO₂," *Chemical Engineering Journal*, vol. 168, no. 1, pp. 446–454, 2011.
- [5] A. Fujishima, T. N. Rao, and D. A. Tryk, "Titanium dioxide photocatalysis," *Journal of Photochemistry and Photobiology C*, vol. 1, no. 1, pp. 1–21, 2000.
- [6] S. Ahmed, M. G. Rasul, R. Brown, and M. A. Hashib, "Influence of parameters on the heterogeneous photocatalytic degradation of pesticides and phenolic contaminants in wastewater: a short review," *Journal of Environmental Management*, vol. 92, no. 3, pp. 311–330, 2010.
- [7] A. L. Linsebigler, G. Lu, and J. T. Yates Jr., "Photocatalysis on TiO₂ surfaces: principles, mechanisms, and selected results," *Chemical Reviews*, vol. 95, no. 3, pp. 735–758, 1995.
- [8] T. Zhang, X. Yan, and D. D. Sun, "Hierarchically multifunctional K-OMS-2/TiO₂/Fe₃O₄ heterojunctions for the photocatalytic oxidation of humic acid under solar light irradiation," *Journal of Hazardous Materials*, vol. 243, pp. 302–310, 2012.

- [9] C. L. Bianchi, S. Gatto, C. Pirola et al., "Photocatalytic degradation of acetone, acetaldehyde and toluene in gas-phase: comparison between nano and micro-sized TiO₂," *Applied Catalysis B: Environmental*, vol. 146, pp. 123–130, 2013.
- [10] J. Herrmann, "Heterogeneous photocatalysis: fundamentals and applications to the removal of various types of aqueous pollutants," *Catalysis Today*, vol. 53, no. 1, pp. 115–129, 1999.
- [11] M. Styliadi, D. I. Kondarides, and X. E. Verykios, "Visible light-induced photocatalytic degradation of Acid Orange 7 in aqueous TiO₂ suspensions," *Applied Catalysis B: Environmental*, vol. 47, no. 3, pp. 189–201, 2004.
- [12] M. M. Khin, A. S. Nair, V. J. Babu, R. Murugan, and S. Ramakrishna, "A review on nanomaterials for environmental remediation," *Energy and Environmental Science*, vol. 5, no. 8, pp. 8075–8109, 2012.
- [13] X. Quan, S. Yang, X. Ruan, and H. Zhao, "Preparation of titania nanotubes and their environmental applications as electrode," *Environmental Science & Technology*, vol. 39, no. 10, pp. 3770–3775, 2005.
- [14] X. Chen and S. S. Mao, "Titanium dioxide nanomaterials: synthesis, properties, modifications and applications," *Chemical Reviews*, vol. 107, no. 7, pp. 2891–2959, 2007.
- [15] C. W. Lai, J. C. Juan, W. B. Ko, and S. B. A. Hamid, "An overview: recent development of titanium oxide nanotubes as photocatalyst for dye degradation," *International Journal of Photoenergy*, vol. 2014, Article ID 524135, 14 pages, 2014.
- [16] F. Niu, L. Zhang, C. Chen et al., "Hydrophilic TiO₂ porous spheres anchored on hydrophobic polypropylene membrane for wettability induced high photodegrading activities," *Nanoscale*, vol. 2, no. 8, pp. 1480–1484, 2010.
- [17] J. Qu and C. Lai, "One-dimensional TiO₂ nanostructures as photoanodes for dye-sensitized solar cells," *Journal of Nanomaterials*, vol. 2003, Article ID 762730, 11 pages, 2013.
- [18] S. Liang, F. Teng, G. Bulgan, R. Zong, and Y. Zhu, "Effect of phase structure of MnO₂ nanorod catalyst on the activity for CO oxidation," *Journal of Physical Chemistry C*, vol. 112, no. 14, pp. 5307–5315, 2008.
- [19] Y. Lia, M. Guo, M. Zhang, and X. Wang, "Hydrothermal synthesis and characterization of TiO₂ nanorod arrays on glass substrates," *Materials Research Bulletin*, vol. 4, pp. 1232–1237, 2009.
- [20] A. S. Attar, M. S. Ghamsari, F. Hajjesmaeilbaigi, S. Mirdamadi, K. Katagiri, and K. Koumoto, "Sol-gel template synthesis and characterization of aligned anatase-TiO₂ nanorod arrays with different diameter," *Materials Chemistry and Physics*, vol. 113, no. 2-3, pp. 856–860, 2009.
- [21] J. J. Wu and C. C. Yu, "Aligned TiO₂ nanorods and nanowalls," *Journal of Physical Chemistry B*, vol. 108, no. 11, pp. 3377–3379, 2004.
- [22] X. J. Feng, J. Zhai, and L. Jiang, "The fabrication and switchable superhydrophobicity of TiO₂ nanorod films," *Angewandte Chemie International Edition*, vol. 44, no. 32, pp. 5115–5118, 2005.
- [23] S. Feng, J. Yang, M. Liu et al., "CdS quantum dots sensitized TiO₂ nanorod-array-film photoelectrode on FTO substrate by electrochemical atomic layer epitaxy method," *Electrochimica Acta*, vol. 8, pp. 321–326, 2012.
- [24] K. Melghit and S. S. Al-Rabaniyah, "Photodegradation of Congo red under sunlight catalysed by nanorod rutile TiO₂," *Journal of Photochemistry and Photobiology A: Chemistry*, vol. 184, no. 3, pp. 331–334, 2006.
- [25] F. Han, V. S. R. Kambala, M. Srinivasan, D. Rajarathnam, and R. Naidu, "Tailored titanium dioxide photocatalysts for the degradation of organic dyes in wastewater treatment: a review," *Applied Catalysis A: General*, vol. 359, no. 1-2, pp. 25–40, 2009.
- [26] H. Yu, J. Yu, B. Cheng, and J. Lin, "Synthesis, characterization and photocatalytic activity of mesoporous titania nanorod/titanate nanotube composites," *Journal of Hazardous Materials*, vol. 147, no. 1-2, pp. 581–587, 2007.
- [27] Q. Mu, Y. Li, Q. Zhang, and H. Wang, "Template-free formation of vertically oriented TiO₂ nanorods with uniform distribution for organics-sensing application," *Journal of Hazardous Materials*, vol. 188, no. 1-3, pp. 363–368, 2011.
- [28] M. Gao, Y. Li, M. Guo, M. Zhang, and X. Wang, "Effect of substrate pretreatment on controllable growth of TiO₂ nanorod arrays," *Journal of Materials Science and Technology*, vol. 28, pp. 577–586, 2012.
- [29] Q. L. Yu and H. J. H. Brouwers, "Design of a novel photocatalytic gypsum plaster: with the indoor air purification property," *Advanced Materials Research*, vol. 65, pp. 751–756, 2013.
- [30] Ö. Kerkez and İ. Boz, "Photo(electro)catalytic activity of Cu²⁺-modified TiO₂ nanorod array thin films under visible light irradiation," *Journal of Physics and Chemistry of Solids*, vol. 75, pp. 611–618, 2014.
- [31] M. Lee, H. J. Yun, S. Yu, and J. Yi, "Enhancement in photocatalytic oxygen evolution via water oxidation under visible light on nitrogen-doped TiO₂ nanorods with dominant reactive 102 facets," *Catalysis Communications*, vol. 43, pp. 11–15, 2014.
- [32] Y. Lv, Z. Fu, B. Yang et al., "Preparation N-F-codoped TiO₂ nanorod array by liquid phase deposition as visible light photocatalyst," *Materials Research Bulletin*, vol. 46, no. 3, pp. 361–365, 2011.
- [33] H. Zhu, B. Yang, J. Xu et al., "Construction of Z-scheme type CdS-Au-TiO₂ hollow nanorod arrays with enhanced photocatalytic activity," *Applied Catalysis B: Environmental*, vol. 90, no. 3-4, pp. 463–469, 2009.
- [34] M. Wu, B. Yang, Y. Lv et al., "Efficient one-pot synthesis of Ag nanoparticles loaded on N-doped multiphase TiO₂ hollow nanorod arrays with enhanced photocatalytic activity," *Applied Surface Science*, vol. 256, no. 23, pp. 7125–7130, 2010.
- [35] J. Z. Y. Tan, Y. Fernández, D. Liu, M. M. Valer, J. Bian, and X. Zhang, "Photoreduction of CO₂ using copper-decorated TiO₂ nanorod films with localized surface plasmon behavior," *Chemical Physics Letters*, vol. 531, pp. 149–154, 2012.
- [36] Y. Liu, B. Zhou, J. Bai et al., "Efficient photochemical water splitting and organic pollutant degradation by highly ordered TiO₂ nanopore arrays," *Applied Catalysis B: Environmental*, vol. 89, pp. 142–148, 2009.
- [37] P. Hoyer, "Formation of a titanium dioxide nanotube array," *Langmuir*, vol. 12, no. 6, pp. 1411–1413, 1996.
- [38] V. Zwilling, E. Darque-Ceretti, A. Boutry-Forveille, D. David, M. Y. Perrin, and M. Aucouturier, "Structure and physicochemistry of anodic oxide films on titanium and TA6V alloy," *Surface and Interface Analysis*, vol. 27, no. 7, pp. 629–637, 1999.
- [39] N. Liu, X. Chen, J. Zhang, and J. W. Schwank, "A review on TiO₂-based nanotubes synthesized via hydrothermal method: formation mechanism, structure modification, and photocatalytic applications," *Catalysis Today*, vol. 225, pp. 34–51, 2014.
- [40] D. Gong, C. A. Grimes, O. K. Varghese et al., "Titanium oxide nanotube arrays prepared by anodic oxidation," *Journal of Materials Research*, vol. 16, no. 12, pp. 3331–3334, 2001.

- [41] D. V. Bavykin, J. M. Friedrich, and F. C. Walsh, "Protonated titanates and TiO₂ nanostructured materials: synthesis, properties, and applications," *Advanced Materials*, vol. 18, no. 21, pp. 2807–2824, 2006.
- [42] T. Peng, A. Hasegawa, J. Qiu, and K. Hirao, "Fabrication of titania tubules with high surface area and well-developed mesostructural walls by surfactant-mediated templating method," *Chemistry of Materials*, vol. 15, no. 10, pp. 2011–2016, 2003.
- [43] J. H. Jung, H. Kobayashi, K. J. C. van Bommel, S. Shinkai, and T. Shimizu, "Creation of novel helical ribbon and double-layered nanotube TiO₂ structures using an organogel template," *Chemistry of Materials*, vol. 14, no. 4, pp. 1445–1447, 2002.
- [44] C. L. Wong, Y. N. Tan, and A. R. Mohamed, "A review on the formation of titania nanotube photocatalysts by hydrothermal treatment," *Journal of Environmental Management*, vol. 92, no. 7, pp. 1669–1680, 2011.
- [45] T. Kasuga, M. Hiramatsu, A. Hoson, T. Sekino, and K. Niihara, "Formation of titanium oxide nanotube," *Langmuir*, vol. 14, no. 12, pp. 3160–3163, 1998.
- [46] X. Chen, S. Cao, X. Weng, H. Wang, and Z. Wu, "Effects of morphology and structure of titanate supports on the performance of ceria in selective catalytic reduction of NO," *Catalysis Communications*, vol. 26, pp. 178–182, 2012.
- [47] B. K. Vijayan, N. M. Dimitrijevic, J. Wu, and K. A. Gray, "The effects of Pt doping on the structure and visible light photoactivity of titania nanotubes," *Journal of Physical Chemistry C*, vol. 114, no. 49, pp. 21262–21269, 2010.
- [48] Z. Tang, F. Li, Y. Zhang, X. Fu, and Y. J. Xu, "Composites of titanate nanotube and carbon nanotube as photocatalyst with high mineralization ratio for gas-phase degradation of volatile aromatic pollutant," *Journal of Physical Chemistry C*, vol. 115, no. 16, pp. 7880–7886, 2011.
- [49] R. Yuan, B. Zhou, D. Hua, and C. Shi, "Enhanced photocatalytic degradation of humic acids using Al and Fe co-doped TiO₂ nanotubes under UV/ozonation for drinking water purification," *Journal of Hazardous Materials*, vol. 262, pp. 527–538, 2013.
- [50] J. Kang, D. Aasi, and Y. Katayama, "Bisphenol A in the aquatic environment and its endocrine-disruptive effects on aquatic organisms," *Critical Reviews in Toxicology*, vol. 37, no. 7, pp. 607–625, 2007.
- [51] T. Zhang, X. W. Zhang, X. L. Yan, J. W. Ng, Y. J. Wang, and D. D. Sun, "Removal of bisphenol A via a hybrid process combining oxidation on β -MnO₂ nanowires with microfiltration," *Colloids and Surfaces A: Physicochemical and Engineering Aspects*, vol. 392, no. 1, pp. 198–204, 2011.
- [52] R. A. Doong, S. M. Chang, and C. W. Tsai, "Enhanced photoactivity of Cu-deposited titanate nanotubes for removal of bisphenol A," *Applied Catalysis B*, vol. 129, pp. 48–55, 2013.
- [53] K. Lin, W. Liu, and J. Gan, "Oxidative removal of bisphenol A by manganese dioxide: efficacy, products, and pathways," *Environmental Science and Technology*, vol. 43, no. 10, pp. 3860–3864, 2009.
- [54] Y. Y. Chen, S. M. Zhang, Y. Yu et al., "Synthesis, characterization, and photocatalytic activity of N-doped TiO₂ nanotubes," *Journal of Dispersion Science and Technology*, vol. 29, no. 2, pp. 245–249, 2008.
- [55] H. Tokudome and M. Miyauchi, "N-doped TiO₂ nanotube with visible light activity," *Chemistry Letters*, vol. 33, no. 9, pp. 1108–1109, 2004.
- [56] J. C. Xu, M. Lu, X. Y. Guo, and H. L. Li, "Zinc ions surface-doped titanium dioxide nanotubes and its photocatalysis activity for degradation of methyl orange in water," *Journal of Molecular Catalysis A: Chemical*, vol. 226, pp. 123–127, 2005.
- [57] M. Pirilä, R. Lenkkeri, W. M. Goldmann, K. Kordás, M. Huuhtanen, and R. L. Keiski, "Photocatalytic degradation of butanol in aqueous solutions by TiO₂ nanofibers," *Topics in Catalysis*, vol. 56, no. 9–10, pp. 630–636, 2013.
- [58] J. Kirchnerova, M.-L. Herrera Cohen, C. Guy, and D. Klvana, "Photocatalytic oxidation of *n*-butanol under fluorescent visible light lamp over commercial TiO₂ (Hombicat UV100 and Degussa P25)," *Applied Catalysis A: General*, vol. 282, no. 1–2, pp. 321–332, 2005.
- [59] L. Song, J. Xiong, Q. Jiang, P. Du, H. Cao, and X. Shao, "Synthesis and photocatalytic properties of Zn²⁺ doped anatase TiO₂ nanofibers," *Materials Chemistry and Physics*, vol. 14, no. 1, pp. 77–81, 2013.
- [60] L. Qin, X. Pan, L. Wang, X. Sun, G. Zhang, and X. Guo, "Facile preparation of mesoporous TiO₂(B) nanowires with well-dispersed Fe₂O₃ nanoparticles and their photochemical catalytic behavior," *Applied Catalysis B: Environmental*, vol. 150–151, pp. 544–553, 2014.
- [61] M. A. Fontecha-Cámara, M. A. Álvarez-Merino, F. Carrasco-Marín, M. V. López-Ramón, and C. Moreno-Castillab, "Heterogeneous and homogeneous Fenton processes using activated carbon for the removal of the herbicide amitrole from water," *Applied Catalysis B: Environmental*, vol. 101, pp. 425–430, 2011.
- [62] B. Liu, A. Khare, and E. S. Aydil, "TiO₂-B/anatase core-shell heterojunction nanowires for photocatalysis," *ACS Applied Materials and Interfaces*, vol. 3, no. 11, pp. 4444–4450, 2011.
- [63] S. Ramasundaram, H. N. Yoo, K. G. Song, J. Lee, K. J. Choi, and S. W. Hong, "Titanium dioxide nanofibers integrated stainless steel filter for photocatalytic degradation of pharmaceutical compounds," *Journal of Hazardous Materials*, vol. 258–259, pp. 124–132, 2013.
- [64] X. W. Zhang, T. Zhang, J. Ng, and D. D. Sun, "High-performance multifunctional TiO₂ nanowire ultrafiltration membrane with a hierarchical layer structure for water treatment," *Advanced Functional Materials*, vol. 19, pp. 3731–3736, 2009.
- [65] A. Hu, X. Zhang, K. D. Oakes, P. Peng, Y. N. Zhou, and M. R. Servos, "Hydrothermal growth of free standing TiO₂ nanowire membranes for photocatalytic degradation of pharmaceuticals," *Journal of Hazardous Materials*, vol. 189, no. 1–2, pp. 278–285, 2011.
- [66] X. W. Zhang, A. J. Du, P. Lee, D. D. Sun, and J. O. Leckie, "TiO₂ nanowire membrane for concurrent filtration and photocatalytic oxidation of humic acid in water," *Journal of Membrane Science*, vol. 313, no. 1–2, pp. 44–51, 2008.
- [67] Z. L. He, W. X. Que, J. Chen, X. T. Yin, Y. C. He, and J. B. Ren, "Photocatalytic degradation of methyl orange over nitrogen-fluorine codoped TiO₂ nanobelts prepared by solvothermal synthesis," *ACS Applied Materials & Interfaces*, vol. 4, pp. 6815–6825, 2012.
- [68] N. T. Q. Hoa, Z. Lee, S. H. Kang, V. Radmilovic, and E. T. Kim, "Synthesis and ferromagnetism of Co-doped TiO(2-delta) nanobelts by metallorganic chemical vapor deposition," *Applied Physics Letters*, vol. 92, no. 12, 2008.
- [69] P. Gao, D. Bao, Y. Wang et al., "Epitaxial growth route to crystalline TiO₂ nanobelts with optimizable electrochemical performance," *ACS Applied Materials & Interfaces*, vol. 2, pp. 368–373, 2013.
- [70] J. Lin, J. Shen, T. Wang et al., "Enhancement of photocatalytic properties of TiO₂ nanobelts through surface-coarsening and

- surface nanoheterostructure construction,” *Materials Science and Engineering B*, vol. 176, pp. 921–925, 2011.
- [71] J. Zhang, W. Liu, X. Wang, B. Hu, and H. Liu, “Enhanced decoloration activity by $\text{Cu}_2\text{O}@\text{TiO}_2$ nanobelts heterostructures via a strong adsorption-weak photodegradation process,” *Applied Surface Science*, vol. 282, pp. 84–91, 2013.
- [72] J. Tian, Y. Sang, Z. Zhao et al., “Enhanced photocatalytic performances of $\text{CeO}_2/\text{TiO}_2$ nanobelt heterostructures,” *Small*, vol. 9, no. 2, pp. 3864–3872, 2013.
- [73] R. Liang, A. Hu, W. J. Li, and Y. N. Zhou, “A chemical approach to accurately characterize the coverage rate of gold nanoparticles,” *Journal of Nanoparticle Research*, vol. 15, p. 1900, 2013.
- [74] M. A. Khan, H. Jung, and O. B. Yang, “Synthesis and characterization of ultrahigh crystalline TiO_2 nanotubes,” *Journal of Physical Chemistry B*, vol. 110, no. 13, pp. 6626–6630, 2006.
- [75] L. Li, X. Qin, G. Wang, L. Qi, G. Du, and Z. Hu, “Synthesis of anatase TiO_2 nanowires by modifying TiO_2 nanoparticles using the microwave heating method,” *Applied Surface Science*, vol. 257, no. 18, pp. 8006–8012, 2011.
- [76] J. Lee, Y. Lee, H. Song, D. Jang, and Y. Choa, “Synthesis and characterization of TiO_2 nanowires with controlled porosity and microstructure using electrospinning method,” *Current Applied Physics*, vol. 11, no. 1, pp. S210–S214, 2011.

Research Article

Effect of Mn Doping on Properties of CdS Quantum Dot-Sensitized Solar Cells

Tianxing Li, Xiaoping Zou, and Hongquan Zhou

Research Center for Sensor Technology, Beijing Key Laboratory for Sensor, Ministry of Education, Key Laboratory for Modern Measurement and Control Technology, School of Applied Sciences, School of Instrumentation Science and Optoelectronics Engineering, Beijing Information Science and Technology University, Jianxiang Qiao Campus, Beijing 100101, China

Correspondence should be addressed to Xiaoping Zou; xpzou2005@gmail.com

Received 4 April 2014; Accepted 4 July 2014; Published 17 July 2014

Academic Editor: Chuanyi Wang

Copyright © 2014 Tianxing Li et al. This is an open access article distributed under the Creative Commons Attribution License, which permits unrestricted use, distribution, and reproduction in any medium, provided the original work is properly cited.

Quantum dot-sensitized solar cells (QDSSCs) have received extensive attention in recent years due to their higher theoretical conversion efficiency and lower production costs. However, the photoelectric conversion efficiency of QDSSCs is still lower than the DSSCs because of the severe recombination of electrons of quantum dots conduction band. In order to improve the photoelectric conversion efficiency of QDSSCs, impurity element Mn^{2+} is doped into the precursor solution of cadmium sulfide (CdS). By optimizing the experimental parameters, the photoelectric conversion efficiency of QDSSCs can be greatly improved. For the deposition of a fixed number of six times, the photoelectric conversion efficiency shows the maximum value (1.51%) at the doped ratio of 1:10.

1. Introduction

Quantum dot-sensitized solar cells (QDSSCs) have been recently drawing great attention due to the characteristics of quantum dots (QDs), such as high absorption coefficient, tunable band gap, and multiple exciton generation (MEG) effect [1–4]. However, its photoelectric conversion efficiency is still low compared to the theoretical value. The main factors limiting the efficiency of QDSSCs include the carriers recombination with redox couple on the semiconductor interface, a slower rate of hole transport, and the properties of the electrode. Recently, many efforts on the improvement of quantum dots (QDs), electrolyte, and electrode have made quite a lot of progress [5–7]. Among those researches doping optically active transition metal ions, such as Mn, Mg, Co, Cu, and In, has achieved obvious improvement in the photoelectric conversion efficiency of QDSSCs [8–12]. The doped system modifies the electronic and photophysical properties of QDs [13]. In addition, it is also possible to tune the optical and electronic properties of semiconductor nanocrystals by controlling the type of dopant [14]. Very

recently, Santra and Kamat fabricated Mn-doped-CdS/CdSe quantum dot solar cells and yielded the efficiency (5.42%) for the QDSSCs [8]. And, the next year, Lee et al. reported on a PbS:Hg QD-sensitized solar cells with an extremely high photocurrent density (38 mA/cm^2) [15].

CdS, as an important II-VI semiconductor compound, with the band gap of 2.42 eV at room temperature [16], has good optical absorption properties in the visible region. Simultaneously, it has a large extinction coefficient and photochemical stability. Moreover, CdS quantum dots of different sizes can be synthesized to achieve broad spectral absorption through the relationship between the particle size and energy level of QDs. Therefore, the CdS quantum dots became a favorite QDs material for many researchers [17].

By the way of doping Mn atoms into CdS quantum dots, we can further regulate the properties of quantum dots for expanding the range of visible light absorption and improve the stability of cells [18, 19].

In this paper, we introduced impurity element Mn^{2+} into the precursor solution of cadmium sulfide (CdS). And Mn-doped-CdS QDs have been in situ deposited onto TiO_2

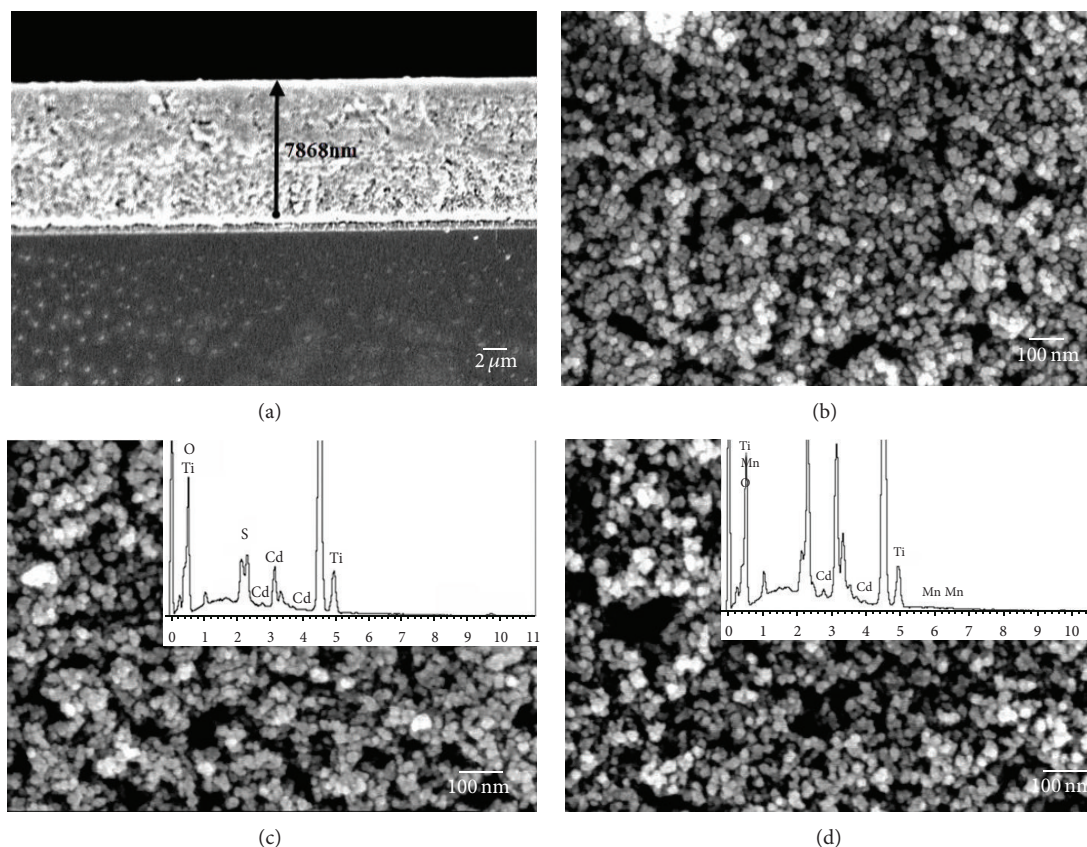


FIGURE 1: SEM images of (a) cross section of Mn-doped-CdS deposition of TiO₂ photoanode; (b) pure TiO₂ mesoporous film surface; (c) the surface of TiO₂ mesoporous film sensitized by CdS quantum dots; and (d) the surface of TiO₂ mesoporous film sensitized by Mn-doped-CdS quantum dots. Among them, the inset in the following two graphs is the corresponding EDS spectrum.

mesoporous substrates by the successive ionic layer adsorption and reaction (SILAR). Then, we assembled Mn-doped-CdS quantum dot-sensitized solar cells with the structure of photoanode/polysulfide electrolyte/Pt counter and incidentally discussed the impact of doping. We emphatically analyzed the effect of doped ratio and SILAR cycles on the properties of QDSSCs. At last, the power conversion efficiency of Mn-doped-CdS QDSSCs showed 1.51% under air mass (AM) 1.5 condition (100 mW/cm²) with the optimized parameters (the doped ratio of Mn:CdS fixed on 1:10 and the six cycles of SILAR) obtained by experiment. Although the conversion efficiency is still low, it is much higher than the undoped CdS QDSSCs. And, with increased doping ratio, the efficiency had no further improvement but beginning to reduce.

2. Experimental

The TiO₂ nanoparticles are uniformly coated on the surface of the FTO (fluorine-doped tin oxide) by screen printing method and then annealed at 450°C for 30 min. And the counter electrode is prepared with Pt which is obtained from the thermal decomposition of chloroplatinic acid. Like the preparation of TiO₂ photoanode, the counter electrode has also been annealed at 450°C for 30 min. A mixed methanol

and deionized water solution (1:1) of Na₂S (0.5 M), S (2 M), and KCl (0.2 M) is used as the polysulfide electrolyte.

Here, in this work, we used C₄H₆MnO₄ which contains impurity elements incorporated into the precursor solution by doping Mn in situ for the fabrication of Mn-doped-CdS QDs on the TiO₂ photoanode. In brief, specific concentration of the C₄H₆MnO₄ was mixed with Cd(NO₃)₂ (0.1 M) in the ethanol solution as cation source. Na₂S (0.1 M) in methanol was used as anion source. The prepared TiO₂ photoanode was immersed in the mixed ethanol solution of C₄H₆MnO₄ and Cd(NO₃)₂ for 5 min, followed by rinsing with ethanol and drying with nitrogen. Subsequently, the TiO₂ photoanode was dipped into Na₂S (0.1 M) methanol solution for 5 min at 30°C. And, then, one cycle of SILAR has been completed. During the experiment, to meet the research needs, we changed the ratio of molar concentration of C₄H₆MnO₄ in the cation source solution (i.e., doping ratio of Mn-doped-CdS).

3. Result and Discussion

Figure 1(a) shows scanning electron micrograph (SEM) of the TiO₂ film deposited by Mn-doped-CdS (1:10) with a thickness of 7.87 μm. Figure 1(d) suggests that the vertical

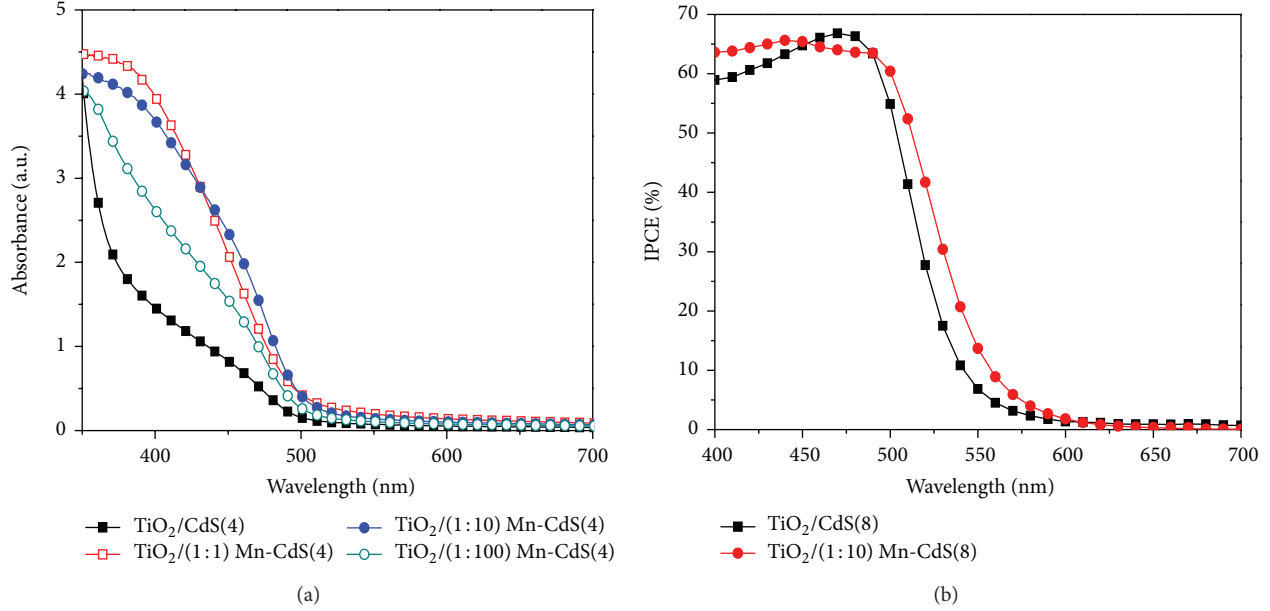


FIGURE 2: (a) UV-Vis absorption spectra and (b) IPCE spectra of undoped CdS QDs and different doped ratio of Mn-doped-CdS QDs.

morphology of TiO₂ photoanode is deposited by Mn-doped-CdS. There is no obvious change of the vertical morphology of the film between (b) and (c) images. It is proved that the QDs are small enough for the interspace of TiO₂ mesoporous film. And the existence of those interspaces makes sure of the full penetration of electrolyte. For the existence of quantum dots is unknown, the EDS spectrum is shown in inset of Figures 1(c) and 1(d). And the comparison between two spectrums demonstrated that the Mn is existent in the film.

Figure 2(a) shows the UV-Vis absorption spectra of different working electrodes based on Mn concentration. Compared to the undoped one; the Mn-doped-CdS show the obvious red shift in the UV-Vis absorption spectra. The initial response in the wavelength of undoped one, like the Mn-doped-CdS QDs, is approximated to be 500 nm. But the spectral response range has been extended after deposition. This phenomenon is due to the introduction of midgap states between the conduction band and the valence band of TiO₂ QDs by Mn doping, which could provide electron in the long wavelength region of the spectrum. And the complementary in the spectral responses can enhance photoelectric conversion efficiency of QDSSCs. The absorption spectra of Mn-CdS (1:1) is very similar to Mn-CdS (1:10), which is red shift compared to the sample of Mn-CdS (1:100).

The incident photon-to-electron conversion efficiency (IPCE) spectra of the doped and undoped QDSSCs at different incident light wavelengths were shown in Figure 2(b). The maximum IPCE value of two samples is about 67%. However, the spectral response range of Mn-doped-CdS QDSSCs is wider than the undoped one. This is due to the fact the introduction of impurities of Mn enhances the spectral response of the CdS QDSSCs, so that more electrons transferred to the external circuit and the generation of dark

TABLE 1: Different photovoltaic parameters for different samples.

| Sample | J_{sc} (mA/cm ²) | V_{oc} (mV) | FF | η (%) |
|-------------------------------------|--------------------------------|---------------|------|------------|
| TiO ₂ /CdS(4) | 4.29 | 474 | 0.35 | 0.71 |
| TiO ₂ /(1:1) Mn-CdS(4) | 4.13 | 482 | 0.44 | 0.88 |
| TiO ₂ /(1:10) Mn-CdS(4) | 5.88 | 514 | 0.41 | 1.24 |
| TiO ₂ /(1:100) Mn-CdS(4) | 4.82 | 438 | 0.33 | 0.70 |

TABLE 2: ICP-OES test data of Mn-doped-CdS.

| Sample | Cd (μ g) | Mn (μ g) | Cd (10^{-6} mol) | Mn (10^{-6} mol) | Molar ratio of Mn |
|--------|---------------|---------------|---------------------|---------------------|-------------------|
| Mn-CdS | 1045 | 5.373 | 9.297 | 0.098 | 1.054% |

current is also suppressed, which is consistent with the UV-visible absorption spectra of samples.

The J - V characteristics of those QDSSCs samples based on diverse doped ratio are presented in Figure 3, with 4 cycles of SILAR. Simultaneously, the corresponding performance parameters of those samples are presented in Table 1.

As can be seen from the chart, Mn-doped-CdS QDSSCs exhibited considerable increment close to 58% (from 0.71% to 1.24%) in the power conversion efficiency, compared to the corresponding undoped sample. The highest overall power conversion efficiency (1.24%) was achieved with the most optimized Mn doped amount. And the actual Mn concentration, applied on an inductively coupled plasma optical emission spectroscopy (ICP-OES), shown in Table 2, was found to be 1.054% in the CdS film. Higher Mn concentration might damage the performance. Therefore, as the proportion of Mn doping gradually reduced, the J_{sc} increased from 4.13 mA/cm² (1:1) to 5.88 mA/cm² (1:10). But when the

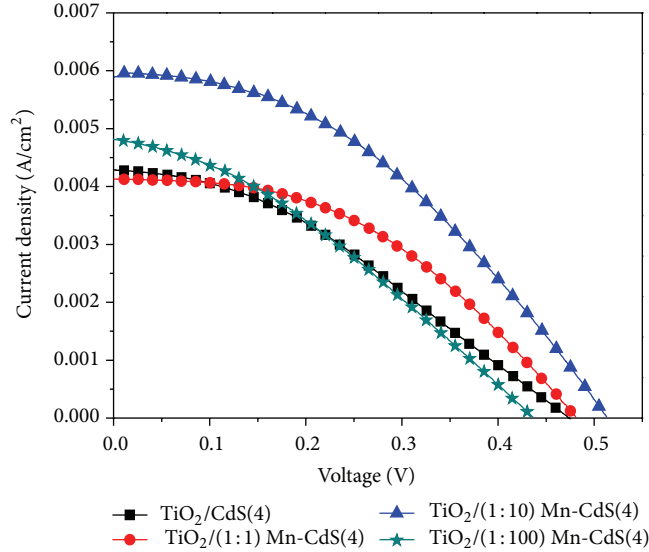


FIGURE 3: The J - V characteristics of different sample based on the doped ratio of Mn doping.

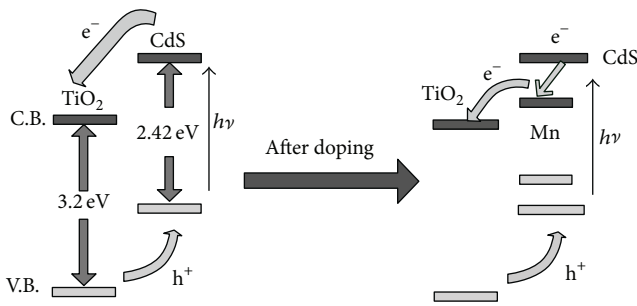


FIGURE 4: The TiO_2/CdS energy level structure diagram before and after doping.

concentration continues to decrease, the performance of cells is declined. Meanwhile, the fill factor (FF) remained stable.

The higher J_{sc} of the Mn-doped-CdS films is mainly attributed to the midgap states created by Mn doping, which not only enhances the capture for electrons and slows the speed of electrons transport but also screens partly the charge recombination with the hole and polysulfide electrolyte after oxidation. Indeed, the improved photovoltage in the QDSSCs with doped semiconductor films indicates that Mn-doping assists in electron accumulation within the QDs layers, thus shifting the Fermi level to more negative potentials and increasing the conduction band of CdS. As shown in Figure 4, the Fermi energy is adjusted to an even lower electric potential, due to the promotion of electron collection by doping.

In addition, the J_{sc} of the CdS QDSSCs will be improved by the Mn doping with the relatively high doped ratio. However, a large number of recombination centers, which have been introduced along with the Mn ions doped on the CdS QDs, are an unfavorable factor for the performance of solar cells. The enhancement for the J_{sc} by Mn doping increased firstly when the doping ratio is decreased. In contrast, as

TABLE 3: Different photovoltaic parameters for different samples.

| SILAR cycles | J_{sc} (mA/cm ²) | V_{oc} (mV) | FF | η (%) |
|---------------------------------|--------------------------------|---------------|------|------------|
| $\text{TiO}_2/(1:10)$ Mn-CdS(2) | 3.67 | 471 | 0.38 | 0.65 |
| $\text{TiO}_2/(1:10)$ Mn-CdS(4) | 6.02 | 501 | 0.31 | 0.92 |
| $\text{TiO}_2/(1:10)$ Mn-CdS(6) | 7.90 | 536 | 0.36 | 1.51 |
| $\text{TiO}_2/(1:10)$ Mn-CdS(8) | 7.13 | 592 | 0.29 | 1.21 |

the doped ratio decreased, the enhancement is weakened. And the crystal defects caused by Mn doping still exist, so that the short-circuit current density and photoelectric conversion efficiency began to decline. In this experiment, we just changed the ratio of molar concentration of $\text{C}_4\text{H}_6\text{MnO}_4$ and $\text{Cd}(\text{NO}_3)_2$. It has little effect on the fill factor, so there is no significant change about it.

Based on the above discussion, the doped ratio is fixed on 1:10 as the most optimized Mn-doped concentration. Figure 5(a) gives the UV-Vis absorption spectra of four samples based on different SILAR cycles. It shows that the exciton absorption peak of those samples moved in a direction toward the long wavelength. And there is a sample exciton absorption peak at about 680 nm, which means manganese sulfur compounds may be formed during the deposition.

The IPCE recorded at different SILAR cycles for QDSC that employ three different photoactive semiconductor electrodes is shown in Figure 5(b). The overall photocurrent response matching the absorption features also increases along with the repetition of SILAR cycles.

The J - V characteristics and the corresponding performance parameters of those Mn-doped-CdS QDSSCs are presented in Figure 6 and Table 3. Obviously, as the times of SILAR cycles increased, there was a clearly different performance from the J_{sc} , FF, and V_{oc} . The best performance is obtained with the sample of 6 cycles of SILAR. When we

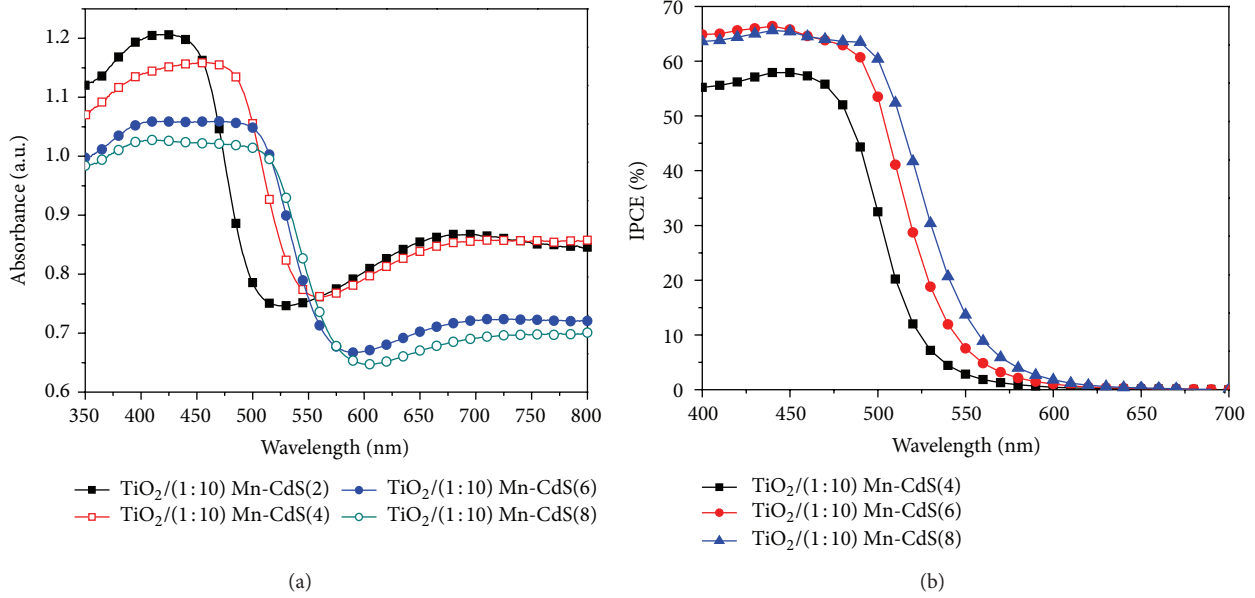


FIGURE 5: (a) UV-Vis absorption spectra and (b) IPCE spectra of mesoscopic TiO_2 photoanode deposited by different SILAR cycles of Mn-doped-CdS QDs.

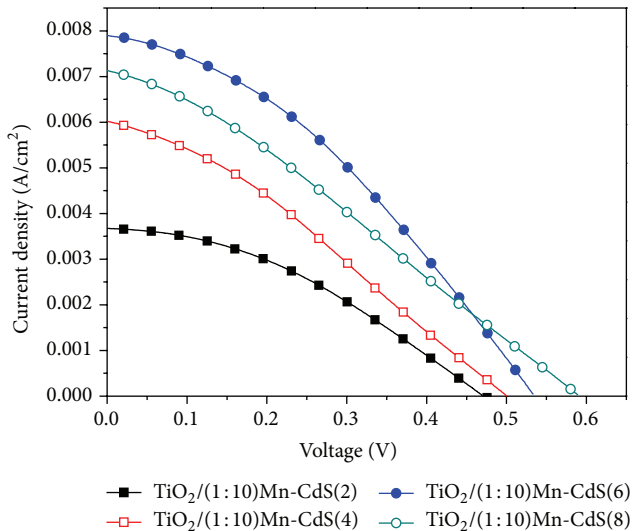


FIGURE 6: The J - V characteristics of different sample based on SILAR cycles.

repeat the process of deposition by Mn-doped-CdS QDs, more QDs will be generated on the mesoscopic TiO_2 film, leading to the accumulation of photo-generated electron. Therefore, the quasi-Fermi level of Mn-doped-CdS QDs is shifted to more negative potentials like the effect of Mn doping. But excessive deposition of QDs caused stoppage of interspace of the mesoscopic TiO_2 film and severe recombination of electrons. So the J_{sc} is enhanced at first but got down finally. In contrast, because the conduction band of QDs increased with the repetition of SILAR cycles, the V_{oc} keep increasing.

4. Conclusions

In summary, the doping of CdS films with Mn has enabled us to achieve a significant improvement as compared to undoped films. After the optimization of experimental parameters, the photoelectric conversion efficiency of Mn-doped-CdS QDSSCs shows the maximum value (1.51%). Although the performance is still lower than the expected value, it gives us another optional approach for making QDSSCs competitive.

Conflict of Interests

The authors declare that there is no conflict of interests regarding the publication of this paper.

Acknowledgments

This work was partially supported by the Key Project of Beijing Natural Science Foundation (3131001), the Key Project of Natural Science Foundation of China (91233201 and 61376057), the Key Project of Beijing Education Committee Science & Technology Plan (KZ201211232040), the State 863 Plan of MOST of China (2011AA050527), the Beijing National Laboratory for Molecular Sciences (BNLMS2012-21), the State Key Laboratory of Solid State Microstructures of Nanjing University (M27019), the State Key Laboratory for Integrated Optoelectronics of Institute of Semiconductors of CAS (IOSKL2012KF11), the State Key Laboratory for New Ceramic and Fine Processing of Tsinghua University (KF1210), the Key Laboratory for Renewable Energy and Gas Hydrate of Chinese Academy of Sciences (y207ka1001), the Beijing Key Laboratory for Sensors of BISTU (KF20131077208), and the

Beijing Key Laboratory for photoelectrical measurement of BISTU (GDKF2013005).

References

- [1] A. J. Nozik, M. C. Beard, J. M. Luther, M. Law, R. J. Ellingson, and J. C. Johnson, "Semiconductor quantum dots and quantum dot arrays and applications of multiple exciton generation to third-generation photovoltaic solar cells," *Chemical Reviews*, vol. 110, no. 11, pp. 6873–6890, 2010.
- [2] J. B. Sambur, T. Novet, and B. A. Parkinson, "Multiple exciton collection in a sensitized photovoltaic system," *Science*, vol. 330, pp. 63–66, 2010.
- [3] P. V. Kamat, "Quantum dot solar cells. Semiconductor nanocrystals as light harvesters," *Journal of Physical Chemistry C*, vol. 112, no. 48, pp. 18737–18753, 2008.
- [4] J. Tang, "Colloidal-quantum-dot photovoltaics using atomic-ligand passivation," *Nature Materials*, vol. 10, pp. 765–771, 2011.
- [5] L. Li, X. C. Yang, J. J. Gao et al., "Highly efficient CdS quantum dot-sensitized solar cells based on a modified polysulfide electrolyte," *Journal of the American Chemical Society*, vol. 133, no. 22, pp. 8458–8460, 2011.
- [6] Q. Shen, A. Yamada, S. Tamura, and T. Toyoda, "CdSe quantum dot-sensitized solar cell employing TiO₂ nanotube working-electrode and Cu₂S counter-electrode," *Applied Physics Letters*, vol. 97, no. 12, Article ID 123107, 2010.
- [7] G. S. Paul, J. H. Kim, M. S. Kim, K. Do, J. Ko, and J. Yu, "Different hierarchical nanostructured carbons as counter electrodes for Cds quantum dot solar cells," *ACS Applied Materials and Interfaces*, vol. 4, no. 1, pp. 375–381, 2012.
- [8] P. K. Santra and P. V. Kamat, "Mn-doped quantum dot sensitized solar cells: a strategy to boost efficiency over 5%," *Journal of the American Chemical Society*, vol. 134, no. 5, pp. 2508–2511, 2012.
- [9] W. Lee, W.-C. Kwak, S. K. Min et al., "Spectral broadening in quantum dots-sensitized photoelectrochemical solar cells based on CdSe and Mg-doped CdSe nanocrystals," *Electrochemistry Communications*, vol. 10, no. 11, pp. 1699–1702, 2008.
- [10] X. P. Zou, S. He, G. Teng, and C. Zhao, "Performance study of CdS/Co-doped-CdSe quantum dot Sensitized solar cells," *Journal of Nanomaterials*, vol. 2014, Article ID 818160, 6 pages, 2014.
- [11] Y. Y. Gao, Z. B. Huang, and X. Zou, "Doped heterojunction used in quantum dot sensitized solar cell," *International Journal of Photoenergy*, vol. 2014, Article ID 179289, 7 pages, 2014.
- [12] L. Li, X. P. Zou, H. Zhou, and G. Teng, "Cu-doped-CdS/In-doped-CdS cosensitized quantum dot solar cells," *Journal of Nanomaterials*, vol. 2014, Article ID 314386, 8 pages, 2014.
- [13] N. S. Karan, D. D. Sarma, R. M. Kadam, and N. Pradhan, "Doping transition metal (Mn or Cu) ions in semiconductor nanocrystals," *Journal of Physical Chemistry Letters*, vol. 1, no. 19, pp. 2863–2866, 2010.
- [14] S. Jana, B. B. Srivastava, and N. J. Pradhan, "Correlation of dopant states and host bandgap in dual-doped semiconductor nanocrystals," *The Journal of Physical Chemistry Letters*, vol. 2, pp. 1747–1752, 2011.
- [15] J. W. Lee, D. Y. Son, T. K. Ahn et al., "Quantum-dot-sensitized solar cell with unprecedentedly high photocurrent," *Scientific Reports*, vol. 3, article 1050, 2013.
- [16] M. Grätzel, "Review article photoelectrochemical cells," *Nature*, vol. 414, no. 15, pp. 338–344, 2001.
- [17] J. Yasuaki, S. Naya, and H. Tada, "Quantum-dot-sensitized solar cell using a photoanode prepared by in situ photodeposition of CdS on nanocrystalline TiO₂ films," *Journal of Physical Chemistry C*, vol. 114, no. 39, pp. 16837–16842, 2010.
- [18] D. S. Kim, Y. J. Cho, J. Park, J. Yoon, Y. Jo, and M. Jung, "(Mn, Zn) Co-doped CdS nanowires," *Journal of Physical Chemistry C*, vol. 111, no. 29, pp. 10861–10868, 2007.
- [19] B. Sambandam and P. T. Manoharan, "Davydov split PL emission and EPR correlation in β -mns layered cds nanorods," *Journal of Physical Chemistry C*, vol. 113, no. 22, pp. 9486–9496, 2009.

Research Article

Photocatalytic Degradation of Anthracene in Closed System Reactor

Faiq F. Karam,¹ Falah H. Hussein,² Sadiq J. Baqir,² Ahmed F. Halbus,²
Ralf Dillert,³ and Detlef Bahnemann³

¹ Chemistry Department, College of Science, Al-Qadisiya University, Al Deewaniya 58002, Iraq

² Chemistry Department, College of Science, Babylon University, Hilla 51002, Iraq

³ Institut für Technische Chemie, Leibniz Universität Hannover, 30167 Hannover, Germany

Correspondence should be addressed to Faiq F. Karam; faiq.karam@yahoo.com

Received 3 April 2014; Revised 24 May 2014; Accepted 7 June 2014; Published 8 July 2014

Academic Editor: Chuanyi Wang

Copyright © 2014 Faiq F. Karam et al. This is an open access article distributed under the Creative Commons Attribution License, which permits unrestricted use, distribution, and reproduction in any medium, provided the original work is properly cited.

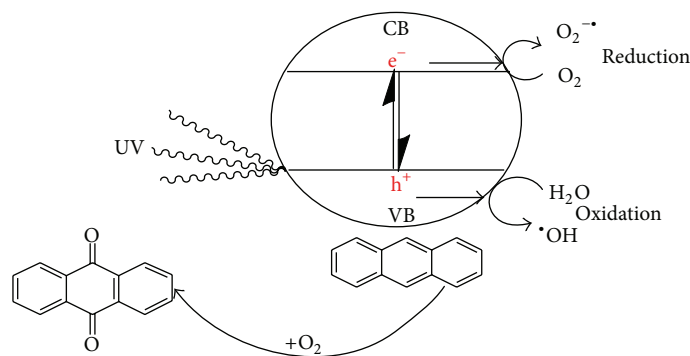
Polycyclic aromatic hydrocarbons (PAHs) represent a large class of persistent organic pollutants in an environment of special concern because they have carcinogenic and mutagenic activity. In this paper, we focus on and discuss the effect of different parameters, for instance, initial concentration of Anthracene, temperature, and light intensity, on the degradation rate. These parameters were adjusted at pH 6.8 in the presence of the semiconductor materials (TiO₂) as photocatalysts over UV light. The main product of Anthracene photodegradation is 9,10-Anthraquinone which is identified and compared with the standard compound by GC-MS. Our results indicate that the optimum conditions for the best rate of degradation are 25 ppm concentration of Anthracene, regulating the reaction vessel at 308.15 K and 2.5 mW/cm² of light intensity at 175 mg/100 mL of titanium dioxide (P25).

1. Introduction

Polycyclic aromatic hydrocarbons (PAHs) constitute an important and hazardous group of priority contaminants [1]. Several researchers determined the concentrations of these compounds by different chromatographic techniques, for instance, HPLC [2–4], GC-MS/MS in [5], and GC-MS in [6, 7]. The main processes that successfully eliminated PAHs from the environment included the microbiological transformation and degradation, bioaccumulation, biological uptake volatilization, photooxidation, and chemical oxidation [8]. Photolysis and ozonation are the most important methods for transformation for most PAHs adsorbed on natural substances in an environment [9]. Photolysis of PAHs led to the formation of photodimers and photooxidation products [10]. In recent years, the release of toxic and organic contaminants into aquatic environment as a result of human activities has drawn much attention and is considering a baffling problem facing researchers today [11]. Zinc oxide and titanium dioxide are universally considered as the most important photocatalysts due to their lower cost and their

considerably low band gap energy (~3.2 eV) [12]. Nanoparticles of titanium dioxide were considered to be more efficient than bulk powder in photocatalytic field [13]. Several previous works used titanium dioxide as catalyst for degradation of different organic pollutants [14–16].

Semiconductors have been used for pollutants degradation in water to be less harmful inorganic material. Both catalysts titanium dioxide and zinc oxide have photocatalytic properties which made these catalysts the best for photodegradation of water pollutants [17]. Attention has been focused in the past decade on using nanocrystalline TiO₂ as a photocatalyst for the organic pollutants degradation. TiO₂ semiconductor has a wide band gap about 3.2 eV, which corresponds to the UV-range radiation. The formation of an electron hole pair occurs within the conduction and valance bands of TiO₂ semiconductor after absorption in UV range. Water molecules can be oxidized to hydroxyl radical by positive hole. Scheme 1 shows the mechanism diagram for photodegradation of Anthracene. The hydroxyl is a radical, frequent, and powerful oxidant. The oxidation of organic pollutants seems to be mediated by a series of

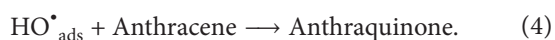
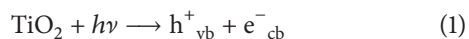


SCHEME 1: Mechanism diagram of photocatalytic degradation for Anthracene.

reactions started by hydroxyl radical on the TiO_2 surface. Recombination for the produced hole from valance band and separated electron from conductive band it can appear either in the volume or on the surface of the semiconductor particle accompanied with heat releasing. To this end, both UV light source and TiO_2 are necessary for photooxidation reaction to occur [18]. The photodegradation of PAHs compounds in water using TiO_2 catalyst has proved high efficiency in [19].

Furthermore, many researchers dealt with the PAHs in water by photocatalytic degradation for TiO_2 . Woo et al. in [20] investigated photocatalytically oxidation using TiO_2 of 5 selected PAHs, namely, naphthalene, acenaphthylene, phenanthrene, Anthracene, and benzo[a]anthracene. Gu et al. in [21] studied degradation of phenanthrene on soil surfaces photocatalytically with the addition of nanoparticulate anatase TiO_2 under UV-irradiation. Vela et al. in [22] discussed photocatalytic processes using semiconductor materials (ZnO and TiO_2) to remove the residual concentrations of several PAHs from groundwater. Theurich et al. in [23] reported the mechanism of the photocatalytic transformation of naphthalene and Anthracene qualitatively in aqueous suspensions of titanium dioxide. Indeed, catalyst TiO_2 can play as efficient photocatalyst in the oxidation of PAHs and convert it to safer compounds especially with Anthracene, Fluorene, and Naphthalene by artificial or sunlight illumination [19, 24]. To this end, our aim in the present paper is to study the effect of photocatalytic reactions on the degradation of Anthracene using titanium dioxide under different experimental conditions.

UV illumination of TiO_2 yields valence band holes and conduction band electrons (1), which interact with the surface adsorbed molecular oxygen to give superoxide radical anions, $\text{O}_2^{\bullet-}$ (2), and finally, the water produces radicals of HO^\bullet (3) [25]. These radicals oxidize target molecule (Anthracene) to Anthraquinone (4):



2. Experimental Procedure

2.1. Chemicals and Reagents. Anthracene was purchased from Sigma Aldrich, Germany, and used without further purification. Acetonitrile (anhydrous, $\geq 99.98\%$), Dichloromethane (anhydrous, $\geq 99.98\%$), Acetone, ethyl acetate (anhydrous, $\geq 99.98\%$), and methanol HPLC-gradient grade were purchased also from Sigma Aldrich, Germany. Titanium dioxide particles were purchased from Degussa (P25), anhydrous Na_2SO_4 (extra pure Allied Signal, Riedel-de—Germany).

2.2. Preparation of Stock Solution of Anthracene. A set of dilutions of Anthracene solution at the concentration of 100 mg/L were made in the following solvents: methanol, dichloromethane, acetonitrile, ethyl acetate, and acetone. Anthracene solutions in the above solvents were prepared and stored in room temperature ($20 \pm 2^\circ\text{C}$) in dark place to keep it from the light degradation. Calibration curve for Anthracene solution has been achieved by preparation several concentrations (0.1, 0.5, 1, 2, 4, 8, 16 and 30) mg/L. All glassware used for experiments was washed in chromic acid mixture for 12 h with methanol, deionized water, and acetone and then dried at 110°C for 3 h.

2.3. Solid Phase Extraction and Sample Preparation. Solid phase extraction (SPE) method was used to extract the Anthracene from the mixture (aqueous solution at different solvents) by Supelcocoan ENV-18 solid phase extraction tube. After passing the specific volume of aqueous solution through extraction column, the extract was treated with anhydrous Na_2SO_4 to remove all the water content from the extract and then it was concentrated by rotary evaporator (BUCHI-RE121-Switzerland made) in temperatures below 35°C by water bath (BUCHI 461 Metrohm/Swiss made) to be in volume 1 mL. Then samples were analyzed by GC 2010 (Shimadzu, Japan). The study revealed that the Anthracene level had no effect on the percent decrease of the compound during evaporation process for the solvent. The average recovery of analytes for every liquid media and corresponding relative standard deviations RSD ($n = 5$) were represented in Table 1. Chromatographic conditions are listed in Table 2.

TABLE 1: The average recovery of Anthracene and relative standard deviations RSD ($n = 5$).

| Organic solvents | Recovery% | RSD% |
|------------------|-----------|------|
| Methanol | 91 | 0.3 |
| Dichloromethane | 88 | 0.5 |
| Acetonitrile | 92 | 0.2 |
| Ethyl acetate | 81 | 0.4 |
| Acetone | 79 | 3.4 |

TABLE 2: Chromatographic conditions were used for determination Anthracene by GC.

| Parameters | Details |
|------------------|---|
| Column | Type: Hp5 (60 m * 0.25 mm * 0.25 μ m) |
| Injection volume | 1 μ L |
| Injector mode | Split less, temp. = 250 $^{\circ}$ C |
| Carrier gas | High purity helium. |
| Detector | Type: FID, temp. = 310 $^{\circ}$ C |

2.4. Photolysis Experiments. The experiments were carried out in glass dual wall reactor closed system type, to keep the temperature constant using chiller (Julabo model EH/Germany) as temperature controller. Agitation of the reaction mixture was provided by a magnetic stirrer (Heidolph-Mr3001). The photoreactor operated in a batch mode. The study was carried out for selected compound Anthracene (Sigma Aldrich) without additional purification. The pH of the reaction solution adjusted about 6.8, pH by adding an exact volume of Sodium hydroxide or sulfuric acid.

2.5. Kinetics of the Photocatalytic Process. Kinetics of Anthracene degradation was calculated by the first-order equation:

$$C_t = C_0 \cdot e^{-kt} \quad (5)$$

or

$$\ln\left(\frac{C_0}{C_t}\right) = kt, \quad (6)$$

where C_0 , C_t are the PAH concentration at times (zero and t), respectively, and k is the rate constant. First-order degradation rate constants were determined by regression analysis.

3. Results and Discussion

Several parameters were studied to indicate the effect of these degradation rates as follows.

3.1. Effect of the Initial Anthracene Concentrations. The effect of initial Anthracene concentration on the reaction rate is the first parameter studied in this work. Figure 1 shows that Anthracene concentrations decrease with time increases. The rate of degradation increases as the initial concentration increases as well. For photochemical reactions the higher

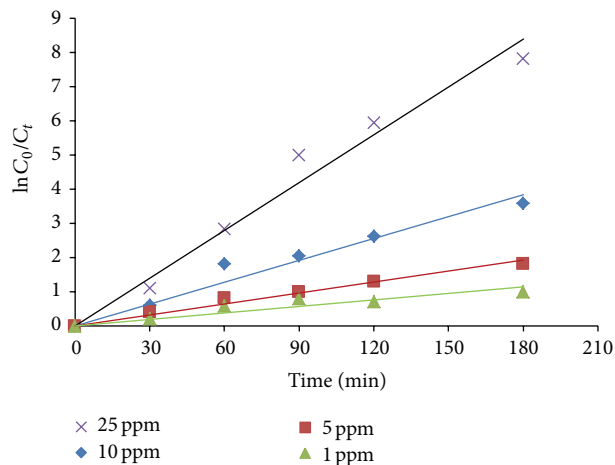
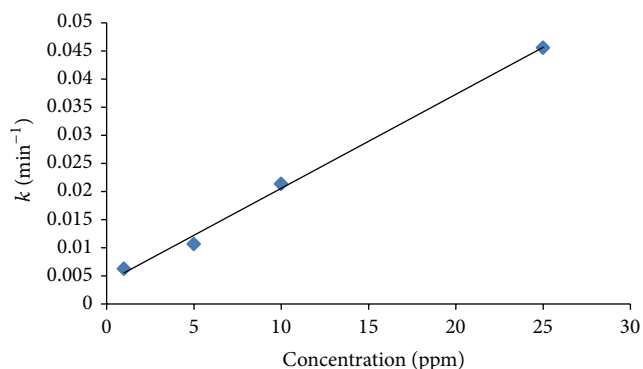
FIGURE 1: The changes of $\ln(C_0/C_t)$ with irradiation times on different Anthracene concentrations by TiO_2 .

FIGURE 2: Effects of initial Anthracene concentrations at a rate constant.

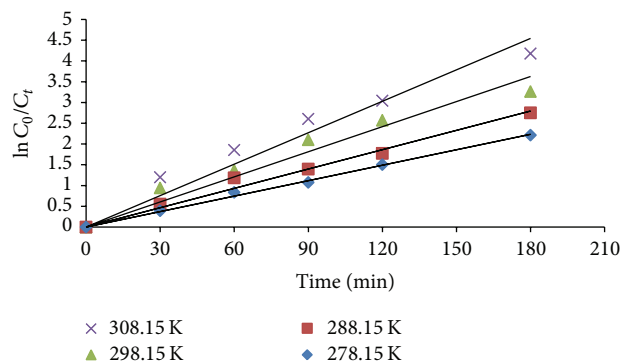


FIGURE 3: Effect of temperature on the degradation rate of Anthracene.

concentration causes a higher light absorption and consequently accelerates the degradation rate [26]. Figure 2 shows the relation between rate constant and initial concentrations of Anthracene.

3.2. Effect of Temperature. The oxidation of Anthracene molecule was studied at different temperatures, to indicate

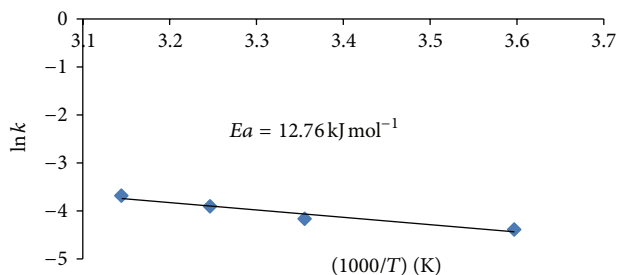


FIGURE 4: Arrhenius plot for photocatalytic degradation of Anthracene on TiO_2 at (278.15–308.15) K.

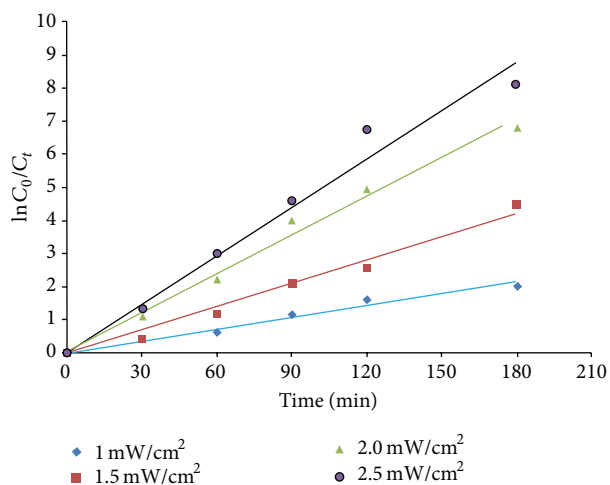


FIGURE 5: Effect of light intensity on the degradation rate of Anthracene.

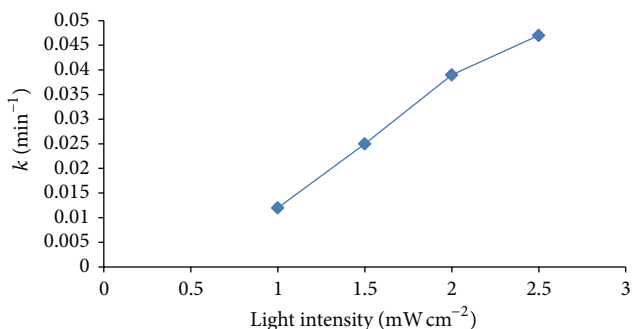


FIGURE 6: The effect of initial light intensity on the rate constant.

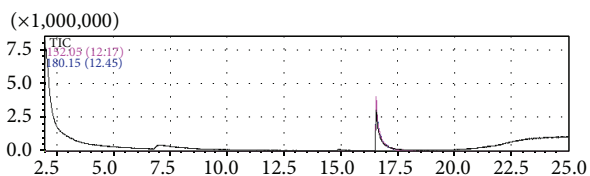


FIGURE 7: Chromatogram of GC-MS for standard 9,10-Anthraquinone and produced by oxidation of Anthracene before exposure to UV light.

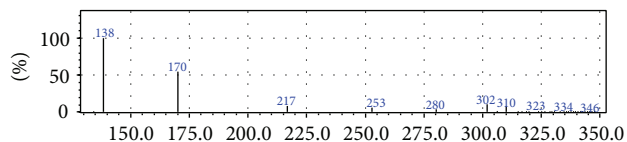


FIGURE 8: Mass spectra for standard 9,10-Anthraquinone before exposure to UV light.

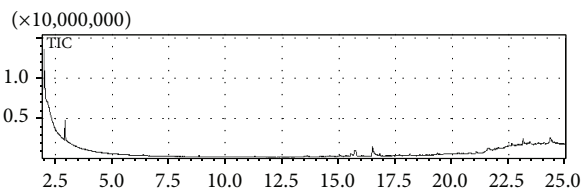


FIGURE 9: Chromatogram of GC-MS for standard 9,10-Anthraquinone after exposure to UV light.

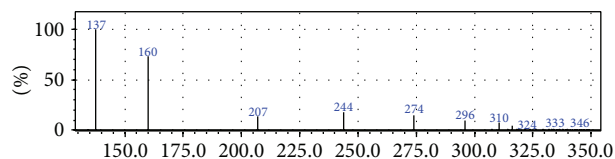


FIGURE 10: Mass spectra for standard 9,10-Anthraquinone after exposure to UV light.

the best one at which the degradation rate is fastest. Figure 3 shows the effect of temperature on the concentration of Anthracene with time of reaction. Figure 4 illustrates the Arrhenius plot for the relation between $\ln k$ and $1/T$, activation energy calculated by Arrhenius equation.

The influence of temperature on the degradation rate is typical. The greatest increase of the rate of degradation about two times can be achieved after about 180 min at 308.15 K; initial rates within the first 30 min appear to increase with increasing the temperature. This phenomenon is related to the effect of temperature on the stability of Anthracene molecule. Luo et al. [27] reported that higher temperature slightly enhances the rate constant of Pyrene.

3.3. Effect of Light Intensity. UV light intensity has an important role in the process of photocatalytic degradation. Figure 5 shows effect of light intensity on the degradation rate of Anthracene molecule. This figure indicates that the reactions followed pseudo-first-order rate constant with increasing UV light intensity from 1–2.5 mW/cm^2 . The results indicate the perfect degradation at light value: 2.5 mW/cm^2 .

Therefore, when light intensity increases the number of photons increases which means that the formation of electrons and holes increases, and hence, electron-hole recombination is negligible. However, at the lower light intensity, electron and hole pair separation competes with recombination which in turn decreases the formation of free radicals [28], causing less effect on the rate of degradation of the Anthracene as shown in Figure 6.

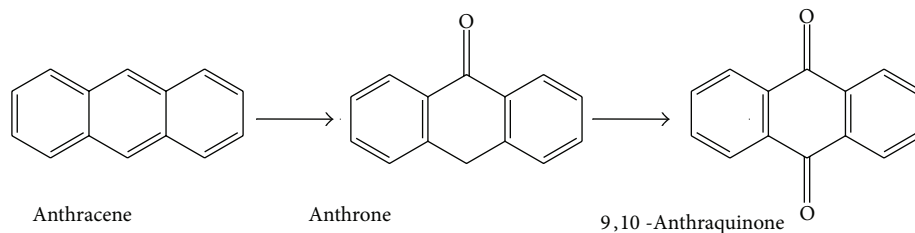


FIGURE II: Proposed pathway degradation of Anthracene.

3.4. Photodegradation Products of Anthracene. The major product for photodegradation of Anthracene is 9,10-Anthraquinone. Anthraquinone is characterized by GC-MS (2010-SHIMADZU). Standard solution 25 ppm of 9,10-Anthraquinone (Sigma Aldrich) was prepared and compared with that produced by oxidation. Figures 7 and 8 illustrate that there are no differences between them. The proposed degradation pathway of Anthracene is as in Figure II.

During the photocatalytic degradation experiments with Anthracene only 9,10-Anthraquinone was detected as an intermediate, in agreement with Theurich et al. [23]. Figures 9 and 10 show the GC chromatogram and mass spectra for 9,10-Anthraquinone after exposure to the light intensity in the same environment of perfect conditions for Anthracene degradation.

4. Conclusions

The photocatalytic degradation of Anthracene using artificial UV light has been achieved. The observations of these investigations demonstrate the importance of selecting the optimum parameters for degradation to obtain a high degradation rate, which is considered essential for any application of photocatalytic oxidation processes. The experimental work in controlled pH media at closed system reactor has found that the main product of oxidation of Anthracene is 9,10-Anthraquinone, which is safer for environment than Anthracene. The rate of photodegradation in present UV light has been found to be maximum in neutral medium with optimum concentration of 25 ppm of Anthracene. The optimum temperature for degradation is 308.15 K. The optimum light intensity is 2.5 mW/cm² at pH 6.8. The degradation of Anthracene increases with the increase of light intensity. Nevertheless, the increase of light intensity leads to the increase of the number of electron-hole pairs and increases the degradation of Anthracene.

Conflict of Interests

The authors declare that there is no conflict of interests regarding the publication of this paper.

Acknowledgments

The authors are gratefully acknowledging the financial support provided by the Arab Science and Technology Foundation (ASTF) without which this research would not have been

possible. The authors also express sincere appreciation to all the staff working at ASTF, Baghdad Office. The authors thank Dr. Amir Hakki for his assistance in the experimental phases of the research.

References

- [1] S. Ledakowicz, J. S. Miller, and D. Olejnik, "Oxidation of PAHs in water solution by ozone combined with ultraviolet radiation," *International Journal of Photoenergy*, vol. 3, no. 2, pp. 95–101, 2001.
- [2] F. J. López-Jiménez, A. Ballesteros-Gómez, and S. Rubio, "Determination of polycyclic aromatic hydrocarbons (PAH4) in food by vesicular supramolecular solvent-based microextraction and LC-fluorescence detection," *Food Chemistry*, vol. 143, pp. 341–347, 2014.
- [3] M. Ciecierska and M. W. Obiedziński, "Polycyclic aromatic hydrocarbons in the bakery chain," *Food Chemistry*, vol. 141, no. 1, pp. 1–9, 2013.
- [4] T. Payanan, N. Leepipatpiboon, and P. Varanusupakul, "Low-temperature cleanup with solid-phase extraction for the determination of polycyclic aromatic hydrocarbons in edible oils by reversed phase liquid chromatography with fluorescence detection," *Food Chemistry*, vol. 141, no. 3, pp. 2720–2726, 2013.
- [5] J. Pincemille, C. Schummer, E. Heinen, and G. Moris, "Determination of polycyclic aromatic hydrocarbons in smoked and non smoked black teas and tea infusion," *Food Chemistry*, vol. 145, pp. 807–813, 2014.
- [6] A. L. V. Escarrone, S. S. Caldas, E. B. Furlong, and V. L. Menghetti, "Polycyclic aromatic hydrocarbons in rice grain dried by different processes: evaluation of quick, easy, cheap, effective, rugged and safe extraction method," *Food Chemistry*, vol. 146, pp. 597–602, 2014.
- [7] A. M. R. Machado, M. G. Cardoso, H. S. Dorea et al., "Contamination of cachaca by PAHs from storage containers," *Food Chemistry*, vol. 146, pp. 65–70, 2014.
- [8] L. Zhang, P. Li, Z. Gong, and A. Oni Adeola, "Photochemical behavior of benzo[a]pyrene on soil surfaces under UV light irradiation," *Journal of Environmental Sciences*, vol. 18, no. 6, pp. 1226–1232, 2006.
- [9] J. Ma, Y. Liu, Q. Ma, C. Liu, and H. He, "Heterogeneous photochemical reaction of ozone with anthracene adsorbed on mineral dust," *Atmospheric Environment*, vol. 72, pp. 165–170, 2013.
- [10] R. Debestani, K. J. Ellis, and M. E. Sigman, "Photodecomposition of anthracene on dry surfaces: products and mechanism," *Journal of Photochemistry and Photobiology A: Chemistry*, vol. 86, no. 1–3, pp. 231–239, 1995.

- [11] N. A. Mir, M. M. Haque, A. Khan, M. Muneer, and C. Boxall, "Photoassisted degradation of a herbicide derivative, dinoseb, in aqueous suspension of titania," *The Scientific World Journal*, vol. 2012, Article ID 251527, 8 pages, 2012.
- [12] F. H. Hussein, "Comparison between solar and artificial photocatalytic decolorization of textile industrial wastewater," *International Journal of Photoenergy*, vol. 2012, Article ID 793648, 10 pages, 2012.
- [13] L. M. Ahmed, I. Ivanova, F. H. Hussein, and D. W. Bahnemann, "Role of platinum deposited on TiO₂ in photocatalytic methanol oxidation and dehydrogenation reactions," *International Journal of Photoenergy*, vol. 2014, Article ID 503516, 9 pages, 2014.
- [14] F. H. Hussein, "Effect of photocatalytic treatment on physical and biological properties of textile dyeing wastewater," *Asian Journal of Chemistry*, vol. 25, no. 16, pp. 9387–9392, 2013.
- [15] F. H. Hussein, "Chemical properties of treated textile dyeing wastewater," *Asian Journal of Chemistry*, vol. 25, no. 16, pp. 9393–9400, 2013.
- [16] F. H. Hussein and A. F. Halbus, "Rapid decolorization of cobalamin," *International Journal of Photoenergy*, vol. 2012, Article ID 495435, 9 pages, 2012.
- [17] A. J. Attia, S. H. Kadhim, and F. H. Hussein, "Photocatalytic degradation of textile dyeing wastewater using titanium dioxide and zinc oxide," *E-Journal of Chemistry*, vol. 5, no. 2, pp. 219–223, 2008.
- [18] W.-Y. Wang, A. Irawan, and Y. Ku, "Photocatalytic degradation of Acid Red 4 using a titanium dioxide membrane supported on a porous ceramic tube," *Water Research*, vol. 42, no. 19, pp. 4725–4732, 2008.
- [19] L. Zhang, P. Li, Z. Gong, and X. Li, "Photocatalytic degradation of polycyclic aromatic hydrocarbons on soil surfaces using TiO₂ under UV light," *Journal of Hazardous Materials*, vol. 158, no. 2-3, pp. 478–484, 2008.
- [20] O. T. Woo, W. K. Chung, K. H. Wong, A. T. Chow, and P. K. Wong, "Photocatalytic oxidation of polycyclic aromatic hydrocarbons: intermediates identification and toxicity testing," *Journal of Hazardous Materials*, vol. 168, no. 2-3, pp. 1192–1199, 2009.
- [21] J. Gu, D. Dong, L. Kong, Y. Zheng, and X. Li, "Photocatalytic degradation of phenanthrene on soil surfaces in the presence of nanometer anatase TiO₂ under UV-light," *Journal of Environmental Sciences*, vol. 24, no. 12, pp. 2122–2126, 2012.
- [22] N. Vela, M. Martínez-Menchón, G. Navarro, G. Pérez-Lucas, and S. Navarro, "Removal of polycyclic aromatic hydrocarbons (PAHs) from groundwater by heterogeneous photocatalysis under natural sunlight," *Journal of Photochemistry and Photobiology A: Chemistry*, vol. 232, pp. 32–40, 2012.
- [23] J. Theurich, D. W. Bahnemann, R. Vogel, F. E. Ehamed, G. Alhakimi, and I. Rajab, "Photocatalytic degradation of naphthalene and anthracene: GC-MS analysis of the degradation pathway," *Research on Chemical Intermediates*, vol. 23, no. 3, pp. 247–274, 1997.
- [24] S. Das, M. Muneer, and K. R. Gopidas, "Photocatalytic degradation of wastewater pollutants. Titanium-dioxide-mediated oxidation of polynuclear aromatic hydrocarbons," *Journal of Photochemistry and Photobiology A: Chemistry*, vol. 77, no. 1, pp. 83–88, 1994.
- [25] N. A. Laoufi, D. Tassalit, and F. Bentahar, "The degradation of phenol in water solution by TiO₂ photocatalysis in helical reactor," *Global NEST Journal*, vol. 10, no. 3, pp. 404–418, 2008.
- [26] J. S. Miller and D. Olejnik, "Photolysis of polycyclic aromatic hydrocarbons in water," *Water Research*, vol. 35, no. 1, pp. 233–243, 2001.
- [27] Z. Luo, K. Katayama-Hirayama, T. Akitsu, and H. Kaneko, "Photocatalytic degradation of pyrene in porous Pt/TiO₂-SiO₂ photocatalyst suspension under UV irradiation," *Nano*, vol. 3, no. 5, pp. 317–322, 2008.
- [28] D. Dong, P. Li, X. Li, Q. Zhao, Y. Zhang, and C. Jia, "Investigation on the photocatalytic degradation of pyrene on soil surfaces using nanometer anatase TiO₂ under UV irradiation," *Journal of Hazardous Materials*, vol. 174, no. 1–3, pp. 859–863, 2010.

Review Article

Recent Progress in TiO₂-Mediated Solar Photocatalysis for Industrial Wastewater Treatment

Tong Zhang,¹ Xiaoguang Wang,¹ and Xiwang Zhang²

¹ National Institute of Clean-and-Low-Carbon Energy, Shenhua NICE, P.O. Box 001, Future Science & Technology Park, Changping District, Beijing 102209, China

² Department of Chemical Engineering, Monash University, Clayton, VIC 3800, Australia

Correspondence should be addressed to Tong Zhang; zhangtong@nicenergy.com and Xiwang Zhang; xiwang.zhang@monash.edu

Received 5 May 2014; Accepted 27 May 2014; Published 8 July 2014

Academic Editor: Qing Wang

Copyright © 2014 Tong Zhang et al. This is an open access article distributed under the Creative Commons Attribution License, which permits unrestricted use, distribution, and reproduction in any medium, provided the original work is properly cited.

The current paper reviews the application of TiO₂-mediated solar photocatalysis for industrial wastewater treatment, starting with a brief introduction on the background of industrial wastewater and the development of wastewater treatment processes, especially advanced oxidation processes (AOPs). We, then, discuss the application of solar TiO₂ photocatalysis in treating different kinds of industrial wastewater, such as paper mill wastewater, textile wastewater, and olive mill wastewater. In the end, we compare solar TiO₂ photocatalysis with other AOPs in terms of effectiveness, energy, and chemical consumption. Personal perspectives are also given, which may provide new insights to the future development of TiO₂ photocatalysis for industrial wastewater.

1. Introduction

Industrial wastewater is of global concern due to its severe effects on the environment. Compared with municipal wastewater, industrial wastewater generally contains high concentration of toxic or nonbiodegradable pollutants, such as fats, oil, grease, heavy metals, phenols, and ammonia [1]. The water quality of wastewater can be indicated by some parameters such as suspended solids (SS), biological oxygen demand (BOD), chemical oxygen demand (COD), and total organic carbon (TOC) [2]. These parameters are typically very high in industrial wastewater, which significantly reduce the performance of conventional wastewater treatment processes. Industrial wastewater also has much more complex composition than other wastewaters. Moreover, the water quality of industrial wastewater varies from one industry to another. Huge difference in water quality of wastewater between different factories may also happen in some cases. For example, the wastewater produced from iron and steel industry contains a large amount of ammonia, cyanide benzene, naphthalene, phenols, and cresols due to the reduction reactions in blast furnace and the production of coke [3]. In contrast, dispersed dyes are considered as

dominant pollutants in textile wastewater and effluent from paper industry generally contains high concentration of SS and BOD [4]. Unlike other wastewaters, high concentration of radioactive materials is present in nuclear industry wastewater. Owing to the high concentration of toxic pollutants and diversity of water quality, the treatment of industry wastewater is always a big challenge. In recent years, various novel technologies such as membrane technology, electrochemical method, and membrane bioreactor (MBR) have been proposed for the treatment of industrial wastewater. Unfortunately, these treatment processes still face several problems, for example, complicated technical requirements, high operational cost, and long reaction time, which severely restrict their applications.

Electrochemical method is to apply a voltage between an anode and cathode to remove pollutants via direct oxidation or reduction on electrodes or indirect oxidation or reduction by the reactive oxygen species generated by electrochemical reactions [5, 6]. Electrochemical method can be categorized to electrodeposition, electrodisinfection, electrocoagulation, electroflotation, electroadsorption, electrooxidation, and electroreduction. Suspended pollutants, colloids, and many charged pollutants can be effectively

removed from wastewater by this method [7]. For instance, electroflotation is successfully used for the treatment of oil mill effluent [8], oily wastewater [9], coking wastewater, and mining wastewater. In addition, electrooxidation process has been extensively investigated since the late 1970s [7]. Although many research works have already been done on optimization of the operation parameters, improvement of the electrocatalytic activity, the degradation mechanisms, and kinetics of pollutants, it is clear that electrode materials have big impact on the degradation of pollutants, which has to be improved in term of stability and durability [10].

With the increasing requirement of water supply and the more stringent environmental regulations, great progresses have been seen globally in membrane technology in past two decades. Compared with other processes, membrane technologies have many advantages such as high removal rate on pollutants, well arranged process conductions, and no addition of chemicals [10]. These superiorities make it suitable for wastewater treatment. However, membrane fouling caused by pollutants in wastewater is a major obstacle, which restricts the large-scale application of membranes in industry. Thus, how to achieve an effective and low cost way to treat wastewater is a crucial point.

Biological wastewater treatment is widely used in municipal wastewater treatment due to its low operation cost compared to other treatment processes such as thermal oxidation and chemical oxidation [11]. MBR is an improved activated sludge system, which is a combination of suspended biomass with a membrane process that replaces gravity sedimentation to clarify the wastewater effluent [12]. MBR process has small footprint, flexible design, and automated operation properties. However, like other membrane technologies, membrane fouling by mixed liquor remains and activated sludge is considered as a major obstacle for its applications. In addition, membranes with high chemical resistance are required due to the chemical cleaning process. Currently, MBR technology is mostly applied in small or moderate scale. Moreover, only biodegradable pollutants can be removed by biological treatment processes. There are still large amounts of toxic nonbiodegradable materials present in industrial wastewater.

Advanced oxidation processes (AOPs), which rely on the generation of highly reactive and oxidizing hydroxyl radicals ($\bullet\text{OH}$), are considered as highly competitive water treatment technologies. As an important technology of AOPs, photocatalytic oxidation (PCO) has attracted increasing attention in recent years because of its excellent performance on pollutants removal, low cost, and photochemical stability and without addition of toxic chemicals [13, 14]. TiO_2 is the most widely used catalyst in heterogeneous photocatalysis, because of its photostability, nontoxicity, low cost, and stability in water under most environmental conditions [15]. Large amount of reactive oxygen species such as hydroxyl radicals ($\bullet\text{OH}$) and superoxide radical anion ($\bullet\text{O}_2^-$) are produced on the surface of TiO_2 under light irradiation, and these reactive radicals are regarded as the major responsible species for the degradation of organic pollutants in wastewater [16–19]. Preis and coworkers [13] studied the degradation of phenolic compounds in wastewater from oil shale under UV-light

irradiation. The results revealed that the wastewater quality characteristics have obvious influence on the photodegradation rate of the pollutants. PCO can also serve as a pretreatment, which can significantly enhance the biodegradability of industrial wastewater to meet requirements of the subsequent biotreatment process. Sioi et al. [19] investigated the decolorization of a typical pharmaceutical wastewater using TiO_2 P25 as a heterogeneous photocatalyst, revealing that photocatalytic oxidation is a powerful alternative technology for the degradation of hematoxilin. Their results also showed that the performance of P25 nanoparticles didn't decrease after reuse and, thus, was suitable for practical wastewater treatment. To further improve the efficiency of wastewater treatment, some other techniques can be combined with PCO process. For example, Kim and Park [20] developed a novel hybrid process combining PCO with biofilm. Their results revealed that the pretreatment using biofilm could largely enhance the efficiency of PCO. Moreover, the integrated technology showed better performance as compared to Fenton oxidation in terms of color and COD removal. PCO process has many advantages, but it also faces some drawbacks. One is the relatively high operating cost because of the use of UV lights. Nevertheless, the UV lights in such systems could be replaced by natural solar radiation, which is free in most areas and feasible especially for industrial wastewater treatment [21]. The PCO process can also be combined with constructed wetlands [22]. The combined system was tested under natural irradiation, showing that organic pollutants, nutrients, and pathogenic bacteria can be effectively removed. More importantly, TiO_2 -mediated solar photocatalytic oxidation is low cost and environmental friendly and thus may be a promising solution for wastewater treatment.

2. Process and Mechanism of Solar Photocatalysis

In last decades, many efforts have been devoted to the degradation of organic pollutants in wastewater using solar photocatalysis [27, 32]. Compared to the counterparts using UV light, solar driven PCO of organic pollutants using solar irradiation can be much more economical [33]. As a typical semiconductor-based heterogeneous photocatalyst, TiO_2 was successfully employed for the degradation of various families of organic pollutants in wastewater under solar light irradiation. Stylidi and coworkers [34] successfully used TiO_2 suspension to degrade azo dyes under solar light; while Herrmann and coworkers applied this technology for the detoxification of wastewater which contains multiple pollutants [32].

In a typical solar photocatalysis process (Figure 1), the electrons (e^-) on the photocatalyst surface can be excited from valence band to conduction band by photons with energy larger than its band gap under solar light irradiation, which forms e^- and holes (h^+) on conduction and valence bands, respectively. The photogenerated electrons and holes then migrate to the surface of the photocatalyst, where they participate in redox reactions with adsorbed species and,

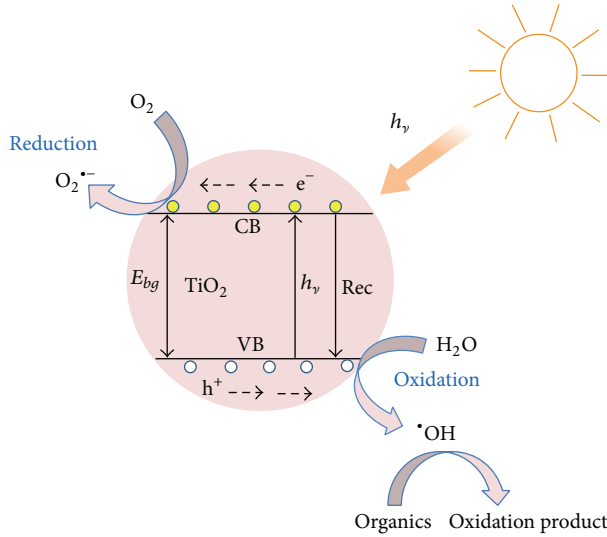
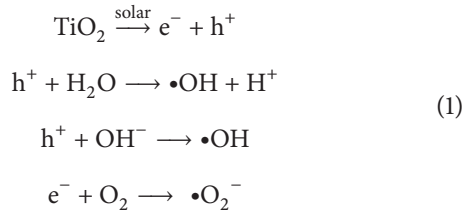


FIGURE 1: General mechanism of TiO_2 in solar photocatalysis process.

thus, form superoxide radical anion ($\bullet\text{O}_2^-$) and hydroxyl radical ($\bullet\text{OH}$), respectively, as follows [13, 16–18, 48, 49]:



The photogenerated reactive oxygen species are very strong oxidizers and play the dominant roles in the degradation of organic pollutants in wastewater. The organics in wastewater can be completely degraded to CO_2 and H_2O and, thus, there is no secondary pollution. However, many e^- and h^+ recombine releasing energy as heat before they participate in the redox reactions, which dramatically inhibit the practical photocatalytic activity of photocatalysts [50]. Moreover, owing to the larger band gap, TiO_2 can be excited only by UV lights, which account for less than 5% energy of the solar spectrum [15, 48, 51]. Thus, it is necessary to develop TiO_2 based materials which can utilize more solar energy. To solve this problem, some noble metals and their derivatives such as Ag, [52], Pt [53], AgBr [54], and CdS [55], have been tried to incorporate with TiO_2 forming hybrid photocatalysts [54], which would extend the photocatalytic activity of the photocatalysts into visible light range. The mechanism can be explained by two aspects. (1) The recombination rate of e^- and h^+ is inhibited because of the presence of incorporated materials, which promotes interfacial electron transfer and consequently facilitates the separation of e^- and h^+ [51]. (2) TiO_2 band gap is narrowed, which makes the excitation of TiO_2 easier. It will facilitate the electrons transfer from valence band to conduction band, and, thus, more oxidative species might be produced [56]. Özkan et al. reported that 1 wt.% Ag could effectively enhance the PCO efficiency [57].

Zang and Farnood found that AgBr can promote the PCO process for the degradation of methyl orange under solar light irradiation [54]. In addition, some researchers have already proven that the band gap of modified TiO_2 is lower than pure TiO_2 [58, 59]. Grzechulska and Morawski [58] investigated the modified commercial TiO_2 with metal hydroxides, and their study revealed that the band gap of modified material is 1.6 eV, which is lower than pure TiO_2 . Moreover, TiO_2 can also be integrated with some other semiconductors with a narrow band gap, for example, CdS, to form composite photocatalysts [60].

3. Application in Industrial Wastewater

3.1. Application in Paper Mill Wastewater. The paper mill is the fifth largest industry in North American economy [61]. Over 50% wastes in Canada's water can be attributed to the pulp and paper industry [62]. Large amounts of water are required by paper industry, which also produced equally large amounts of wastewater [63, 64]. Previous study indicated that 2000–6000 gallons water were consumed to produce one ton of paper [61]. The wastewater produced by this industry is commonly treated by biological process [65]. However, the effluent from paper industry contains highly toxic and refractory compounds, which restricts the application of biological method. In pulp and paper industry, water is required in each stage, and wastewater is also generated in each stage. The produced pollutants at different steps of a paper mill plant are shown in Figure 2 [23, 66]. Among these processes, the cellulose pulp bleaching stage produced the largest amount of high-strength wastewater, which contains several chlorinated compounds and some toxic organics [63]. Previous reports [67] showed that wastewater with BOD/COD ratio smaller than 0.3 is not suitable for biological treatment. Thompson and coworkers [68] reported that the biodegradability index of wastewater from pulp bleaching process is around 0.02–0.07, which indicated a further treatment process should be taken after biological process for the complete removal of pollutants. For example, Bajpai et al. [69] studied the degradation of pollutants from pulp and paper mill by anaerobic technology, and they found that the treated wastewater still contains high residual COD due to the incomplete degradation. In addition, the typical characteristics of paper mill wastewater at different processes are shown in Table 1 [23]. It shows that the pollutants vary dramatically from one plant to another plant.

Another important work was conducted by Ghaly and coworkers [24]. The paper mill wastewater was treated by a synthesized nanosized TiO_2 under solar light, and they found that the biodegradability index of the paper mill wastewater increased from 0.16 to 0.35. It indicates that solar photocatalytic oxidation of the paper mill wastewater can be used as an efficient pretreatment method before biological treatment process.

Many factors can influence the performance of solar TiO_2 photocatalysis on the treatment of paper mill wastewater [24]. The first one is the size of TiO_2 . New physical and chemical properties will emerge when the size of TiO_2 is reduced

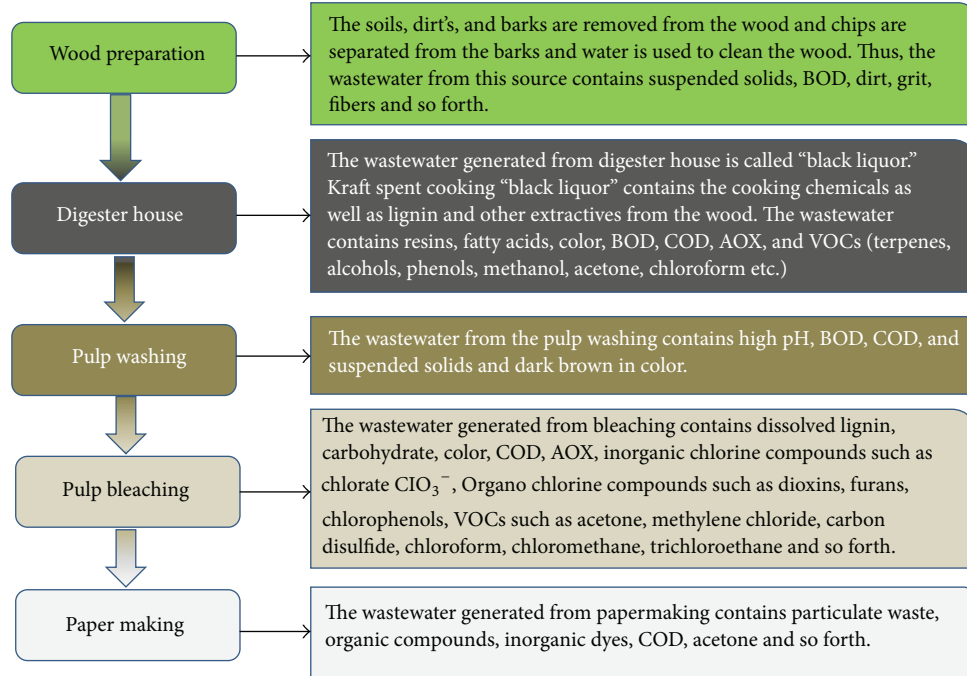


FIGURE 2: Pollutants produced in different stages of paper industry. (Figure 2 is reproduced from reference [23]. Copyright 2004, with permission from Elsevier).

TABLE 1: Typical characteristics of wastewater at different pulp and paper processes. (Table 1 is reproduced from [23]. Copyright 2004, with permission from Elsevier).

| Process | Parameters | | | | | Reference |
|----------------------------------|------------|----------|----------|------------------------|-----------|-----------|
| | PH | TS (ppm) | SS (ppm) | BOD ₅ (ppm) | COD (ppm) | |
| Large mills (India) | 11.0 | 5250 | 1233 | 983 | 2530 | [35] |
| Small mills (India) | 12.3 | 15120 | 4890 | 2628 | 6145 | [35] |
| Digester house | 11.6 | 51589 | 23319 | 13088 | 38588 | [36] |
| Combined effluent | 7.6 | 3318 | 2023 | 103 | 675 | [36] |
| TMP whitewater | 4.7 | — | 91 | 1090 | 2440 | [37] |
| TMP whiterwater | 4.7 | — | 105 | 1125 | 2475 | [38] |
| Kraft mill | 8.2 | 8260 | 3620 | — | 4112 | [39] |
| Pulping | 10 | 1810 | 256 | 360 | — | [40] |
| Kraft mill (unbleached) | 8.2 | 1200 | 150 | 175 | — | [41] |
| Bleached pulp mill | 7.5 | — | 1133 | 1566 | 2572 | [42] |
| Bleaching | 2.5 | 2285 | 216 | 140 | — | [40] |
| Pulp and paper | 7.8 | 4200 | 1400 | 1050 | 4870 | [43] |
| News air and land paper deinking | 8.3 | 450 | 400 | 16 | 78 | [44] |
| Paper making | 7.8 | 1844 | 760 | 561 | 953 | [45] |
| Paper mill | 8.7 | 2415 | 935 | 425 | 845 | [46] |
| Paper machine | 4.5 | — | 503 | 170 | 723 | [42] |
| Paper machine | 8.3 | — | 1032 | 240 | — | [40] |

down to nanoscale. Due to this, the nanosized material may possess with better performance as compared to a conventional bulk material [70]. Chen and Mao [48] reported that morphology of nanomaterials can also affect their properties and performance in specific applications. Nowadays, researchers have put many efforts to develop new functional nanomaterials for the removal of pollutants [71–73]. Ghaly

et al. [24] synthesized nanosized TiO_2 via a conventional sol-gel process using TiCl_4 as the precursor. The synthesized material exhibited good photocatalytic activity under sunlight irradiation because of its mixture phase of anatase and rutile [18]. As shown in Figure 3 [24], the PCO process was carried out in aqueous suspensions where TiO_2 was irradiated by concentrated sunlight. In a typical operation

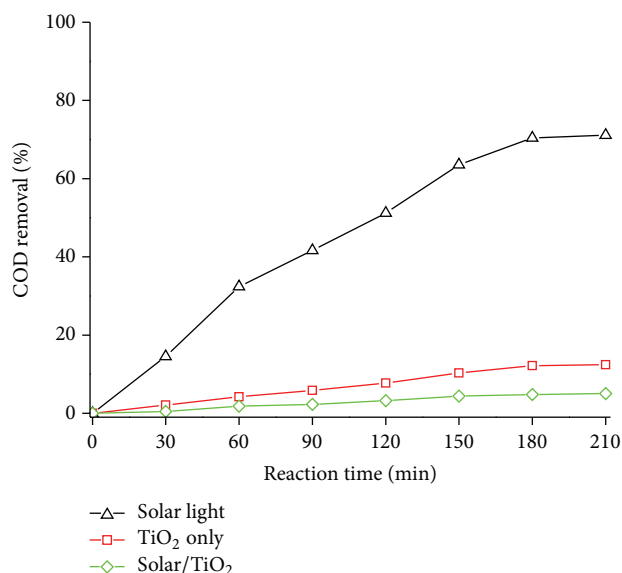


FIGURE 3: %COD removal during the treatment of the wastewater by different oxidation processes against reaction time, with solar light only, with TiO₂ only, and with solar/TiO₂ [TiO₂ = 0.75 g/L, pH = 6.5]. (Figure 3 is reproduced from reference [24]. Copyright 2011, with permission from Elsevier).

process, the wastewater from paper mill was fed into the solar reactor, where it was stirred with the synthesized TiO₂ in dark for 10 min. After the adsorption equilibrium between wastewater and TiO₂ was achieved, solar energy was applied for the photodegradation of the pollutants in wastewater. Subsequently, the wastewater and TiO₂ would circulate in the system and, thus, the treatment efficiency can be enhanced by this continuous process. The COD removal rates under different conditions were evaluated by the authors and shown in Figure 3 [24]. Over 70% COD was removed after the PCO process, indicating that solar photocatalysis is effective for the treatment of paper mill wastewater. It is worth noting that some intermediate compounds may be produced in the process which would retard the degradation of pollutants [24]. In addition, COD concentration decreased in the absence of solar light, which can be attributed to the adsorption effect of TiO₂ on the pollutants in wastewater.

Recent studies indicated that the dosage of photocatalysts is another important influencing factor [63]. It should be noticed that the increase of photocatalyst would increase the reaction sites on the material and, thus, enhance the PCO efficiency. However, some experiments [63] revealed that high TiO₂ concentration does not imply a high reaction performance. According to the previous reports [74], the optimal photocatalyst concentration for industrial wastewater treatment is several hundred mg/L in solar photoreactors. This phenomenon can be explained by the turbidity effect of TiO₂. Excess TiO₂ would affect the penetration of sunlight through the suspensions due to the light scattering effects [63, 75, 76]. Hence, the dosage of TiO₂ in the photoreactor should be optimized, which can also lower the cost on photocatalyst. As shown in Figure 4(a), the optimum TiO₂ concentration is

0.75 g/L in the system [24]. Liu and coworkers reported that the optimum dosage of catalyst was determined not only by the type and concentration of pollutants but also by the design of photoreactors [77]. Thus, the dosage of catalyst should be investigated for each individual system.

In addition, pH values of wastewater can also affect the PCO efficiency because the generation of hydroxyl radicals is related with pH conditions [76]. Several studies showed that the COD removal rates increased with the increase of pH values, as shown in Figure 4(b) [24, 78]. It can be attributed to the following reasons. Firstly, H⁺ can interact with aromatic organic pollutants in paper mill wastewater and lower the electron densities at the polycyclic groups, leading to the decrease of hydroxyl radicals [78]. Secondly, the TiO₂ particles tend to agglomerate under acidic condition and, thus, lead to the decrease of reaction sites for the degradation of pollutants in paper mill wastewater [79]. Finally, the surface of TiO₂ would be negatively charged under high pH conditions due to the presence of OH⁻, which acted as an efficient trap for the generation of h⁺ and hydroxyl radicals. These oxidative species are responsible for the degradation of organic pollutants [79]. Thus, pH condition can be considered as a key factor for the production of hydroxyl radicals, which finally affect the efficiency of solar photocatalysis.

3.2. Application in Textile Wastewater. Owing to the large amount of discharge and the degradation-resistant composition, textile wastewater is considered as a major resource of pollutants from industry [80]. There are several processes for textile industry, such as sizing of fibers, scouring, desizing, bleaching, rinsing, mercerizing, dyeing, and finishing [81]. A brief textile process was shown in Figure 5, revealing that large quantities of organics are involved in this technology. Although various textile products can be obtained nowadays, many contaminants are released into environment through indiscriminate discharge of wastewater, which causes severe pollution. Previous reports indicated that textile wastewater contains dyes, detergents, grease, oil, heavy metal, inorganic salts, and fibers [2]. Among them, dye residue is considered as a dominant pollutant which is mainly produced in the step of finishing [25]. An obvious characteristic of textile wastewater is the strong color due to the presence of various dyes. According to the Easton's reports [82], over 30% of the used dyestuffs remain in the reactor after the dyeing process, which results in that a huge amount of azo dyes enter into wastewater. Azo dyes have been considered as a mutagen and carcinogen by the US National Institute for Occupational Safety and Health [83, 84]. It is important to notice that this kind of dyes is difficult to be decolorized [47, 85].

Although most of the textile wastewater is treated before discharge, the conventional treatment process such as aerobic biological process and physical-chemical treatment cannot meet the requirement of elevated discharge standards [2]. A typical characteristic of wastewater from a textile dyeing process is summarized in Table 2 [86]. We can find that the wastewater contains high strength COD, which may destroy

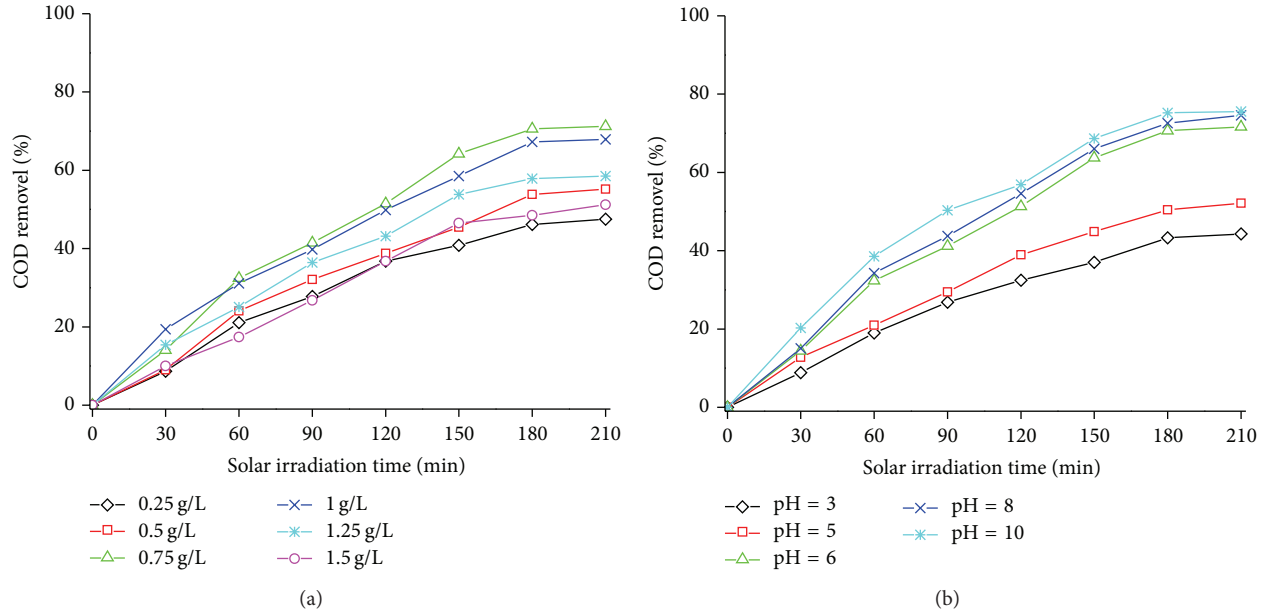


FIGURE 4: (a) %COD removal during the treatment of the wastewater by solar photocatalytic oxidation against solar irradiation time at different loading of TiO_2 [pH = 6.5], (b) %COD removal during the treatment of the wastewater by solar photocatalytic oxidation against solar irradiation time at different pH values [$\text{TiO}_2 = 0.75 \text{ g/L}$]. (Figure 4 is reproduced from reference [24]. Copyright 2011, with permission from Elsevier).

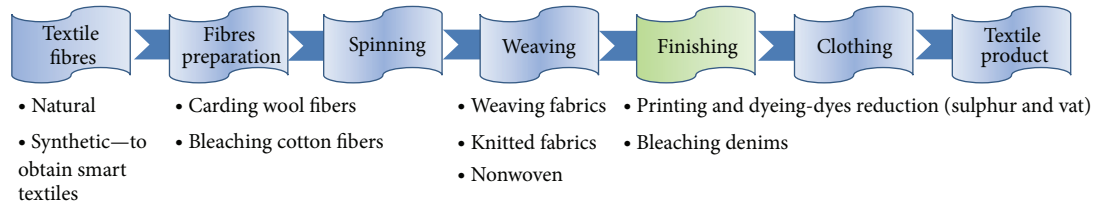


FIGURE 5: A typical textile process [25].

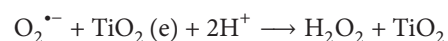
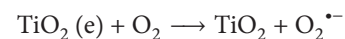
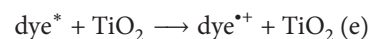
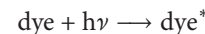
TABLE 2: Typical characteristics of wastewater from a textile dyeing process. (Table 2 is reproduced from [47]. Copyright 1986, with permission from Elsevier).

| Aspect/component | Value |
|------------------------|---------|
| pH | 2–10 |
| Temperature, °C | 30–80 |
| COD, mg/L | 50–5000 |
| BOD, mg/L | 200–300 |
| TSS, mg/L | 50–500 |
| Organic nitrogen, mg/L | 18–39 |
| Total phosphorus, mg/L | 0.3–15 |
| Total chromium, mg/L | 0.2–0.5 |
| Color, mg/L | >300 |

the microorganisms in a biological wastewater treatment system.

Vilar and coworkers studied the treatment of textile wastewater by solar-driven advanced oxidation processes [26]. In this research, commercial TiO_2 P25 was used as the photocatalyst. Figure 6 shows the decolorization and

mineralization of the textile wastewater by TiO_2 solar photocatalysis [26]. We can find that almost 70% of colour in the wastewater was removed when the catalyst concentration was 200 mg/L. The dosage of catalyst was considered as an optimum concentration for the photoreactor used in the study [87]. However, the mineralization of organics in this treatment process is relatively low, which can be attributed to the high concentration of chloride. Owing to the presence of chloride, the produced hydroxyl radicals would be scavenged and some less reactive inorganic radicals such as $\text{Cl}\cdot$, $\text{Cl}_2^{\cdot-}$ and $\text{SO}_4^{\cdot-}$ would also be generated [26, 88]. In addition, previous reports indicated that some organic dyes are capable of photosensitizing TiO_2 due to the absorption of visible light [51]. The major initial steps of the photosensitization reactions are shown in the following equations [89]:



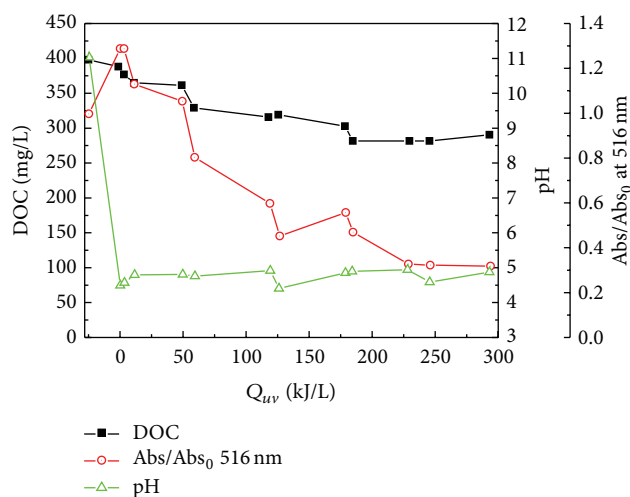
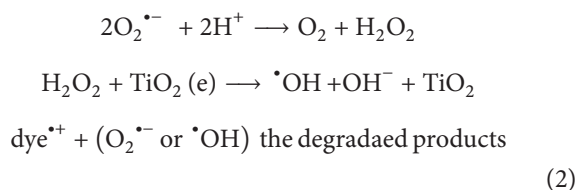


FIGURE 6: Decolourisation and mineralization of the textile wastewater by TiO_2 solar photocatalysis: DOC degradation curve, Abs/Abs₀ AT 516 nm and pH evolution. (Figure 6 is reproduced from reference [26]. Copyright 2011, with permission from Elsevier).



It is clearly shown that the photosensitized degradation of dyes under visible light irradiation is another pathway beside the PCO process. Moreover, some transition or posttransition metal ions such as Cu^{2+} , Zn^{2+} , and Fe^{3+} also have significant effect on the degradation of dyes in textile wastewater via a similar photosensitization [89]. Thus, the decolorization of textile wastewater is relatively easier as compared to the mineralization process.

Some other reports [27, 28, 81, 90] also proved that TiO_2 is a powerful photocatalyst for the degradation of pollutants in textile wastewater. Neppolian et al. [27] found that dye molecules could be completely degraded to CO_2 , SO_4^{2-} , NO_3^- , NH_4^+ , and H_2O by solar photocatalysis, and addition of other auxiliary chemicals such as H_2O_2 and Na_2CO_3 could greatly promote and inhibit the photodegradation efficiency, respectively. pH also plays an important role in the treatment of textile wastewater because it affects both the generation of hydroxyl radicals in PCO process and the structure of dye pollutants. Figure 7 reveals that a neutral pH condition would facilitate the degradation of dyes in solar photocatalysis process. High concentration of proton would retard the photodegradation of dyes under acidic conditions; while basic conditions also have suppressive effect on the solar photocatalysis process because the dyes become chemically stable at high pH ranges [27].

Although TiO_2 based materials have many advantages for environmental application, the separation of them from the suspension of textile wastewater is still a big issue which restricts the reuse of photocatalyst. Alinsafi et al. [91] reported

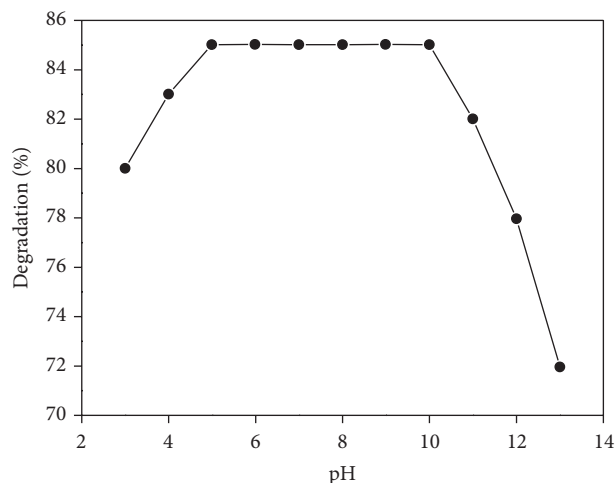


FIGURE 7: Influence of pH on the degradation of the dye. (Figure 7 is reproduced from reference [27]. Copyright 2002, with permission from Elsevier).

that TiO_2 can be immobilised on various substrates such as glass slides and glass fibers. Although the performance of the supported photocatalysts was strongly dependent on the chemical structure of dyes and other additives, the immobilized photocatalysts presented excellent decolourization ability for the treatment of textile industry wastewater. Furthermore, Rao et al. [28] developed a novel pebble bed photocatalytic reactor for textile wastewater treatment under solar irradiation. TiO_2 was successfully coated onto the silica rich white pebbles, and a pebble bed photoreactor was further constructed, as shown in Figure 8. In this research, catalyst loading, pH, and initial concentrations of dyes were found as important influencing factors. In addition, the recirculation flow rate in the system was also investigated, presenting that the conversion of pollutants decreased with the increment of flow rate. This phenomenon can be explained by the nonideal flow behaviour of the photoreactor. The flow diversion should be controlled, which enhances the contact area between the textile wastewater and the coated photocatalysts [28].

3.3. Application in Olive Mill Wastewater (OMW). OMW is considered as one of the most important agricultural pollutants, which was largely produced by some countries such as Spain, Italy, and Greece [92]. The annual production of olive oil was estimated in 2.5×10^6 t, resulting in huge amount of OMW [93]. Production of 1000 kg of olives may generate $0.5\text{--}1.5 \text{ m}^3$ of OMW which is dependent on the oil extraction methods [94, 95]. OMW contains high strength of suspended solids and organic pollutants, such as polysaccharides, sugars, phenols, polyalcohols, proteins, organic acids, and oil [96, 97]. Due to the high concentration of organic pollutants, COD and COD values of OMW are high up to 220 g/L and 100 g/L, respectively [94]. In addition, the characteristics of OMW are variable with the change of climatic conditions, different type of olives, methods of extraction, and regions [94]. The extraction process of olive oil is shown in Figure 9.

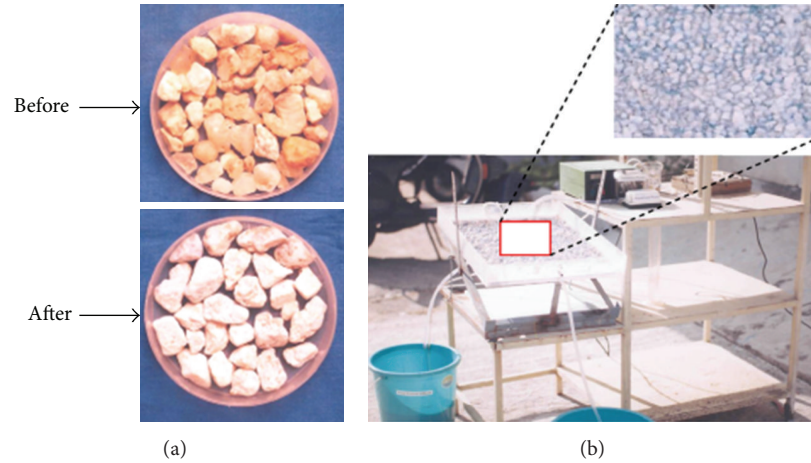


FIGURE 8: (a) Pebbles before and after TiO₂ coating, (b) solar photocatalytic pebble bed reactor, and the close-up of pebbles. (Figure 8 is reproduced from reference [28]. Copyright 2012, with permission from Elsevier).

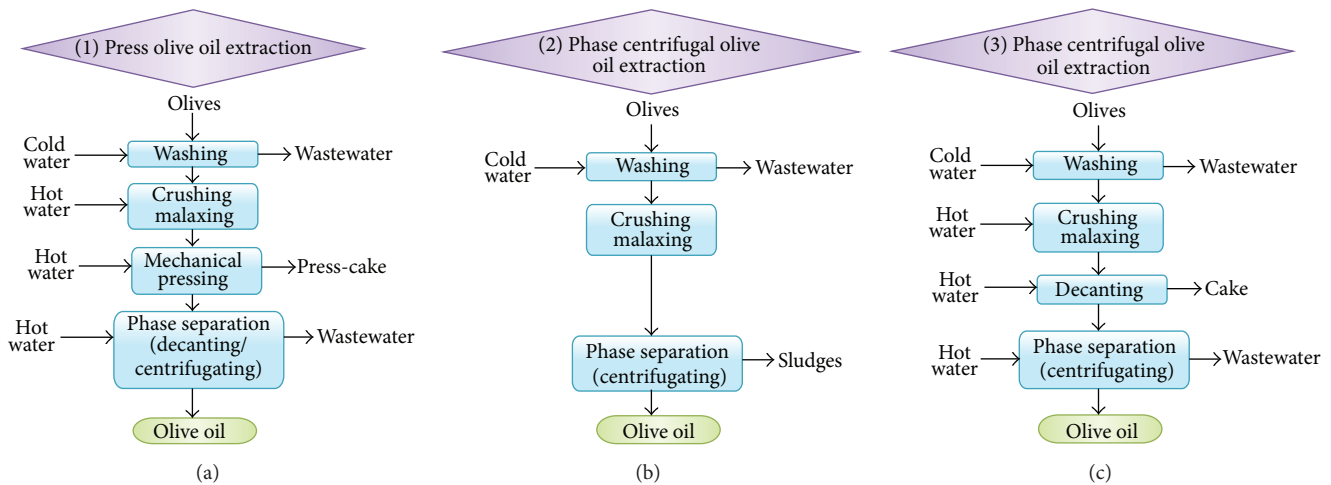


FIGURE 9: Olive oil extraction processes. (Figure 9 is reproduced from reference [29]. Copyright 2012, with permission from Elsevier).

Currently, the main olive process method used in many countries is the 3-phase system, which possesses some advantages such as high working capacity and automation of the industrial plants [29]. Although the olive oil, solids, and wastewater can be separated in this system, it requires a considerable volume of warm water for the dilution of olive paste. Thus, the production of OMW is still a big problem. It is estimated that 30 million m³ OMW is discharged per year [29, 98]. OMW is characterized by a dark-colour due to the polymerization of phenolic compounds and lignin. Moreover, inorganic metals, high conductivity, and acidic condition of the wastewater can also affect the choice of the treatment methods [29].

Gernjak et al. compared two solar photocatalytic pilot-plant reactors (Figures 10(a) and 10(b)) for the degradation of OMW with different concentrations and from different sources [99]. For the compound parabolic collector (CPC), a complete module is formed by a series of collectors connected in a row. Wastewater flows simultaneously through all parallel tubes, and the number of collector components

modules has no limit [30]. For the falling film reactor (FFR), the components contain flat plate, top distributor, bottom receiver, batch tank, and a centrifugal pump. Wastewater in a batch bank flows through the flat plate to bottom receiver, and this is a circulatory system [31]. As a cheaper alternative of CPC, the designed FFR shows comparable results to the CPC in terms of COD degradation rate based on the previous report [31]. Due to the open nonconcentrating geometry of the FFR, there is no reflectivity or transmissivity loss in the reactor. In addition, the shortage of the FFR is the short pathlength of the reactor, but it can be neglected because of the extremely high light absorption of the OMW [31]. Moreover, the temperature in the FFR is lower than that in the CPC due to the heat losses suffered from evaporation of water. This may retard the removal of volatile organic compounds. However, the low temperature would cause less foaming, and the decomposition of hydrogen peroxide can also be reduced [31].

In addition, some other researchers also studied the treatment of OMW using a TiO₂/UV system [100, 101].



(a)



(b)

FIGURE 10: (a) Two compound parabolic collectors (CPCs) of one prototype module, (b) falling film reactor (FFR). (Figure 10(a) is reproduced from reference [30]. Copyright 1999, with permission from Elsevier; Figure 10(b) is reproduced from reference [31]. Copyright 2004, with permission from Elsevier).

Although the UV light source is not economical as compared to the solar source, these studies can also provide some important references for the future work [102]. El Hajjouji et al. [100] investigated the removal rate of COD, colour scale, and phenols in OMW using a TiO_2/UV system. They found that colour and phenols were more difficult to be removed compared to COD, which can be attributed to the degradation of some nonconservative water pollutants in OMW. Chatzisyseon et al. [101] investigated the effect of operating conditions in a photocatalytic treatment process of OMW. Their results indicated that the removal of COD was determined by contact time. Thus, the hydraulic retention time of OMW in a photoreactor is a key factor. Moreover, the detoxification of OMW is strongly dependent on the residual organic matters, indicating that a complete degradation of COD is still required in future application.

4. Conclusions

Solar photocatalysis has been investigated as an effective wastewater treatment process during the past decades.

Although fundamental and engineering researches have established the solar photocatalysis technology in wastewater treatment, the industrial application is still in an infantile stage and some challenges are still needed to be smoothed out, such as the solar utilization efficiency, the construction and operation of photoreactor, and the separation of photocatalysts. Photocatalytic membranes or microspheres might be able to solve the separation problem of photocatalysts [102–104]. Their photocatalytic activities for real wastewater need to be tested under solar irradiation in the future studies. Modification of the current photocatalysts such as doping is a good pathway to enhance the PCO efficiency under solar irradiation considering the low fabrication cost. More attention is also needed to be paid to the design of photoreactors to optimize the operational factors for the system's activity, and recycling should also be comprehensively considered for large-scale applications. We believe that solar TiO_2 photocatalysis method can provide a promising pathway for the deep degradation of the pollutants in industrial wastewaters.

Conflict of Interests

The authors declare that there is no conflict of interests regarding the publication of this paper.

Acknowledgment

The authors would like to thank the financial support by the National Natural Science Foundation of China (51134017).

References

- [1] N. S. A. Mutamim, Z. Z. Noor, M. A. A. Hassan, and G. Olsson, "Application of membrane bioreactor technology in treating high strength industrial wastewater: a performance review," *Desalination*, vol. 305, pp. 1–11, 2012.
- [2] W. Lau and A. F. Ismail, "Polymeric nanofiltration membranes for textile dye wastewater treatment: preparation, performance evaluation, transport modelling, and fouling control: a review," *Desalination*, vol. 245, no. 1–3, pp. 321–348, 2009.
- [3] J. J. Langenfeld, S. B. Hawthorne, and D. J. Miller, "Quantitative analysis of fuel-related hydrocarbons in surface water and wastewater samples by solid-phase microextraction," *Analytical Chemistry*, vol. 68, no. 1, pp. 144–155, 1996.
- [4] P. P. Wu, T. Wu, W. W. He, L. L. Sun, Y. J. Li, and D. Sun, "Adsorption properties of dodecylsulfate-intercalated layered double hydroxide for various dyes in water," *Colloids and Surfaces A: Physicochemical and Engineering Aspects*, vol. 436, pp. 726–731, 2013.
- [5] M. Alsheyab, J. Q. Jiang, and C. Stanford, "On-line production of ferrate with an electrochemical method and its potential application for wastewater treatment—A review," *Journal of Environmental Management*, vol. 90, no. 3, pp. 1350–1356, 2009.
- [6] C. Zhang, Y. Jiang, Y. Li, Z. Hu, L. Zhou, and M. Zhou, "Three-dimensional electrochemical process for wastewater treatment: a general review," *Chemical Engineering Journal*, vol. 228, pp. 455–467, 2013.
- [7] G. H. Chen, "Electrochemical technologies in wastewater treatment," *Separation and Purification Technology*, vol. 3, no. 1, pp. 11–41, 2004.

- [8] C. C. Ho and C. Y. Chan, "The application of lead dioxide-coated titanium anode in the electroflotation of palm oil mill effluent," *Water Research*, vol. 20, no. 12, pp. 1523–1527, 1986.
- [9] A. Y. Hosny, "Separating oil from oil-water emulsions by electroflotation technique," *Separations Technology*, vol. 6, no. 1, pp. 9–17, 1996.
- [10] T. Zhang, Y. Wang, J. Ng, and D. D. Sun, "A free-standing, hybrid TiO₂/K-OMS-2 hierarchical nanofibrous membrane with high photocatalytic activity for concurrent membrane filtration applications," *RSC Advances*, vol. 2, no. 9, pp. 3638–3641, 2012.
- [11] A. Joss, E. Keller, A. C. Alder et al., "Removal of pharmaceuticals and fragrances in biological wastewater treatment," *Water Research*, vol. 39, no. 14, pp. 3139–3152, 2005.
- [12] M. A. Shannon, P. W. Bohn, M. Elimelech, J. G. Georgiadis, B. J. Mariás, and A. M. Mayes, "Science and technology for water purification in the coming decades," *Nature*, vol. 452, no. 7185, pp. 301–310, 2008.
- [13] M. R. Hoffmann, S. T. Martin, W. Choi, and D. W. Bahnemann, "Environmental applications of semiconductor photocatalysis," *Chemical Reviews*, vol. 95, no. 1, pp. 69–96, 1995.
- [14] M. N. Chong, B. Jin, C. W. K. Chow, and C. Saint, "Recent developments in photocatalytic water treatment technology: a review," *Water Research*, vol. 44, no. 10, pp. 2997–3027, 2010.
- [15] T. Zhang, X. Yan, and D. D. Sun, "Hierarchically multifunctional K-OMS-2/TiO₂/Fe₃O₄ heterojunctions for the photocatalytic oxidation of humic acid under solar light irradiation," *Journal of Hazardous Materials*, vol. 243, pp. 302–310, 2012.
- [16] Y. Kuwahara, T. Kamegawa, K. Mori, and H. Yamashita, "Design of new functional Titanium oxide-based photocatalysts for degradation of organics diluted in water and air," *Current Organic Chemistry*, vol. 14, no. 7, pp. 616–629, 2010.
- [17] A. Fujishima, T. N. Rao, D. A. Tryk, and J. Photoch, "Titanium dioxide photocatalysis," *Journal of Photochemistry and Photobiology C: Photochemistry Reviews*, vol. 1, no. 1, pp. 1–21, 2000.
- [18] A. L. Linsebigler, G. Q. Lu, and J. T. Yates Jr., "Photocatalysis on TiO₂ surfaces: principles, mechanisms, and selected results," *Chemical Reviews*, vol. 95, no. 3, pp. 735–758, 1995.
- [19] M. Sioi, A. Bolosis, E. Kostopoulou, and I. Poullos, "Photocatalytic treatment of colored wastewater from medical laboratories: photocatalytic oxidation of hematoxylin," *Journal of Photochemistry and Photobiology A: Chemistry*, vol. 184, no. 1–2, pp. 18–25, 2006.
- [20] D. S. Kim and Y. S. Park, "Comparison study of dyestuff wastewater treatment by the coupled photocatalytic oxidation and biofilm process," *Chemical Engineering Journal*, vol. 139, no. 2, pp. 256–263, 2008.
- [21] S. Malato, J. Blanco, J. Cáceres, A. R. Fernández-Alba, A. Agüera, and A. Rodríguez, "Photocatalytic treatment of water-soluble pesticides by photo-Fenton and TiO₂ using solar energy," *Catalysis Today*, vol. 76, pp. 209–220, 2002.
- [22] A. Antoniadis, V. Takavakoglou, G. Zalidis, E. Darakas, and I. Poullos, "Municipal wastewater treatment by sequential combination of photocatalytic oxidation with constructed wetlands," *Catalysis Today*, vol. 151, no. 1–2, pp. 114–118, 2010.
- [23] D. Pokhrel and T. Viraraghavan, "Treatment of pulp and paper mill wastewater—a review," *Science of the Total Environment*, vol. 333, no. 1–3, pp. 37–58, 2004.
- [24] M. Y. Ghaly, T. S. Jamil, I. E. El-Seesy, E. R. Souaya, and R. A. Nasr, "Treatment of highly polluted paper mill wastewater by solar photocatalytic oxidation with synthesized nano TiO₂," *Chemical Engineering Journal*, vol. 168, no. 1, pp. 446–454, 2011.
- [25] M. Sala and M. C. Gutiérrez-Bouzán, "Electrochemical techniques in textile processes and wastewater treatment," *International Journal of Photoenergy*, vol. 2012, Article ID 629103, 12 pages, 2012.
- [26] V. J. P. Vilar, L. X. Pinho, A. M. A. Pintor, and R. A. R. Boaventura, "Treatment of textile wastewaters by solar-driven advanced oxidation processes," *Solar Energy*, vol. 85, no. 9, pp. 1927–1934, 2011.
- [27] B. Neppolian, H. C. Choi, S. Sakthivel, B. Arabindoo, and V. Murugesan, "Solar light induced and TiO₂ assisted degradation of textile dye reactive blue 4," *Chemosphere*, vol. 46, no. 8, pp. 1173–1181, 2002.
- [28] N. N. Rao, V. Chaturvedi, and G. Li Puma, "Novel pebble bed photocatalytic reactor for solar treatment of textile wastewater," *Chemical Engineering Journal*, vol. 184, pp. 90–97, 2012.
- [29] H. Zbakh and A. El Abbassi, "Potential use of olive mill wastewater in the preparation of functional beverages: a review," *Journal of Functional Foods*, vol. 4, no. 1, pp. 53–65, 2012.
- [30] J. Blanco, S. Malato, P. Fernández et al., "Compound parabolic concentrator technology development to commercial solar detoxification applications," *Solar Energy*, vol. 67, no. 4–6, pp. 317–330, 1999.
- [31] W. Gernjak, M. I. Maldonado, S. Malato et al., "Pilot-plant treatment of olive mill wastewater (OMW) by solar TiO₂ photocatalysis and solar photo-Fenton," *Solar Energy*, vol. 77, no. 5, pp. 567–572, 2004.
- [32] J. Herrmann, C. Guillard, J. Disdier, C. Lehaut, S. Malato, and J. Blanco, "New industrial titania photocatalysts for the solar detoxification of water containing various pollutants," *Applied Catalysis B: Environmental*, vol. 35, no. 4, pp. 281–294, 2002.
- [33] D. S. Bhatkhande, V. G. Pangarkar, and A. A. C. M. Beenackers, "Photocatalytic degradation of nitrobenzene using titanium dioxide and concentrated solar radiation: chemical effects and scaleup," *Water Research*, vol. 37, no. 6, pp. 1223–1230, 2003.
- [34] M. Styliidi, D. I. Kondarides, and X. E. Verykios, "Pathways of solar light-induced photocatalytic degradation of azo dyes in aqueous TiO₂ suspensions," *Applied Catalysis B: Environmental*, vol. 40, no. 4, pp. 271–286, 2003.
- [35] S. K. Srivastava, R. Bembi, A. K. Singh, and A. Sharma, "Physicochemical studies on the characteristics and disposal problems of small and large pulp and paper mill effluents," *Indian Journal of Environmental Protection*, vol. 10, no. 6, pp. 438–442, 1990.
- [36] R. S. Singh, S. S. Marwaha, and P. K. Khanna, "Characteristics of pulp and paper mill effluents," *Journal of Industrial Pollution Control*, vol. 12, no. 2, pp. 163–172, 1996.
- [37] S. J. Jahren and H. Oedegaard, "The use of Computational Fluid Dynamics for improving the design and operation of water and wastewater treatment plants," *Water Science and Technology*, vol. 40, no. 4–5, pp. 81–90, 1999.
- [38] S. J. Jahren, J. A. Rintala, and H. Ødegaard, "Aerobic moving bed biofilm reactor treating thermomechanical pulping whitewater under thermophilic conditions," *Water Research*, vol. 36, no. 4, pp. 1067–1075, 2002.
- [39] R. S. Rohella, S. Choudhury, M. Manthan, and J. S. Murty, "Removal of colour and turbidity in pulp and paper mill effluents using polyelectrolytes," *Indian Journal of Environmental Health*, vol. 43, no. 4, pp. 159–163, 2001.
- [40] F. B. Dilek and C. F. Gokcay, "Treatment of effluents from hemp-based pulp and paper industry: I - Waste characterization and physico-chemical treatability," *Water Science and Technology*, vol. 29, no. 9, pp. 161–163, 1994.

- [41] N. L. Nemerow and A. Dasgupta, *Industrial and Hazardous Waste Management*, Van Nostrand Reinhold, New York, NY, USA, 1991.
- [42] N. T. Yen, N. T. K. Oanh, L. B. Reutergard, D. L. Wise, and N. T. T. Lan, "An integrated waste survey and environmental effects of COGIDO, a bleached pulp and paper mill in Vietnam, on the receiving waterbody," *Studies in Environmental Science*, vol. 66, pp. 349–361, 1997.
- [43] T. N. Mandal and T. N. Bandana, "Studies on physicochemical and biological characteristics of pulp and paper mill effluents and its impact on human beings," *Journal of the Freshwater Biology*, vol. 8, pp. 191–196, 1996.
- [44] A. G. Vlyssides and D. G. Economides, "Characterization of wastes from a newspaper wash deinking process," *Fresenius Environmental Bulletin*, vol. 6, no. 11-12, pp. 734–739, 1997.
- [45] A. Gupta, "Pollution load of paper mill effluent and its impact on biological environment," *Journal of Ecotoxicology and Environmental Monitoring*, vol. 7, pp. 101–112, 1997.
- [46] S. K. Dutta, "Study of the physicochemical properties of effluent of the paper mill that affected the paddy plants," *Journal of Environmental Pollution*, vol. 6, no. 2-3, pp. 181–188, 1999.
- [47] U. Pagga and D. Brown, "The degradation of dyestuffs. Part II: behaviour of dyestuffs in aerobic biodegradation tests," *Chemosphere*, vol. 15, no. 4, pp. 479–491, 1986.
- [48] X. Chen and S. S. Mao, "Titanium dioxide nanomaterials: synthesis, properties, modifications and applications," *Chemical Reviews*, vol. 107, no. 7, pp. 2891–2959, 2007.
- [49] X. Zhang, T. Zhang, J. H. Pan, J. Ng, and D. D. Sun, "Transformation of bromine species in TiO₂ photocatalytic system," *Environmental Science & Technology*, vol. 44, no. 1, pp. 439–444, 2010.
- [50] H. Honda, A. Ishizaki, R. Soma, K. Hashimoto, and A. Fujishima, "Application of photocatalytic reactions caused by TiO₂ film to improve the maintenance factor of lighting systems," *Journal of the Illuminating Engineering Society*, vol. 27, no. 1, pp. 42–47, 1998.
- [51] F. Han, V. S. R. Kambala, M. Srinivasan, D. Rajarathnam, and R. Naidu, "Tailored titanium dioxide photocatalysts for the degradation of organic dyes in wastewater treatment: a review," *Applied Catalysis A: General*, vol. 359, no. 1-2, pp. 25–40, 2009.
- [52] V. S. R. Kambala, B. Lavédrine, and P. Boule, "Influence of metallic species on TiO₂ for the photocatalytic degradation of dyes and dye intermediates," *Journal of Photochemistry and Photobiology A: Chemistry*, vol. 154, no. 2-3, pp. 189–193, 2003.
- [53] A. Wold, "Photocatalytic properties of TiO₂," *Chemistry of Materials*, vol. 5, no. 3, pp. 280–283, 1993.
- [54] Y. Zang and R. Farnood, "Photocatalytic activity of AgBr/TiO₂ in water under simulated sunlight irradiation," *Applied Catalysis B: Environmental*, vol. 79, no. 4, pp. 334–340, 2008.
- [55] Y. Bessekhoud, D. Robert, J. V. Weber, and J. Photochem, "Bi₂S₃/TiO₂ and CdS/TiO₂ heterojunctions as an available configuration for photocatalytic degradation of organic pollutant," *Journal of Photochemistry and Photobiology A: Chemistry*, vol. 163, no. 3, pp. 569–580, 2004.
- [56] M. Sökmen, D. W. Allen, F. Akkas, N. Kartal, and F. Acar, "Photo-degradation of some dyes using Ag-loaded titanium dioxide," *Water, Air, & Soil Pollution*, vol. 132, pp. 153–163, 2001.
- [57] A. Özkan, M. H. Özkan, R. Gürkan, M. Akçay, and M. Sökmen, "Photocatalytic degradation of a textile azo dye, Sirius Gelb GC on TiO₂ or Ag-TiO₂ particles in the absence and presence of UV irradiation: the effects of some inorganic anions on the photocatalysis," *Journal of Photochemistry and Photobiology A: Chemistry*, vol. 163, pp. 29–35, 2004.
- [58] J. Grzechulska and A. W. Morawski, "Photocatalytic decomposition of azo-dye acid black 1 in water over modified titanium dioxide," *Applied Catalysis B*, vol. 36, no. 1, pp. 45–51, 2002.
- [59] L. C. Chen, C. M. Huang, and F. R. Tsai, "Characterization and photocatalytic activity of K⁺-doped TiO₂ photocatalysts," *Journal of Molecular Catalysis A: Chemical*, vol. 265, no. 1-2, pp. 133–140, 2007.
- [60] C. Barglik-Chory, C. Remenyi, H. Strohm, and G. Müller, "Adjustment of the band gap energies of biostabilized CdS nanoparticles by application of statistical design of experiments," *Journal of Physical Chemistry B*, vol. 108, no. 23, pp. 7637–7640, 2004.
- [61] N. L. Nemerow and A. Dasgupta, *Industrial and hazardous waste management*, Van Nostrand Reinhold, New York, NY, USA, 1991.
- [62] Ottawa, Canadian Government Publishing Centre, 1990.
- [63] A. C. Rodrigues, M. Boroski, N. S. Shimada, J. C. Garcia, J. Nozaki, and N. Hioka, "Treatment of paper pulp and paper mill wastewater by coagulation-flocculation followed by heterogeneous photocatalysis," *Journal of Photochemistry and Photobiology A: Chemistry*, vol. 194, no. 1, pp. 1–10, 2008.
- [64] S. Lacorte, A. Latorre, D. Barceló, A. Rigol, A. Malmqvist, and T. Welander, "Organic compounds in paper-mill process waters and effluents," *TrAC—Trends in Analytical Chemistry*, vol. 22, no. 10, pp. 725–737, 2003.
- [65] L. T. Angenenta, K. Karim, M. H. Al-Dahhan, B. A. Wrenn, and R. Domínguez-Espinosa, "Production of bioenergy and biochemicals from industrial and agricultural wastewater," *Trends in Biotechnology*, vol. 22, no. 9, pp. 477–486, 2004.
- [66] US EPA, "Permit guidance document: pulp, paper and paperboard manufacturing point source category," EPA-821B00003, 2000.
- [67] J. L. de Moraes, C. Sirtori, and P. G. Peralta-Zamora, "Treatment of landfill leachates by heterogeneous photocatalysis integrated to a conventional biological process," *Química Nova*, vol. 29, no. 1, pp. 20–23, 2006.
- [68] G. Thompson, J. Swain, M. Kay, and C. F. Forster, "The treatment of pulp and paper mill effluent: a review," *Bioresource Technology*, vol. 77, no. 3, pp. 275–286, 2001.
- [69] P. Bajpai, *Treatment of Pulp and Paper Mill Effluents with Anaerobic Technology*, Pira International, Leatherhead, UK.
- [70] C. G. Granqvist, A. Azens, P. Heszler, L. B. Kish, and L. Österlund, "Nanomaterials for benign indoor environments: electrochromics for "smart windows", sensors for air quality, and photo-catalysts for air cleaning," *Solar Energy Materials and Solar Cells*, vol. 91, pp. 355–365, 2007.
- [71] J. Yuan, K. Laubernds, J. Villegas, S. Gomez, and S. L. Suib, "Spontaneous formation of inorganic paper-like materials," *Advanced Materials*, vol. 16, no. 19, pp. 1729–1732, 2004.
- [72] J. Yuan, X. Liu, O. Akbulut et al., "Superwetting nanowire membranes for selective absorption," *Nature Nanotechnology*, vol. 3, no. 6, pp. 332–336, 2008.
- [73] X. Zhang, J. H. Pan, A. J. Du, W. Fu, D. D. Sun, and J. O. Leckie, "Combination of one-dimensional TiO₂ nanowire photocatalytic oxidation with microfiltration for water treatment," *Water Research*, vol. 43, no. 5, pp. 1179–1186, 2009.
- [74] S. Malato, P. Fernández-Ibáñez, M. I. Maldonado, J. Blanco, and W. Gernjak, "Decontamination and disinfection of water by solar photocatalysis: recent overview and trends," *Catalysis Today*, vol. 147, no. 1, pp. 1–59, 2009.

- [75] M. Pera-Titus, V. García-Molina, M. A. Bãnos, J. Giménez, and S. Esplugas, "Degradation of chlorophenols by means of advanced oxidation processes: a general review," *Applied Catalysis B: Environmental*, vol. 47, no. 4, pp. 219–256, 2004.
- [76] P. R. Gogate and A. B. Pandit, "A review of imperative technologies for wastewater treatment I: oxidation technologies at ambient conditions," *Advances in Environmental Research*, vol. 8, no. 3-4, pp. 501–551, 2004.
- [77] S. Liu, J. Yang, and J. Choy, "Microporous SiO₂-TiO₂ nanosols pillared montmorillonite for photocatalytic decomposition of methyl orange," *Journal of Photochemistry and Photobiology A: Chemistry*, vol. 179, no. 1-2, pp. 75–80, 2006.
- [78] I. Konstantinou and T. Albanis, "TiO₂-assisted photocatalytic degradation of azo dyes in aqueous solution: kinetic and mechanistic investigations: a review," *Applied Catalysis B: Environmental*, vol. 49, no. 1, pp. 1–14, 2004.
- [79] M. A. Fox and M. T. Dulay, "Heterogeneous photocatalysis," *Chemical Reviews*, vol. 93, no. 1, pp. 341–357, 1993.
- [80] V. Correia, T. Stephenson, and S. J. Judd, "Characterisation of textile wastewaters—a review," *Environmental Technology*, vol. 15, no. 10, pp. 917–929, 1994.
- [81] P. A. Pekakis, N. P. Xekoukoulotakis, and D. Mantzavinos, "Treatment of textile dyehouse wastewater by TiO₂ photocatalysis," *Water Research*, vol. 40, no. 6, pp. 1276–1286, 2006.
- [82] J. Easton, *Colour in Dyehouse Effluent*, Alden Press, Oxford, UK, 1995.
- [83] B. W. Manning, C. E. Cerniglia, and T. W. Federle, "Metabolism of the benzidine-based azo dye direct black 38 by human intestinal microbiota," *Applied and Environmental Microbiology*, vol. 50, no. 1, pp. 10–15, 1985.
- [84] E. R. Bandala, M. A. Peláez, A. J. García-López, M. J. Salgado, and G. Moeller, "Photocatalytic decolourisation of synthetic and real textile wastewater containing benzidine-based azo dyes," *Chemical Engineering and Processing*, vol. 47, pp. 169–176, 2008.
- [85] C. M. Carliell, S. J. Barclay, N. Naidoo, C. A. Buckley, D. A. Mulholland, and E. Senior, "Microbial decolourisation of a reactive azo dye under anaerobic conditions," *Water SA*, vol. 21, no. 1, pp. 61–69, 1995.
- [86] M. Marcucci, I. Ciabatti, A. Matteucci, and G. Vernaglione, "Membrane technologies applied to textile wastewater treatment," *Annals of the New York Academy of Sciences*, vol. 984, pp. 53–64, 2003.
- [87] R. S. Malato, G. J. Blanco, R. M. I. Maldonado et al., "Engineering of solar photocatalytic collectors," *Solar Energy*, vol. 77, no. 5, pp. 513–524, 2004.
- [88] C. Guillard, H. Lachheb, A. Houas, M. Ksibi, E. Elaloui, and J. Herrmann, "Influence of chemical structure of dyes, of pH and of inorganic salts on their photocatalytic degradation by TiO₂ comparison of the efficiency of powder and supported TiO₂," *Journal of Photochemistry and Photobiology A: Chemistry*, vol. 158, no. 1, pp. 27–36, 2003.
- [89] C. Chen, X. Li, W. Ma, J. Zhao, H. Hidaka, and N. Serpone, "Effect of transition metal ions on the TiO₂-assisted photodegradation of dyes under visible irradiation: a probe for the interfacial electron transfer process and reaction mechanism," *The Journal of Physical Chemistry B*, vol. 106, no. 2, pp. 318–324, 2002.
- [90] I. Arslan, I. A. Balcioglu, and D. W. Bahnemann, "Heterogeneous photocatalytic treatment of simulated dyehouse effluents using novel TiO₂-photocatalysts," *Applied Catalysis B: Environmental*, vol. 26, no. 3, pp. 193–206, 2000.
- [91] A. Alinsafi, F. Evenou, E. M. Abdulkarim et al., "Treatment of textile industry wastewater by supported photocatalysis," *Dyes and Pigments*, vol. 74, no. 2, pp. 439–445, 2007.
- [92] L. Rizzo, G. Lofrano, M. Grassi, and V. Belgiorno, "Pre-treatment of olive mill wastewater by chitosan coagulation and advanced oxidation processes," *Separation and Purification Technology*, vol. 63, no. 3, pp. 648–653, 2008.
- [93] M. Brenes, A. García, P. García, J. J. Rios, and A. Garrido, "Phenolic compounds in Spanish olive oils," *Journal of Agricultural and Food Chemistry*, vol. 47, no. 9, pp. 3535–3540, 1999.
- [94] P. Paraskeva and E. Diamadopoulos, "Technologies for olive mill wastewater (OMW) treatment: a review," *Journal of Chemical Technology and Biotechnology*, vol. 81, no. 9, pp. 1475–1485, 2006.
- [95] A. C. Barbera, C. Maucieri, V. Cavallaro, A. Ioppolo, and G. Spagna, "Effects of spreading olive mill wastewater on soil properties and crops, a review," *Agricultural Water Management*, vol. 119, pp. 43–53, 2013.
- [96] M. Beccari, G. Carucci, A. M. Lanz, M. Majone, and M. P. Papini, "Removal of molecular weight fractions of COD and phenolic compounds in an integrated treatment of olive oil mill effluents," *Biodegradation*, vol. 13, no. 6, pp. 401–410, 2002.
- [97] F. Cabrera, R. López, A. Martínez-Bordiú, E. de Dupuy Lome, and J. M. Murillo, "Land Treatment of Olive Oil Mill Wastewater," *International Biodeterioration and Biodegradation*, vol. 38, no. 3-4, pp. 215–225, 1996.
- [98] I. Sabbah, T. Marsook, and S. Basheer, "The effect of pretreatment on anaerobic activity of olive mill wastewater using batch and continuous systems," *Process Biochemistry*, vol. 39, no. 12, pp. 1947–1951, 2004.
- [99] W. Gernjak, M. L. Maldonado, S. Malato et al., "Pilot-plant treatment of olive mill wastewater (OMW) by solar TiO₂ photocatalysis and solar photo-Fenton," *Solar Energy*, vol. 77, no. 5, pp. 567–572, 2004.
- [100] H. El Hajjouji, F. Barje, E. Pinelli et al., "Photochemical UV/TiO₂ treatment of olive mill wastewater (OMW)," *Biore-source Technology*, vol. 99, no. 15, pp. 7264–7269, 2008.
- [101] E. Chatzisyneon, N. P. Xekoukoulotakis, and D. Mantzavinos, "Determination of key operating conditions for the photocatalytic treatment of olive mill wastewaters," *Catalysis Today*, vol. 144, no. 1-2, pp. 143–148, 2009.
- [102] X. Zhang, D. Wang, and J. C. Diniz da Costa, "Recent progress on fabrication of photocatalytic membranes for water treatment," *Catalysis Today*, vol. 230, pp. 47–54, 2014.
- [103] X. Zhang, T. Zhang, J. Ng, and D. D. Sun, "High-Performance Multifunctional TiO₂ Nanowire Ultrafiltration Membrane with a Hierarchical Layer Structure for Water Treatment," *Advanced Functional Materials*, vol. 19, no. 23, pp. 3731–3736, 2009.
- [104] X. Zhang, J. H. Pan, A. J. Du, J. Ng, D. D. Sun, and J. O. Leckie, "Fabrication and photocatalytic activity of porous TiO₂ nanowire microspheres by surfactant-mediated spray drying process," *Materials Research Bulletin*, vol. 44, no. 5, pp. 1070–1076, 2009.

Research Article

Sol-Gel to Prepare Nitrogen Doped TiO₂ Nanocrystals with Exposed {001} Facets and High Visible-Light Photocatalytic Performance

Hui-Ying Ai,¹ Jian-Wen Shi,¹ Rui-Xi Duan,² Jian-Wei Chen,¹
Hao-Jie Cui,¹ and Ming-Lai Fu¹

¹ Key Laboratory of Urban Environment and Health, Institute of Urban Environment, Chinese Academy of Sciences, No. 1799, Jimei Road, Xiamen, Fujian 361021, China

² China National Petroleum Offshore Engineering Co., Ltd., Beijing 100028, China

Correspondence should be addressed to Jian-Wen Shi; shijwn@163.com and Ming-Lai Fu; mlfu@iue.ac.cn

Received 1 April 2014; Revised 3 June 2014; Accepted 17 June 2014; Published 7 July 2014

Academic Editor: Qing Wang

Copyright © 2014 Hui-Ying Ai et al. This is an open access article distributed under the Creative Commons Attribution License, which permits unrestricted use, distribution, and reproduction in any medium, provided the original work is properly cited.

A series of N-doped TiO₂ nanocrystals with exposed {001} facets was prepared successfully by sol-gel method for the first time. The physicochemical properties of these resultant photocatalysts were characterized by XRD, TEM, XPS, and DRS, and their photocatalytic performances were evaluated by photocatalytic decoloration of methylene blue solution under visible light ($\lambda > 420$ nm) irradiation. The results showed that the N-doped TiO₂ nanocrystals with exposed {001} facets showed higher photocatalytic activity than P25. The enhanced photocatalytic performance can be attributed to synergistic effects of several factors, such as good crystallinity, better light response characteristic, and high reactivity of {001} facets.

1. Introduction

TiO₂ with exposed {001} facets has attracted great attention in recent years because of its outstanding advantages in photocatalysis field [1–3], such as excellent thermodynamic stability, strong oxidizing power, and low cost. Many researchers have participated in optimizing its photocatalytic activity since the large percentage of {001} reactive facets were prepared by one-pot hydrothermal method using TiF₄ as precursor firstly [4]. It is widely believed that {001} facets of anatase TiO₂ provide more active sites for photocatalytic oxidation reaction [5, 6], so its photocatalytic activity can be improved significantly. However, the photocatalytic activity of TiO₂ is still limited by narrow light absorption (only responsive to UV with wavelength below 387 nm due to its wide band-gap) and rapid recombination of photon-generated carriers. To promote the better performance of TiO₂, anion doping, especially nitrogen doping, would be effective solution. Experiments and theories have proved that the doping of nitrogen can introduce a new impurity level in the band gap of TiO₂, which provides a springboard for

electron transition and promotes the visible-light response of TiO₂ [7–9].

The popular approach to synthesize TiO₂ with exposed {001} facets is hydro(solvo)thermal method [10, 11], and anion doped TiO₂ (e.g., N, C, S) with exposed {001} facets has been synthesized successfully by hydro(solvo)thermal method in recent years [12–14]. The resultant samples are usually with a larger size, submicron, and even several microns [15], which is disadvantaged to the photocatalytic activity of TiO₂. Therefore, anion doped TiO₂ with exposed {001} facets and smaller size is still desirable. Lots of publications have proved that sol-gel is an ideal method to prepare uniform TiO₂ powder with smaller size. Therefore, sol-gel method may be a good attempt to obtain anion doped TiO₂ nanocrystals with exposed {001} facets [16]. However, the sol-gel preparation of anion doped TiO₂ nanocrystals with exposed {001} facets has not been reported so far.

In this study, we prepared N-doped TiO₂ nanocrystals with exposed {001} facets by using sol-gel method successfully. The as-synthesized N-doped TiO₂ nanocrystals with exposed {001} facets showed higher photocatalytic activity

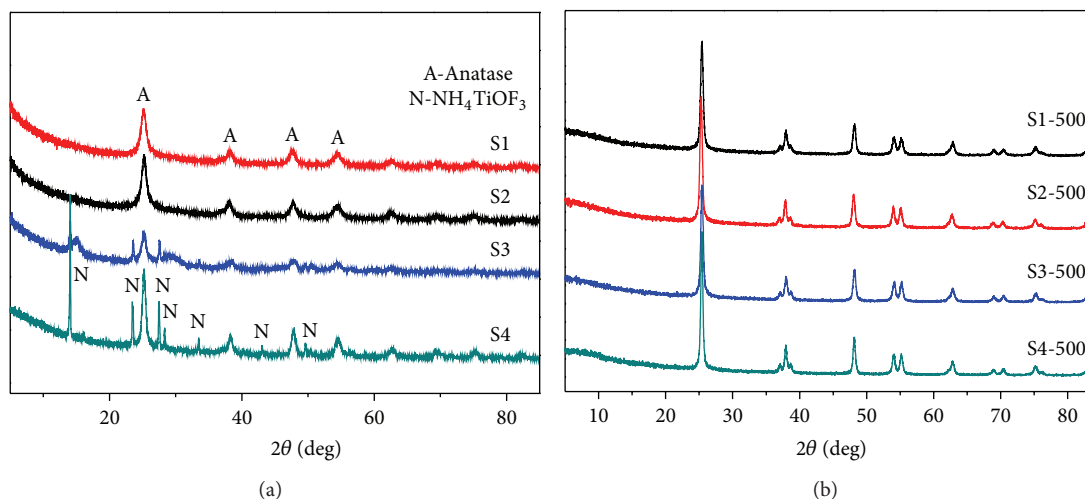


FIGURE 1: XRD patterns of all samples ((a) the uncalcined samples, (b) the calcined samples).

than P25 in the degradation of methylene blue (MB) dye under visible-light illumination, and the influenced factors of photocatalytic activity were discussed in detail. To our knowledge, this is the first time to prepare N-doped TiO_2 nanocrystals with exposed {001} facets successfully by using sol-gel method, and the excellent visible-light activity has rarely been reported.

2. Experimental

2.1. Preparation of N-Doped TiO_2 Nanocrystals with Exposed {001} Facets. N-doped TiO_2 nanocrystals with exposed {001} facets were synthesized by a sol-gel method [17]. Firstly, 6.85 mL of tetrabutyl titanate was dispersed in 15.5 mL of absolute ethanol under vigorous stirring for 30 min in a conical flask with cover (solution A). Secondly, a given amount of NH_4F (the molar ratio of Ti to N was controlled at 1:4, 1:2, 1:1, 2:1), 7.75 mL of absolute ethanol, 8 mL of acetic acid, and 2.88 mL of pure water were mixed in a beaker (solution B). Then, solution B was dropwise added to solution A with vigorous magnetic agitation. Subsequently, the obtained mixtures were kept in incubator chamber at 90°C for 12 h. The obtained gel from the sol-gel reaction was dried at 80°C in an oven and then porphyzied into powders. The as-obtained samples were named S1, S2, S3, and S4, respectively. In order to improve the crystallinity, the four samples were calcined at 500°C in a furnace for 2 h to obtain the samples labeled as S1-500, S2-500, S3-500, and S4-500, respectively.

2.2. Characterization. Powder X-ray diffraction (XRD) patterns were recorded at room temperature with an X'pert diffractometer (PANalytical, Holland) with copper $\text{K}_{\alpha 1}$ radiation to determine the crystalline structure of the samples. SEM images were obtained by a field emission scanning electron microscopy (S-4800, Hitachi, Japan) equipment and TEM images were carried out on a transmission electron

microscope (JEM 2100, JEOL, Japan) to characterize morphology of the samples. XPS analyses were tested on an X-ray photoelectron spectrometer (ESCALAB250, Thermo Scientific, USA) with aluminum K_{α} radiation to analyze the chemical nature of surface elements. UV-visible diffuse reflectance spectra (DRS) were obtained with a UV-visible spectrophotometer (UV-2450, Shimadzu, Japan) and the baseline correction was done using a standard sample of BaSO_4 to describe the absorption of light at different wavelengths.

2.3. Photocatalytic Performance. The photocatalytic decomposition of methylene blue (MB) was carried out in a photo reaction system (as illustrated in our previous publication [18]). The visible light source was offered by a 1000 W Xe lamp equipped with a glass filter (removing the UV irradiation below 420 nm wavelength) positioned in the center of a water-cooled system. The reactive bottle is a 50 mL cylindrical vessel 4 cm away from the light source. In the bottom of the reactive bottle, a magnetic stirrer was rotated to achieve effective dispersion. The temperature of the reaction solution was maintained at $30 \pm 0.5^\circ\text{C}$ by cooling water. 50 mg of samples was added to 50 mL of 10 mg/L MB solution to form suspension. After the suspensions were stirred in the dark for 1 h to reach the adsorption-desorption equilibrium, the suspensions were irradiated with visible light and stirred continuously. At given time interval, 2 mL of suspension was taken out and immediately centrifuged to eliminate the solid particles. The absorbance of the filtrate was measured by a spectrophotometer at the maximum absorbance peak 665 nm.

3. Results and Discussion

3.1. XRD. The XRD patterns of four samples are displayed in Figure 1. It can be clearly seen from Figure 1(a) the variations of products with the different dosages of NH_4F .

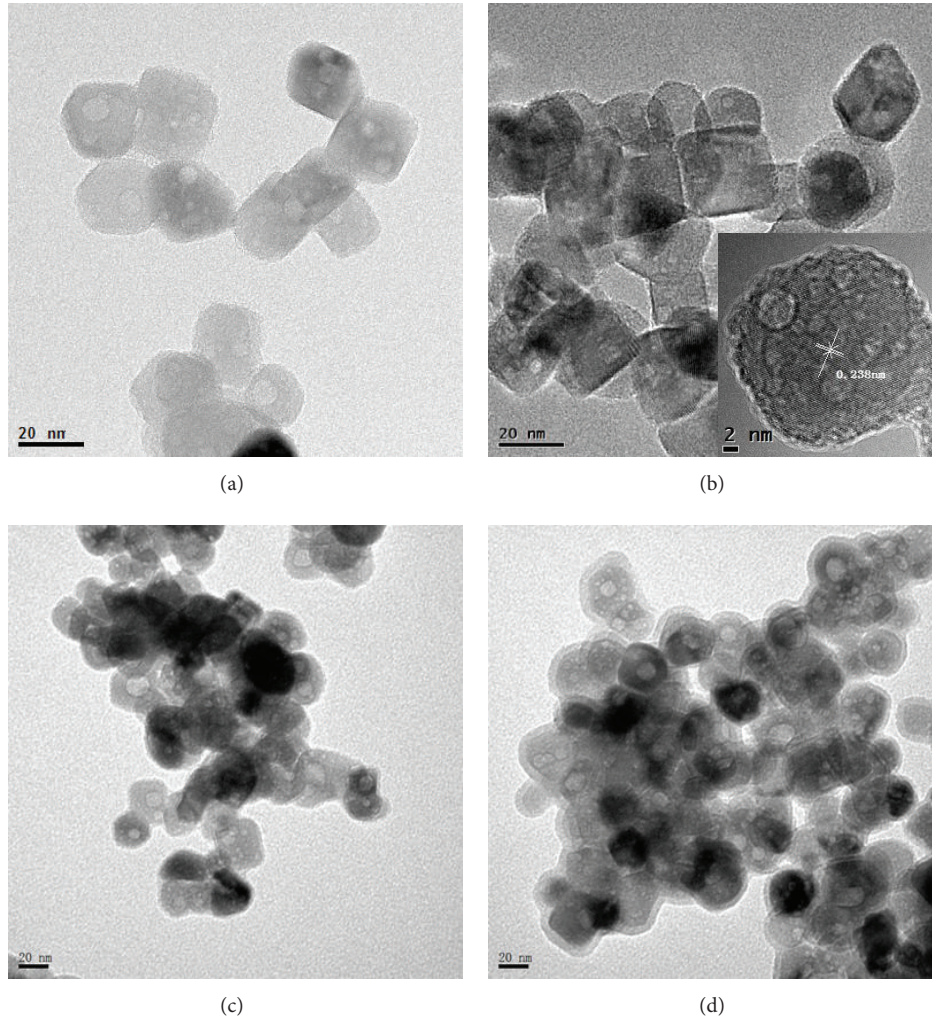


FIGURE 2: TEM pictures of all samples ((a) S1-500, (b) S2-500, (c) S3-500, and (d) S4-500).

The peaks at $2\theta = 25.28^\circ$, 37.80° , 48.05° , 53.89° , 55.06° , and 62.69° belong to anatase TiO_2 (reference no. 00-021-1272), and the peaks at $2\theta = 14.08^\circ$, 23.57° , 27.56° , 28.37° , 33.59° , and 49.65° are corresponding to NH_4TiOF_3 (reference no. 00-052-1674). From the contrast of four samples, we can see all the peaks of S1 and S2 belong to anatase TiO_2 , indicating that only anatase TiO_2 formed when the dosages of NH_4F are relative low. With the increasing of the dosage of NH_4F , new peaks corresponding to NH_4TiOF_3 appear in the XRD patterns of S3 and S4, indicating that both anatase TiO_2 and NH_4TiOF_3 formed when the dosages of NH_4F are relative higher, and the anatase TiO_2 contents in S3 and S4 are 75.3% and 60.1%, respectively. Figure 2(b) presents the XRD patterns of the samples after calcination. Both of the two samples (S3 and S4) are transformed into anatase TiO_2 because of the heating effect. Compared with the samples without calcination treatment, the diffraction peak intensities of anatase TiO_2 are increased and the Full Width Half Maximums (FWHM) are obviously narrowed due to heat treatment, which demonstrates that the crystallization degree

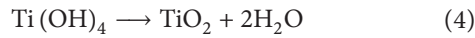
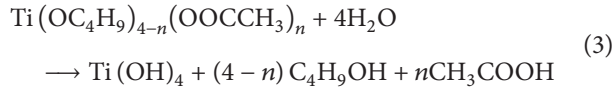
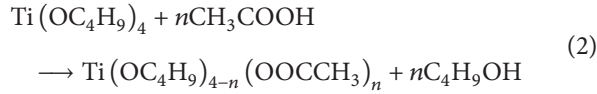
of anatase TiO_2 is enhanced due to the calcination at 500°C for 2 h. The average crystal size of all samples was calculated using the Scherrer equation

$$D = \frac{k\lambda}{\beta \cos \theta}, \quad (1)$$

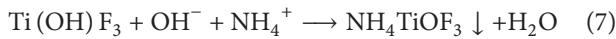
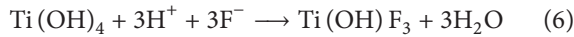
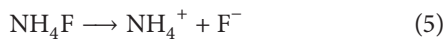
where D is the average crystal size, k is a constant (shape factor, about 0.89), λ is the X-ray wavelength, β is the FWHM of the diffraction line, and θ is the diffraction angle. The calculated results are 16.89, 17.70, 37.73, and 25.26 nm for S1-500, S2-500, S3-500, and S4-500, respectively.

The above results can be explained by the following reasons. Because of the high hydrolytic activity of tetranbutyl titanate, it is necessary to slow down the speed of hydrolysis by adding depressor such as acetic acid. In the reaction, acetate is used as a ligand for titanium to control the rate of tetranbutyl titanate hydrolysis effectively; thus the formation of gel can be stable and controllable. Then, the coordinate

polymers are transformed into TiO_2 by condensation polymerization [16]. The followings are the reaction approaches:



It is adverse to the production of TiO_2 when the dosage of NH_4F is excessive, and the reason can be ascribed to the following reactions:



3.2. TEM. Figure 2 shows the TEM images of the four calcined samples (the TEM images of uncalcined samples were not shown here due to their obscure {001} facets). As shown in Figure 2(a), when the NH_4F dosage is a quarter of titanium in amount, TiO_2 nanocrystals with the size of 15~20 nm present square outline, which is different from the morphology of TiO_2 nanocrystals prepared by traditional sol-gel method where crystal surface control agent (F^-) was absent [17], indicating the formation of nanocrystals with exposed {001} facets [19]. In Figure 2(b), TiO_2 nanocrystals show quite distinct square outline as the increasing of the dosage of NH_4F , and the nanocrystals are about 20 nm in length, about 15 nm in thickness, and about 40% in the percentage of {001} facets. When the NH_4F dosage is equal to titanium in amount, nanocrystals appear in an irregular shape and some nanocrystals are aggregated to some extent, which can be obviously seen from the TEM image (Figure 2(c)). When the NH_4F dosage is double that of the titanium, the shapes of crystals are more irregular, and the edges are obscure; the reason can be ascribed to the production of NH_4TiOF_3 . That is, the anatase TiO_2 produced in the sol-gel process can likely show {001} facets after calcination. The inset in Figure 2(b) (HR-TEM of S2-500) clearly shows the continuous (004) atomic planes with a lattice spacing of 0.238 nm, corresponding to the {004} planes of anatase TiO_2 single crystals, which further confirms that the exposed crystal facet is {001} facet.

3.3. XPS. Figure 3(a) displays the XPS survey scan patterns of typical samples S2 and S2-500. Two significant differences can be observed by comparing the two samples. One of them is that the two peaks centered at 830.0 eV and 685.2 eV, which can be assigned to F (A) and F 1s, respectively, appear in uncalcined sample, and are removed due to calcination [20], indicating F groups anchored on the surface of S2 can be removed by calcinations at 500°C for 2 h. The other one is that the peak centered at about 400.0 eV is weakened, which can

be ascribed to the removal of adsorbed nitrogen groups due to calcination. The small peak at about 400.0 eV in sample S2-500 can be ascribed to N 1s, implying that N-doping has been realized. As shown in Figure 3(b), two peaks can be obtained by fitting the N 1s spectrum of S2. The peak at 399.7 eV (peak 1) can be assigned to Ti-(N-O) bond [21–24], and the peak at 401.4 eV (peak 2) is attributed to the interstitial N atoms in N-O bonds [25], indicating that some nitrogen groups are adsorbed on the surface or interspace of TiO_2 . In Figure 3(c), two peaks at 399.7 eV (peak 1) and 402.9 eV (peak 3) can be fitted from the N1s spectrum of S2-500, which can be assigned to Ti-(N-O) bond and $\text{O}_X\text{-Ti-N}_Y$ bond [23, 26], implying that nitrogen atoms are doped in the lattices of TiO_2 . The doping amount of nitrogen is 0.52% in atom.

3.4. DRS. Figure 4 gives the UV-Vis diffuse reflectance spectra of all samples. The optical absorption edges of S1, S2, S3, S4, and S1-500 locate at 420 nm, which is similar to pure TiO_2 (Figure 4(a)). However, the optical absorption edges of S2-500, S3-500, and S4-500 shift to the lower-energy region (about 550 nm) due to the N-doping (Figure 4(b)). These phenomena can be explained by combining UV-Vis diffuse reflectance results and XPS analysis results. Before calcination, nitrogen groups are just adsorbed on the surface or interspace of TiO_2 , not doped into the lattices of TiO_2 , which cannot change the band gaps of S1, S2, S3, and S4. Therefore, the optical absorption edges of the four samples do not shift towards long wavelength. After calcination, the optical absorption edge of S1-500 still locates at 420 nm, which can be ascribed to the low NH_4F dosage. The optical absorption edges of S2-500, S3-500, and S4-500 are shifted to the lower-energy region, implying that nitrogen atoms are doped into the lattices of TiO_2 due to the heat-treatment at high temperature and enough NH_4F dosage. It is widely accepted that the nitrogen incorporation into the crystal matrix of TiO_2 modifies the electronic band structure of TiO_2 , leading to a new substitution N 2p band formed above O 2p valance band, which narrows the band gap of TiO_2 and shifts optical absorption to the visible light region [8, 12, 27]. In conclusion, the shift of optical absorption edge can be ascribed to the formation of impurity states in the band gap due to N-doping, which is realized by calcination treatment.

3.5. Photocatalytic Performances. Figure 5 shows the photocatalytic performance of all samples (due to low photocatalytic efficiency, the photocatalytic performances of these uncalcined samples were not shown). For comparison, P25, a standard photocatalyst, was also tested at the same conditions. From the comparison of the as-prepared four samples, it can be concluded that the photocatalytic performance of S2-500 is the optimal, and its photocatalytic performances is superior to P25 to a large extent. The high photocatalytic performance of S2-500 can be attributed to its high crystallization, better light response characteristic, and high reactivity of {001} facets.

3.5.1. Crystallization. Crystallization plays a significant role in the photocatalytic activity of TiO_2 . A better crystallization

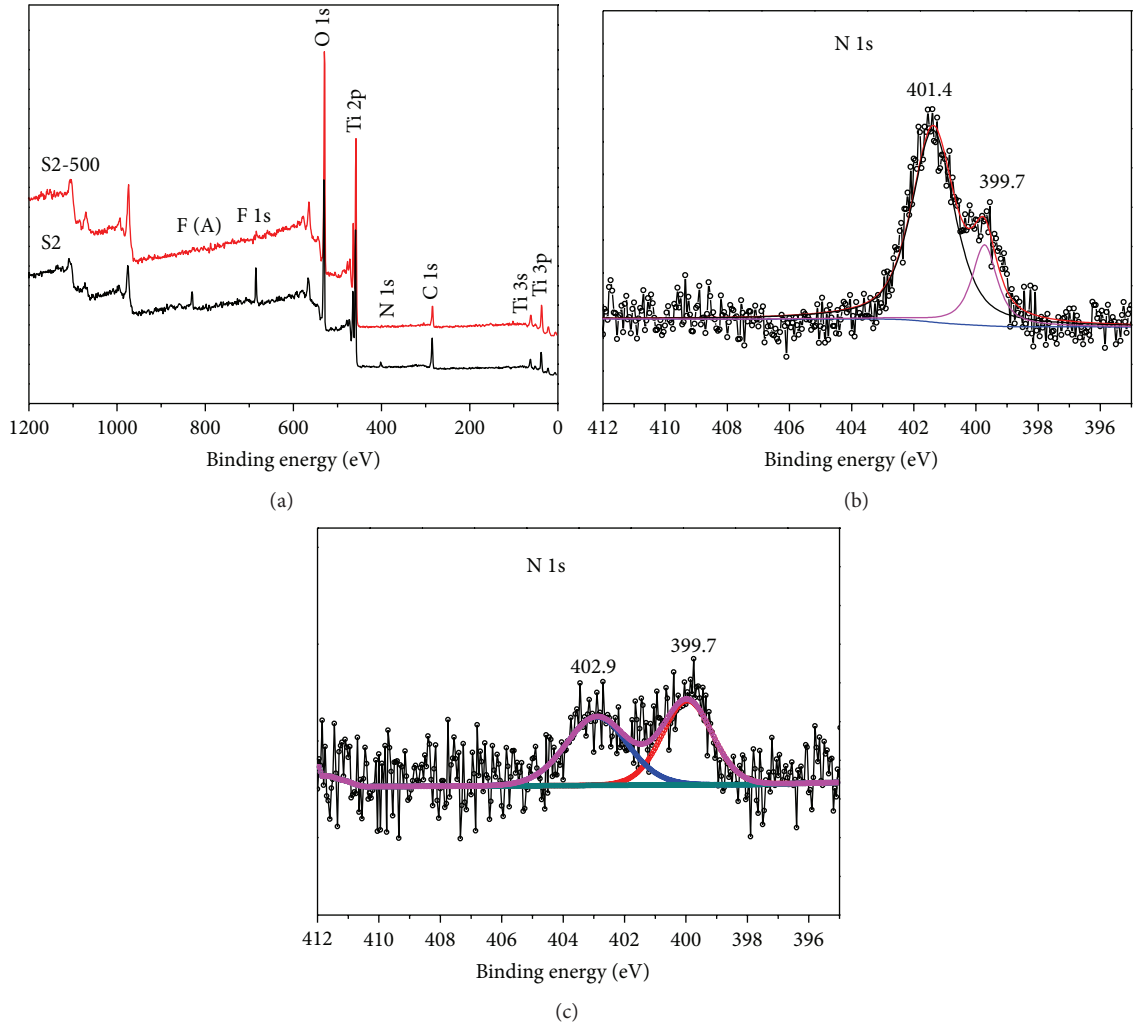


FIGURE 3: The XPS survey scan patterns of samples ((a) S2 and S2-500; (b) N 1s of S2; (c) N 1s of S2-500).

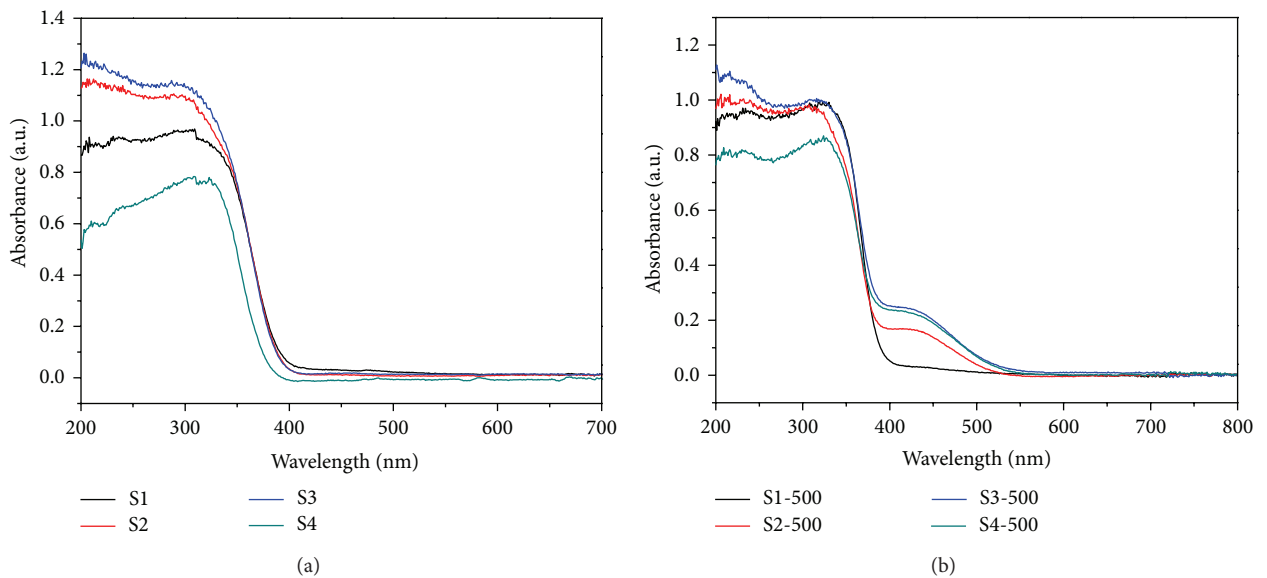


FIGURE 4: UV-Vis diffuse reflectance spectra of all samples ((a) the uncalcined samples, (b) the calcined samples).

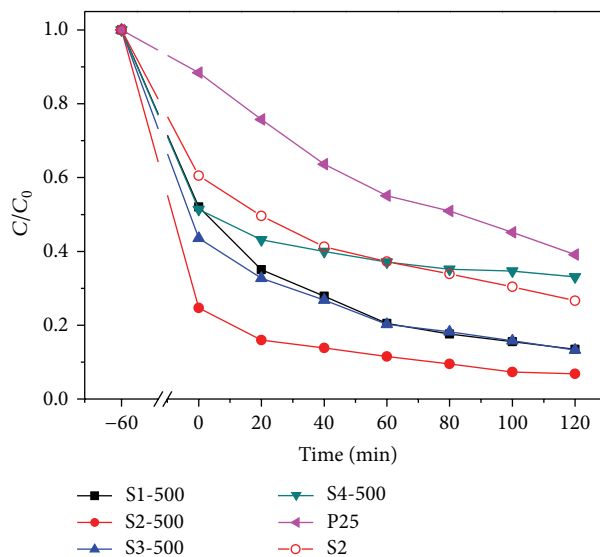


FIGURE 5: The photocatalytic performance of samples.

means the decrease of crystal defects, which are the recombination centers of photoinduced charges [28, 29]. Therefore, in a sense, the improvement in photocatalytic activity of TiO_2 can be achieved by increasing the crystallization of TiO_2 [30], while, heat treatment is one of the methods to improve the crystallization of TiO_2 [31, 32]. In current work, the photocatalytic performances of calcined samples are higher than those of the corresponding uncalcined samples, which can be attributed to the fact that the calcined samples possess better crystallization than the corresponding uncalcined samples, which has been confirmed from their XRD patterns.

3.5.2. Light Response Characteristic. It is well known that light absorption characteristic of photocatalyst is an important factor influencing photocatalytic activity. The enhancement of absorbance in the UV-Vis region increases the number of photogenerated electrons and holes to participate in the photocatalytic reaction, which can enhance the photocatalytic activity of TiO_2 [33, 34]. It has been confirmed from Figure 4 that the optical absorption edge of samples is shifted to 550 nm from 420 nm due to the calcination treatment, which is one of the reasons why the photocatalytic performances of calcined samples are higher than those of the corresponding uncalcined samples.

3.5.3. High Reactivity of {001} Facets. The surface energy of {001} facets is higher than that of {101} facets due to the 100% surface unsaturated Ti_{5C} atoms on {001} facets while only 50% for the {101} facets. Therefore, the {001} facets are theoretically considered more reactive than {101} and {010} facets [35, 36], which is in agreement with most experimental results. Under Wu's experimental conditions, the higher the percentage of {001} facets, the higher the photooxidation reactivity, for the TiO_2 crystals with the same size [6]. D'Arienzo et al. think that {001} surfaces can be considered as oxidation sites with a significant role in the photooxidation

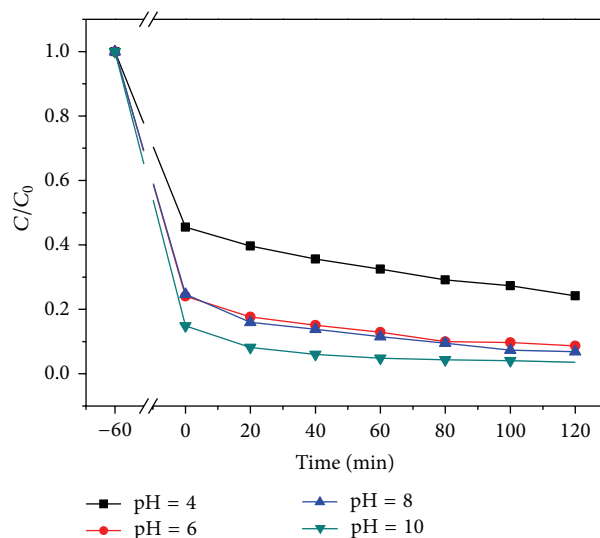


FIGURE 6: The effect of pH on the photocatalytic degradation efficiencies.

of TiO_2 [37]; the concentration of trapped holes (O^- centers) increases with increasing {001} surface area and photoactivity in vacuum conditions. In our experiments, the high reactivity of S2-500 can be due to its high percentage of {101} facets and small size.

3.6. Factors Influencing the Photocatalytic Degradation Efficiencies. Sample S2-500 is used as the model catalyst to study the factors which influence the degradation efficiencies.

3.6.1. Effect of pH. The decoloration efficiencies of MB at different pH values are displayed in Figure 6. It shows that both the adsorption capacity and photocatalytic degradation

efficiencies will rise as pH increases. The reasons can be interpreted from the following aspects.

Firstly, pH value may influence the surface electrical behavior of TiO_2 [38]. In general, the more negative of zeta potential indicates that there are more hydroxides on the surface of TiO_2 . The point of zero charge (pzc) of S2-500 is at pH 4.8; thus, the TiO_2 surface is positively charged when $\text{pH} < 4.8$ while it is negatively charged when $\text{pH} > 4.8$. It is believed that organic molecules can be adsorbed more easily onto the surface of samples with the increasing of pH.

Secondly, the changes of pH can affect the yield of $\cdot\text{OH}$ radicals in the photocatalytic oxidation. The holes are considered as the major oxidation specie at low pH value whereas $\cdot\text{OH}$ radicals are considered as the predominant specie at medium or high pH levels [39, 40]. It is known that $\cdot\text{OH}$ radicals are easier to be generated on TiO_2 surface in alkaline environment; hence the photocatalytic activity is enhanced.

Thirdly, the stability of organic pollutants can be transformed by pH value. It is reported that MB is more stable in acid solution than that in alkaline solution [41]. Therefore, MB molecules can be degraded more easily as pH increases.

3.6.2. Effect of Catalyst Concentration. Figure 7 shows that the effect of catalyst concentration on the photocatalytic performances. It clearly displays that the adsorption capacity can be improved as the increasing of catalyst concentration. However, the photocatalytic degradation rates will not increase when the concentration exceeds a certain value. Generally, the more the dosage of catalyst, the higher the photocatalytic rate. However, excess catalysts are not favorable to boost the reaction speed for spare catalysts will shut out visible light. The optimal catalyst concentration is $1.0 \text{ g}\cdot\text{L}^{-1}$ in the case of our experiment condition.

3.6.3. Effect of Initial Substrate Concentration. It can be observed from Figure 8 that the photocatalytic activity of the catalyst can be influenced by substrate concentration. The degradation efficiencies decline with the increasing of substrate concentration, which can be ascribed to the following two reasons. One cause is that the generation of $\cdot\text{OH}$ radicals on the surface of catalysts will be reduced because the active sites will be covered by organic ions for high substrate concentrations. Another reason is the light-screening effect of high substrate concentration, especially for dye solution; a considerable amount of light may be absorbed by dye molecules rather than TiO_2 particles, and thus it will reduce the efficiency due to the low production of $\cdot\text{OH}$ radicals [42, 43].

3.6.4. Effect of Substrates. In order to confirm the universality of the catalyst, two more typical organics are used as target pollutants, namely, congo red (10 mg/L, CR) and diclofenac sodium (20 mg/L, DCF). Figure 9 shows the photocatalytic performance of S2-500 via degrading three different organic pollutants. It can be seen that the removal rates all exceed 90%. From the result, we could deduce that the synthesized nitrogen doped TiO_2 with exposed {001} facets possesses

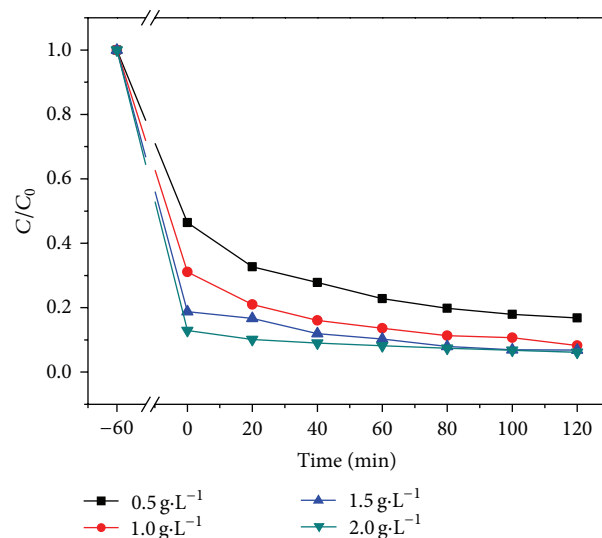


FIGURE 7: The effect of catalyst concentration on the photocatalytic degradation efficiencies.

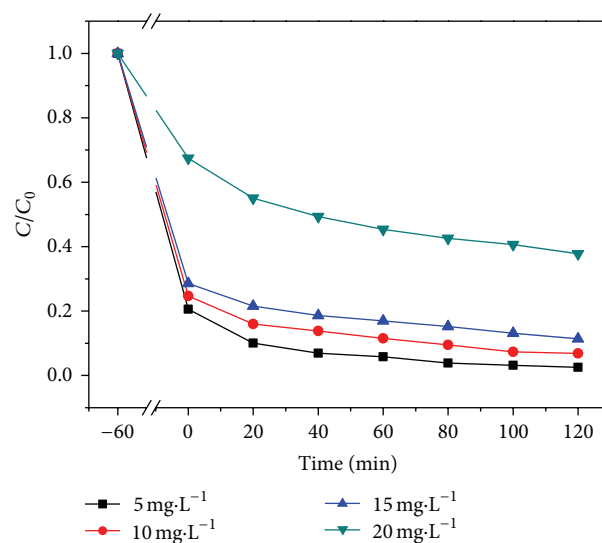


FIGURE 8: The effect of substrate concentration on the photocatalytic degradation efficiencies.

excellent photocatalytic performance in the degradation of organic pollutants.

4. Conclusions

In this study, nitrogen-doped TiO_2 nanocrystals with exposed {001} facets were prepared by sol-gel method firstly. The as-obtained N-doped TiO_2 nanocrystals with exposed {001} facets showed higher photocatalytic activity than P25 in the degradation of methylene blue dye under the visible-light illumination. The enhanced photocatalytic performance can be attributed to synergistic effects of several factors, such

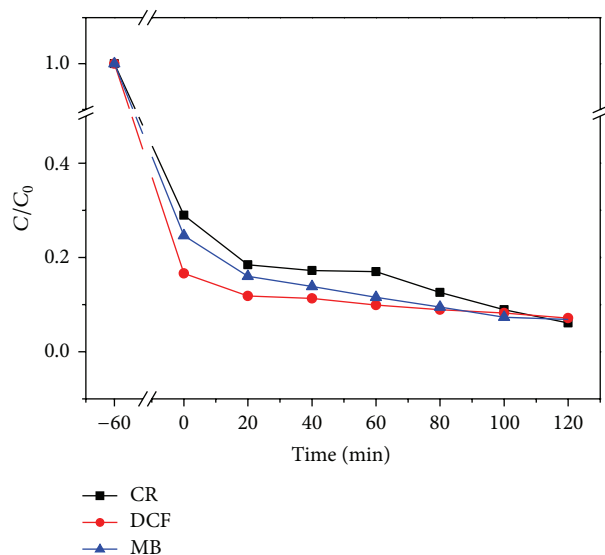


FIGURE 9: The photocatalytic performance of S2-500 in the degradation of different organic pollutants.

as good crystallinity, better light response characteristic, and high reactivity of {001} facets.

Conflict of Interests

The authors declare that there is no conflict of interests regarding the publishing of this paper.

Acknowledgments

This work was supported by the Key Project of Science and Technology Plan of Fujian Province (no. 2012Y0066), Xiamen Distinguished Young Scholar Award (no. 3502Z20126011), and Xiamen Science & Technology Major Program (no. 3502Z20131018). The valuable comments of anonymous reviewers are greatly appreciated.

References

- [1] F. Pei, Y. Liu, S. Xu, J. Lü, C. Wang, and S. Cao, "Nanocomposite of graphene oxide with nitrogen-doped TiO₂ exhibiting enhanced photocatalytic efficiency for hydrogen evolution," *International Journal of Hydrogen Energy*, vol. 38, no. 6, pp. 2670–2677, 2013.
- [2] W. Wang, C. H. Lu, Y. R. Ni, J. B. Song, M. X. Su, and Z. Z. Xu, "Enhanced visible-light photoactivity of 001 facets dominated TiO₂ nanosheets with even distributed bulk oxygen vacancy and Ti³⁺," *Catalysis Communications*, vol. 22, pp. 19–23, 2012.
- [3] D. Q. Zhang, G. S. Li, X. F. Yang, and J. C. Yu, "A micrometer-size TiO₂ single-crystal photocatalyst with remarkable 80% level of reactive facets," *Chemical Communications*, no. 29, pp. 4381–4383, 2009.
- [4] H. G. Yang, C. H. Sun, S. Z. Qiao et al., "Anatase TiO₂ single crystals with a large percentage of reactive facets," *Nature*, vol. 453, no. 7195, pp. 638–641, 2008.
- [5] T. R. Gordon, M. Cargnello, T. Paik et al., "Nonaqueous synthesis of TiO₂ nanocrystals using TiF₄ to engineer morphology, oxygen vacancy concentration, and photocatalytic activity," *Journal of the American Chemical Society*, vol. 134, no. 15, pp. 6751–6761, 2012.
- [6] Q. Wu, M. Liu, Z. Wu, Y. Li, and L. Piao, "Is photooxidation activity of 001 facets truly lower than that of 101 facets for anatase TiO₂ crystals?" *The Journal of Physical Chemistry C*, vol. 116, no. 51, pp. 26800–26804, 2012.
- [7] N. Serpone, "Is the band gap of pristine TiO₂ narrowed by anion- and cation-doping of titanium dioxide in second-generation photocatalysts?" *Journal of Physical Chemistry B*, vol. 110, no. 48, pp. 24287–24293, 2006.
- [8] R. Asahi, T. Morikawa, T. Ohwaki, K. Aoki, and Y. Taga, "Visible-light photocatalysis in nitrogen-doped titanium oxides," *Science*, vol. 293, no. 5528, pp. 269–271, 2001.
- [9] D. Jing, S. Yao, P. Chen et al., "A multichannel system for rapid determination of the activity for photocatalytic H₂ production," *AIChE Journal*, vol. 58, no. 11, pp. 3593–3596, 2012.
- [10] H. Zhang, X. Liu, Y. Li, and H. Zhao, "001 facets dominated anatase TiO₂: morphology, formation/etching mechanisms and performance," *Science China Chemistry*, vol. 56, no. 4, pp. 402–417, 2013.
- [11] H. G. Yang, G. Liu, S. Z. Qiao et al., "Solvothermal synthesis and photoreactivity of anatase TiO₂ nanosheets with dominant 001 facets," *Journal of the American Chemical Society*, vol. 131, no. 11, pp. 4078–4083, 2009.
- [12] G. Liu, G. Y. Hua, X. Wang et al., "Visible light responsive nitrogen doped anatase TiO₂ sheets with dominant 001 facets derived from TiN," *Journal of the American Chemical Society*, vol. 131, no. 36, pp. 12868–12869, 2009.
- [13] J. Yu, G. Dai, Q. Xiang, and M. Jaroniec, "Fabrication and enhanced visible-light photocatalytic activity of carbon self-doped TiO₂ sheets with exposed 001 facets," *The Journal of Physical Chemistry C*, vol. 21, no. 4, pp. 1049–1057, 2011.
- [14] G. Liu, C. Sun, S. C. Smith, L. Wang, G. Q. M. Lu, and H. M. Cheng, "Sulfur doped anatase TiO₂ single crystals with a high percentage of 001 facets," *Journal of Colloid and Interface Science*, vol. 349, no. 2, pp. 477–483, 2010.
- [15] G. Liu, J. C. Yu, G. Q. Lu, and H.-M. Cheng, "Crystal facet engineering of semiconductor photocatalysts: motivations, advances and unique properties," *Chemical Communications*, vol. 47, no. 24, pp. 6763–6783, 2011.
- [16] K. Terabe, K. Kato, H. Miyazaki, S. Yamaguchi, A. Imai, and Y. Iguchi, "Microstructure and crystallization behaviour of TiO₂ precursor prepared by the sol-gel method using metal alkoxide," *Journal of Materials Science*, vol. 29, no. 6, pp. 1617–1622, 1994.
- [17] J. Shi, S. Chen, S. Wang, and Z. Ye, "Sol-gel preparation and visible light photocatalytic activity of nitrogen doped titania," *Procedia Engineering*, vol. 27, pp. 564–569, 2012.
- [18] J. Shi, X. Zong, X. Wu et al., "Carbon-doped titania hollow spheres with tunable hierarchical macroporous channels and enhanced visible light-induced photocatalytic activity," *Chem-CatChem*, vol. 4, no. 4, pp. 488–491, 2012.
- [19] L. Sun, Z. Zhao, Y. Zhou, and L. Liu, "Anatase TiO₂ nanocrystals with exposed facets via molecular grafting for enhanced photocatalytic activity," *Nanoscale*, vol. 4, no. 2, pp. 613–620, 2012.
- [20] X. Zhou, F. Peng, H. Wang, H. Yu, and Y. Fang, "A simple preparation of nitrogen doped titanium dioxide nanocrystals with exposed (001) facets with high visible light activity," *Chemical Communications*, vol. 48, no. 4, pp. 600–602, 2012.

- [21] Y. Cong, J. Zhang, F. Chen, and M. Anpo, "Synthesis and characterization of nitrogen-doped TiO₂ nanophotocatalyst with high visible light activity," *The Journal of Physical Chemistry C*, vol. 111, no. 19, pp. 6976–6982, 2007.
- [22] E. György, A. Pérez del Pino, P. Serra, and J. L. Morenza, "Depth profiling characterisation of the surface layer obtained by pulsed Nd:YAG laser irradiation of titanium in nitrogen," *Surface and Coatings Technology*, vol. 173, no. 2-3, pp. 265–270, 2003.
- [23] C. Chen, H. Bai, and C. Chang, "Effect of plasma processing gas composition on the nitrogen-doping status and visible light photocatalysis of TiO₂," *The Journal of Physical Chemistry C*, vol. 111, no. 42, pp. 15228–15235, 2007.
- [24] R. Asahi and T. Morikawa, "Nitrogen complex species and its chemical nature in TiO₂ for visible-light sensitized photocatalysis," *Chemical Physics*, vol. 339, no. 1-3, pp. 57–63, 2007.
- [25] C. S. Gopinath, "Comment on 'photoelectron spectroscopic investigation of nitrogen-doped titania nanoparticles,'" *Journal of Physical Chemistry B*, vol. 110, no. 13, pp. 7079–7080, 2006.
- [26] N. Yang, G. Li, W. Wang, X. Yang, and W. F. Zhang, "Photophysical and enhanced daylight photocatalytic properties of N-doped TiO₂/g-C₃N₄ composites," *Journal of Physics and Chemistry of Solids*, vol. 72, no. 11, pp. 1319–1324, 2011.
- [27] H. Irie, S. Washizuka, N. Yoshino, and K. Hashimoto, "Visible-light induced hydrophilicity on nitrogen-substituted titanium dioxide films," *Chemical Communications*, vol. 9, no. 11, pp. 1298–1299, 2003.
- [28] J. Yu, G. Wang, B. Cheng, and M. Zhou, "Effects of hydrothermal temperature and time on the photocatalytic activity and microstructures of bimodal mesoporous TiO₂ powders," *Applied Catalysis B: Environmental*, vol. 69, no. 3-4, pp. 171–180, 2007.
- [29] M. Mrowetz, W. Balcerski, A. J. Colussi, and M. R. Hoffmann, "Oxidative power of nitrogen-doped TiO₂ photocatalysts under visible illumination," *The Journal of Physical Chemistry B*, vol. 108, no. 45, pp. 17269–17273, 2004.
- [30] J. Ovenstone, "Preparation of novel titania photocatalysts with high activity," *Journal of Materials Science*, vol. 36, no. 6, pp. 1325–1329, 2001.
- [31] H. Wang, Y. Wu, and B.-Q. Xu, "Preparation and characterization of nanosized anatase TiO₂ cuboids for photocatalysis," *Applied Catalysis B: Environmental*, vol. 59, no. 3-4, pp. 139–146, 2005.
- [32] M. Salmi, N. Tkachenko, V. Vehmanen, R. Lamminmäki, S. Karvinen, and H. Lemmetyinen, "The effect of calcination on photocatalytic activity of TiO₂ particles: femtosecond study," *Journal of Photochemistry and Photobiology A: Chemistry*, vol. 163, no. 3, pp. 395–401, 2004.
- [33] D. Li, H. Haneda, S. Hishita, and N. Ohashi, "Visible-light-driven nitrogen-doped TiO₂ photocatalysts: effect of nitrogen precursors on their photocatalysis for decomposition of gas-phase organic pollutants," *Materials Science and Engineering B*, vol. 117, no. 1, pp. 67–75, 2005.
- [34] M. Hamadani, A. Reisi-Vanani, and A. Majedi, "Synthesis, characterization and effect of calcination temperature on phase transformation and photocatalytic activity of Cu, S-codoped TiO₂ nanoparticles," *Applied Surface Science*, vol. 256, no. 6, pp. 1837–1844, 2010.
- [35] A. Selloni, "Crystal growth: anatase shows its reactive side," *Nature Materials*, vol. 7, no. 8, pp. 613–615, 2008.
- [36] X. Gong and A. Selloni, "Reactivity of anatase TiO₂ nanoparticles: the role of the minority (001) surface," *The Journal of Physical Chemistry B*, vol. 109, no. 42, pp. 19560–19562, 2005.
- [37] M. D'Arienzo, J. Carbajo, A. Bahamonde et al., "Photogenerated defects in shape-controlled TiO₂ anatase nanocrystals: a probe to evaluate the role of crystal facets in photocatalytic processes," *Journal of the American Chemical Society*, vol. 133, no. 44, pp. 17652–17661, 2011.
- [38] M. A. Fox and M. T. Dulay, "Heterogeneous photocatalysis," *Chemical Reviews*, vol. 93, no. 1, pp. 341–357, 1993.
- [39] L. Lucarelli, V. Nadochenko, and J. Kiwi, "Environmental photochemistry: quantitative adsorption and FTIR studies during the TiO₂-photocatalyzed degradation of orange II," *Langmuir*, vol. 16, no. 3, pp. 1102–1108, 2000.
- [40] W. Z. Tang and C. P. Huang, "Photocatalyzed oxidation pathways of 2,4-dichlorophenol by CdS in basic and acidic aqueous solutions," *Water Research*, vol. 29, no. 2, pp. 745–756, 1995.
- [41] N. Bélaz-David, L. A. Decosterd, M. Appenzeller et al., "Spectrophotometric determination of methylene blue in biological fluids after ion-pair extraction and evidence of its adsorption on plastic polymers," *European Journal of Pharmaceutical Sciences*, vol. 5, no. 6, pp. 335–345, 1997.
- [42] I. K. Konstantinou and T. A. Albanis, "TiO₂-assisted photocatalytic degradation of azo dyes in aqueous solution: kinetic and mechanistic investigations: a review," *Applied Catalysis B: Environmental*, vol. 49, no. 1, pp. 1–14, 2004.
- [43] N. Daneshvar, D. Salari, and A. R. Khataee, "Photocatalytic degradation of azo dye acid red 14 in water: investigation of the effect of operational parameters," *Journal of Photochemistry and Photobiology A: Chemistry*, vol. 157, no. 1, pp. 111–116, 2003.

Research Article

Layer-by-Layer Assembly and Photocatalytic Activity of Titania Nanosheets on Coal Fly Ash Microspheres

Xing Cui, Jianwen Shi, Zhilong Ye, Zhaoji Zhang, Bin Xu, and Shaohua Chen

Key Laboratory of Urban Environment and Health, Institute of Urban Environment, Chinese Academy of Sciences, Xiamen 361021, China

Correspondence should be addressed to Shaohua Chen; shchen@iue.ac.cn

Received 27 March 2014; Accepted 29 April 2014; Published 25 May 2014

Academic Editor: Jia Hong Pan

Copyright © 2014 Xing Cui et al. This is an open access article distributed under the Creative Commons Attribution License, which permits unrestricted use, distribution, and reproduction in any medium, provided the original work is properly cited.

In order to address the problem with titania distribution and recovery, series of $\text{Ti}_{0.91}\text{O}_2/\text{CFA}$ photocatalysts ($\text{Ti}_{0.91}\text{O}_2/\text{CFA}-n$, $n = 2, 4, 6$, and 8) were fabricated by assembling $\text{Ti}_{0.91}\text{O}_2$ nanosheets on coal fly ash (CFA) microspheres via the layer-by-layer assembly (LBLA) process and characterized by scanning electron microscopy (SEM), X-ray diffraction analysis (XRD), N_2 -sorption, and ultraviolet-visible absorption (UV-vis) techniques. The SEM images and UV-vis spectra illustrated that $\text{Ti}_{0.91}\text{O}_2$ nanosheets were immobilized successfully on the CFA by the LBLA approach and changed the characteristics of CFA noticeably. The photocatalytic activity of $\text{Ti}_{0.91}\text{O}_2/\text{CFA}$ was evaluated by the photodegradation of methylene blue (MB) under UV irradiation. The results demonstrated that $\text{Ti}_{0.91}\text{O}_2/\text{CFA}-6$ showed the best photocatalytic activity among the series of $\text{Ti}_{0.91}\text{O}_2/\text{CFA}$ irradiated for 60 min, with a decoloration rate above 43%. After photocatalysis, the $\text{Ti}_{0.91}\text{O}_2/\text{CFA}$ could be easily separated and recycled from aqueous solution and $\text{Ti}_{0.91}\text{O}_2$ nanosheets were still anchored on the CFA.

1. Introduction

Fabrication of multilayers of colloidal particles through electrostatic attraction has been studied since 1966 [1]. Generally, the composites consist of organic or inorganic particles as cores and inorganic nano-coatings as shells. For the great potentials of core-shell composites in photonics and catalysis areas, many researches have been focused on the preparation of core-shell structure via the layer-by-layer assembly (LBLA) approach in recent years [2–4]. The LBLA method has been applied to assemble charged thin films of various materials on oppositely charged templates. The inorganic coatings are deposited on the templating cores via electrostatic attraction, so the shell coatings can be adsorbed on the cores uniformly and firmly. Titanium oxide is popular with researchers for its excellent performance of high photocatalytic activity, chemical inertness, stability against photocorrosion, and cost-effectiveness [5]. Titania nanosheet ($\text{Ti}_{1-x}\text{O}_2^{4x-}$), synthesized by chemical delamination and exfoliation of precursor, is of typical 2D structure and the lateral size of it ranges from hundreds of nanometers to a few micrometers and the thickness of the individual layer is approximately 1 nm

[6]. The titania nanosheets after exfoliation are negatively charged, so titania nanosheets can be assembled on substrates via the LBLA approach coupled with cationic polyelectrolyte [7]. Multilayer titania nanosheets possess unique properties besides photocatalytic activity [8], such as optical absorption properties [7, 9], high anisotropy [10], photoelectrochemical properties [11], and high thermal resistance [12].

Titania nanosheet hollow shells and hollow spheres consisting of titania and graphene nanosheets have been fabricated by the layer-by-layer assembly method in previous studies [13, 14]. However, the titania nanosheet hollow spheres are hard to separate spontaneously and recycle from aqueous suspension after photocatalysis, which limits their practical application in wastewater treatment. In order to improve the convenience of separation and recovery of nano- TiO_2 , photocatalysts by immobilizing nano- TiO_2 on some substrates were recently prepared, such as on glass, polymer, and active carbon [15–17]. However, most substrate materials are expensive, and cheap and stable substrates are desired. In our early work, photocatalysts of TiO_2 immobilized on coal fly ash (CFA) were prepared [18–20]. CFA is one of the solid wastes generated from thermal power plants. CFA chosen as

a supporter has advantages as follows: (1) CFA particles are microspheres and easy to precipitate in water, so photocatalysts supported by CFA are easy to recycle from aqueous solution after reaction; (2) CFA, consisting primarily of Al_2O_3 and SiO_2 , as a supporter can inhibit recombination of electron and hole effectively [21, 22]; (3) the cost of preparation and a source of environment pollution can be reduced. However, it is difficult to control uniform distribution of TiO_2 on CFA [17, 23], which greatly restrains the activity of the photocatalyst and the availability of substrate. Because the lateral size of titania nanosheets is in the micron range and CFA particle size is less than $100\ \mu\text{m}$, the problem can be solved by loading titania nanosheets on CFA through electrostatic attraction via layer-by-layer assembly method at ambient temperature [24]. The LBLA method involves electrostatic sequential deposition of negatively charged titania nanosheets onto substrate along with an oppositely charged polymer. Based on this principle, an assembly of layered titanate on CFA is expected to achieve very well.

In this paper, the titania nanosheet ($\text{Ti}_{1-x}\text{O}_2^{4x-}$) referred to is $\text{Ti}_{0.91}\text{O}_2^{0.36-}$ and is abbreviated as $\text{Ti}_{0.91}\text{O}_2$. This study describes the fabrication of $\text{Ti}_{0.91}\text{O}_2/\text{CFA}$ by the LBLA approach for controlling the uniform distribution of $\text{Ti}_{0.91}\text{O}_2$. The layered $\text{Ti}_{0.91}\text{O}_2$ nanosheets were obtained by swelling and exfoliation of layered protonic titanate ($\gamma\text{-FeOOH}$ type) in $(\text{C}_4\text{H}_9)_4\text{NOH}$ (TBAOH) solution and were negatively charged. The surface of CFA was modified by cationic polyelectrolyte beforehand. $\text{Ti}_{0.91}\text{O}_2$ nanosheets were adsorbed on the surface of CFA due to the electrostatic attraction and immobilized continually by repeating the LBLA procedure. $\text{Ti}_{0.91}\text{O}_2$ nanosheets anchored served as a shell and CFA could be regarded as core. The photocatalytic activity of $\text{Ti}_{0.91}\text{O}_2/\text{CFA}$ was also evaluated by the decoloration of methylene blue (MB).

2. Experimental Section

2.1. Reagent and Materials. Cs_2CO_3 (99.99% metals basis), TiO_2 (AR), polyethylenimine (PEI) (99% purity) and poly(diallyldimethylammonium chloride) (PDDA) (35 wt.% aqueous solution), and TBAOH ($\sim 0.8\ \text{M}$) were purchased from Aladdin Reagent Company. $\text{Ti}_{0.91}\text{O}_2$ nanosheets were synthesized by a previously reported method [25]. Briefly, the protonic titanate ($\text{H}_{0.7}\text{Ti}_{1.825}\text{O}_4\cdot\text{H}_2\text{O}$) was prepared from cesium titanate ($\text{Cs}_{0.7}\text{Ti}_{1.825}\text{O}_4$) by acid exchange for 3 days. And then, $\text{H}_{0.7}\text{Ti}_{1.825}\text{O}_4\cdot\text{H}_2\text{O}$ (0.4 g) was shaken vigorously (300 rpm) in 100 mL aqueous solution of TBAOH (0.004 M) for 2 weeks, so the layered hosts underwent osmotic swelling and exfoliating into nanosheets. The colloid produced stood for storage. CFA, calcined at 800°C , was immersed in a bath of 1/1 methanol/HCl and concentrated H_2SO_4 with stirring for 20 min each and then washed with copious water to remove acid residue. The pretreated CFA was dried for use later. Deionized water was used throughout the experiments.

2.2. Fabrication Procedure. Core/shell composites (CFA was employed as a substrate core and $\text{Ti}_{0.91}\text{O}_2$ nanosheets were

inorganic shell) were fabricated by electrostatic sequential deposition approach [13, 14]. For $\text{Ti}_{0.91}\text{O}_2$ nanosheets were negatively charged, in order to load $\text{Ti}_{0.91}\text{O}_2$ nanosheets onto the CFA by electrostatic deposition, the surface of CFA was modified by cationic polyelectrolytes (PEI and PDDA). The detailed fabrication procedure of layer-by-layer assembly (LBLA) method is as follows: 5 g CFA was dispersed in 200 mL PEI solution ($2.5\ \text{g}\cdot\text{L}^{-1}$, $\text{pH} = 9$) and further stirred for 60 min to ensure PEI was adsorbed on the CFA surface for introducing positive charges. After the mixture was centrifuged at 3000 rpm for 20 min, the supernatant was removed and then the CFA was washed dried in a drying oven under 60°C . Subsequently, the PEI-coated CFA (CFA/PEI) was dispersed in $\text{Ti}_{0.91}\text{O}_2$ colloidal suspension (200 mL) and further stirring was carried out for 60 min. Small flocculated aggregates formed in the solution during this process for electrostatic attraction. The resulting CFA/PEI/ $\text{Ti}_{0.91}\text{O}_2$ was washed by water for 2 cycles to remove excess $\text{Ti}_{0.91}\text{O}_2$ nanosheets. After drying, it was dispersed in 200 mL PDPA solution ($20\ \text{g}\cdot\text{L}^{-1}$, $\text{pH} = 9$), as the same as the PEI modifying process, and CFA/PEI/ $\text{Ti}_{0.91}\text{O}_2$ /PDPA was fabricated. The procedure for PDPA/ $\text{Ti}_{0.91}\text{O}_2$ alternative deposition was repeated m frequencies to synthesize a multilayer assembly-PEI/ $\text{Ti}_{0.91}\text{O}_2$ /(PDPA/ $\text{Ti}_{0.91}\text{O}_2$) $_m$ ($m = 1, 3, 5$, and 7). In this study, the photocatalysts as-prepared were abbreviated as $\text{Ti}_{0.91}\text{O}_2/\text{CFA}-n$ ($n = 2, 4, 6$, and 8), where n represented the loading frequency of $\text{Ti}_{0.91}\text{O}_2$ nanosheets by LBLA.

2.3. Characterizations. The morphologies of the samples were observed by a field emission scanning electron microscope (SEM) and the Ti elemental mapping was detected with an energy dispersive X-ray spectrometer (EDX) (S-4800, Japan). X-ray diffraction (XRD) data of the samples were collected using diffractometer (X'Pert PRO, Holland) with $\text{Cu K}\alpha$ irradiation. The morphology of the exfoliated nanosheets was observed by transmission electron microscope (TEM, H-7650, Japan). UV-vis absorption spectra of all samples were recorded by a Shimadzu spectrophotometer (UV-2450, Japan). The chemical composition of CFA was characterized by quantitative X-ray fluorescence spectrum (XRF) analysis (Axios mAX, Holland). The N_2 adsorption-desorption isotherms, Brunauer-Emmett-Teller (BET) surface area, and Barrett-Joyner-Halenda (BJH) pore size distribution were obtained by surface area and porosity analyzer (ASAP 2020 M+C, America).

2.4. Evaluation of Photocatalytic Activity. The photocatalytic reaction was carried out in a photochemical reaction system as described before [18]. Briefly, the initial concentration and volume of MB were $20\ \text{mg}/\text{L}$ and $50\ \text{mL}$, respectively. The dosage of $\text{Ti}_{0.91}\text{O}_2/\text{CFA}-n$ was $0.2\ \text{g}$. A $500\ \text{W}$ UV lamp with major emission at $365\ \text{nm}$ was used as a light source, and the irradiation time was 60 min. After reaction and settling for a while, the upper solution was centrifuged at 3000 rpm for 20 min to eliminate fine particles. Then the absorbance of supernatant was analyzed at the wavelength of $664\ \text{nm}$ by a UV-vis spectrophotometer.

3. Results and Discussion

3.1. SEM Analysis of Samples. SEM was used to define the morphology of the $\text{Ti}_{0.91}\text{O}_2/\text{CFA}$ microstructure. The images present CFA before (Figures 1(a) and 1(b)) and after (Figures 1(c)–1(h)) $\text{Ti}_{0.91}\text{O}_2$ nanosheets were loaded by the LBLA approach. From Figures 1(a) and 1(b), it can be found that the surface of the CFA is smooth and barren. There are no obvious attachments on the CFA surface after rinsing with H_2SO_4 and CH_3OH , which indicates that the impurities on the surface had been removed. After $\text{Ti}_{0.91}\text{O}_2$ nanosheets were deposited on the CFA by LBLA, some aggregates consisting of $\text{Ti}_{0.91}\text{O}_2$ multilayer nanosheets were adhered to the CFA (Figures 1(c)–1(h)). With the increase of loading frequency, the area covered by corrugation was enlarged, and multilayers can be seen. It can be observed in Figure 1(c) that only very few aggregates are anchored on the surface of the CFA after twice repeated layer-by-layer loading. When the loading took place 4 times, the area of agglomerates was obviously enhanced (Figure 1(e)). Under high magnification (Figure 1(f)), there are more nanosheet agglomerates than with two loadings (Figure 1(d)). When the layer-by-layer loading frequency was further raised to 8, the agglomerates almost covered the CFA surface (Figures 1(g) and 1(h)). There is an obvious difference between the $\text{Ti}_{0.91}\text{O}_2$ nanosheet agglomerates here and the TiO_2 nanoparticle agglomerates loaded on CFA. The $\text{Ti}_{0.91}\text{O}_2$ agglomerates are of approximate rectangle sheet shape (Figure 2), and their counterparts (anatase TiO_2) are nanosphere agglomerates of 3D structure [19]. This is ascribed to the different loading methods. The conventional loading methods for fabricating TiO_2 include the sol-gel-adsorption method and the hydrothermal method [26, 27], and the TiO_2 agglomerates prepared are usually granular after calcination. In this study, the $\text{Ti}_{0.91}\text{O}_2/\text{CFA}$ was fabricated without calcination under high temperature, so $\text{Ti}_{0.91}\text{O}_2$ was able to keep its original crystalline phase and did not transform into anatase or rutile. Therefore, the $\text{Ti}_{0.91}\text{O}_2$ nanosheets were still lamellar after loading on CFA. From the images of the morphology of the $\text{Ti}_{0.91}\text{O}_2/\text{CFA}$, it is certain that the $\text{Ti}_{0.91}\text{O}_2$ nanosheets are successfully immobilized on the surface of CFA with layer-by-layer approach, although the amount of $\text{Ti}_{0.91}\text{O}_2$ is smaller compared to our earlier work [19].

3.2. UV-Vis Absorption Spectra of Samples. The UV-vis absorption spectra demonstrate the optical absorption characteristics of the CFA and $\text{Ti}_{0.91}\text{O}_2/\text{CFA}$ samples. In Figure 3, the absorbances of the CFA do not change much along the range of wavelengths (200 nm–800 nm), except for a weak and broad peak at around 370 nm. Compared to the spectrum of the CFA, the spectra of the $\text{Ti}_{0.91}\text{O}_2/\text{CFA}$ illustrate a characteristic absorption change along the whole range of wavelengths, with two strong absorption peaks at around 266 nm and 375 nm. The peak at around 375 nm was dependent on the immobilized multilayer nanosheets which were not completely exfoliated into monolayer nanosheets. So the absorption peak has a micro red-shift. The peak of the absorption curve around 266 nm is in accord with the multilayer titania nanosheets which had been studied [7], but

the absorption peak is broader than that in the study of Sasaki et al. [28]. This may be attributed to the fact that the selected substrates are different. The previous substrates were quartz glass platelets and silicon wafer chips ($1 \times 5 \text{ cm}^2$), which had a flat surface and different size from CFA. However, the substrate in this study was CFA of microsphere shape and the particle size of CFA was below $100 \mu\text{m}$. Therefore, the assembly style of titania nanosheets on the substrate was not exactly the same. This led to the discrepancy. It can be also observed that the absorption peak of $\text{Ti}_{0.91}\text{O}_2/\text{CFA}$ -6 around 266 nm is stronger than the others. It may be explained that the peak around 266 nm was previously found to be unilamellar $\text{Ti}_{0.91}\text{O}_2$ nanosheets [7], and there were more unilamellar $\text{Ti}_{0.91}\text{O}_2$ nanosheets on the surface of the CFA than other types. On $\text{Ti}_{0.91}\text{O}_2/\text{CFA}$ -2, 4, 8, the incompletely exfoliated nanosheets made up a larger proportion than $\text{Ti}_{0.91}\text{O}_2/\text{CFA}$ -6, which weakened the intensity of the peak around 266 nm.

3.3. Crystal Structure of Samples. XRD was used to investigate phase structure changes of the CFA before and after $\text{Ti}_{0.91}\text{O}_2$ were immobilized by LBLA. CFA and $\text{Ti}_{0.91}\text{O}_2/\text{CFA}$ crystalline patterns are shown in Figures 4(a)–4(c). In Figure 4(a), CFA primarily contains mullite ($\text{Al}_{4.5}\text{Si}_{1.5}\text{O}_{9.75}$) and quartz (SiO_2), which is similar to the previous study [29]. After $\text{Ti}_{0.91}\text{O}_2$ were loaded, there was no obvious difference between CFA and $\text{Ti}_{0.91}\text{O}_2/\text{CFA}$. It could be two reasons: (1) $\text{Ti}_{0.91}\text{O}_2$ nanosheets were adhered to the surface of CFA through electrostatic force, not entering the crystal lattices of mullite and quartz; (2) the amount of deposited $\text{Ti}_{0.91}\text{O}_2$ nanosheets was small, so the influence on overall diffraction peak was little relatively. Therefore, no prominent changes in crystalline patterns of the CFA were observed clearly. However, there are still tiny differences between CFA and $\text{Ti}_{0.91}\text{O}_2/\text{CFA}$ in the range of 2θ among 26° – 27° (Figure 4(b)) and 39° – 40° (Figure 4(c)), which are partially enlarged details of Figure 4(a). At $2\theta = 26.6^\circ$, before $\text{Ti}_{0.91}\text{O}_2$ were loaded, the peak of the CFA is very weak; after LBLA was carried out for several frequencies, there is a small peak, which is higher than the CFA sample. At $2\theta = 39.5^\circ$, the intensity of the CFA peak decreases remarkably after $\text{Ti}_{0.91}\text{O}_2$ were immobilized. Figure 4(d) depicts the XRD pattern of protonic titanate before exfoliation. The peak at 9.5° is a characteristic of protonic titanate, and it disappears on $\text{Ti}_{0.91}\text{O}_2/\text{CFA}$, which can prove that slight changes of $\text{Ti}_{0.91}\text{O}_2/\text{CFA}$ XRD pattern at $2\theta = 26.6^\circ$ and 39.5° resulted from the loaded titania nanosheets via LBLA, not protonic titanate. This confirms that LBLA method is feasible to immobilize $\text{Ti}_{0.91}\text{O}_2$ nanosheets.

3.4. N_2 Adsorption-Desorption and Pore Distribution of Samples. The BET surface area of the $\text{Ti}_{0.91}\text{O}_2/\text{CFA}$ as-prepared is summarized in Table 2. Before $\text{Ti}_{0.91}\text{O}_2$ were loaded, the BET surface area of CFA was $2.62 \text{ m}^2/\text{g}$. After $\text{Ti}_{0.91}\text{O}_2$ nanosheets were loaded, the BET surface area of $\text{Ti}_{0.91}\text{O}_2/\text{CFA}$ -2 declined instead, so did the surface area of $\text{Ti}_{0.91}\text{O}_2/\text{CFA}$ -4. When the loading frequency was 6, the specific surface area of $\text{Ti}_{0.91}\text{O}_2/\text{CFA}$ -6 reduced to the minimum which is about

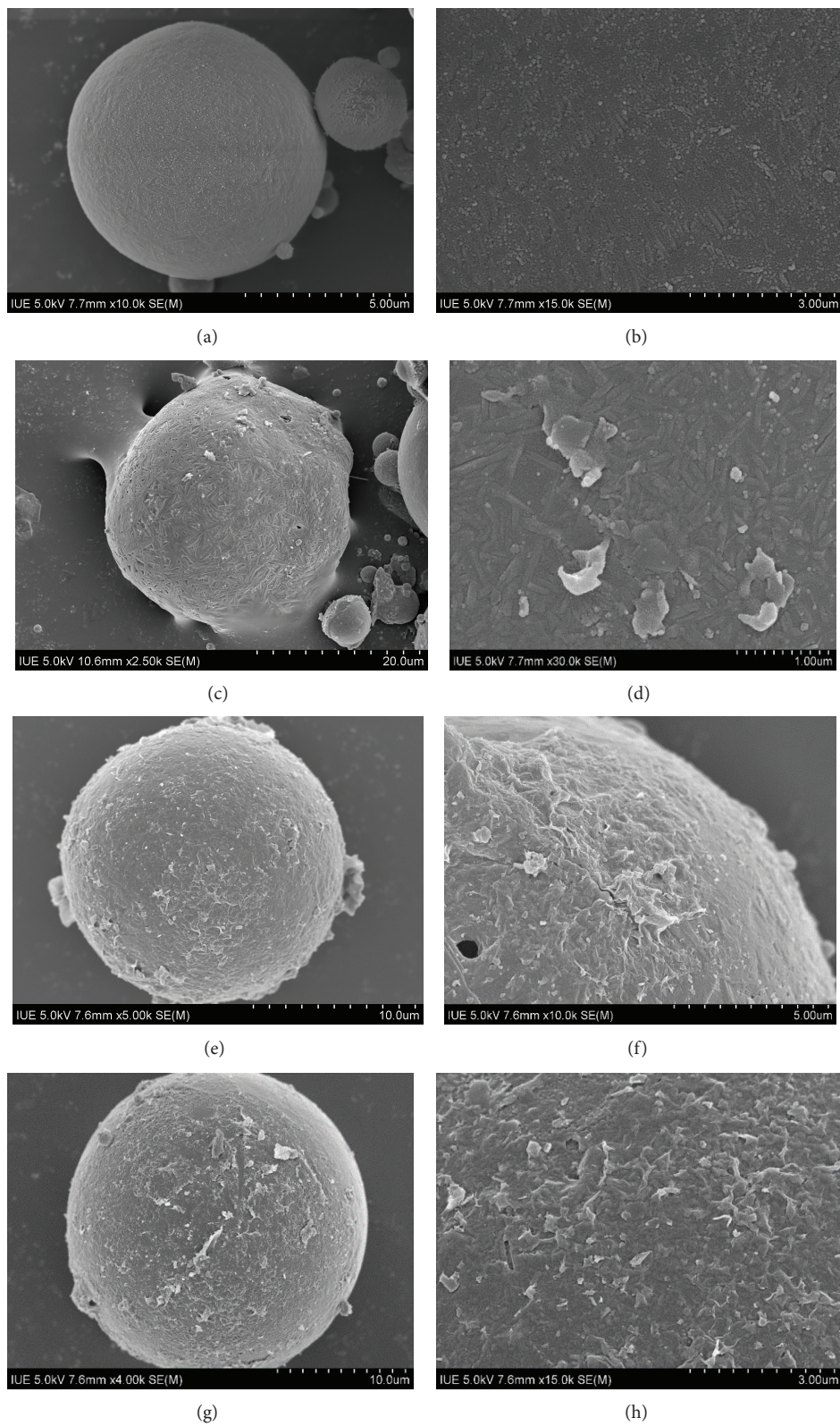


FIGURE 1: The SEM images of samples as-prepared: (a) and (b) CFA; (c) and (d) $Ti_{0.91}O_2/CFA-2$; (e) and (f) $Ti_{0.91}O_2/CFA-4$; (g) and (h) $Ti_{0.91}O_2/CFA-8$.

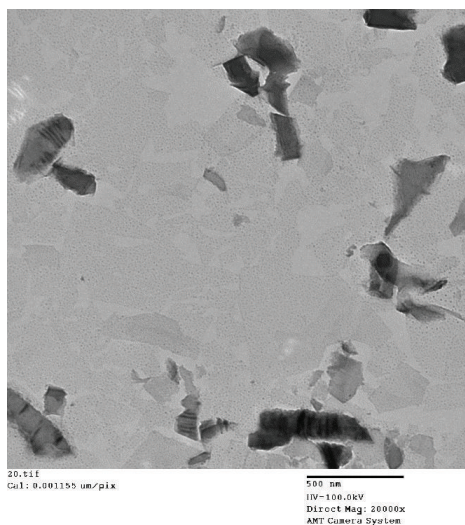


FIGURE 2: TEM of exfoliated titania nanosheets.

1.26 m²/g; the specific surface area increases slightly while the loading frequency rose to 8, however, still below 2 m²/g. The specific surface area decreased gradually with the increase in loading Ti_{0.91}O₂ nanosheets, similar to the results reported previously [30, 31]. The reason may be that Ti_{0.91}O₂ nanosheets immobilized by LBLA on the surface of the CFA were a few and lamellar, so it was difficult to form porous structure, which could not change the surface area much. The specific surface area of Ti_{0.91}O₂/CFA-6 was the smallest among the samples. Combined with UV-vis absorption analysis, this can be attributed to the monolayer nanosheets. Unilamellar Ti_{0.91}O₂ nanosheets were loaded more regularly than multilayer (incompletely exfoliated nanosheets) on the surface of CFA, so the surface structure of Ti_{0.91}O₂/CFA-6 is less complicated than others with a smaller surface area.

Figure 5 shows the N₂ adsorption-desorption isotherms of CFA and Ti_{0.91}O₂/CFA samples. It can be seen that all the samples can be assigned as an isotherm of type 2 in the IUPAC classification [32, 33]. The fact that the hysteresis loop is difficult to observe and volume adsorbed is very small reveals that the samples are typically nonporous characteristic by LBLA [34]. Moreover, it is shown that the adsorption capacity of the Ti_{0.91}O₂/CFA is lower than the CFA. With the loaded Ti_{0.91}O₂ nanosheets increasing, adsorption capacity and the hysteresis loop of Ti_{0.91}O₂/CFA became low and small gradually, respectively, which implies that immobilization of Ti_{0.91}O₂ nanosheets resulted in forming new structure (not 3D network), but did not increase the pore volume.

The pore size distribution of the CFA and Ti_{0.91}O₂/CFA in Figure 6 illustrates that pores of all samples are micropores and mesopores in a wide distribution range (<2 nm to 50 nm). Pores below 3 nm of all samples take a large amount with small pore volume. This can be explained by the fact that the specific surface area was very small and the samples were nearly nonporous. After Ti_{0.91}O₂ nanosheets were anchored by LBLA on CFA, the mesopore distribution

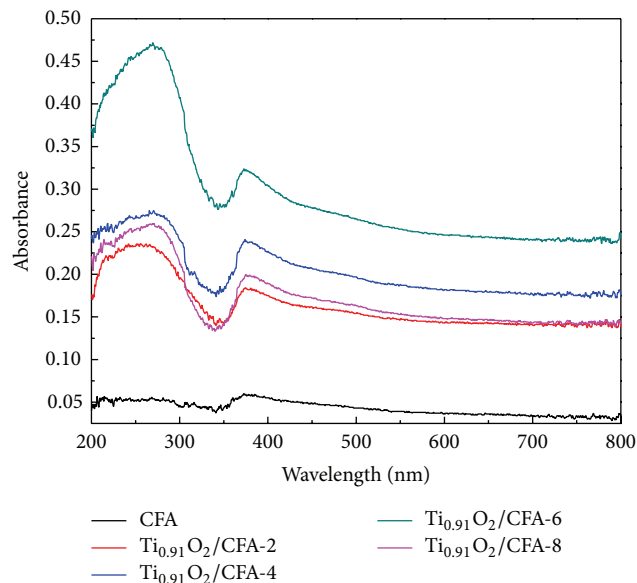


FIGURE 3: UV-vis absorption spectra of CFA and Ti_{0.91}O₂/CFA.

of the Ti_{0.91}O₂/CFA samples slightly shifts to 18 nm compared with 15 nm of the CFA, and the specific surface area of Ti_{0.91}O₂/CFA drops correspondingly. However, Ti_{0.91}O₂ nanosheets did not change the pore size distribution much either.

The results above of BET surface area, N₂ adsorption-desorption isotherms, and pore size distribution demonstrate that the loaded Ti_{0.91}O₂ by LBLA do not change the pore structure of the CFA. It is ascribed to Ti_{0.91}O₂ nanosheets which are lamellar with general lateral size of submicrons to microns and unilamellar thickness of ~1 nm. In this study, the lateral size of Ti_{0.91}O₂ nanosheets presented in Figure 2 is in the range of 200 nm–500 nm. The nanosheets are bigger than the pores of CFA and can cover them. However, the particle diameter of the CFA was above 5 μm and greatly larger than the size of Ti_{0.91}O₂ nanosheets, so Ti_{0.91}O₂ nanosheets stacked on the surface of CFA closely to form new structure but cannot fundamentally change the architecture of CFA. This conclusion is further supported by the image magnification of the Ti_{0.91}O₂/CFA in Figure 1.

3.5. Photocatalytic Activity. The photocatalytic activity of Ti_{0.91}O₂/CFA was investigated by the degradation of MB solution as a test reaction. Blank experiment (MB solution without CFA and Ti_{0.91}O₂/CFA) was served as a comparison. Before the photocatalytic reaction began, the adsorption experiment in the dark lasted for 60 min to reach adsorption equilibrium [35]. The absorbance of MB is proportional to its concentration, so the decoloration rate can be calculated by the equation as follows: $\eta(\%) = 100(A_0 - A_t)/A_0\% = 100(C_0 - C_t)/C_0\%$, where A_0 and A_t are the absorbances of MB solution at initial and t time, respectively.

Figure 7(a) shows MB was eliminated only ~10% by adsorption of samples and did not degrade in the blank experiment when the UV light was switched off. When the

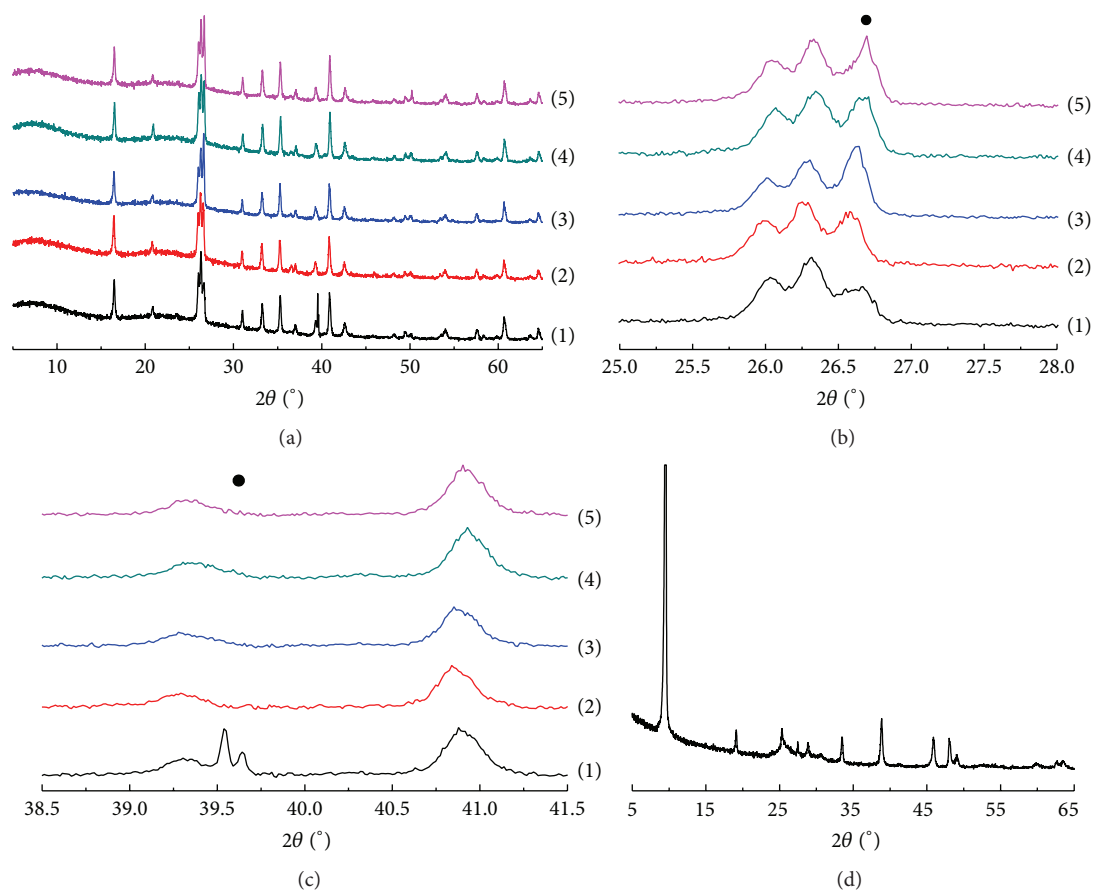


FIGURE 4: XRD patterns of (a–c) CFA and $\text{Ti}_{0.91}\text{O}_2/\text{CFA}$ samples and (d) protonic titanate: (1) CFA; (2) $\text{Ti}_{0.91}\text{O}_2/\text{CFA}$ -2; (3) $\text{Ti}_{0.91}\text{O}_2/\text{CFA}$ -4; (4) $\text{Ti}_{0.91}\text{O}_2/\text{CFA}$ -6; (5) $\text{Ti}_{0.91}\text{O}_2/\text{CFA}$ -8.

TABLE 1: The chemical composition of CFA (wt.%).

| Al_2O_3 | SiO_2 | Fe_2O_3 | CaO | TiO_2 | K_2O | Others |
|-------------------------|----------------|-------------------------|--------------|----------------|----------------------|--------|
| 35.8 | 54.7 | 2.52 | 1.74 | 1.32 | 1.17 | 2.75 |

UV light was on, the MB degraded rapidly. In the initial 10 min, the decoloration efficiencies of $\text{Ti}_{0.91}\text{O}_2/\text{CFA}$ - n are almost equivalent to that during 1h adsorption without UV irradiation. The concentration of MB decreases further with the prolonged UV light. After 60 min of photocatalysis reaction, the concentration of MB reduces to half of the initial. Figure 7(b) displays the decoloration rates of all the samples after 60 min UV light illumination. It can be seen that the removal efficiency of blank is much lower than that of the CFA and $\text{Ti}_{0.91}\text{O}_2/\text{CFA}$. This indicates that MB is removed through photocatalysis primarily under UV irradiation, not photolysis. Meanwhile, all $\text{Ti}_{0.91}\text{O}_2/\text{CFA}$ samples have higher decoloration rate above 24% than CFA which is about 15%. A poor photocatalytic characteristic of CFA originated from its chemical component (Table 1), which was the same as our early work [18], so $\text{Ti}_{0.91}\text{O}_2$ contributes to photocatalytic activity principally. This demonstrates again that it is successful to load $\text{Ti}_{0.91}\text{O}_2$ nanosheets on CFA via LBLA.

Generally, the photocatalytic activity is enhanced with increasing the $\text{Ti}_{0.91}\text{O}_2$ layer-by-layer loading frequency. With two frequencies loading, the decoloration rate of the $\text{Ti}_{0.91}\text{O}_2/\text{CFA}$ -2 achieved 24.7% correspondingly; when $\text{Ti}_{0.91}\text{O}_2$ loading accomplished 4 frequencies, the photocatalytic activity of the $\text{Ti}_{0.91}\text{O}_2/\text{CFA}$ improved remarkably, with a decoloration rate of 41.8%, due to more $\text{Ti}_{0.91}\text{O}_2$ nanosheets immobilized. While the loading frequency was raised to 6 further, the activity improved a little, up to a maximum decoloration rate about 43.2%. Nevertheless, the activity of $\text{Ti}_{0.91}\text{O}_2/\text{CFA}$ -8 was lower than $\text{Ti}_{0.91}\text{O}_2/\text{CFA}$ -4, 6. It is understandable that the amount of $\text{Ti}_{0.91}\text{O}_2$ nanosheets anchored on CFA influences the photocatalytic activity. The more $\text{Ti}_{0.91}\text{O}_2$ nanosheets were loaded, the higher activity the sample had. However, the excessive $\text{Ti}_{0.91}\text{O}_2$ nanosheets would block the UV illumination into the interior of photocatalyst, with a depressed availability of UV irradiation, which was consistent with other studies [36–38]. Meanwhile, the transfer of charge carrier may be also limited. It should be noted that $\text{Ti}_{0.91}\text{O}_2/\text{CFA}$ -6 exhibited the highest photocatalytic activity whose specific surface area and pore volume are the smallest. It may be also explained that there are more $\text{Ti}_{0.91}\text{O}_2$ monolayer nanosheets (with high photocatalytic activity by themselves and not blocking UV illumination) on the surface of $\text{Ti}_{0.91}\text{O}_2/\text{CFA}$ -6 than others for its UV absorbance spectral

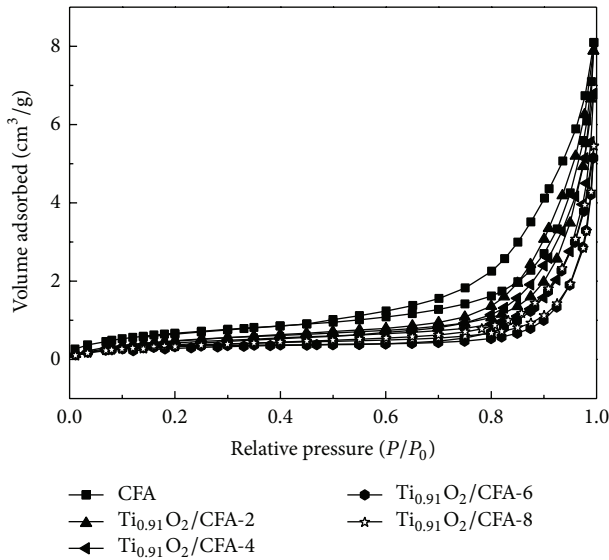


FIGURE 5: Nitrogen adsorption-desorption isotherms of CFA and $\text{Ti}_{0.91}\text{O}_2/\text{CFA}$.

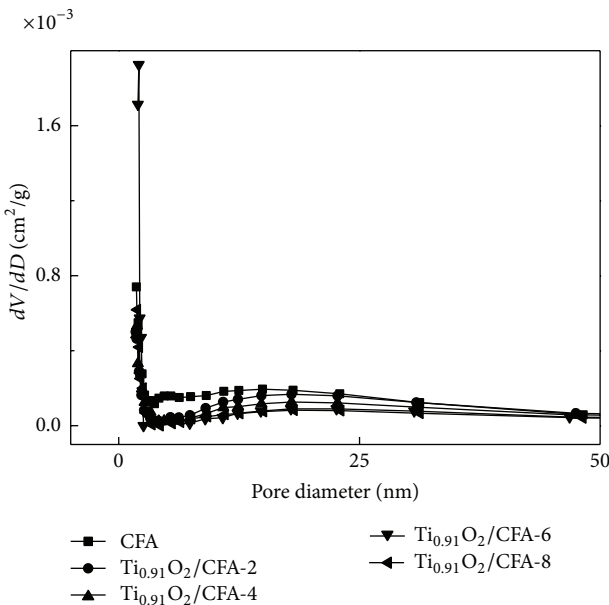
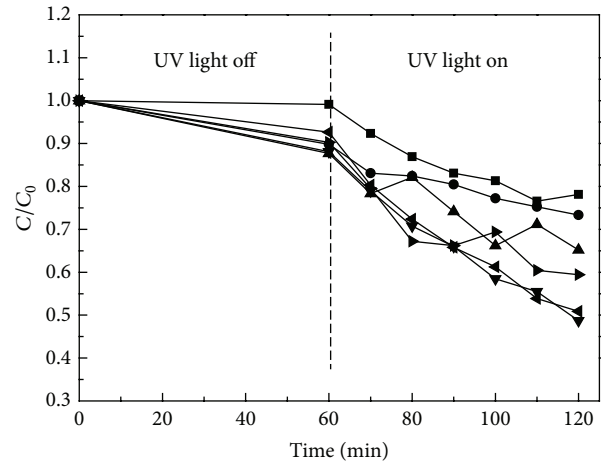


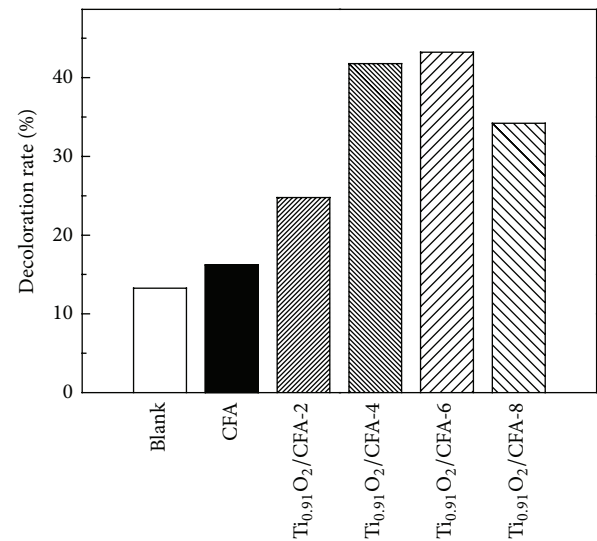
FIGURE 6: Pore size distributions of CFA and $\text{Ti}_{0.91}\text{O}_2/\text{CFA}$.

profile with a stronger peak at 266 nm, which had been discussed in UV-vis and BET analysis. Although the decoloration rate (43.2%) was not too high when $\text{Ti}_{0.91}\text{O}_2/\text{CFA}-n$ were used as photocatalysts, $\text{Ti}_{0.91}\text{O}_2/\text{CFA}-n$ are very easy to separate and recycle from aqueous suspension due to the weight of CFA, which facilitates the recycle and reuse, as mentioned in our previous publication [18–20].

Figure 8 illustrates the SEM and EDX micrographs of the $\text{Ti}_{0.91}\text{O}_2/\text{CFA}-6$ before (Figures 8(a) and 8(b)) and after photocatalysis (Figures 8(c) and 8(d)). It is obvious that there are almost no changes in the appearance of $\text{Ti}_{0.91}\text{O}_2/\text{CFA}-6$, and $\text{Ti}_{0.91}\text{O}_2$ nanosheets can be still found on the surface



(a)



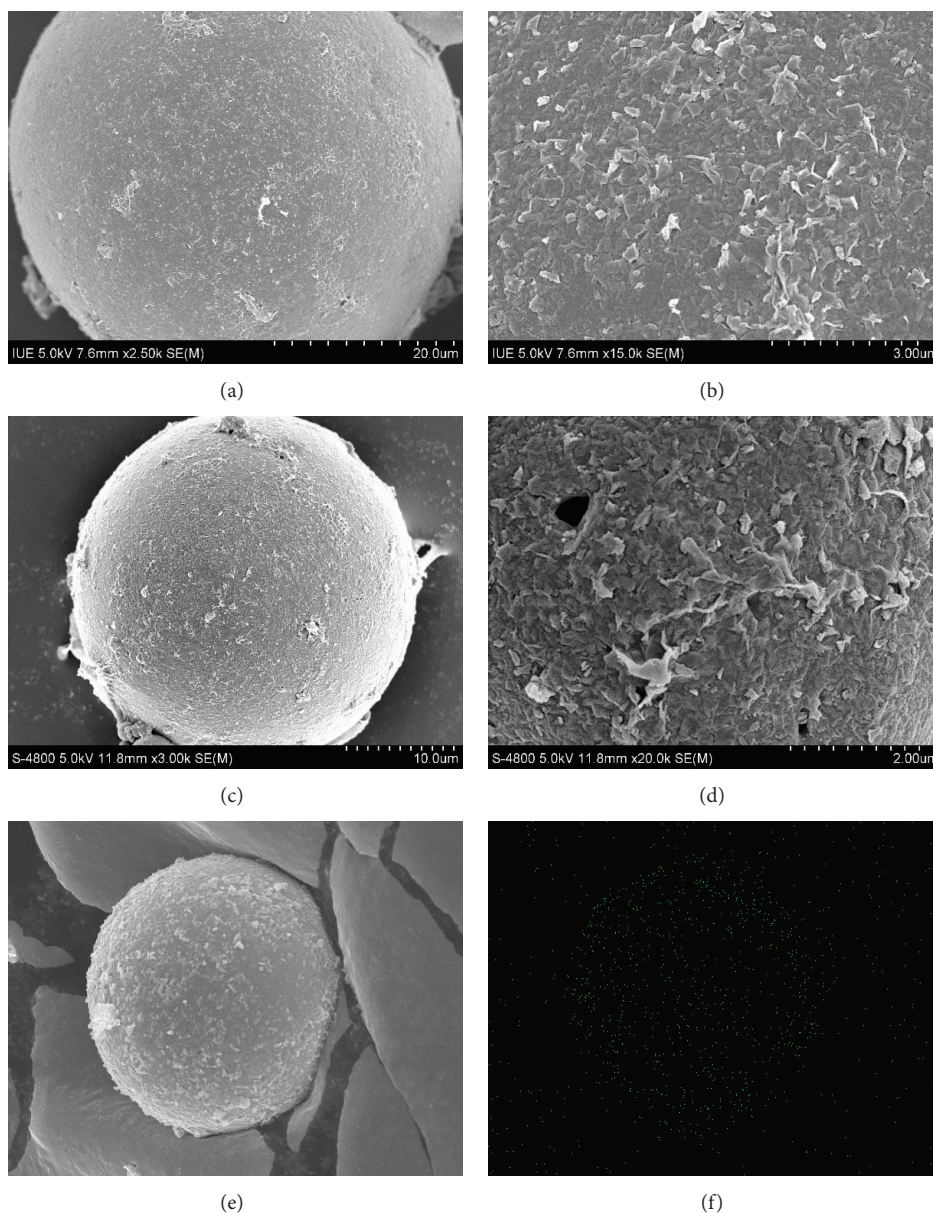
(b)

FIGURE 7: Photocatalytic activities of all samples.

of CFA microspheres with a considerable amount, which suggests that $\text{Ti}_{0.91}\text{O}_2$ nanosheets can stick to CFA firmly through the LBLA method. From Figure 8(d), the enlargement of Figure 8(c), it is observed that the morphology of $\text{Ti}_{0.91}\text{O}_2$ nanosheets changes a little. The edge of certain $\text{Ti}_{0.91}\text{O}_2$ nanosheets bends slightly, called “warping,” which may be ascribed to the illumination of UV-light [8, 39]. However, this did not influence the stability for their partial existences on the surface of substrate. Figure 8(f) is the Ti mapping of $\text{Ti}_{0.91}\text{O}_2/\text{CFA}$ as presented in Figure 8(e) which shows the distribution of Ti-containing species on the surface of CFA microsphere. This indicates that there is another difference between $\text{Ti}_{0.91}\text{O}_2/\text{CFA}$ and conventional TiO_2 cluster immobilized on substrates. In conventional studies, it was difficult to control TiO_2 cluster loaded on

TABLE 2: BET surface area and pore volume of CFA and $\text{Ti}_{0.91}\text{O}_2/\text{CFA}$.

| Samples | CFA | $\text{Ti}_{0.91}\text{O}_2/\text{CFA-2}$ | $\text{Ti}_{0.91}\text{O}_2/\text{CFA-4}$ | $\text{Ti}_{0.91}\text{O}_2/\text{CFA-6}$ | $\text{Ti}_{0.91}\text{O}_2/\text{CFA-8}$ | TBA-intercalated layered titanate [42] |
|--|------|---|---|---|---|--|
| S_{BET} (m^2/g) | 2.62 | 1.94 | 1.72 | 1.26 | 1.41 | 24 |
| Pore volume (cm^3/g) $\times 10^3$ | 12.6 | 12.2 | 10.6 | 7.9 | 8.5 | 0 |

FIGURE 8: SEM images and EDX analysis of $\text{Ti}_{0.91}\text{O}_2/\text{CFA-6}$: (a) and (b) sample as-prepared; (c) and (d) sample after photocatalysis; (e) and (f) Ti mapping of sample.

supporters uniformly [40, 41]. However, from $\text{Ti}_{0.91}\text{O}_2/\text{CFA}$ as-prepared in our work, it can be seen that Ti element is well-distributed, which can improve the availability of substrate. It is a unique feature of $\text{Ti}_{0.91}\text{O}_2/\text{CFA}$. In a word, the unilamellar nanosheets can be easily and compactly immobilized on the CFA by LBLA, which is in favor of maintaining the stability of $\text{Ti}_{0.91}\text{O}_2/\text{CFA}$.

4. Conclusion

We fabricated a novel photocatalyst successfully via the layer-by-layer assembly method. $\text{Ti}_{0.91}\text{O}_2$ nanosheets were immobilized on CFA by using sequential modification of cationic polyelectrolyte and $\text{Ti}_{0.91}\text{O}_2$ nanosheets. Since $\text{Ti}_{0.91}\text{O}_2$ nanosheets have special properties, $\text{Ti}_{0.91}\text{O}_2/\text{CFA}$

exhibits different characteristics, which can be concluded as follows.

- (1) Difference in morphology depends on the loading frequency. The amount of $\text{Ti}_{0.91}\text{O}_2$ nanosheets on the CFA surface increases with the layer-by-layer assembly frequency increasing. $\text{Ti}_{0.91}\text{O}_2$ nanosheets distribute uniformly on the surface of CFA whose availability can be improved.
- (2) CFA exhibits weak optical absorption in whole range of wavelength compared with $\text{Ti}_{0.91}\text{O}_2/\text{CFA}$, which proves that the immobilization of $\text{Ti}_{0.91}\text{O}_2$ nanosheets by LBLA can enhance the UV-absorption of the CFA. $\text{Ti}_{0.91}\text{O}_2/\text{CFA}$ has a UV-absorption peak around 266 nm.
- (3) $\text{Ti}_{0.91}\text{O}_2/\text{CFA}$ shows photocatalytic activity. Significant enhancement in decoloration of MB can be achieved by $\text{Ti}_{0.91}\text{O}_2/\text{CFA}$ compared to barren CFA. $\text{Ti}_{0.91}\text{O}_2/\text{CFA}$ is also easy to recycle and of mechanical stability, causing little secondary pollution.

Conflict of Interests

The authors declare that there is no conflict of interests regarding the publication of this paper.

Acknowledgments

This work was supported by Key Project of Science and Technology Plan of Fujian Province (no. 2012Y0066); National Key Technology Support Program (2012BAC25B04); Science and Technology Major Project of Fujian Province (2013YZ0001-1). We thank Professor M. L. Fu and Dr. J. W. Chen for their kind help.

References

- [1] R. K. Iler, "Multilayers of colloidal particles," *Journal of Colloid And Interface Science*, vol. 21, no. 6, pp. 569–594, 1966.
- [2] G. Decher, "Fuzzy nanoassemblies: toward layered polymeric multicomposites," *Science*, vol. 277, pp. 1232–1237, 1997.
- [3] F. Caruso, R. A. Caruso, and H. Möhwald, "Nanoengineering of inorganic and hybrid hollow spheres by colloidal templating," *Science*, vol. 282, no. 5391, pp. 1111–1114, 1998.
- [4] F. Caruso, X. Shi, R. Caruso, and A. Susa, "Hollow titania spheres from layered precursor deposition on sacrificial colloidal core particles," *Advanced Materials*, vol. 13, pp. 740–744, 2001.
- [5] J. H. Pan, H. Dou, Z. Xiong, C. Xu, J. Ma, and X. S. Zhao, "Porous photocatalysts for advanced water purifications," *Journal of Materials Chemistry*, vol. 20, no. 22, pp. 4512–4528, 2010.
- [6] R. Ma and T. Sasaki, "Nanosheets of oxides and hydroxides: ultimate 2D charge-bearing functional crystallites," *Advanced Materials*, vol. 22, no. 45, pp. 5082–5104, 2010.
- [7] T. Sasaki, Y. Ebina, M. Watanabe, and G. Decher, "Multilayer ultrathin films of molecular titania nanosheets showing highly efficient UV-light absorption," *Chemical Communications*, no. 21, pp. 2163–2164, 2000.
- [8] T. Shibata, N. Sakai, K. Fukuda, Y. Ebina, and T. Sasaki, "Photocatalytic properties of titania nanostructured films fabricated from titania nanosheets," *Physical Chemistry Chemical Physics*, vol. 9, no. 19, pp. 2413–2420, 2007.
- [9] T. Sasaki and M. Watanabe, "Semiconductor nanosheet crystallites of quasi- TiO_2 and their optical properties," *The Journal of Physical Chemistry B*, vol. 101, pp. 10159–10161, 1997.
- [10] T. Maluangnont, K. Matsuba, F. Geng, R. Ma, Y. Yamauchi, and T. Sasaki, "Osmotic swelling of layered compounds as a route to producing high-quality two-dimensional materials. A comparative study of tetramethylammonium versus tetrabutylammonium cation in a lepidocrocite-type titanate," *Chemistry of Materials*, vol. 25, pp. 3137–3146, 2013.
- [11] N. Sakai, Y. Ebina, K. Takada, and T. Sasaki, "Electronic band structure of titania semiconductor nanosheets revealed by electrochemical and photoelectrochemical studies," *Journal of the American Chemical Society*, vol. 126, no. 18, pp. 5851–5858, 2004.
- [12] K. Fukuda, Y. Ebina, T. Shibata, T. Aizawa, I. Nakai, and T. Sasaki, "Unusual crystallization behaviors of anatase nanocrystallites from a molecularly thin titania nanosheet and its stacked forms: increase in nucleation temperature and oriented growth," *Journal of the American Chemical Society*, vol. 129, no. 1, pp. 202–209, 2007.
- [13] L. Wang, T. Sasaki, Y. Ebina, K. Kurashima, and M. Watanabe, "Fabrication of controllable ultrathin hollow shells by layer-by-layer assembly of exfoliated titania nanosheets on polymer templates," *Chemistry of Materials*, vol. 14, no. 11, pp. 4827–4832, 2002.
- [14] W. Tu, Y. Zhou, Q. Liu et al., "Robust hollow spheres consisting of alternating titania nanosheets and graphene nanosheets with high photocatalytic activity for CO_2 conversion into renewable fuels," *Advanced Functional Materials*, vol. 22, no. 6, pp. 1215–1221, 2012.
- [15] D. Robert, A. Piscopo, O. Heintz, and J. V. Weber, "Photocatalytic detoxification with TiO_2 supported on glass-fibre by using artificial and natural light," *Catalysis Today*, vol. 54, no. 2-3, pp. 291–296, 1999.
- [16] M. E. Fabiyi and R. L. Skelton, "Photocatalytic mineralisation of methylene blue using buoyant TiO_2 -coated polystyrene beads," *Journal of Photochemistry and Photobiology A: Chemistry*, vol. 132, no. 1-2, pp. 121–128, 2000.
- [17] B. Gao, P. S. Yap, T. M. Lim, and T.-T. Lim, "Adsorption-photocatalytic degradation of Acid Red 88 by supported TiO_2 : effect of activated carbon support and aqueous anions," *Chemical Engineering Journal*, vol. 171, no. 3, pp. 1098–1107, 2011.
- [18] J. Shi, S. Chen, S. Wang, P. Wu, and G. Xu, "Favorable recycling photocatalyst TiO_2/CFA : effects of loading method on the structural property and photocatalytic activity," *Journal of Molecular Catalysis A: Chemical*, vol. 303, pp. 141–147, 2009.
- [19] J. Shi, S. Chen, Z. Ye, S. Wang, and P. Wu, "Favorable recycling photocatalyst TiO_2/CFA : effects of loading percent of TiO_2 on the structural property and photocatalytic activity," *Applied Surface Science*, vol. 257, pp. 1068–1074, 2010.
- [20] J. Shi, S. Chen, S. Wang, Z. Ye, P. Wu, and B. Xu, "Favorable recycling photocatalyst TiO_2/CFA : effects of calcination temperature on the structural property and photocatalytic activity," *Journal of Molecular Catalysis A: Chemical*, vol. 330, pp. 41–448, 2010.
- [21] D. Zhao, C. Chen, Y. Wang et al., "Enhanced photocatalytic degradation of dye pollutants under visible irradiation on Al(III)-modified TiO_2 : structure, interaction, and interfacial

- electron transfer," *Environmental Science and Technology*, vol. 42, no. 1, pp. 308–314, 2008.
- [22] W. Kim, T. Tachikawa, T. Majima, and W. Choi, "Photocatalysis of dye-sensitized TiO₂ nanoparticles with thin overcoat of Al₂O₃: enhanced activity for H₂ production and dechlorination of CCl₄," *Journal of Physical Chemistry C*, vol. 113, no. 24, pp. 10603–10609, 2009.
- [23] Y.-T. Yu, "Preparation of nanocrystalline TiO₂-coated coal fly ash and effect of iron oxides in coal fly ash on photocatalytic activity," *Powder Technology*, vol. 146, no. 1-2, pp. 154–159, 2004.
- [24] T. Sasaki, Y. Ebina, T. Tanaka, M. Harada, M. Watanabe, and G. Decher, "Layer-by-layer assembly of titania nanosheet/polycation composite films," *Chemistry of Materials*, vol. 13, no. 12, pp. 4661–4667, 2001.
- [25] T. Sasaki and M. Watanabe, "Osmotic swelling to exfoliation. Exceptionally high degrees of hydration of a layered titanate," *Journal of the American Chemical Society*, vol. 120, no. 19, pp. 4682–4689, 1998.
- [26] Y. Li, M. Guo, M. Zhang, and X. Wang, "Hydrothermal synthesis and characterization of TiO₂ nanorod arrays on glass substrates," *Materials Research Bulletin*, vol. 44, no. 6, pp. 1232–1237, 2009.
- [27] J. Shi, J. Zheng, P. Wu, and X. Ji, "Immobilization of TiO₂ films on activated carbon fiber and their photocatalytic degradation properties for dye compounds with different molecular size," *Catalysis Communications*, vol. 9, no. 9, pp. 1846–1850, 2008.
- [28] T. Sasaki, Y. Ebina, K. Fukuda, T. Tanaka, M. Harada, and M. Watanabe, "Titania nanostructured films derived from a titania nanosheet/polycation multilayer assembly via heat treatment and UV irradiation," *Chemistry of Materials*, vol. 14, no. 8, pp. 3524–3530, 2002.
- [29] K. Xu, T. Deng, J. Liu, and W. Peng, "Study on the phosphate removal from aqueous solution using modified fly ash," *Fuel*, vol. 89, no. 12, pp. 3668–3674, 2010.
- [30] X. Wang, Y. Liu, Z. Hu, Y. Chen, W. Liu, and G. Zhao, "Degradation of methyl orange by composite photocatalysts nano-TiO₂ immobilized on activated carbons of different porosities," *Journal of Hazardous Materials*, vol. 169, no. 1–3, pp. 1061–1067, 2009.
- [31] H. Nishikiori, M. Furukawa, and T. Fujii, "Degradation of trichloroethylene using highly adsorptive allophane-TiO₂ nanocomposite," *Applied Catalysis B: Environmental*, vol. 102, no. 3-4, pp. 470–474, 2011.
- [32] G. S. J. and K. Sing, *Adsorption, Surface Area and Porosity*, Academic Press, London, UK, 1982.
- [33] Y. Zhang, D. Wang, and G. Zhang, "Photocatalytic degradation of organic contaminants by TiO₂/sepiolite composites prepared at low temperature," *Chemical Engineering Journal*, vol. 173, no. 1, pp. 1–10, 2011.
- [34] J. Yu, Y. Su, and B. Cheng, "Template-free fabrication and enhanced photocatalytic activity of hierarchical Macro/Mesoporous titania," *Advanced Functional Materials*, vol. 17, pp. 1984–1990, 2007.
- [35] F. Chen, Z. Liu, Y. Liu, P. Fang, and Y. Dai, "Enhanced adsorption and photocatalytic degradation of high-concentration methylene blue on Ag₂O-modified TiO₂-based nanosheet," *Chemical Engineering Journal*, vol. 221, pp. 283–291, 2013.
- [36] T. A. McMurray, J. A. Byrne, P. S. M. Dunlop, J. G. M. Winkelman, B. R. Eiggins, and E. T. McAdams, "Intrinsic kinetics of photocatalytic oxidation of formic and oxalic acid on immobilised TiO₂ films," *Applied Catalysis A: General*, vol. 262, no. 1, pp. 105–110, 2004.
- [37] H. T. Chang, N.-M. Wu, and F. Zhu, "A kinetic model for photocatalytic degradation of organic contaminants in a thin-film TiO₂ catalyst," *Water Research*, vol. 34, no. 2, pp. 407–416, 2000.
- [38] J.-M. Lee, M.-S. Kim, and B.-W. Kim, "Photodegradation of bisphenol-A with TiO₂ immobilized on the glass tubes including the UV light lamps," *Water Research*, vol. 38, no. 16, pp. 3605–3613, 2004.
- [39] N. Sakai, A. Fujishima, T. Watanabe, and K. Hashimoto, "Quantitative evaluation of the photoinduced hydrophilic conversion properties of TiO₂ thin film surfaces by the reciprocal of contact angle," *Journal of Physical Chemistry B*, vol. 107, no. 4, pp. 1028–1035, 2003.
- [40] Y. Xu, B. Lei, L. Guo, W. Zhou, and Y. Liu, "Preparation, characterization and photocatalytic activity of manganese doped TiO₂ immobilized on silica gel," *Journal of Hazardous Materials*, vol. 160, no. 1, pp. 78–82, 2008.
- [41] R. Yuan, R. Guan, W. Shen, and J. Zheng, "Photocatalytic degradation of methylene blue by a combination of TiO₂ and activated carbon fibers," *Journal of Colloid and Interface Science*, vol. 282, no. 1, pp. 87–91, 2005.
- [42] J.-H. Choy, H.-C. Lee, H. Jung, H. Kim, and H. Boo, "Exfoliation and restacking route to anatase-layered titanate nanohybrid with enhanced photocatalytic activity," *Chemistry of Materials*, vol. 14, no. 6, pp. 2486–2491, 2002.

Research Article

Theoretical Study of One-Intermediate Band Quantum Dot Solar Cell

Abou El-Maaty Aly^{1,2} and Ashraf Nasr^{2,3}

¹ Power Electronics and Energy Conversion Department, Electronics Research Institute (ERI), National Research Centre Building (NRCB), El-Tahrir Street, Dokki, Giza 12622, Egypt

² Computer Engineering Department, College of Computer, Qassim University, P.O. Box 6688, Buryadah 51452, Saudi Arabia

³ Radiation Engineering Department, NCRRT, Atomic Energy Authority, P.O. Box 29, Nasr City, Egypt

Correspondence should be addressed to Abou El-Maaty Aly; abouelmaaty67@gmail.com

Received 3 January 2014; Accepted 3 February 2014; Published 24 March 2014

Academic Editor: Xiwang Zhang

Copyright © 2014 A.-M. Aly and A. Nasr. This is an open access article distributed under the Creative Commons Attribution License, which permits unrestricted use, distribution, and reproduction in any medium, provided the original work is properly cited.

The intermediate bands (IBs) between the valence and conduction bands play an important role in solar cells. Because the smaller energy photons than the bandgap energy can be used to promote charge carriers transfer to the conduction band and thereby the total output current increases while maintaining a large open circuit voltage. In this paper, the influence of the new band on the power conversion efficiency for the structure of the quantum dots intermediate band solar cell (QDIBSC) is theoretically investigated and studied. The time-independent Schrödinger equation is used to determine the optimum width and location of the intermediate band. Accordingly, achievement of maximum efficiency by changing the width of quantum dots and barrier distances is studied. Theoretical determination of the power conversion efficiency under the two different ranges of QD width is presented. From the obtained results, the maximum power conversion efficiency is about 70.42% for simple cubic quantum dot crystal under full concentration light. It is strongly dependent on the width of quantum dots and barrier distances.

1. Introduction

The intermediate band solar cells (IBSCs) have attracted great attention due to the possibility of exceeding the Shockley-Queisser (SQ) limit [1–4]. From the analysis by Luque et al. [5, 6], the IBSC's concept yields a maximum theoretical efficiency of 63.2%, surpassing the limit of 40.7% of single gap solar cells under maximum light concentration (the sun being assumed as a blackbody at 6000 K) [7]. Since its introduction in 1997, there have been many theoretical and experimental efforts to explore this idea [8]. The use of quantum dot (QD) technology is proposed as a near term proof of concept of the operating principles of an intermediate band solar cell (IBSC). This intermediate band allows the extra generation of electron-hole pairs through the two-step absorption of subbandgap photons. In the first step, an electron is pumped from the valence band (VB) to the intermediate band (IB), while in the second step, another electron is launched from the IB to the CB [9]. Quantum

dot heterojunctions may implement an IBSC because of their ability to provide the three necessary bands [10]. In comparison to conventional quantum well superlattices or multiple quantum well structures, quantum dot superlattice (QDS) that consists of multiple arrays of quantum dots has many advantages due to its modified density of electronic states and optical selection rules. For example, due to relaxed intraband optical selection rules in QDS, they are capable of absorbing normally incident radiation, for example, Indium gallium nitride ($\text{In}_x\text{Ga}_{1-x}\text{N}$) alloys feature a bandgap ranging from the near infrared (~ 0.7 eV) to ultraviolet (~ 3.42 eV); this range corresponds very closely to the solar spectrum, making $\text{In}_x\text{Ga}_{1-x}\text{N}$ alloys a promising material for future solar cells. $\text{In}_x\text{Ga}_{1-x}\text{N}$ alloys solar cells have been fabricated with different indium contents and the results are encouraging [11]. However, it is not possible in quantum well superlattices. The latter makes QDS a good candidate for infrared photodetector applications [12]. As considered in [13], 3D-ordered QDS with the closely spaced quantum

dots and high quality interfaces allow a strong wave function overlap and the formation of minibands. In such structures, the quantum dots play a similar role to that of atoms in real crystals. To distinguish such nanostructures from the disordered multiple arrays of quantum dots, we refer to them as quantum dot supracrystals (QDC). Other assumptions that include the rules for solving the Schrödinger equation for determining the IBs are considered in the following sections. The remainder of the paper is organized as follows. In Section 2, the basic assumptions and a superlattice model description are presented. The intermediate band energy and wavevectors of a charge carrier are calculated in Section 3. The induced photocurrent density and power conversion energy are described in Section 4. The numerical results and discussions are summarized in Section 5. Finally, a conclusion of the results is outlined in Section 5.

2. Basic Assumptions and Superlattice Model Description

In this paper, the investigations are devoted to one intermediate band solar cell. We explain the various behaviors of this model depending on the QD solar cell parameters, such as quantum dot size, interdot distance, and type of composition alloy. Meanwhile, in the next step, the multi-intermediate bands are investigated. Therefore, the following are the basic assumptions that are used in the QD one intermediate band solar cell model [11–14].

- (a) The solar cell model is thick enough; carrier mobility will be high enough to ensure the full absorption of photons. All photons with energy greater than the lowest energy gap in the QDIBS model are absorbed.
- (b) The quasi-Fermi energy levels which are equivalent to infinite carrier mobility are constant throughout the model.
- (c) The transitions occurring between the bands are only radiative recombination.
- (d) The solar cell absorbs blackbody radiation at a sun temperature, 6000 K, and the temperature of the solar cell, 300 K, and emits blackbody radiation at 300 K only.
- (e) No carriers can be extracted from the intermediate band; the net pumping of electrons from the VB to the IB must equal the net pumping of electrons from the IB to the CB.
- (f) The shape of the QDs is cubic and they must be arranged in a periodic lattice in order to establish well-placed intermediate band boundaries. For simplicity, the energy corresponding to the top of the valence band is the same both in the barrier and the QD material; therefore there is no valence band offset and only confining potential occurs at the conduction band offset.

- (g) The intermediate band should be approximately half-filled with electrons in order to receive electrons from the valence energy band and pump electrons to the conduction energy band.

When charge carriers in semiconductors can be confined by potential barriers in three dimensions, it is called quantum dots. QDs periodic arrays from semiconductor with a smaller bandgap are sandwiched between two layers of another second semiconductor having a larger bandgap (n or p type). This configuration creates the potential barriers. Two potential wells are formed in this structure; one is for conduction band electrons and the other for valence band holes. The well (QDs layer) depth for electrons is called the conduction band offset, which is the difference between the conduction band edges of the well and barrier semiconductors. The well depth for holes is called the valence band offset. If the offset for either the conduction or valence bands is zero, then only one carrier will be confined in a well. In this structure, if the barrier thickness between adjacent wells prevents significant electronic coupling between the wells, then each well is electronically isolated. On the other hand, if the barrier thickness is sufficiently thin to allow electronic coupling between wells, then the electronic charge distribution can become delocalized along the direction normal to the well layers, therefore producing new minibands (see Figure 1).

The electronic coupling rapidly increases with decreasing the barrier thickness and miniband formation is very strong below 2 nm [15]. Superlattice structures yield efficient charge transport normal to the layers because the charge carriers can move through the minibands. As a result the barrier will be narrower and the miniband and the carrier mobility will be wider and higher, respectively.

3. Wavevectors of a Charge Carrier

The wavevector of a charge carrier (single electron or hole) can be described by the time-independent Schrödinger equation, which has the following form [11, 16]:

$$\left(\frac{-\hbar^2}{2m} \nabla^2 + V \right) \psi = E \psi, \quad (1)$$

where \hbar is the Planck's constant, m is the effective mass, ∇^2 is a second order differential operator, V is the potential energy, E is the total energy of charge carrier, and k is the wavevector. The Kronig-Penney model solved this equation by the one-dimensional periodic potential shown also in Figure 1.

This model assumes that the wave travelling of charge carrier is in the positive x direction for one-dimensional only. Therefore, the mathematical form of the repeating unit of the potential is

$$V(x) = \begin{cases} V_0, & \text{for } x = L_B, \\ 0, & \text{for } x = L_{\text{QD}}. \end{cases} \quad (2)$$

Here, V_0 is the conduction band offset, L_B is the barrier width, and L_{QD} is the quantum dot width. The period T of the

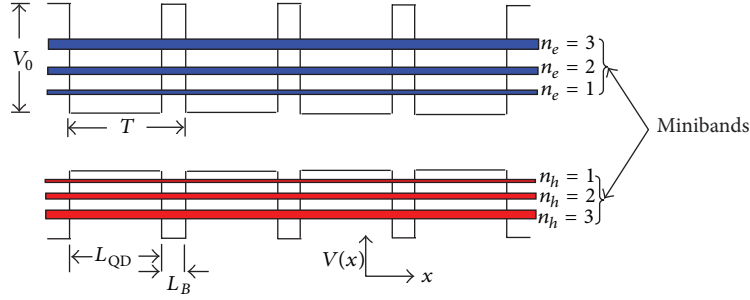


FIGURE 1: Minibands formation in the superlattice structure and Kronig-Penney potential.

considered potential is equal to $(L_{\text{QD}} + L_{\text{B}})$. The Schrödinger equation for this model is [10, 17, 18]. Consider

$$\frac{d^2k}{dx^2} + \frac{2mE}{\hbar^2}k = 0, \quad \text{for } x = L_{\text{QD}}, \quad (3a)$$

$$\frac{d^2k}{dx^2} + \frac{2m(E - V_0)}{\hbar^2}k = 0, \quad \text{for } x = L_{\text{B}}. \quad (3b)$$

According to the Kronig-Penney model, the solution of (3a) and (3b) can be expressed as

$$\begin{aligned} & \frac{\sigma^2 - \delta^2}{2\sigma\delta} \sinh(\sigma L_{\text{B}}) \sin(\delta L_{\text{QD}}) - \cosh(\sigma L_{\text{B}}) \cos(\delta L_{\text{QD}}) \\ & = \cos(L_{\text{B}} + L_{\text{QD}})k. \end{aligned} \quad (4)$$

For simplicity, one can assume the following symbols for internal terms in (4):

$$\begin{aligned} \sigma^2 &= \frac{2m_{\text{B}}(V_0 - E)}{\hbar^2} = \frac{2m_{\text{B}}V_0}{\hbar^2}(1 - \epsilon), \\ \delta^2 &= \frac{2m_{\text{Q}}V_0}{\hbar^2} \frac{E}{V_0} = \frac{2m_{\text{Q}}V_0}{\hbar^2}\epsilon, \quad \epsilon = \frac{E}{V_0}, \end{aligned} \quad (5)$$

where m_{B} , m_{Q} are effective mass of electron in barrier region and effective mass of electron in quantum dots region, respectively.

Therefore, from (4), the factor into the first term plays an important role for investigating this proposed QDIBSC model. It can be expressed as follows:

$$\frac{\sigma^2 - \delta^2}{2\sigma\delta} = \frac{m_{\text{Q}} - (m_{\text{Q}} + m_{\text{B}})\epsilon}{2(m_{\text{Q}}m_{\text{B}}\epsilon)^{1/2}(\epsilon - 1)^{1/2}}. \quad (6)$$

Furthermore, the other arguments in (4) for hyperbolic and sinusoidal functions can be defined as

$$\begin{aligned} \sigma L_{\text{B}} &= \mu A_{\text{B}}(1 - \epsilon)^{1/2}, \quad \delta L_{\text{QD}} = A_{\text{Q}}\epsilon^{1/2}, \\ \mu &= \frac{L_{\text{B}}}{L_{\text{QD}}}, \quad A_{\text{B}} = L_{\text{QD}} \left(\frac{2m_{\text{B}}V_0}{\hbar^2} \right)^{1/2}, \\ A_{\text{Q}} &= L_{\text{QD}} \left(\frac{2m_{\text{Q}}V_0}{\hbar^2} \right)^{1/2}. \end{aligned} \quad (7)$$

Substituting these definitions into (4), it will become as

$$\begin{aligned} & \frac{m_{\text{Q}} - (m_{\text{Q}} + m_{\text{B}})\epsilon}{2(m_{\text{Q}}m_{\text{B}}\epsilon)^{1/2}(1 - \epsilon)^{1/2}} \sinh[\mu A_{\text{B}}(1 - \epsilon)^{1/2}] \sin(A_{\text{Q}}\epsilon^{1/2}) \\ & + \cosh[\mu A_{\text{B}}(1 - \epsilon)^{1/2}] \cos(A_{\text{Q}}\epsilon^{1/2}) \\ & = \cos[kL_{\text{QD}}(1 + \mu)], \quad \text{for } \epsilon < 1, \end{aligned} \quad (8a)$$

$$\begin{aligned} & \frac{m_{\text{Q}} - (m_{\text{Q}} + m_{\text{B}})\epsilon}{2(m_{\text{Q}}m_{\text{B}}\epsilon)^{1/2}(\epsilon - 1)^{1/2}} \sin[\mu A_{\text{B}}(\epsilon - 1)^{1/2}] \\ & \times \sin(A_{\text{Q}}\epsilon^{1/2}) + \cos[\mu A_{\text{B}}(\epsilon - 1)^{1/2}] \cos(A_{\text{Q}}\epsilon^{1/2}) \\ & = \cos[kL_{\text{QD}}(1 + \mu)], \quad \text{for } \epsilon > 1, \end{aligned} \quad (8b)$$

$$\cos A_{\text{Q}} - \frac{\mu A_{\text{B}}}{2} \sin A_{\text{Q}} = \cos[kL_{\text{QD}}(1 + \mu)], \quad (8c)$$

for $\epsilon = 1$.

The left-hand side of (8a), (8b), and (8c) can be represented by $F(\epsilon)$ for all values of the ratio of total energy of electrons over conduction band offset: ($\epsilon = E/V_0$). Consider

$$F(\epsilon) = \cos[kL_{\text{QD}}(1 + \mu)]. \quad (9)$$

Equation (9) cannot be solved analytically, but it can be solved graphically. Figure 2 shows the left-hand side of (9), $F(\epsilon)$, against ϵ at fixed values of μ and A . The concerned QDIBSC model depends on the considered alloys in previous studies for comparing the results; the quantum dot width: $L_{\text{QD}} = 4.5$ nm (InAs_{0.9}N_{0.1}, $m_{\text{Q}} = 0.0354 m_0$), barrier width: $L_{\text{B}} = 2$ nm (GaAs_{0.98}Sb_{0.02}, $m_{\text{B}} = 0.066 m_0$), and $V_0 = 1.29$ eV [12]. But in further studies, other alloys will be processed. The left-hand side is not constrained to ± 1 and is a function of energy only. The right-hand side is constrained to a range of ± 1 and is a function of k only. The limits of the right-hand side ± 1 occur at $k = 0$ to $(\pm\pi/T)$. The two horizontal red lines in Figure 2 represent the two extreme values of $\cos[kL_{\text{QD}}(1 + \mu)]$. The only allowed values of E are those for which $F(\epsilon)$ lies between the two horizontal red lines; see Table 1.

Figure 2 and Table 1 show the allowed energy ranges or bands, E , which fall into continuous regions separated by

TABLE 1: The allowed energy ranges or bands as E for the proposed composition from Figure 2.

| Band | Range of E , (eV) |
|------|---------------------|
| 1 | 0.2039–0.2369 |
| 2 | 0.8140–0.9852 |
| 3 | 1.6638–2.2775 |
| 4 | 2.4758–3.5439 |

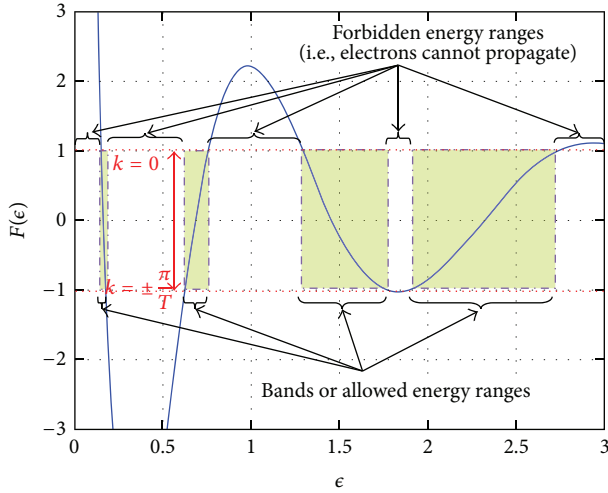


FIGURE 2: The left-hand side of (9), $F(\epsilon)$, against ϵ at fixed values of μ and A . This graph shows allowed and forbidden electron energy bands for the simple cubic QD with the quantum dot width $L_{\text{QD}} = 4.5$ nm (InAs_{0.9}N_{0.1}, $m_{\text{Q}} = 0.0354m_0$), barrier width $L_{\text{B}} = 2$ nm (GaAs_{0.98}Sb_{0.02}, $m_{\text{B}} = 0.066m_0$), and $V_0 = 1.29$ eV.

gaps. This distribution of allowed energies illustrates the band structure of crystalline solids. According to Figure 2 and Table 1, when the values of E are from 0 to 0.2039 eV, $F(\epsilon)$ is greater than one and so there is no real value of k that satisfies (9). At $E = 0.2039$ eV the wavevector will be equal to zero. As E varies from 0.2039 eV to 0.2369 eV, $\cos[kL_{\text{QD}}(1 + \mu)]$ varies from +1 to -1 and $kL_{\text{QD}}(1 + \mu)$ varies from 0 to $(\pm\pi)$. As E varies from 0.2369 eV to 0.8140 eV, there is no real value of k that satisfies (9). At $E = 0.8140$ eV, the argument of the right-hand side, $kL_{\text{QD}}(1 + \mu)$, will be equal to (π) . At $E = 0.9852$ eV, the argument of the right-hand side, $kL_{\text{QD}}(1 + \mu)$, will be equal to (2π) . Other bandgaps will periodically appear with the same behavior.

Figure 3 shows the allowed energy bands and the wavevector states in one-dimensional crystal with the same data as in Figure 2. In this case, the wavevector is changed from 0 to $(\pm\pi/T)$, and the allowed energy bands into the electron energy is assigned. Also, the curve shows that the slope (dE/dk) is zero at the k boundaries (i.e., 0 and $\pm\pi/T$). Thus, the velocity of the electrons approaches zero at the boundaries. This means that the electron trajectory or momentum is confined to stay within the allowable k . Figure 4 denotes more explanation for the considered energy allowed bands as in Figure 3. It shows the allowed E - k states with the bandgaps that appear when $k = N\pi/T$. The

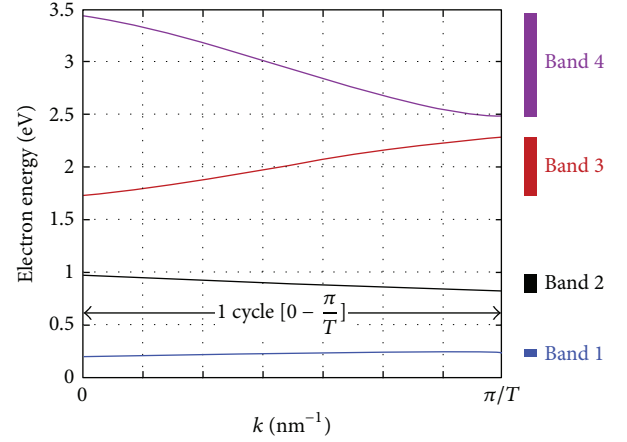


FIGURE 3: Allowed E - k states in one-dimensional crystal with the same data in Figure 2.

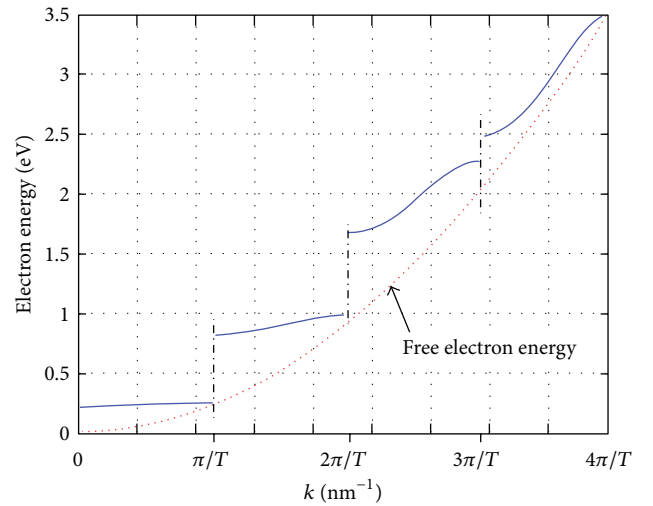


FIGURE 4: Allowed E - k states and free electrons energy.

dashed line represents E - k states for free electrons energy. It can be obtained by letting $V_0 = 0$ in (4). Therefore, the free energy of electron is $E = \hbar^2 k^2 / 2m$. After the essential equations and assumptions are demonstrated, the following section is concerned with the determination of the effect of intermediate band, alloy construction, and dot and barrier width in each of induced photocurrent density and corresponding power efficiency.

4. Induced Current Density and Power Conversion Efficiency

The photon generated current density in QDIBSC with one intermediate band is derived in this section. Then, the sensitivity of the power conversion efficiency as a function of the intermediate band energy level will be investigated. According to the assumptions in Section 2, the only radiative transitions occur between the bands therefore the generation

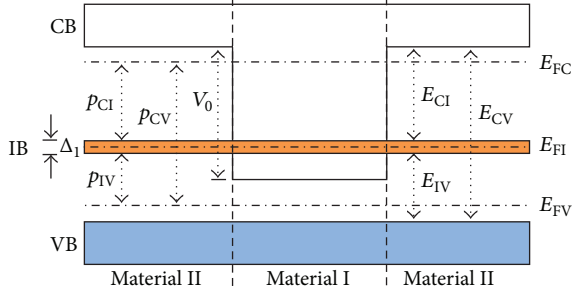


FIGURE 5: Construction of energy band diagram for two semiconductor materials (material I; $\text{InAs}_{0.9}\text{N}_{0.1}$: quantum dot, material II; $\text{GaAs}_{0.98}\text{Sb}_{0.02}$: barrier width) to create a heterostructure for one intermediate band solar cell.

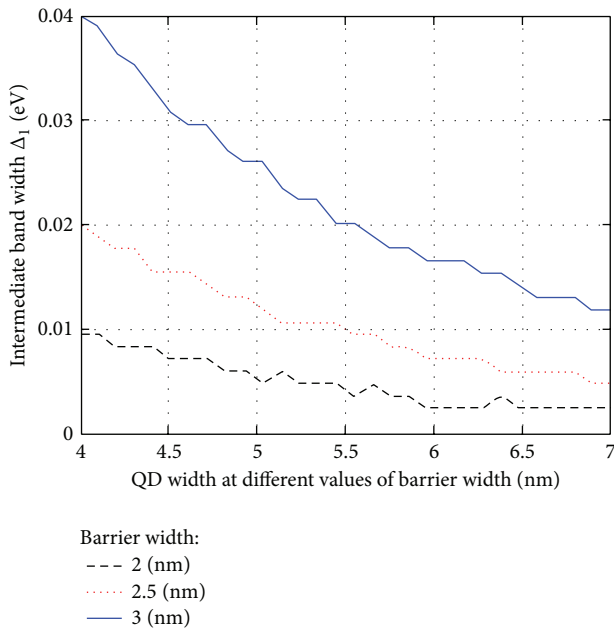


FIGURE 6: Change width of intermediate band (Δ_1) with change QD width for the first allowable range at three different values of barrier width.

and recombination events are represented by photon absorption and emission. Figure 5 illustrates the construction of an energy band diagram for a heterostructure in the case of one intermediate band solar cell. An electron in the valence band can be excited to either the intermediate or conduction band. Also, an electron in the intermediate band can be excited to the conduction band. Therefore, there are three upward energy transitions: E_{VI} , E_{CI} , and E_{CV} . E_{VI} represents valence to intermediate band, E_{CI} represents intermediate to conduction band, and E_{CV} represents the conventional bandgap between the valence and conduction band. The two intermediate transitions E_{VI} and E_{CI} are independent of each other, while the bandgap transition E_{CV} is a function of the two intermediate ones: $E_{CV} = E_{VI} + E_{CI}$.

The photon flux density, N , is the number of photons per second per unit area per unit wavelength and behaves like

a blackbody flux density and according to the Roosbroeck-Shockley equation [19–22] is given by

$$N(E_{VI}, E_{CI}, T, p) = \frac{2\pi\xi}{h^3 C^2} \int_{E_{VI}}^{E_{CI}} \frac{E^2 dE}{e^{(E-p)/k_B T} - 1}, \quad (10)$$

where T is the temperature, ξ is geometric factor, h is Planck constant, k_B is Boltzmann constant, C is speed of light, and p is chemical potential. To simplify the analysis, assume that $E_{VI} \leq E_{CI} \leq E_{CV}$. Therefore the photons with energy greater than E_{VI} and less than E_{CI} are absorbed and electrons transfer from valence band to intermediate band and leave holes in the valence band. Any excess energy greater than E_{VI} and less than E_{CI} will be lost due to thermalization and carriers will relax to the band edges before another radiative occurs. One can notice that this thermalization value is very small in comparison with its value in the case of bulk based semiconductor solar cells. This means that an absorbed photon with energy greater than E_{VI} and less than E_{CI} has the same effect as an absorbed photon with energy equal to E_{VI} .

Photons with energy greater than E_{CI} and less than E_{CV} are absorbed and an electron transfers from intermediate band to conduction band. The excess energy behavior has the same effect as considered in the previous case regarding the difference in the transition band process. Photons with energy greater than E_{CV} are absorbed and an electron transfers from valence band to conduction band and creates a hole in the valence band. The absorbed photon with energy greater than E_{CV} has the same effect as an absorbed photon with energy equal to E_{CV} taking into account the excess energy process. The net photon flux is equal to the number of charge carrier flux collected at the contact. When the charge carrier flux is multiplied by the electric charge of electron, q , the current density of the QDIBSC for one intermediate band is [11, 13, 14]:

$$j = q \left\{ \left[C_f \xi N(E_{CV}, \infty, T_s, 0) + (1 - C_f \xi) N(E_{CV}, \infty, T_a, 0) - pN(E_{CV}, \infty, T_a, qV) \right] + \left[C_f \xi N(E_{CI}, E_{CV}, T_s, 0) + (1 - C_f \xi) N(E_{CI}, E_{CV}, T_a, 0) - N(E_{CI}, E_{CV}, T_a, p_{CI}) \right] \right\}, \quad (11)$$

where C_f is concentration factor, T_s is temperature of sun (6000 K), T_a is ambient temperature (300 K), qV is quasi-Fermi energy, and p_{CI} is chemical potential between conduction and intermediate bands. The terms in the first bracket represent the current density generated when the electrons transfer from the valence band to the conduction band as typically for conventional solar cell. While the terms in the second bracket represent the current density generated when the electrons transfer from the intermediate band to the conduction band. In both bracketed terms, the QDIBSC absorbs radiation from the sun at the temperature T_s and

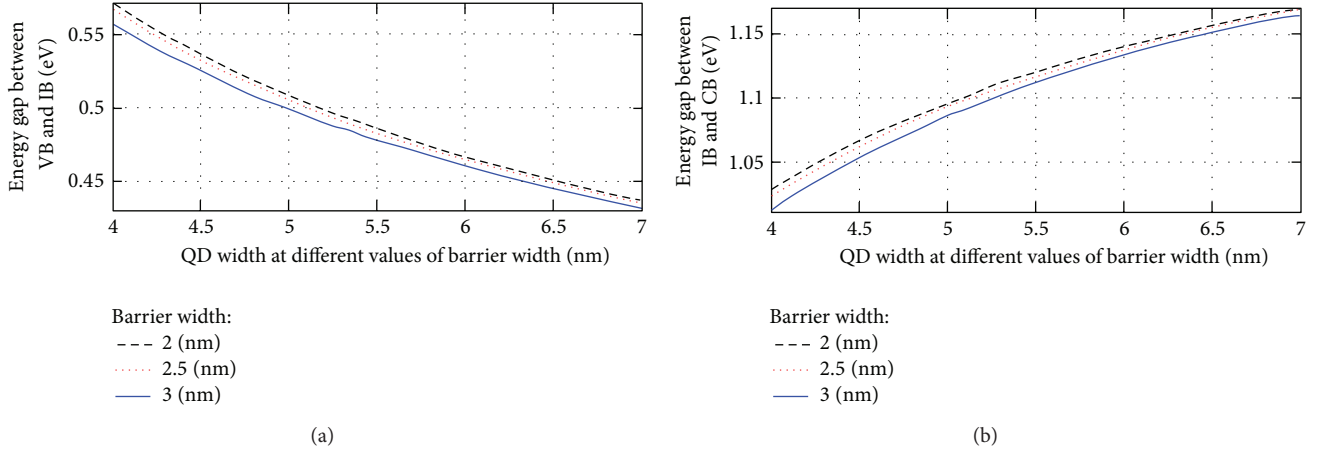


FIGURE 7: (a) Change energy gap between VB and IB according to change in QD width for the first allowable range at different values of barrier width. (b) Change energy gap between IB and CB with the same conditions in (a).

T_a , respectively, while it emits radiation at the temperature T_a and a corresponding chemical potential. The current density of the QDIBSC is formulated according to the proper operation of the QDIBSC which requires that there is no current extracted from the intermediate band; that is, the current entering the intermediate band must equal the current leaving the intermediate band. Therefore, the second term in (11) can be rewritten as [14, 23, 24]

$$\begin{aligned}
 & q \left[C_f \xi N(E_{CI}, E_{CV}, T_s, 0) + (1 - C_f \xi) \right. \\
 & \quad \left. \times N(E_{CI}, E_{CV}, T_a, 0) - N(E_{CI}, E_{CV}, T_a, p_{CI}) \right] \\
 & = q \left[C_f \xi N(E_{VI}, E_{CI}, T_s, 0) + (1 - C_f \xi) \right. \\
 & \quad \left. \times N(E_{VI}, E_{CI}, T_a, 0) - N(E_{VI}, E_{CI}, T_a, p_{IV}) \right]. \quad (12)
 \end{aligned}$$

The output voltage can be described as the difference of the chemical potentials between CB and VB; that is, $qV_{oc} = p_{CV} = p_{CI} + p_{IV}$.

In this work, the light intensity on QDIBSC is calculated by the number of suns, where 1 sun (or concentration factor $C_f = 1$) means the standard intensity at the surface of the Earth's atmosphere. Therefore, at the surface of the Earth's atmosphere the power density falling on a QDIBSC is $P_{in} = \xi \sigma_s T_s^4 = 1587.2 \text{ w/m}^2$, where σ_s is Stefan's constant and T_s is temperature of sun (6000 K). Theoretically, the full concentration would be achieved when $C_f = 1/\xi = 46296$. The power conversion efficiency, η , of the QDIBSC is dependent on P_{in} , so that it varies with the level concentration of C_f . We concentrate our study on the QDIBSC efficiencies with unconcentrated light $C_f = 1$ and also compared it with full concentration light $C_f \times \xi = 1$. The power conversion efficiency equation of the QDIBSC is

$$\eta = \frac{V_{oc} \times J_{sc} \times FF}{P_{in}} = \frac{J_m \times V_m}{C_f \xi \sigma_s T_s^4} = \frac{J_m \times V_m}{C_f \times 1587.2}, \quad (13)$$

where V_{oc} is open circuit voltage, J_{sc} is short circuit current density, FF is fill factor, V_m is maximum voltage of the QDIBSC, and J_m is maximum current density of the QDIBSC. After mathematical concepts and assumptions are defined in previous sections for assigned composition of material, the following section reports some features of the QDIBSCs performance for one intermediate band case.

5. Numerical Results and Discussions

The discussion firstly starts by manifesting the relation between QDIBSC parameters and the distribution of IB energies in the gap between valence and conduction bands. When the Schrödinger equation (1) is solved, many solutions are obtained. Some of them can be satisfied but others cannot. From the satisfied solutions, there are multi-intermediate bands as pointed from Figures 2, 3, and 4. They are essentially dependent on QDIBSC parameters such as QD, barrier widths. Here, we are concerned only with the effect of the first intermediate band, IB, into the behavior of the proposed model. From the obtained results, we found two ranges of quantum dot widths that vary the positions of intermediate bands. Other ranges of quantum dot widths will denote unachievable behavior. In the following discussions, the energy distributions, J - V characteristics, and corresponding power conversion efficiency are studied for each range. Comparisons between the two ranges outcomes are processed. A summary of all the related values describing the model is considered in Table 2. For the first range (QD width changes from 4–7 nm), the dependence of first intermediate band width, Δ_1 , on QD width at different barrier widths is depicted in Figure 6. One can recognize that the width of IB, Δ_1 , is decreased with an increase in the QD width. This behavior is consistent with the previous investigations that demonstrate that the decreasing of Δ_1 IB will assist in the fall down of the power conversion efficiency, as will be described later [11, 14]. Also the same trend will be found in the second range of QD and barrier widths, which also denotes the first IB. Also, Figure 6 illustrates that when the barrier width increases in

TABLE 2: Three different values of QD width ($\text{InAs}_{0.9}\text{N}_{0.1}$) and barrier width ($\text{GaAs}_{0.98}\text{Sb}_{0.02}$) for two different ranges of QD available widths at full concentration and unconcentration.

| Two available ranges | Parameters | | | | Full concentration | | | | | Unconcentration | | | | |
|------------------------|----------------------|------------|-------------------------|----------------------|---|---------------------|--|-------|-------------------------|----------------------|--|---------------------|---|-------|
| | L_{QD} (nm) | L_B (nm) | η_{max} (%) | V_{max} (v) | $J_{\text{max}} \times \xi$ (mA/cm^2) | V_{oc} (v) | $J_{\text{sc}} \times \xi$ (mA/cm^2) | FF | η_{max} (%) | V_{max} (v) | J_{max} (mA/cm^2) | V_{oc} (v) | J_{sc} (mA/cm^2) | FF |
| "1st range" 4–7 nm | 4 | 2 | 63.2 | 1.503 | 66.8 | 1.57 | 67.9 | 0.942 | 51.6 | 1.231 | 66.5 | 1.33 | 67.9 | 0.906 |
| | 4.5 | 2 | 61.2 | 1.505 | 64.6 | 1.58 | 65.6 | 0.938 | 50.0 | 1.233 | 64.3 | 1.34 | 65.6 | 0.902 |
| | 5 | 2 | 59.6 | 1.507 | 62.8 | 1.58 | 63.8 | 0.939 | 48.7 | 1.235 | 62.5 | 1.34 | 63.8 | 0.903 |
| | 4 | 2 | 63.2 | 1.503 | 66.8 | 1.57 | 67.9 | 0.942 | 51.6 | 1.231 | 66.5 | 1.33 | 67.9 | 0.906 |
| | 4 | 2.5 | 63.1 | 1.514 | 66.2 | 1.58 | 67.3 | 0.943 | 51.6 | 1.242 | 65.9 | 1.34 | 67.3 | 0.908 |
| | 4 | 3 | 63.0 | 1.516 | 65.9 | 1.58 | 67.0 | 0.944 | 51.5 | 1.244 | 65.7 | 1.35 | 67.0 | 0.904 |
| "2nd range" 7–11 nm | 8.1 | 1.98 | 70.4 | 1.508 | 74.1 | 1.57 | 75.3 | 0.945 | 57.5 | 1.238 | 73.7 | 1.34 | 75.3 | 0.904 |
| | 8.6 | 1.98 | 68.4 | 1.510 | 71.9 | 1.57 | 73.1 | 0.946 | 55.9 | 1.238 | 71.6 | 1.34 | 73.1 | 0.905 |
| | 9.1 | 1.98 | 66.7 | 1.512 | 70.0 | 1.58 | 71.2 | 0.941 | 54.5 | 1.241 | 69.8 | 1.34 | 71.2 | 0.908 |
| | 8.1 | 1.98 | 70.4 | 1.508 | 74.1 | 1.57 | 75.3 | 0.945 | 57.5 | 1.238 | 73.7 | 1.34 | 75.3 | 0.904 |
| | 8.1 | 2.48 | 70.3 | 1.519 | 73.4 | 1.58 | 74.7 | 0.945 | 57.5 | 1.248 | 73.1 | 1.35 | 74.6 | 0.906 |
| | 8.1 | 2.98 | 70.2 | 1.522 | 73.2 | 1.59 | 74.4 | 0.942 | 57.4 | 1.250 | 72.9 | 1.35 | 74.4 | 0.907 |

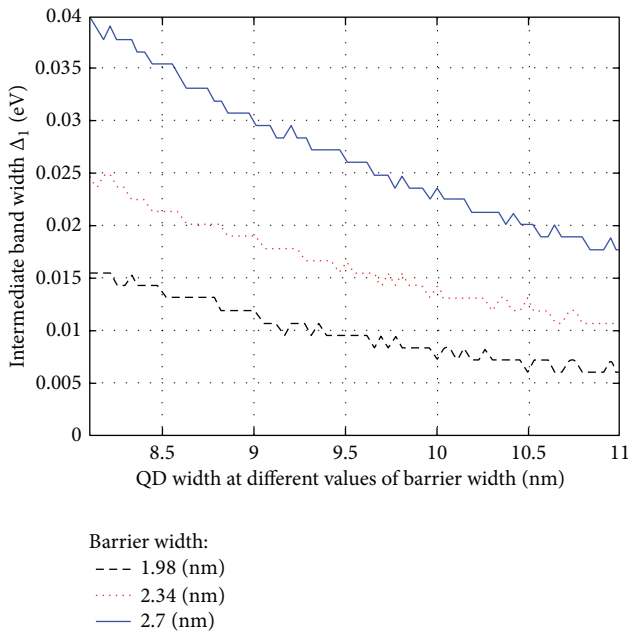


FIGURE 8: Change width of intermediate band (Δ_1) with change QD width for the second allowable range at three different values of barrier width.

the allowable range (2–3 nm), Δ_1 IB somewhat increases. At the same time, the increase of barrier width will somewhat inversely decrease the energy gap between IB width and each of VB and CB, as this behavior is shown in Figures 7(a) and 7(b). It is expected that when Δ_1 IB enlarges, the energy gap difference between it and the considered VB and CB will be decreased, as the total distance E_{cv} is constant [11, 14]. The first range power efficiency and J - V characteristics will be compared with the second range in the last part of these discussions.

For the second allowable range (QD width changes from 8.1–9.1 nm) and at the same barrier width range (2–3 nm), the intermediate band width, Δ_1 , with QD width at different values of barrier width is considered in Figure 8. When comparing this figure with the previous Figure 6, they gave the same trend. On the other hand, the varying Δ_1 in the first range covers a longer range of energy in comparison with the second one. Moreover, the allowable barrier width range in this second range is shifted left to be from 1.98 nm to 2.7 nm. The energy gap between the IB and each of VB and CB is illustrated in Figures 9(a) and 9(b). As a result of changing the values of Δ_1 , the corresponding values of energy gaps will be changed for the composition of the model, QD width ($\text{InAs}_{0.9}\text{N}_{0.1}$) and barrier width ($\text{GaAs}_{0.98}\text{Sb}_{0.02}$). Also the curves in this case tend to be straight in comparison with their equivalent in Figures 7(a) and 7(b). One can notice that the second range investigations were not considered before in previous studies. Although it gives an enhancement of power conversion efficiency as shown in the next results.

An example of the J - V characteristics for the second range of the proposed model is mentioned in Figure 10. It is important to note that the short circuit current density is related to the quantum dot width directly; meanwhile the open circuit voltage is approximately constant. Additionally, the wide range of the J - V characteristics with short circuit current and open circuit voltage values is confirmed in Table 2. This will contribute to the enhancement of obtained power conversion efficiency as shown in Figure 11. One can notice that the behavior of efficiency is in full agreement with the obtained results in [25]. But the new contribution is that the efficiency in this case, full concentration, reached up to (70.4%) (see also Table 2). The observed enhancement of the efficiency returns to discovering second range. Comparison between J - V characteristics for fully and unconcentrated cases are described in Figure 12. From this figure and Table 2, one can recognize that the second range denotes higher values of J_{sc} and a small amount of increase of V_{oc} in comparison to

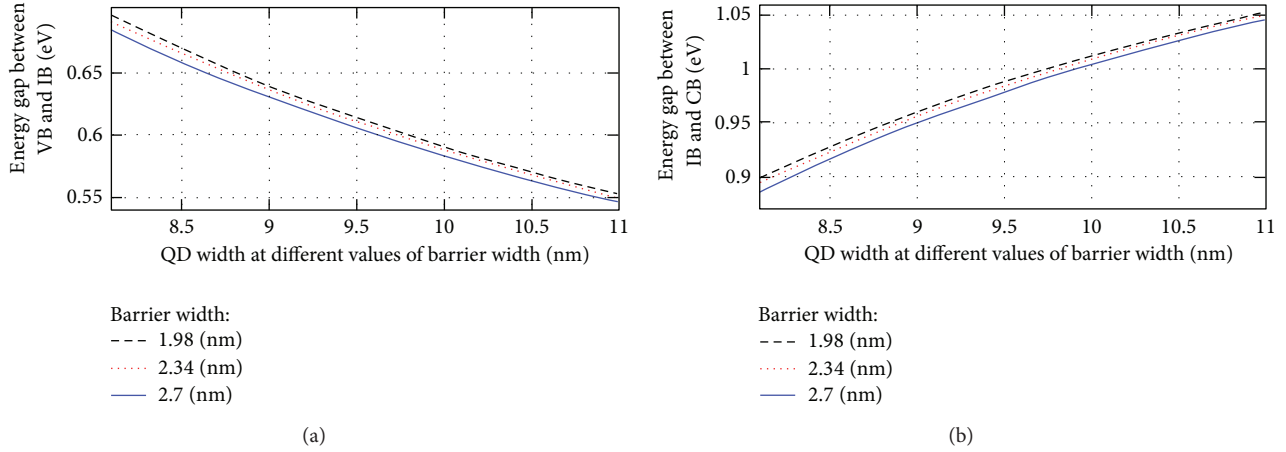


FIGURE 9: (a) Change energy gap between VB and IB according to change in QD width for the second allowable range at different values of barrier width. (b) Change energy gap between IB and CB with the same conditions in (a).

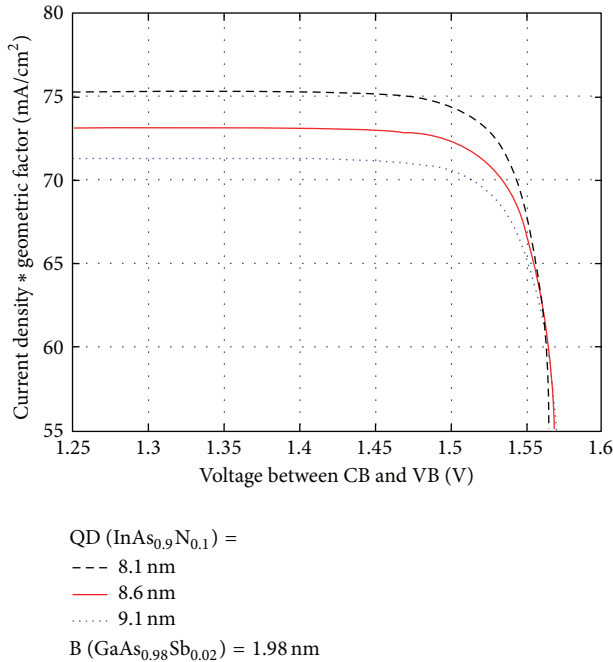


FIGURE 10: Current density for QDIBSC at full concentration with varying the quantum dot width and barrier width held constant.

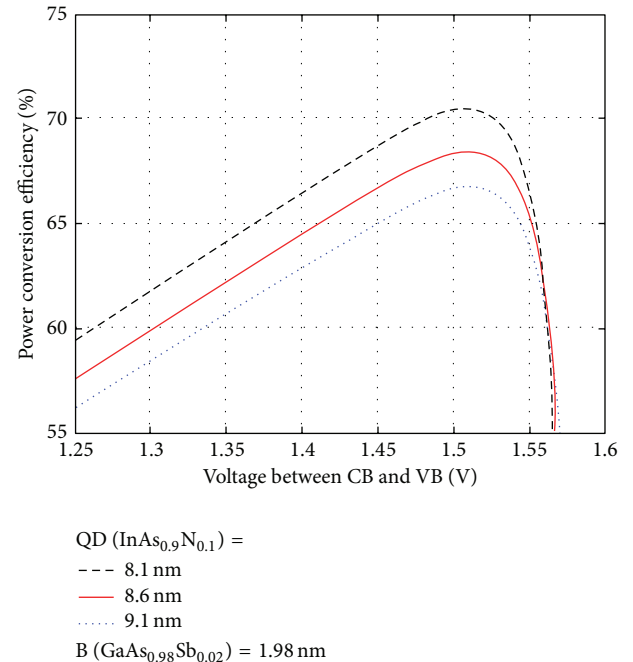


FIGURE 11: Power conversion efficiency for QDIBSC at full concentration with varying the quantum dot width and barrier width held constant.

the first range. But in the two considered ranges, the values of V_{oc} in the full concentration case are higher than that in the unconcentrated case. From a solar cell point of view, this behavior normally happens because the allowable large width of quantum dots will acquire high photons and it then excites a large number of electrons: high induced current density. For the same cases considered before, the comparison between the power conversion efficiency is depicted in Figure 13. Also, the corresponding power conversion efficiency, η , J_{max} , V_{max} , J_{sc} , V_{oc} , and fill factor, FF , for each combination of QD width (L_{QD}) and barrier width (L_B) for fully and unconcentration are considered in Table 2. The fill factor pointed in the table

is determined from (13). It also indicates an enhancement of power conversion efficiency, where FF is greater than 93% and 90% in the considered cases, respectively. The main target of these demonstrations is to compare the obtained power conversion efficiency from the first and second ranges. When a full concentration case is taken in the theoretical calculation, higher values of each of the open circuit voltage and short circuit current density are obtained that correspondingly gave higher power conversion efficiency. When one held comparison between our obtained results and others in the fully and unconcentrated cases: $\eta_{max} = 70.4\%$

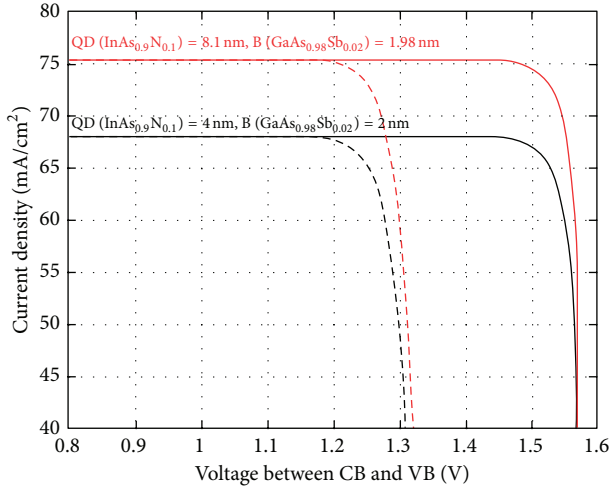


FIGURE 12: Comparison between current density for QDIBSC at full concentration (solid) and unconcentrated (dash) cases at specified values of quantum dot and barrier widths that give maximum efficiency.

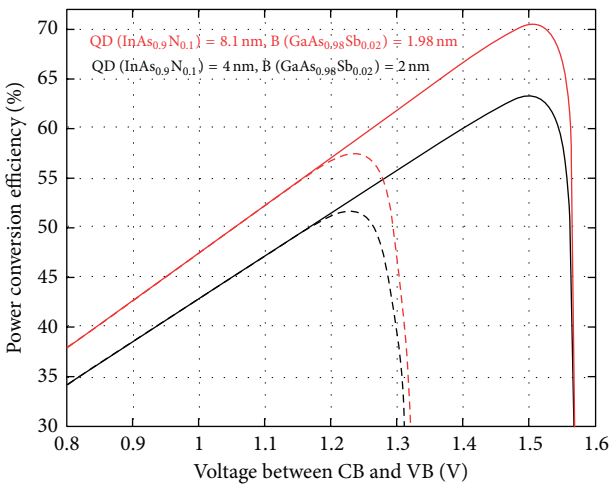


FIGURE 13: Power conversion efficiency for QDIBSC at full concentration (solid) and unconcentrated (dash) cases at specified values of quantum dot and barrier widths that give maximum efficiency.

rather than 63.2% [11, 14, 26, 27], and $\eta_{\max} = 57.5\%$ rather than of 46.8%, respectively, [14]. The numerical results in Table 2 can be utilized also for experimental achievements. In further investigations, the effect of two intermediate bands for different alloys into the power conversion efficiency will be studied.

6. Conclusion

In this work, a theoretical study for the QDIBSC that would contain one intermediate band between the valence and conduction bands was investigated. This intermediate band exploits the low energy photons to enhance the transferring process of charge carriers from valence to conduction bands. Otherwise, it would normally be lost as heat or not

absorbed by the conventional solar cell. As a sequence of utilizing the proposed model, the incoming photons would be well-matched with the energies among bands; thereby the thermalization is reduced. From the obtained results, the open circuit voltage is approximately constant while the short circuit current density is increased. As a result, the fill factor will be enhanced by more than 90%. The power conversion efficiency was calculated under two different ranges of QD width, specified by three different values of barrier width; that is, L_{QD} from 4–7 nm, at L_{B} values 2, 2.5, and 3 nm and L_{QD} from 7–11 nm, at L_{B} values 1.98, 2.34, and 2.7 nm, respectively. The power conversion efficiency is affected by changing the QD and barrier widths. It reaches the maximum value, 63.2%, for full concentration light case in the first range when QD width is 4 nm and barrier width is 2 nm, which agrees with previous studies. The new facts that have not been addressed before are (a) for the second range, power conversion efficiency reaches 70.4% when QD width is 8.1 nm and the barrier width is 1.98 nm in the case of full concentration and (b) the maximum efficiency for unconcentrated light case is 51.5% at the first range and 57.5% for another range. One can recognize from the obtained results an enhancement for efficiency in each of the unconcentrated cases into two ranges and the case of full concentration in the second range. These results of efficiencies create more motivation for further research in this type of structure; therefore future work will concentrate on two intermediate bands: QD solar cell and other alloys with different compositions.

Conflict of Interests

The authors declare that there is no conflict of interests regarding the publication of this paper.

References

- [1] W. Shockley and H. J. Queisser, "Detailed balance limit of efficiency of p - n junction solar cells," *Journal of Applied Physics*, vol. 32, no. 3, pp. 510–519, 1961.
- [2] A. Martí, E. Antolín, E. Cánovas, N. López, and A. Luque, "Progress in quantum-dot intermediate band solar cell research," in *Proceedings of the 21st European Photovoltaic Solar Energy Conference*, Dresden, Germany, 2006.
- [3] A. Nasr and A. Aly, "Theoretical investigation of some parameters into the behavior of quantum dot solar cells," under publication.
- [4] A. Nasr, "Theoretical study of the photocurrent performance into quantum dot solar cells," *Optics & Laser Technology*, vol. 48, pp. 135–140, 2013.
- [5] A. Luque and A. Martí, "Increasing the efficiency of ideal solar cells by photon induced transitions at intermediate levels," *Physical Review Letters*, vol. 78, no. 26, pp. 5014–5017, 1997.
- [6] A. Luque, P. G. Linares, E. Antolín et al., "Understanding the operation of quantum dot intermediate band solar cells," *Journal of Applied Physics*, vol. 111, Article ID 044502, 2012.
- [7] P. G. Linares, C. D. Farmerb, E. Antolína et al., " $\text{In}_x(\text{Ga}_y\text{Al}_{1-y})_{1-x}$ As quaternary alloys for quantum dot intermediate band solar cells," *Energy Procedia*, vol. 2, no. 1, pp. 133–141, 2009.

- [8] C. - Lin, W.-L. Liu, and C.-Y. Shih, "Detailed balance model for intermediate band solar cells with photon conservation," in *Proceedings of the 37th IEEE Photovoltaic Specialists Conference (PVSC '11)*, 2011.
- [9] L. Cuadra, A. Martí, and A. Luque, "Present status of intermediate band solar cell research," *Thin Solid Films*, vol. 451-452, pp. 593-599, 2004.
- [10] M. Y. Levy, C. Honsberg, A. Marti, and A. Luque, "Quantum dot intermediate band solar cell material systems with negligible valence band offsets," in *Proceedings of the 31st IEEE Photovoltaic Specialists Conference*, pp. 90-93, January 2005.
- [11] Q. Deng, X. Wang, C. Yang et al., "Theoretical study on $\text{In}_x\text{Ga}_{1-x}\text{N}/\text{GaN}$ quantum dots solar cell," *Physica B: Condensed Matter*, vol. 406, no. 1, pp. 73-76, 2011.
- [12] O. L. Lazarenkova and A. A. Balandin, "Miniband formation in a quantum dot crystal," *Journal of Applied Physics*, vol. 89, no. 10, pp. 5509-5515, 2001.
- [13] Q. Shao, A. A. Balandin, A. I. Fedoseyev, and M. Turowski, "Intermediate-band solar cells based on quantum dot supercrystals," *Applied Physics Letters*, vol. 91, no. 16, Article ID 163503, 2007.
- [14] E. J. Steven, *Quantum dot intermediate band solar cells: design criteria and optimal materials [Ph.D. thesis]*, Drexel University, Philadelphia, Pa, USA, 2012.
- [15] T. Soga, *Nanostructured Materials for Solar Energy Conversion*, 1st edition, 2006.
- [16] S. Birner, *Modeling of Semiconductor Nanostructures and Semiconductor-Electrolyte Interfaces*, 2011.
- [17] S. P. Day, H. Zhou, and D. L. Pulfrey, "The Kronig-Penney approximation: may it live on," *IEEE Transactions on Education*, vol. 33, no. 4, pp. 355-358, 1990.
- [18] R. Aguinaldo, *Modeling solutions and simulations for advanced III-V photovoltaics based on nanostructures [M.S. thesis in materials science & engineering]*, College of Science, Rochester Institute of Technology, Rochester, NY, USA, 2008.
- [19] W. van Roosbroeck and W. Shockley, "Photon-radiative recombination of electrons and holes in germanium," *Physical Review*, vol. 94, no. 6, pp. 1558-1560, 1954.
- [20] A. Martí, L. Cuadra, and A. Luque, "Quasi-drift diffusion model for the quantum dot intermediate band solar cell," *IEEE Transactions on Electron Devices*, vol. 49, no. 9, pp. 1632-1639, 2002.
- [21] L. A. Kosyachenko, *Solar Cells—New Aspects and Solutions*, 2011.
- [22] S. P. Bremner and C. B. Honsberg, "Intermediate band solar cell with non-ideal band structure under AM1.5 spectrum," in *Proceedings of the 38th IEEE Photovoltaic Specialists Conference (PVSC '12)*, 2012.
- [23] A. Martí, L. Cuadra, and A. Luque, "Partial filling of a quantum dot intermediate band for solar cells," *IEEE Transactions on Electron Devices*, vol. 48, no. 10, pp. 2394-2399, 2001.
- [24] J. Ojajarvi, *Tetrahedral chalcopyrite quantum dots in solar-cell applications [M.S. thesis]*, Department of Physics, University of Jyväskylä, 2010.
- [25] A. Luque, A. Martí, and L. Cuadra, "Impact-ionization-assisted intermediate band solar cell," *IEEE Transactions on Electron Devices*, vol. 50, no. 2, pp. 447-454, 2003.
- [26] Q.-W. Deng, X.-L. Wang, C.-B. Yang et al., "Computational investigation of $\text{In}_x\text{Ga}_{1-x}\text{N}/\text{InN}$ quantum-dot intermediate-band solar cell," *Chinese Physics Letters*, vol. 28, no. 1, Article ID 018401, 2011.
- [27] A. Nasr, "Theoretical model for observation of the conversion efficiency into quantumdot solar cells," under publication.

Research Article

Steric and Solvent Effect in Dye-Sensitized Solar Cells Utilizing Phenothiazine-Based Dyes

Hany Kafafy,^{1,2} Hongwei Wu,¹ Ming Peng,¹ Hsienwei Hu,¹ Kai Yan,¹
Reda M. El-Shishtawy,³ and Dechun Zou¹

¹ Beijing National Laboratory for Molecular Sciences, Key Laboratory of Polymer Chemistry and Physics of Ministry of Education, College of Chemistry and Molecular Engineering, Peking University, Beijing 100871, China

² Dyeing, Printing and Textile Auxiliaries Department, Textile Research Division, National Research Center, Dokki, Cairo 12622, Egypt

³ Chemistry Department, Faculty of Science, King Abdulaziz University, P.O. Box 80203, Jeddah 21589, Saudi Arabia

Correspondence should be addressed to Dechun Zou; dczou@pku.edu.cn

Received 11 December 2013; Accepted 14 February 2014; Published 17 March 2014

Academic Editor: Chuanyi Wang

Copyright © 2014 Hany Kafafy et al. This is an open access article distributed under the Creative Commons Attribution License, which permits unrestricted use, distribution, and reproduction in any medium, provided the original work is properly cited.

Three phenothiazine-based dyes have been prepared and utilized as dye-sensitized solar cells (DSSCs). The effects of dye-adsorption solvent on the performances of dye-sensitized solar cells based on phenothiazine dyes were investigated in this study. The highest conversion efficiency of 3.78% was obtained using ethanol (EtOH) and 2.53% for tetrahydrofuran (THF), respectively, as dye-adsorption solvents. Cell performance using EtOH as a dye-adsorption solvent showed relatively higher performance than that using THF. Electrochemical and photochemical tests of phenothiazine dyes in solution and adsorbed on the TiO₂ surface showed less dye loading and coverage on the TiO₂ surface during adsorption in the case of THF, which decreased the solar cell performance of the DSSC using THF as adsorption solvent compared with using EtOH as adsorption solvent. Meanwhile, the steric effect of phenothiazine-based (PT1–3) dyes was also investigated. Dye with longer and branched aliphatic chain in the order of PT1, PT2, and PT3 showed an increased resistance of the recombination reaction and electron lifetime, thereby increasing V_{oc} and enhancing the overall cell performance because of the sterically hindered conformation of the phenothiazines.

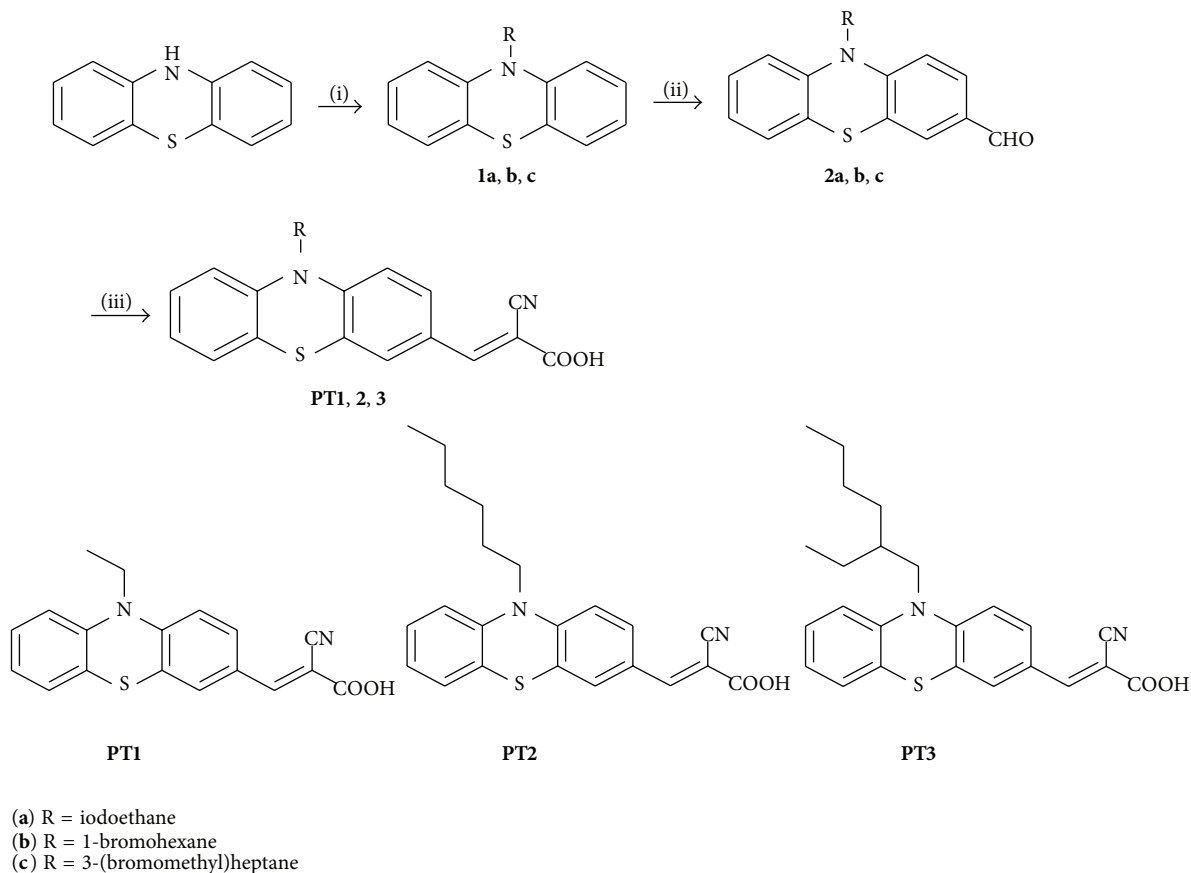
1. Introduction

The increasing consumption of fossil and the more serious crisis of environment pollution have led us to the search for new and renewable energy sources. Solar energy is widely recognized as the most promising candidate in helping solve this problem. Dye-sensitized solar cells (DSSCs), also known as Grätzel cells, offer a viable alternative to conventional all-inorganic solar cells because of their lower production cost. During the past decades, DSSCs have attracted significant attention as an alternative to silicon solar cell because they use environmentally benign materials through low cost process and exhibit commercially realistic energy-conversion efficiency [1–3]. The photon-to-current conversion of DSSCs is achieved by ultrafast electron injection from a photoexcited dye into the conduction band of the TiO₂, followed by dye regeneration and hole transportation to

the counter electrode. To enhance the performance of the DSSC, extensive research has been performed on semiconductor nanocrystalline TiO₂ electrodes [4–6], dye molecule [7–10], electrolytes [11–14], and counter electrodes [15].

Compared with the rare and expensive metal complexes, organic dyes have the advantages of being eco-friendly, having flexible and diverse form of molecular structures, lower cost, generally high molar extinction coefficients, and easier preparation and purification. Metal-free organic dyes have been widely investigated recently, many of which exhibited an energy-to-electricity conversion efficiency close to that of N719 [16–21].

The design of organic dyes for DSSCs is important to improve the value of the short-circuit current (J_{sc}) and the open-current voltage (V_{oc}). The π -conjugation of the J_{sc} must be improved so the organic chromophore can harvest light energy to a large extent. An effort of reducing the rate of



SCHEME 1: Synthesis route of phenothiazine (PT). Dyes: (i) KOC (CH₃)₃, THF, 66°C, 18 h; (ii) DMF, CHCl₃, 0°C, phosphorus oxychloride, reflux overnight; (iii) cyanoacetic acid, NH₄OAc, AcOH, 90–100°C.

charge recombination is necessary for the V_{oc} to minimize current leakage.

Whether the low voltages from organic dyes may be due to fast recombination kinetics is still being debated [22, 23]. A strong interaction between organic dye and iodine in the electrolyte has been proposed to be responsible for accelerating recombination [24, 25]. Also, the lack of electron donating moiety in the oxidized organic dye has also been proposed to have an influence on fast recombination reaction, compared with N719 with electron donating NCS ligand [26]. In addition, dye aggregation due to planar or sterically less-hindered structure has also been proposed as one of major factors for the lowering voltage [27, 28]. Thus, a molecular structure of organic dye must be designed to reduce recombination and/or prevent dye aggregation. Recently, heterocyclic phenothiazine (PT), originally used in drug applications [29, 30], has been adopted as a novel electron donor in organic dye because PT contains electron-rich sulfur-nitrogen heteroatoms and its ring has sterically hindered nonplanar butterfly conformation. In addition, the incorporation of PT derivatives in organic dye backbone is expected to inhibit molecular aggregation.

Most studies have focused on enhancing the properties of the photoelectrode, specifically the dye, which is responsible for most light absorption. Some of the important properties that need to be considered when designing sensitizers for

DSSCs are the geometric structures, molecular orbital energy, absorption profiles, and aggregation states of the dye [31, 32].

In this study, the effect of THF and EtOH on the absorption and solar cell performance was studied and evaluated. The synthesis and application of three dyes composed of N-substituted phenothiazine units (PT1–3) shown in Scheme 1 as sensitizers in dye-sensitized solar cells have been investigated. A cyanoacrylate group was attached to one side of the compound, acting as an electron acceptor. We envisioned that the nonplanar conformation of phenothiazine can reduce the rate of charge recombination and molecular aggregation. The synthetic procedures of PT1–3 are described in Scheme 1. All structures have been confirmed by their NMR, MS, and spectroscopic data. The photovoltaic performance and electrochemical properties of devices based on the three dyes using THF and EtOH solvents were evaluated by different spectroscopic techniques.

2. Experimental Section

2.1. Materials and Synthesis

2.1.1. *General Considerations.* Reagents, catalysts, ligands, and solvents were purchased reagent grade and used without further purification. The details of the synthetic procedure

of the **PTI-3** dyes were prepared according to the literature procedures, as shown in Scheme 1 [33–35]. N-alkylation of phenothiazine followed by Vilsmeier-Haack formylation and then Knoevenagel condensation between the carbaldehyde and cyanoacetic acid in the presence of ammonium acetate affords the desired dyes. Column chromatography was made using silica gel 60, mesh 70–230. TLC silica gel plates, 60 F₂₅₄, were also used. Lithium perchlorate (LiClO₄, 99%) and 4-tert-butylpyridine (TBP) were obtained from Sigma-Aldrich. Acetonitrile (AN) solvent as purchased from Siyou Inc., Tianjin, China. The substance I₂ (AR) was acquired from the Beijing Chemical Reagent Company. FTO glasses and TiO₂ paste (DSL-18NR-T), with diameter of 20 nm, and the electrolyte components were obtained from Heptachroma Inc., Dalian, China.

2.2. Characterization and Measurement. UV-Vis absorbance spectra were recorded on a lambda 35 UV/Vis Spectrometer (Perkin Elmer). All dyes were dissolved in THF and EtOH solution as bath solvent, and the concentrations of solutions used in the absorption experiment were set as 5×10^{-5} M. ¹H NMR and ¹³C NMR spectra were measured at room temperature on a 400 MHz (Bruker) spectrometers, respectively, using DMSO-d₆ or CDCl₃ as the solvents. The electrospray ionization mass spectra (ESI-MS) were characterized on an APEX IV Fourier transform ion cyclotron resonance mass spectrometer (Bruker).

2.3. Fabrication of DSSCs. The TiO₂ paste (DSL-18NR-T, diameter: 20 nm) was created on FTO glasses by screen printing. The obtained FTO glasses were sintered at 150°C for 15 min in a muffle furnace and then at 450°C for 30 min sequentially. The thickness of the TiO₂ film is approximately 3.5 μm after one screen printing. Through reciprocating the above steps three times, the TiO₂ film can reach up to 10.5 μm thick. After the last heated process, the TiO₂ electrodes were cooled to 100°C and then immersed into dye bath solution. After 24 h, the sensitized TiO₂ photoanodes were taken out from the dye solution, eluted by methanol to remove the excess dye from the TiO₂ surface, and were kept in vacuum drying oven at room temperature overnight. The counter electrode with a Pt film (thickness: approximate 50 nm) on the FTO glasses was prepared by magnetic sputtering. The obtained dye-adsorbed photoanodes (test area: ca. 0.25 cm²) and the Pt counter cathodes were assembled to form DSSCs and isolated by 25 μm thick hot-melt ionomer film (Surlyn, Dupont). The electrolytes were then injected into solar cells by preset pores in the counter electrode. Finally, the devices were sealed by Surlyn film to enhance the stability of the DSSCs.

2.4. Dye Bath Solutions. In this study, EtOH and THF bath solutions of **PTI-3** dyes (5×10^{-4} M) were prepared. The devices were soaked in EtOH and THF solution sensitizers for 24 h, respectively.

2.5. Measurement of Absorption Spectra in TiO₂. The TiO₂ paste was made on FTO glasses by screen printing.

The obtained FTO glasses were sintered at 150°C for 15 min in a muffle furnace and then at 450°C for 30 min sequentially. The thickness of the TiO₂ film was approximately 3.5 μm after one screen printing. The TiO₂ films were cooled to 100°C, and then immersed into different dye bath solutions. After 24 h, the sensitized TiO₂ photoanodes were taken out from the dye solution and eluted by methanol to remove the excess dye from the TiO₂ surface. The sensitized TiO₂ photoanodes were then immersed in 0.1 M solution of (CH₃)₄NOH base in ethanol overnight to extract the dye from the TiO₂ film. The film area was 0.64 cm² and thickness 10.5 μm and it was extracted in 9 mL of the (CH₃)₄NOH base in ethanol solution. The absorption spectra of the dyes in the extraction solution were then obtained.

2.6. Components of Electrolytes. The electrolyte used was iodide liquid electrolyte that was composed of acetonitrile solution of 0.03 M iodine, 0.6 M 1-butyl-3-methylimidazolium iodide (BMII), 0.05 M lithium perchlorate (LiClO₄), and 0.5 M 4-tert-butylpyridine (TBP).

2.7. Characterization of the Photoelectrochemical and Photovoltaic Properties. The photovoltaic performance of the devices was measured under AM 1.5 simulated sunlight illumination with a light intensity of 100 mW/cm². The simulated sunlight source was YSS-50A (Yamashita DESO). The electrochemical impedance spectra (EIS) were implemented on the Autolab (Frequency range: 100 kHz to 10 mHz). Two parameters, namely, chemical capacitance (C_m) and charge recombination resistance (R_{rec}), were obtained by fitting the EIS at different reverse biases with Z-View software according to the transmitting line mode. The incident photon-to-current efficiency (IPCE) was measured from 300 nm to 800 nm under SolarCellScan-100 (Beijing ZOLIX Corp.).

3. Results and Discussion

3.1. Synthesis. **PTI-3** dyes were prepared according to the literature procedures [33–37]. The sequence of reaction steps proceeds smoothly and efficiently to give a good yield of the product. Thus, N-alkylation of phenothiazine with different alkyl groups afforded the corresponding compounds **1a–c**, which upon Vilsmeier-Haack formylation gave the carbaldehyde **2a–c**. Knoevenagel condensation between **2a–c** and cyanoacetic acid in the presence of ammonium acetate produced the desired phenothiazine dyes **PTI-3**. All chemical structures were characterized by their spectroscopic data.

3.2. Absorption Spectra. The UV-Vis absorption spectra of all dyes in the EtOH and THF solutions are shown in Figure 1. Table 1 shows all the parameters; all the dyes exhibited broad absorption in the range of 250–350 nm and 370–525 nm. The short wavelength region at 280–340 nm is attributed to the localized π - π^* and n - π^* transitions, whereas the long wavelength region in the range of 390–510 nm is attributed to the charge transfer transitional energy of the delocalized π - π^* transition as a result of donor- π -acceptor system. Compared with THF, the absorption bands of all dyes are relatively

TABLE 1: Absorption properties of **PT1-3** dyes in the EtOH and THF solutions.

| Dye | EtOH | | THF | |
|-----|---|-----------------------------|---|-----------------------------|
| | ϵ ($M^{-1} \text{ cm}^{-1}$) | λ_{max} (nm) | ϵ ($M^{-1} \text{ cm}^{-1}$) | λ_{max} (nm) |
| 1 | 9993 | 436 | 12027 | 447 |
| 2 | 10090 | 428 | 12719 | 447 |
| 3 | 10082 | 414 | 11014 | 436 |

TABLE 2: Photovoltaic performances of **PT1-3** dyes in different adsorption solutions.

| Device | V_{oc} (V) | J_{sc} (mA/cm^2) | FF | PCE |
|--------|---------------------|---|-------|-------|
| E1 | 691 | 6.08 | 0.693 | 2.91% |
| E2 | 726 | 6.29 | 0.697 | 3.18% |
| E3 | 779 | 6.66 | 0.730 | 3.78% |
| T1 | 644 | 4.08 | 0.698 | 1.83% |
| T2 | 676 | 4.62 | 0.680 | 2.12% |
| T3 | 726 | 4.83 | 0.720 | 2.53% |

E: EtOH; T: THF solutions. Photovoltaic performance was measured under AM 1.5 simulated sunlight illuminations with the light intensity $100 \text{ mW}/\text{cm}^2$. Soaking time was 24 h. Electrolyte: mixture of 0.03 M iodine, 0.6 M (BMII), 0.05 M (LiClO_4), and 0.5 M (TBP) dissolved in AN.

blue-shifted using EtOH. This behavior would be attributed to the solvent effect. As **PT1-3** dyes are donor- π -acceptor system, charge transfer absorption band is destabilized in protic solvent such as ethanol due to hydrogen bonding interactions between ethanol and the donor and/or acceptor moieties [38, 39]. On the other hand, THF is aprotic solvent and less polar than EtOH; such effect does not exist and thus transfer absorption band is more favorable in this solvent than EtOH.

3.3. Photovoltaic Performance. Figure 2 shows the photocurrent-voltage curves and IPCE spectra for the **PT1-3** sensitized DSSCs in the EtOH and THF adsorption solvent. The corresponding photovoltaic parameters are listed in Table 2. The device performance of **PT1-3** dyes indicates that the devices using EtOH show a higher J_{sc} and a significantly higher V_{oc} than those obtained using THF, with a higher light conversion efficiency of **PT3** dye compared with those of **PT2** and **PT1**. The reasons for this inferior performance for the dyes using THF solution as mentioned before would be attributed to the smaller amount of adsorbed dye in the TiO_2 semiconductor due to the propensity of dye molecules to exist more in THF solvent rather than to get adsorbed and also due to the hydrogen bond interaction of the oxygen of the tetrahydrofuran and the hydrogen of the carboxylic acid of the dyes [40, 41]. Meanwhile, it was also noted that dyes with more branched alkyl groups show higher V_{oc} and J_{sc} in both EtOH and THF dye-bath solvent. We will discuss these afterwards.

The incident photon-to-current efficiency (IPCE) spectra as a function of the wavelength for DSSCs based on the **PT1-3** dyes in THF and EtOH is shown in Figure 4(c). The IPCE values of DSSCs based on **PT1-3** dyes when using EtOH exceeded 80% from 425 nm to 500 nm (with the highest value

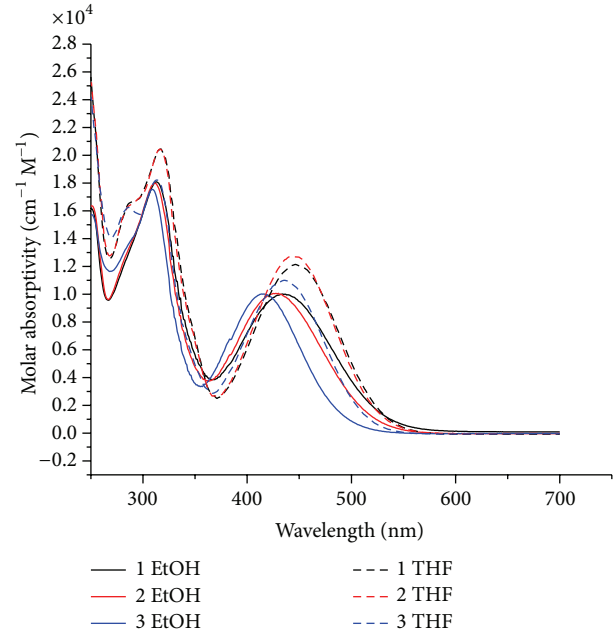


FIGURE 1: Absorption spectra of $5 \times 10^{-5} \text{ M}$ solutions of **PT1-3** dyes in EtOH and THF, respectively.

of 80.5% at 460 nm for **PT3** sensitized), whereas using THF only exceeded 50% from 425 nm to 475 nm (with the highest value of 55% at 430 nm **PT3** sensitized). The higher IPCE for **PT1**-, **2**-, and **3**-sensitized solar cells using EtOH can be ascribed to the larger adsorbed amount of **PT1-3** dyes compared with those obtained using THF, which is consistent with the obtained photovoltaic data for the **PT1-3** sensitizers under the same conditions, wherein the J_{sc} for the devices that use EtOH are much higher than those obtained using THF as dye-adsorption solvent.

The absorption spectra of all dyes extracted from the surface of TiO_2 film are shown in Figure 3. The absorption band displayed a blue shift of ca. 1–38 nm with respect to those in the solutions. The blue shift appeared to be a result of deprotonation of the carboxylic acid when anchored onto the titanium oxide surface. Similar to the case of ethanol effect on the absorption compared with THF, it is anticipated that deprotonation of the carboxylic group would lower its acceptability for electrons and thus would lead to the observed blue shift upon anchoring with TiO_2 . Additionally, a possible formation of H-aggregation for these dyes in the surface of TiO_2 would also lead to the observed blue shift [42].

3.4. Effect of the Adsorption Solvent on DSSC Performance. The adsorption solvent has an indispensable role in the efficiency of solar cells that influences the dye loading on the TiO_2 surface and also has an important role in the formation of dye solvent- TiO_2 complex [43]. The cell performances of the **PT1**, **2**, and **3** dyes using EtOH and THF as dye-adsorption solvents are listed in Table 2. All the photovoltaic parameters, such as the J_{sc} , V_{oc} , and FF, were affected by the adsorption solvent. THF provides lower photovoltaic values

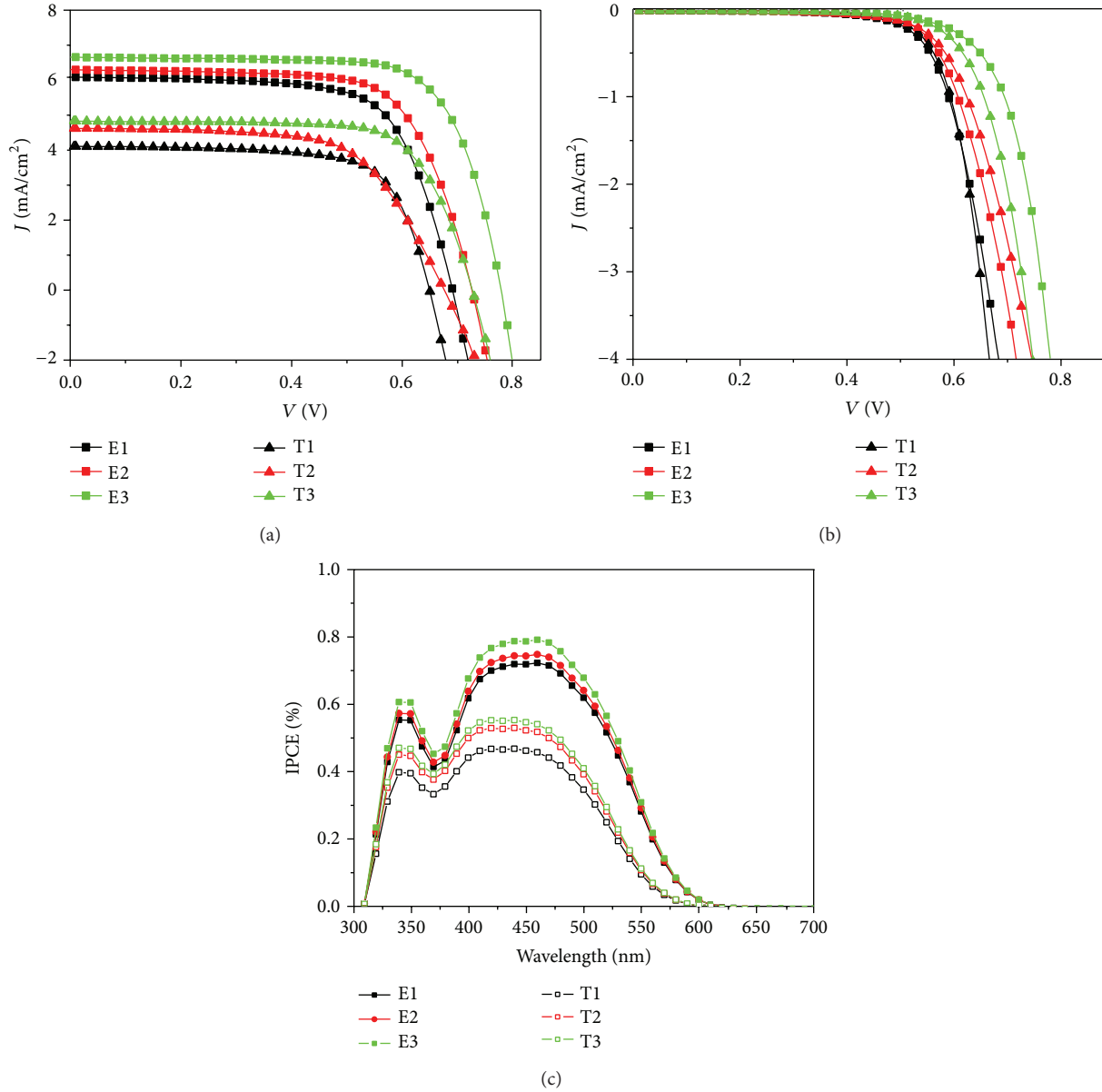


FIGURE 2: J - V plots under (a) simulated standard sunlight and (b) dark condition; (c) IPCE of devices E1-3 and T1-3.

compared with the EtOH measured under AM 1.5 simulated sunlight illuminations with the light intensity 100 mW/cm² conditions.

The use of THF as adsorption solvent decreases the photovoltaic efficiencies with respect to EtOH, which can be ascribed to the less dye loading from THF solution on the TiO₂ surface relative to EtOH, as shown in Figure 3. The use of THF as adsorption solvent decreases the photovoltaic efficiencies compared with EtOH case, which could be ascribed to the less dye loading from THF solution on the TiO₂ surface as shown in Figure 3. Compared with THF, EtOH seems favorable medium for dye loading onto TiO₂ owing to its high polarity that would facilitate better dye adsorption onto TiO₂ surface. The dye loading for PT1-3 in EtOH and THF is 439 nmol/cm² (PT1-EtOH), 432 nmol/cm²

(PT2-EtOH), 337 nmol/cm² (PT3-EtOH), 288 nmol/cm² (PT1-THF), 266 nmol/cm² (PT2-THF), and 205 nmol/cm² (PT3-THF), respectively. Meanwhile, the conversion efficiency strongly depended on the dielectric constant of the dye-adsorption solvent. The amount of dye adsorption increased as the dielectric constant of the dye-adsorption solvent increased [44]. The higher conversion efficiency obtained when EtOH was used as dye-adsorption solvent can also be attributed to the higher dielectric constant for ethanol ($k = 24.5$) compared with THF ($k = 7.8$). Table 2 shows that the J_{sc} of the device using EtOH as dye-adsorption solvent are drastically higher than those using THF as dye-adsorption solvent. Thus, a higher IPCE value of DSSCs based on PT1-3 dyes was obtained using EtOH, which exceeded 80% from 425 nm to 500 nm, compared with using THF,

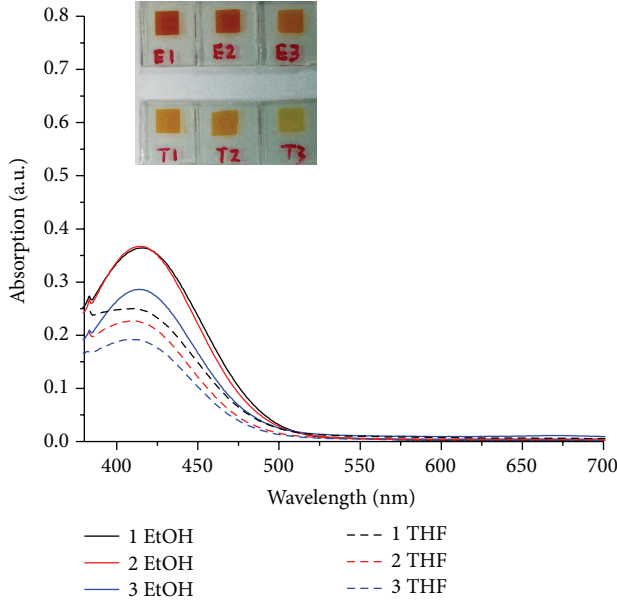


FIGURE 3: UV-vis absorption spectra of **PT1-3** dyes extracted from the surface of TiO_2 film in EtOH and THF.

which only exceeded 50% from 425 nm to 475 nm, as shown in Figure 2(c).

Meanwhile, the dye loading in case of **PT3** was relatively less than **PT1** and **PT2** in both cases of THF and EtOH solution but the J_{sc} values and the overall conversion efficiency were comparatively higher for **PT3** more than **PT1** and **PT2** in both dye-bath solvents EtOH and THF, indicating that the steric hinder effect of **PT3** dye with the branched aliphatic chain has the ability of decreasing the dye aggregation on the TiO_2 film as well as decreasing the electron recombination reaction rate at the interfaces between TiO_2 /dye and the electrolyte species, hence increasing the performance of the device.

To further elucidate the lower performance of the DSSC sensitized by **PT1-3** that uses THF, the electron lifetime and EIS were implemented on the Autolab (Frequency range: 100 kHz to 10 mHz). Two parameters, namely, chemical capacitance (C_m) and charge recombination resistance (R_{rec}), were obtained by fitting the EIS at different reverse biases with Z-View software, according to the transmitting line mode. Figures 4(a) and 4(b) show the Nyquist plot and recombination resistance, where the applied voltage is 0.65 V under dark condition for the **PT1-3** sensitizers using EtOH and THF as dye-adsorption solvents. In the Nyquist plots, a major semicircle was observed for all dyes, which is related to the electron recombination transport process at the interfaces between TiO_2 and the electrolyte/dye [45]. The data listed in Table 3 is related to the electron lifetime (τ), the electrochemical capacity (C), and the electron recombination (R_{rec}); for example, a smaller R_{rec} indicates faster electron recombination and hence a larger dark current as shown in Figure 2(b).

The recombination resistance (R_{rec}) decreased in the order of **PT3** ($154.4 \Omega \cdot \text{cm}^2$) > **PT2** ($35.68 \Omega \cdot \text{cm}^2$) > **PT1**

TABLE 3: Recombination resistance, electron life time, and the electrochemical capacity for the **PT1-3**-sensitizers using EtOH and THF as dye-adsorption solvents.

| Device | R_{rec} ($\Omega \cdot \text{cm}^2$) | C (F/cm^2) | T (ms) |
|--------|--|--------------------------------|----------|
| E1 | 18.23 | 0.001638 | 29.86 |
| E2 | 35.68 | 0.001572 | 56.09 |
| E3 | 154.4 | 0.001442 | 222.64 |
| T1 | 6.606 | 0.001582 | 10.45 |
| T2 | 13.63 | 0.001529 | 20.84 |
| T3 | 57.26 | 0.001476 | 84.52 |

($18.23 \Omega \cdot \text{cm}^2$) in EtOH, consistent with the values of the V_{oc} that significantly increased using EtOH **PT3** (779 mV), **PT2** (726 mV), and **PT1** (691 mV), much more than that using THF **PT3** (726 mV), **PT2** (676 mV), and **PT1** (644 mV) as dye-adsorption solvent, and that could be ascribed to the bent and the sterically hindered conformation of phenothiazine with a branched and long aliphatic chain for **PT3** > **PT2** > **PT1**; the longer and branched aliphatic chain can prevent the direct contact between the electrolyte and the TiO_2 surface as well as inhibits or reduces dye aggregation. This behavior was clearly observed in case of using EtOH as the dye-adsorption solvent because of the higher dye loading and coverage on the TiO_2 surface and can thus reduce the charge recombination reaction rate.

Figure 4(c) shows the electron lifetime for all devices. A larger value of V_{oc} corresponds to the significantly longer electron lifetime for all sensitizers in EtOH $\tau = 222.64$ ms, 56.09 ms, and 29.86 ms for **PT3**, **PT2**, and **PT1**, respectively, whereas, that of THF, V_{oc} was comparatively lower than EtOH because of the comparatively lower electron lifetime $\tau = 8452$ ms, 20.84 ms, and 10.45 ms for **PT3**, **PT2**, and **PT1**, respectively, which can be attributed as mentioned above to the sterically hindered conformation of phenothiazine with a branched and long aliphatic chain of phenothiazine on one hand and on the other hand because of the higher dye loading when using EtOH more than that when using THF as dye-adsorption solvent.

4. Conclusion

Three phenothiazine-based sensitizers, namely, **PT1**, **PT2**, and **PT3**, were synthesized, and the photovoltaic performances of the three dyes were tested in EtOH and THF solution as dye-adsorption solvents, and it was found that the three sensitizers were influenced by the dye-adsorption solvent condition. The highest conversion efficiency 3.78% was obtained in the case of using EtOH as dye-bath solvent. The conversion efficiency of the DSSC was found to strongly depend not only on the kind of solvent but also on the steric hindered effect of the dye structure. The DSSCs that used dye with higher steric hindered effect showed higher J_{sc} value and higher overall conversion efficiency than the DSSCs that used dye with lower steric hindered effect.

The device that used THF as a dye-bath solvent showed lower J_{sc} value and lower conversion efficiency than

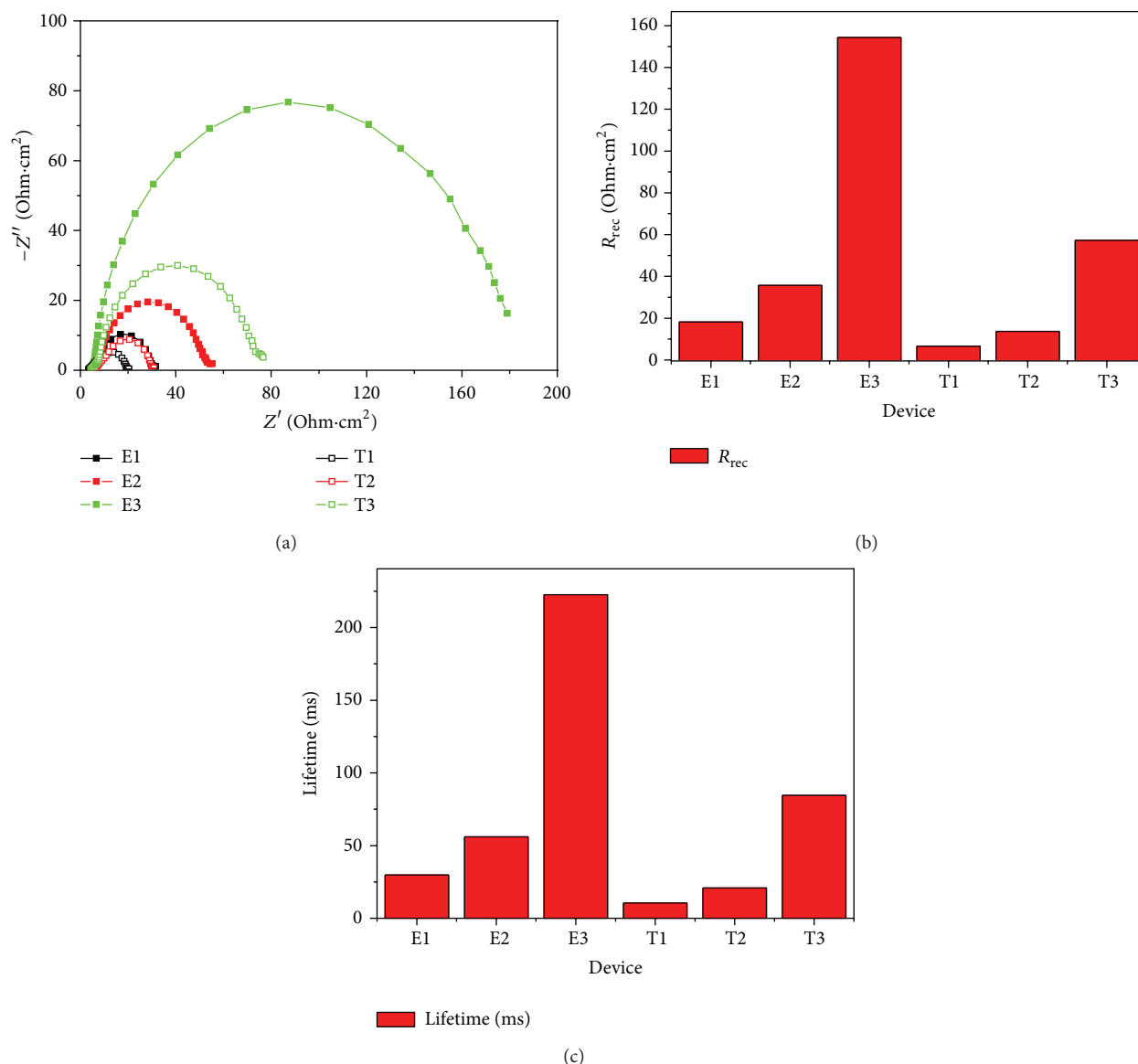


FIGURE 4: (a) Electrochemical impedance spectra (Nyquist plots) applied voltage is 0.65 V under dark condition, (b) recombination resistance (R_{rec}), and (c) lifetime for the DSSCs using EtOH and THF as a dye bath solvent, respectively.

the device that used EtOH, due to increase in the dye aggregates at the TiO_2 surface during the adsorption process in case of using THF and consequence lowering the overall cell performance which is attributed mainly to less dye loading on the TiO_2 surface in case of THF, the lower dielectric constant for the THF, the hydrogen bond interaction of the oxygen of the tetrahydrofuran, and the hydrogen of the carboxylic acid moiety of the dye.

This study revealed that designing of phenothiazine dyes with longer and branched aliphatic chain increases the steric hindered effect which was mainly responsible for increasing the electron lifetime and decreases the dye aggregation as well as increasing the electron recombination resistance rate at the TiO_2 -dye-electrolyte interface, hence, enhancing the overall cell performance. Moreover the dye-bath solvent has a

significant role for the overall cell performance and choosing a compatible dye-adsorption solvent leads to enhancement of the performance of DSSCs.

Conflict of Interests

The authors declare that there is no conflict of interests regarding the publication of this paper.

Acknowledgments

This work is jointly supported by the Ministry of Science and Technology (no. 2011CB933300), the Ministry of Education of China (no. 20120001140010), the National Natural Science

Foundation of China (no. 91333107), and the fund from Beijing (no. Z121100001312009).

References

- [1] M. Grätzel, "Conversion of sunlight to electric power by nanocrystalline dye-sensitized solar cells," *Journal of Photochemistry and Photobiology A*, vol. 164, no. 1–3, pp. 3–14, 2004.
- [2] B. O'Regan and M. Grätzel, "A low-cost, high-efficiency solar cell based on dye-sensitized colloidal TiO₂ films," *Nature*, vol. 353, no. 6346, pp. 737–740, 1991.
- [3] S. Kambe, K. Murakoshi, T. Kitamura et al., "Mesoporous electrodes having tight agglomeration of single-phase anatase TiO₂ nanocrystallites: application to dye-sensitized solar cells," *Solar Energy Materials and Solar Cells*, vol. 61, no. 4, pp. 427–441, 2000.
- [4] A. Kay and M. Grätzel, "Dye-sensitized core-shell nanocrystals: improved efficiency of mesoporous tin oxide electrodes coated with a thin layer of an insulating oxide," *Chemistry of Materials*, vol. 14, no. 7, pp. 2930–2935, 2002.
- [5] Z.-S. Wang, C.-H. Huang, Y.-Y. Huang et al., "A highly efficient solar cell made from a dye-modified ZnO-covered TiO₂ nanoporous electrode," *Chemistry of Materials*, vol. 13, no. 2, pp. 678–682, 2001.
- [6] Z.-S. Wang, H. Kawauchi, T. Kashima, and H. Arakawa, "Significant influence of TiO₂ photoelectrode morphology on the energy conversion efficiency of N719 dye-sensitized solar cell," *Coordination Chemistry Reviews*, vol. 248, no. 13–14, pp. 1381–1389, 2004.
- [7] M. K. Nazeeruddin, P. Péchy, T. Renouard et al., "Engineering of efficient panchromatic sensitizers for nanocrystalline TiO₂-based solar cells," *Journal of the American Chemical Society*, vol. 123, no. 8, pp. 1613–1624, 2001.
- [8] T. Renouard, R.-A. Fallahpour, M. K. Nazeeruddin et al., "Novel ruthenium sensitizers containing functionalized hybrid tetradentate ligands: synthesis, characterization, and INDO/S analysis," *Inorganic Chemistry*, vol. 41, no. 2, pp. 367–378, 2002.
- [9] S. M. Zakeeruddin, M. K. Nazeeruddin, P. Pechy et al., "Molecular engineering of photosensitizers for nanocrystalline solar cells: synthesis and characterization of Ru dyes based on phosphonated terpyridines," *Inorganic Chemistry*, vol. 36, no. 25, pp. 5937–5946, 1997.
- [10] A. Islam, H. Sugihara, M. Yanagida et al., "Efficient panchromatic sensitization of nanocrystalline TiO₂ films by β -diketonato ruthenium polypyridyl complexes," *New Journal of Chemistry*, vol. 26, no. 8, pp. 966–968, 2002.
- [11] Y. Saito, W. Kubo, T. Kitamura, Y. Wada, and S. Yanagida, "I⁻/I₃⁻ redox reaction behavior on poly(3,4-ethylenedioxythiophene) counter electrode in dye-sensitized solar cells," *Journal of Photochemistry and Photobiology A: Chemistry*, vol. 164, no. 1–3, pp. 153–157, 2004.
- [12] Z. Kebede and S.-E. Lindquist, "Donor-acceptor interaction between non-aqueous solvents and I₂ to generate I₃⁻, and its implication in dye sensitized solar cells," *Solar Energy Materials and Solar Cells*, vol. 57, no. 3, pp. 259–275, 1999.
- [13] K. Hara, T. Horiguchi, T. Kinoshita, K. Sayama, and H. Arakawa, "Influence of electrolytes on the photovoltaic performance of organic dye-sensitized nanocrystalline TiO₂ solar cells," *Solar Energy Materials and Solar Cells*, vol. 70, no. 2, pp. 151–161, 2001.
- [14] F. Cecchet, A. M. Gioacchini, M. Marcaccio et al., "Solvent effects on the oxidative electrochemical behavior of *cis*-bis(isothiocyanato)ruthenium(II)-bis-2,2'-bipyridine-4,4'-dicarb oxylie acid," *Journal of Physical Chemistry B*, vol. 106, no. 15, pp. 3926–3932, 2002.
- [15] E. Olsen, G. Hagen, and S. Eric Lindquist, "Dissolution of platinum in methoxy propionitrile containing LiI/I₂," *Solar Energy Materials and Solar Cells*, vol. 63, no. 3, pp. 267–273, 2000.
- [16] Z.-S. Wang, Y. Cui, K. Hara, Y. Dan-Oh, C. Kasada, and A. Shinpo, "A high-light-harvesting-efficiency coumarin dye for stable dye-sensitized solar cells," *Advanced Materials*, vol. 19, no. 8, pp. 1138–1141, 2007.
- [17] D. Kuang, S. Uchida, R. Humphry-Baker, S. M. Zakeeruddin, and M. Grätzel, "Organic dye-sensitized ionic liquid based solar cells: remarkable enhancement in performance through molecular design of indoline sensitizers," *Angewandte Chemie*, vol. 47, no. 10, pp. 1923–1927, 2008.
- [18] S. Ko, H. Choi, M.-S. Kang et al., "Silole-spaced triarylamine derivatives as highly efficient organic sensitizers in dye-sensitized solar cells (DSSCs)," *Journal of Materials Chemistry*, vol. 20, no. 12, pp. 2391–2399, 2010.
- [19] J. J. Cid, J. H. Yum, S. R. Jang et al., "Molecular cosensitization for efficient panchromatic dye-sensitized solar cells," *Angewandte Chemie*, vol. 46, no. 44, pp. 8358–8362, 2007.
- [20] C.-L. Mai, W.-K. Huang, H.-P. Lu et al., "Synthesis and characterization of diporphyrin sensitizers for dye-sensitized solar cells," *Chemical Communications*, vol. 46, no. 5, pp. 809–811, 2010.
- [21] A. Yella, H.-W. Lee, H. N. Tsao et al., "Porphyrin-sensitized solar cells with cobalt (II/III)-based redox electrolyte exceed 12 percent efficiency," *Science*, vol. 334, no. 6056, pp. 629–634, 2011.
- [22] L. M. Peter, "Dye-sensitized nanocrystalline solar cells," *Physical Chemistry Chemical Physics*, vol. 9, no. 21, pp. 2630–2642, 2007.
- [23] S. E. Koops, P. R. F. Barnes, B. C. O'Regan, and J. R. Durrant, "Kinetic competition in a coumarin dye-sensitized solar cell: injection and recombination limitations upon device performance," *Journal of Physical Chemistry C*, vol. 114, no. 17, pp. 8054–8061, 2010.
- [24] B. C. O'Regan, I. López-Duarte, M. V. Martínez-Díaz et al., "Catalysis of recombination and its limitation on open circuit voltage for dye sensitized photovoltaic cells using phthalocyanine dyes," *Journal of the American Chemical Society*, vol. 130, no. 10, pp. 2906–2907, 2008.
- [25] K. Hara, K. Miyamoto, Y. Abe, and M. Yanagida, "Electron transport in coumarin-dye-sensitized nanocrystalline TiO₂ electrodes," *Journal of Physical Chemistry B*, vol. 109, no. 50, pp. 23776–23778, 2005.
- [26] N. Robertson, "Optimizing dyes for dye-sensitized solar cells," *Angewandte Chemie*, vol. 45, no. 15, pp. 2338–2345, 2006.
- [27] A. Mishra, M. K. R. Fischer, and P. Büerle, "Metal-Free organic dyes for dye-sensitized solar cells: from structure: property relationships to design rules," *Angewandte Chemie*, vol. 48, no. 14, pp. 2474–2499, 2009.
- [28] G. Li, K.-J. Jiang, Y.-F. Li, S.-L. Li, and L.-M. Yang, "Efficient structural modification of triphenylamine-based organic dyes for dye-sensitized solar cells," *Journal of Physical Chemistry C*, vol. 112, no. 30, pp. 11591–11599, 2008.
- [29] J. M. Vanderkooi, "Photoreduction of membrane bound cytochrome C by excited state phenothiazine," *Biochemical and Biophysical Research Communications*, vol. 69, no. 4, pp. 1043–1049, 1976.

- [30] L. Levy, T. N. Tozer, L. D. Tuck, and D. B. Loveland, "Stability of some phenothiazine free radicals," *Journal of Medicinal Chemistry*, vol. 15, no. 9, pp. 898–905, 1972.
- [31] P. J. Walsh, K. C. Gordon, D. L. Officer, and W. M. Campbell, "A DFT study of the optical properties of substituted Zn(II)TPP complexes," *Journal of Molecular Structure*, vol. 759, no. 1–3, pp. 17–24, 2006.
- [32] R. M. El-Shishtawy, "Functional dyes, and some Hi-Tech applications," *International Journal of Photoenergy*, vol. 2009, Article ID 434897, 21 pages, 2009.
- [33] T. Meyer, D. Ogermann, A. Pankrath, K. Kleinermanns, and T. J. J. Müller, "Phenothiazinyl rhodanylidene merocyanines for dye-sensitized solar cells," *Journal of Organic Chemistry*, vol. 77, no. 8, pp. 3704–3715, 2012.
- [34] S. S. Park, Y. S. Won, Y. C. Choi, and J. H. Kim, "Molecular design of organic dyes with double electron acceptor for dye-sensitized solar cell," *Energy and Fuels*, vol. 23, no. 7, pp. 3732–3736, 2009.
- [35] Y. J. Chang, P.-T. Chou, Y.-Z. Lin et al., "Organic dyes containing oligo-phenothiazine for dye-sensitized solar cells," *Journal of Materials Chemistry*, vol. 22, pp. 21704–21712, 2012.
- [36] T.-Y. Wu, M.-H. Tsao, F.-L. Chen et al., "Synthesis and characterization of organic dyes containing various donors and acceptors," *International Journal of Molecular Sciences*, vol. 11, no. 1, pp. 329–353, 2010.
- [37] S. Agrawal, M. Pastore, G. Marotta et al., "Optical properties and aggregation of phenothiazine-based dye sensitizers for solar cells applications: a combined experimental and computational investigation," *The Journal of Physical Chemistry C*, vol. 117, no. 19, pp. 9613–9622, 2013.
- [38] A. Baheti, P. Tyagi, K. R. J. Thomas, Y.-C. Hsu, and J. T. Lin, "Simple triarylamine-based dyes containing fluorene and biphenyl linkers for efficient dye-sensitized solar cells," *Journal of Physical Chemistry C*, vol. 113, no. 20, pp. 8541–8547, 2009.
- [39] P. Singh, A. Baheti, K. R. Justin Thomas, Ch.-P. Lee, and K.-C. Ho, "Fluorene-based organic dyes containing acetylene linkage for dye-sensitized solar cells," *Dyes and Pigments*, vol. 95, no. 3, pp. 523–533, 2012.
- [40] M. P. Balanay, K. H. Kim, S. H. Lee, and D. H. Kim, "Tuning the photovoltaic parameters of β -substituted porphyrin analogues: an experimental and theoretical approach," *Journal of Photochemistry and Photobiology A: Chemistry*, vol. 248, pp. 63–72, 2012.
- [41] M. J. Griffith, M. James, G. Triani, P. Wagner, G. G. Wallace, and D. L. Officer, "Determining the orientation and molecular packing of organic dyes on a TiO₂ surface using X-ray reflectometry," *Langmuir*, vol. 27, no. 21, pp. 12944–12950, 2011.
- [42] Y. Hua, H. Wang, X. Zhu et al., "New simple panchromatic dyes based on thiadiazolo[3,4-c]pyridine unit for dye-sensitized solar cells," *Dyes and Pigments*, vol. 102, pp. 196–203, 2014.
- [43] H. Imahori, S. Kang, H. Hayashi et al., "Photoinduced charge carrier dynamics of Zn-Porphyrin-TiO₂ electrodes: the key role of charge recombination for solar cell performance," *Journal of Physical Chemistry A*, vol. 115, no. 16, pp. 3679–3690, 2011.
- [44] H. Ozawa, M. Awa, T. Ono, and H. Arakawa, "Effects of dye-adsorption solvent on the performances of the dye-sensitized solar cells based on black dye," *Chemistry*, vol. 7, no. 1, pp. 156–162, 2012.
- [45] D. Kim, M.-S. Kang, K. Song, S. O. Kang, and J. Ko, "Molecular engineering of organic sensitizers containing indole moiety for dye-sensitized solar cells," *Tetrahedron*, vol. 64, no. 45, pp. 10417–10424, 2008.

Research Article

Equilibrium and Kinetic Aspects in the Sensitization of Monolayer Transparent TiO₂ Thin Films with Porphyrin Dyes for DSSC Applications

Rita Giovannetti, Marco Zannotti, Leila Alibabaei, and Stefano Ferraro

Chemistry Unit, School of Science and Technology, University of Camerino, Via S. Agostino 1, 62032 Camerino, Italy

Correspondence should be addressed to Rita Giovannetti; rita.giovannetti@unicam.it

Received 24 October 2013; Accepted 4 December 2013; Published 2 January 2014

Academic Editor: JiaHong Pan

Copyright © 2014 Rita Giovannetti et al. This is an open access article distributed under the Creative Commons Attribution License, which permits unrestricted use, distribution, and reproduction in any medium, provided the original work is properly cited.

Free base, Cu(II) and Zn(II) complexes of the 2,7,12,17-tetrapropionic acid of 3,8,13,18-tetramethyl-21H,23H porphyrin (CPI) in solution and bounded to transparent monolayer TiO₂ nanoparticle films were studied to determine their adsorption on TiO₂ surface, to measure the adsorption kinetics and isotherms, and to use the results obtained to optimize the preparation of DSSC photovoltaic cells. Adsorption studies were carried out on monolayer transparent TiO₂ films of a known thickness. Langmuir and Freundlich adsorption constants of CPI-dyes on TiO₂ monolayer surface have been calculated as a function of the equilibrium concentrations in the solutions. The amount of these adsorbed dyes showed the accordance with Langmuir isotherm. Kinetic data on the adsorption of dyes showed significantly better fits to pseudo-first-order model and the evaluated rate constants linearly increased with the grow of initial dye concentrations. The stoichiometry of the adsorption of CPI-dyes into TiO₂ and the influence of presence of coadsorbent (chenodeoxycholic acid) have been established. The DSSC obtained in the similar conditions showed that the best efficiency can be obtained in the absence of coadsorbent with short and established immersion times.

1. Introduction

TiO₂ is a stable, semiconductor with large band gap well known for its considerable applications in dye-sensitized solar cell (DSSC) systems [1, 2] and, for this, several preparation methods have been performed [3–6]. TiO₂ nanoparticles layer, together with the dye-sensitizer loaded on its surface, is one of the most important parts of the DSSC structure and, therefore, the optimization of these parameters can enhance the DSSC efficiency.

In the search of new dyes with high extinction coefficient and high DSSC performances, new ruthenium dyes [7], porphyrin dyes [8], and other metal-free dyes [9, 10] are synthesized.

Porphyrins are particularly interesting as photosensitizers for DSSC for the absorption in the 400–450 nm region of Soret band and in the 500–700 nm region of Q-bands and also for the appropriate LUMO and HOMO energy levels; this makes them promising candidates as substitutes for ruthenium dyes in DSSC applications [11].

The increase in the use of porphyrin dyes as sensitizers in DSSC has been very important to clarify the role of natural porphyrins as light harvesting in the photosynthesis; the imitation of this process has been obtained using chlorophyll derivatives as dye sensitizers for nano-TiO₂ films [12, 13], showing also the importance of free carboxylic groups for the anchoring on the TiO₂ surface [12, 14, 15]. Numerous paper reports have been published on porphyrin dyes as sensitizer for DSSC [5, 16–21].

Cu(II) and Zn(II) complexes of coproporphyrin-I (2,7,12,17-tetrapropionic acid of 3,8,13,18-tetramethyl-21H,23H porphyrin or CPI) have been synthesized in our laboratory and tested as sensitizers in DSSC [22] but mechanism and kinetic in the adsorption of these new porphyrin dyes on TiO₂ surface are not clear.

Only few studies, however, focused on kinetics and equilibrium studies on dyes sensitization [23–25]. The aim of this paper was to understand the adsorption mechanism of CPI-dyes on TiO₂, also with the use of coadsorbent, to find a suitable equilibrium isotherm and kinetic model useful to

establish the best operating conditions for the optimization of the DSSC performances. An analytical study of adsorption equilibrium and kinetic control of dyes adsorption is first presented. Successively, the optical properties of CPI-dyes TiO_2 composite thin films are investigated with the purpose of ascertaining the monolayer coverage. Finally, the results obtained are used to optimize the preparation of the photovoltaic cells.

2. Experimental

2.1. Materials. All chemicals (Sigma-Aldrich) were of analytical grade and used without further purification. All the CPI (Figure 1) solutions were prepared into anhydrous ethanol. Copper and zinc CPI complexes (CPICu and CPIZn), synthesized in our laboratory [22], are dissolved with ethanol and 10% DMSO, respectively. Solutions of chenodeoxycholic acid (4×10^{-2} M) were prepared in ethanol and in ethanol with 10% DMSO and used after dilution from 5 to 20 mM.

2.2. Transparent TiO_2 Films Fabrication. Transparent TiO_2 screen-printed monolayer films used in this study were prepared, from Laboratory for Photonics and Interfaces of Ecole Polytechnique Federale of Lausanne, printing $2.7 \mu\text{m}$ thick film of 20 nm TiO_2 nanoparticles on the conducting glass electrode (fluorine doped SnO_2 (FTO)) and coating with a second layer of 5 nm thick, composed of 400 nm sized light-scattering anatase particles (CCI, Japan). TiO_2 nanoparticles and paste were prepared as described elsewhere [26]. The porosity for the 20 nm TiO_2 transparent layer, evaluated with BET measurements, was 59% (Monosorb, USA).

2.3. Optical Properties of the CPI-Dyes/ TiO_2 Transparent Films. TiO_2 electrodes are sintered at 400°C , cooled to 24°C , immersed every 2 minutes in each dye solutions, washed for remove the dye molecules excess, and, at the end, dried with nitrogen. The UV-visible adsorption of dye/ TiO_2 films was recorded on a Hewlett-Packard 8452A diode array spectrophotometer; the absorbance, to remove the interference, was monitored after subtracting TiO_2 film spectrum.

UV-vis absorption intensities of dyes were compared with the data of a calibration curve obtained from different reference solutions after adsorption on TiO_2 films; the content of adsorbed dyes was indicated as surface concentration of dyes (S) and was calculated as reference [23].

2.4. Device Fabrication. The sintered TiO_2 electrodes were immersed for established time in the respective dye solutions, dried by blowing nitrogen, and then assembled with a thermal platinized FTO/glass counter electrode. The working and counter electrodes, separated by a 25 mm thick hot melt ring (Surlyn, DuPont), were sealed by heating; in the internal space Z960 electrolyte [27] was added with a vacuum pump and a Surlyn sheet covered with a thin glass has been used for sealing the hole.

2.5. Photovoltaic Characterization. To characterize the solar cells, A 450 W xenon light source (Oriol, USA) was used. A

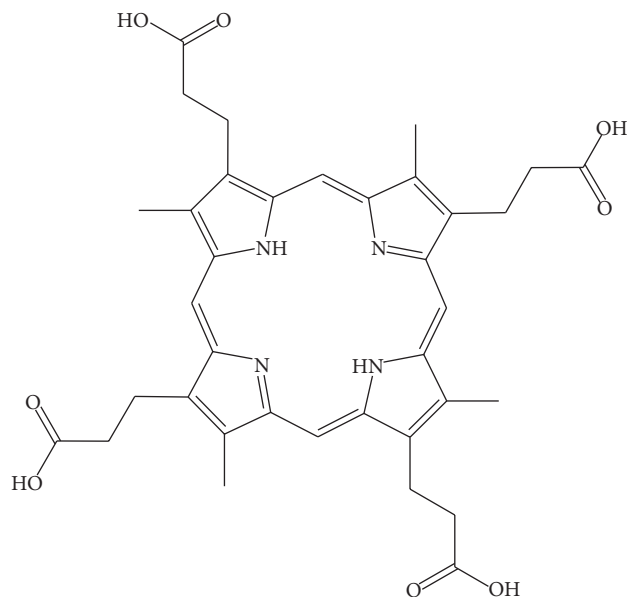


FIGURE 1: Molecular structure of coproporphyrin-I.

Schott K113 Tempax sunlight filter (Präzisions Glas & Optik GmbH, Germany) was used to match the spectral output of the lamp in the region of 350–750 nm so as to reduce the mismatch between the simulated and true solar spectra to less than 2%. The current-voltage characteristics of the cell under these conditions were obtained by applying an external potential bias to the cell and measuring the generated photocurrent with a Keithley model 2400 digital source meter (Keithley, USA). To control the incident photon-to-current conversion efficiency (IPCE) measurement a similar data acquisition system was used. Under computer control, light from a 300 W xenon lamp (ILC Technology, USA) was focused through a Gemini-180 double monochromator (Jobin Yvon Ltd., UK) onto the photovoltaic cell under test. The devices were masked to attain an illuminated active area of 0.16 cm^2 .

3. Results and Discussion

3.1. UV-Vis Absorption Spectra of CPI-Dyes/ TiO_2 Transparent Films. Figure 2 shows the UV-vis spectra of CPI, CPIZn, and CPICu molecules adsorbed into the films and demonstrates the effective dyes adsorption into the TiO_2 films. All the spectra show the typical strong Soret band of porphyrin molecules (region 400–450 nm) and weak Q bands (region 500–650 nm) that are not changed with respect to solution spectra proving that, in this process, the adsorbed molecules have not modified their structural properties.

3.2. Equilibrium of CPI-Dyes Adsorption. For a good knowledge of adsorption mechanism, necessary for the optimization of the design of an adsorption system, it is important to correlate equilibrium data with theoretical and empirical equations.

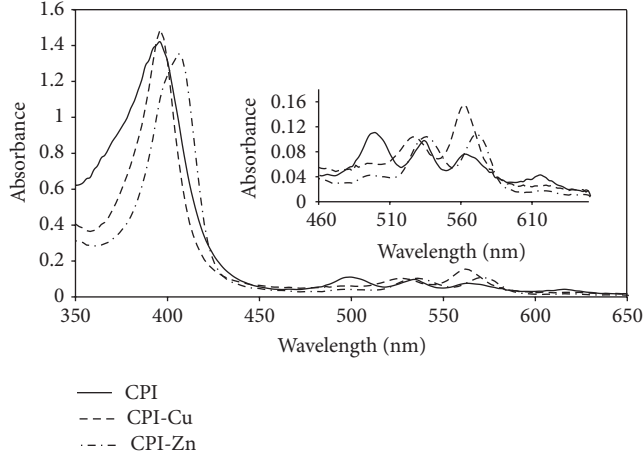


FIGURE 2: UV-vis spectra and in insert Q-bands magnification for CPI, CPI-Cu, and CPI-Zn incorporated into the TiO_2 films.

To evaluate how the dyes concentration in the original solution influences the adsorption capacity of TiO_2 films, different concentration samples have been used. Figure 3 shows the grow of surface concentration of CPI in the different TiO_2 films increasing CPI solution concentrations. The adsorption is already high for small dye concentrations and increases to obtain a high value when the solution concentration is about 3.04×10^{-4} M; when the solutions are more concentrated, dye saturation of the film occurs. Similar behaviour has been obtained for Cu and Zn CPI-dyes.

To establish as the dye concentration influence the adsorption process, the equilibrium data has been analyzed by Freundlich (1) and Langmuir (2) isotherms [28, 29]:

$$Q_e = K_F C_e^{1/n} \quad (1)$$

$$Q_e = \frac{(K_L C_e)}{(1 + a_L C_e)} \quad (2)$$

where C_e (M) is the concentration of the dye solution, Q_e is the amount of dye adsorbed on TiO_2 at equilibrium, K_F is the Freundlich constant that represents the adsorption capacity, $1/n$ is the adsorption intensities, K_L and a_L are the Langmuir constants, and the ratio K_L/a_L gives the theoretical saturation capacity of the TiO_2 monolayer, Q_0 . The linear forms of the two equations can be, respectively, written as follows:

$$\ln Q_e = \ln K_F + \left(\frac{1}{n}\right) \ln C_e \quad \frac{C_e}{Q_e} = \left(\frac{1}{K_L}\right) + \left(\frac{a_L}{K_L}\right) C_e \quad (3)$$

The linearized isotherm plots were used to calculate the adsorption isotherm constants and the results were summarized in Table 1 that shows the adsorption data fitting to the Langmuir and Freundlich isotherm models.

The correlation coefficients (R_L^2) for the Langmuir isotherm are highest in comparison to the values obtained for the Freundlich (R_F^2) isotherms, indicating that, in the studied concentration range, a Langmuir adsorption relation

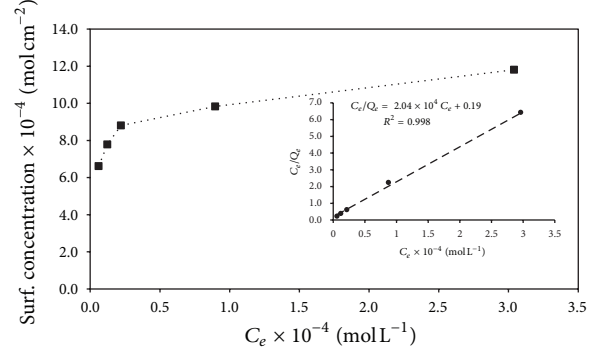


FIGURE 3: Grow of surface CPI concentration in the different TiO_2 films increasing CPI solution concentrations from 6.08×10^{-6} to 3.04×10^{-4} M; in insert, plot of C_e/Q_e versus C_e according to the Langmuir model.

TABLE 1: Langmuir (L) and Freundlich (F) CPI-dyes adsorption constants on TiO_2 monolayer surface.

| | CPI | CPI-Zn | CPI-Cu |
|---------|-----------------------|-----------------------|-----------------------|
| K_L | 5.051 | 3.178 | 3.037 |
| Q_0 | 4.90×10^{-5} | 5.03×10^{-5} | 6.50×10^{-5} |
| a_L | 1.03×10^5 | 6.31×10^4 | 4.67×10^4 |
| R_L^2 | 0.998 | 0.999 | 0.998 |
| K_F | 7.005 | 2.323 | 1.732 |
| R_F^2 | 0.965 | 0.805 | 0.825 |

provides a good description of the CPI-dyes/ TiO_2 interaction during the adsorption process. As example the plot of C_e/Q_e versus C_e is shown in insert of Figure 3 for CPI adsorption, and the other CPI-dyes show similar behaviour.

According to the Langmuir model, it may be deduced that, in this adsorption process, all dye molecules incorporated into the film have similar adsorption energy, the number of adsorption sites is limited, and the maximum adsorption corresponds to a saturated one layer of dye molecules on the adsorbent TiO_2 surface that cannot contribute to an additional incorporation of other molecules.

Interesting to note that, using CPI, when its concentration is greater than 3.04×10^{-4} M, the autoadsorption of dye occurred on TiO_2 surface, for probable dye aggregation. In fact, poorly resolved spectrum in the Soret band has been obtained while the absorbance profile in the Q band show typical spectrum of CPI aggregates [22] as reported in Figure 4. Similar behaviour is not obtained for the other CPI-dyes because, for the influence of central metal ion in the complexes, the aggregation of these may occur only at highest concentration.

3.3. Kinetics of CPI-Dyes Adsorption. The absorption of CPI-dyes molecules into TiO_2 films was strictly depending on the immersion time as reported in Figure 5 that shows the spectral change in the time for CPI-Zn dyes adsorbed into monolayer transparent TiO_2 films and the evolution in the

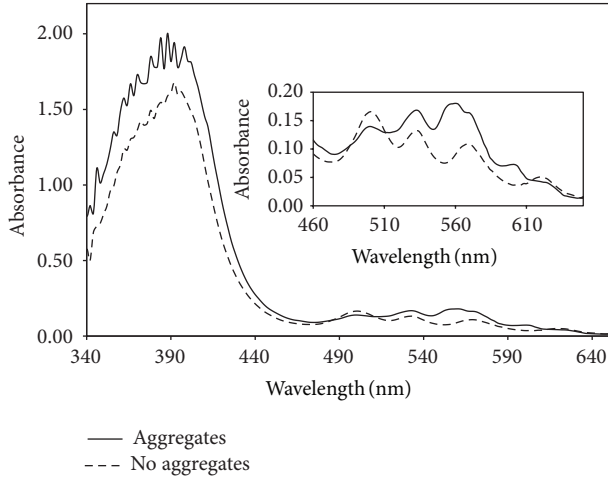


FIGURE 4: Absorbance profiles in the Q band: comparison between UV-vis spectra of CPI, aggregates (3.04×10^{-4} M) and no aggregates (8.96×10^{-5} M), adsorbed into TiO_2 films.

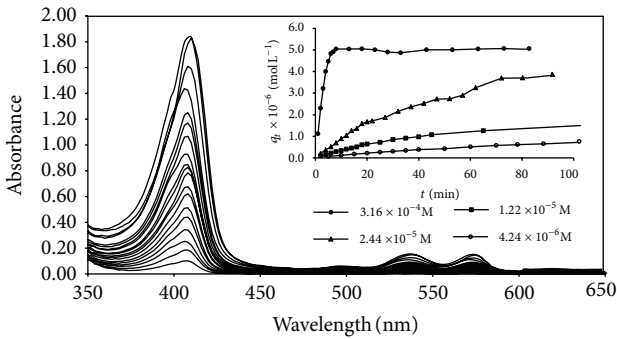


FIGURE 5: Spectral change in the time of CPIZn adsorbed on TiO_2 surface after immersion into CPIZn solution of 2.44×10^{-5} M; in insert evolution in the time of CPIZn surface concentrations q_t for different initial solution concentrations.

time of the surface concentrations of dyes q_t at different solution concentrations of dyes.

The curves obtained at higher dyes concentration show two zones: in the first, the amount of adsorbed molecules grows rapidly while in the second a slowdown of the process occurs because the saturation approaches; all the results showed that the absorption rates depended on initial dye concentrations.

For a correct interpretation of the absorption kinetics, the experimental points were compared with different adsorption kinetic models and the best fit has been observed with a pseudo-first-order model that is a procedure frequently used for the adsorption of a solute from solution [30] and can be expressed by:

$$q_t = q_e [1 - \exp(-k_1 t)] \quad (4)$$

where q_t is the amount of dye adsorbed at time t , q_e is equilibrium solid phase concentration, and k_1 is first-order

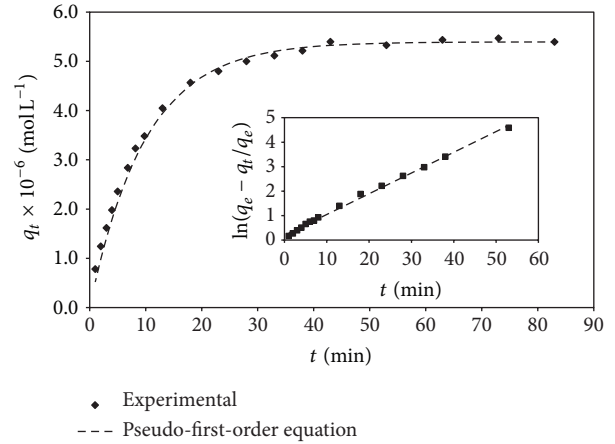


FIGURE 6: Comparison between measured and modelled time profiles for the adsorption of 8.96×10^{-5} M of CPI.

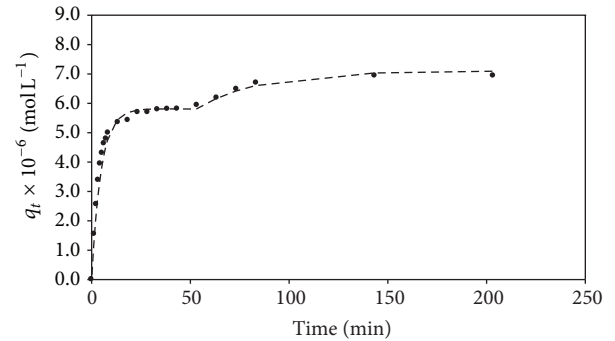


FIGURE 7: Evolution in the time of the CPI surface concentration Q_t with CPI concentration of 3.04×10^{-4} M.

rate constant for adsorption. The linear form is given as follows:

$$\ln \left[\frac{(q_e - q_t)}{q_e} \right] = -k_1 t. \quad (5)$$

Plotting the first term of (5) versus t , good straight lines are obtained and the values of k_1 can be deduced (Tables 2, 3, and 4). In the insert of Figure 6 a comparison of calculated and measured results for 8.96×10^{-5} M of CPI-dyes, over the entire range of time studied, is reported as an example, showing a good fit to the model; the results indicate therefore that the pseudo-first-order equation provides the best correlation for the these adsorption processes.

However, only for CPI, at concentration of 3.04×10^{-4} M, the adsorption took place in two stages (Figure 7) that followed first-order kinetics with respect to CPI concentrations: in the first stage quickly adsorption of CPI occurred while in the slower second step an autoadsorption of CPI was observed.

In Table 2 are reported the values of respective kinetic constants that demonstrate that the monolayer adsorption is about six time faster with respect to layer on layer CPI adsorption. This result can be explained by the adsorption/aggregation competition between CPI molecules and

TABLE 2: Kinetic constants for adsorption of different CPI concentrations on TiO_2 .

| CPI mol L^{-1} | k_1 $\text{l mol}^{-1} \text{min}^{-1}$ |
|--|--|
| 6.08×10^{-6} | 3.54×10^{-3} |
| 1.23×10^{-5} | 1.02×10^{-2} |
| 2.21×10^{-5} | 1.34×10^{-2} |
| 8.96×10^{-5} | 1.01×10^{-1} |
| 3.04×10^{-4} | $19.31 \times 10^{-1*}$ |
| 3.04×10^{-4} | $3.21 \times 10^{-1^\circ}$ |
| $k_1 = 1188.9 C_{\text{CPI}} - 0.0066$ | $R^2 = 0.992$ |

* first step kinetic; $^\circ$ second step kinetic.

TABLE 3: Kinetic constants for adsorption of different CPIZn concentrations on TiO_2 .

| CPIZn mol L^{-1} | k_1 $\text{l mol}^{-1} \text{min}^{-1}$ |
|---|--|
| 4.24×10^{-6} | 3.41×10^{-3} |
| 1.22×10^{-5} | 1.48×10^{-2} |
| 2.44×10^{-5} | 3.73×10^{-2} |
| 3.16×10^{-4} | 64.67×10^{-2} |
| $k_1 = 2.08 \times 10^3 C_{\text{CPIZn}} - 9.68 \times 10^{-3}$ | $R^2 = 0.999$ |

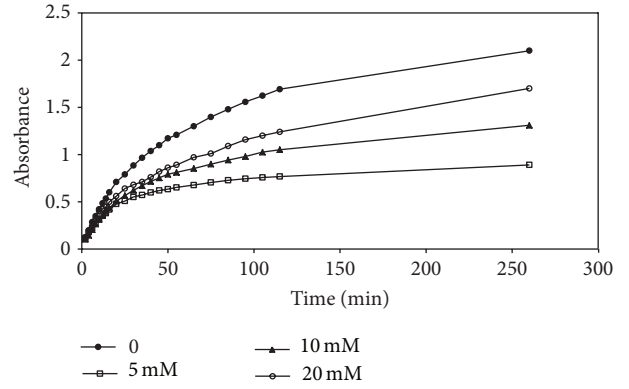
their aggregate forms, which could be more significant with higher concentration of CPI solutions.

The values of the kinetic constants obtained, reported in Tables 2–4, are in accordance with those of other authors [24] and indicate that the rate of dyes adsorption linearly increases with the growing of initial solutions concentrations of dyes and also that the dependence of rate constants with the dye concentrations shows high correlation and can be expressed by linear equations.

3.4. Effect of Chenodeoxycholic Acid on the Dyes Adsorption.

The effect of aggregation on the TiO_2 surface must be carefully considered and clarified for improving the cell performance of porphyrin-based DSSC [31]; the porphyrin molecules aggregation is the result of π -stacking and is a serious problem because the aggregates do not generate photocurrent [31]. The addition of a coadsorbent onto the dye solutions, during the dye-coating process, can be useful for the suppression of dye aggregation on the TiO_2 surface. Chenodeoxycholic acid (CDCA) is the most popular coadsorbent that, adsorbing on the TiO_2 surface thanks to their carboxyl and hydroxyl groups, restricting dye aggregation in DSSC assembly [18, 32].

For evaluating the effect of CDCA concentrations on the adsorption of CPI-dyes on TiO_2 surfaces, solutions of dyes with different CDCA concentrations have been used. In Figure 8 are reported, as example, the adsorption kinetics for CPI varying the CDCA concentrations, which clearly demonstrate that the adsorption of dyes decreased with an competitive effect on the adsorption that depended on CDCA concentrations. Also the kinetics of these process changed

FIGURE 8: Effect of CDCA concentration from 0 to 20 mM on the adsorption of CPI 2.21×10^{-5} M.TABLE 4: Kinetic constants for adsorption of different CPCu concentrations on TiO_2 .

| CPCu mol L^{-1} | k_1 $\text{l mol}^{-1} \text{min}^{-1}$ |
|--|--|
| 3.23×10^{-6} | 4.91×10^{-2} |
| 1.50×10^{-5} | 1.89×10^{-2} |
| 3.01×10^{-5} | 4.01×10^{-2} |
| 2.47×10^{-4} | 23.85×10^{-2} |
| $k_1 = 9.44 \times 10^2 C_{\text{CPCu}} + 5.89 \times 10^{-3}$ | $R^2 = 0.999$ |

TABLE 5: Comparison between the degree of covering, theoretical $(\text{DC})_T$ and experimental $(\text{DC})_E$ for different CPI-dyes.

| Dyes | Concentration (M) | CDCA (mM) | $(\text{DC})_T/(\text{DC})_E$ |
|--------|-----------------------|--------------|-------------------------------|
| CPI | 3.04×10^{-4} | 0 | 0.943 |
| | | 2 | 0.888 |
| | | 10 | 0.747 |
| | | 20 | 0.393 |
| CPI-Zn | 3.04×10^{-4} | 0 | 0.939 |
| | | 20 | 0.648 |
| CPI-Cu | 3.04×10^{-4} | 0 | 1.011 |
| | | 2 | 0.935 |
| | | 20 | 0.843 |

confirming the competition of CDCA in the adsorption of CPI-dyes for the suppression of the adsorption of CPI-dye molecules on the TiO_2 surface.

3.5. Stoichiometry of the Adsorption Process and Photovoltaic Measurements. The evaluation of the number of CPI-dye molecules adsorbed on the TiO_2 surface permits calculating the stoichiometry of the adsorption process. The effective adsorption surface of TiO_2 monolayer has been calculated from the TiO_2 roughness [33], porosity, and exposed surface parameters. Therefore, assuming full coverage of this, it is possible to estimate the number of CPI-dye molecules which

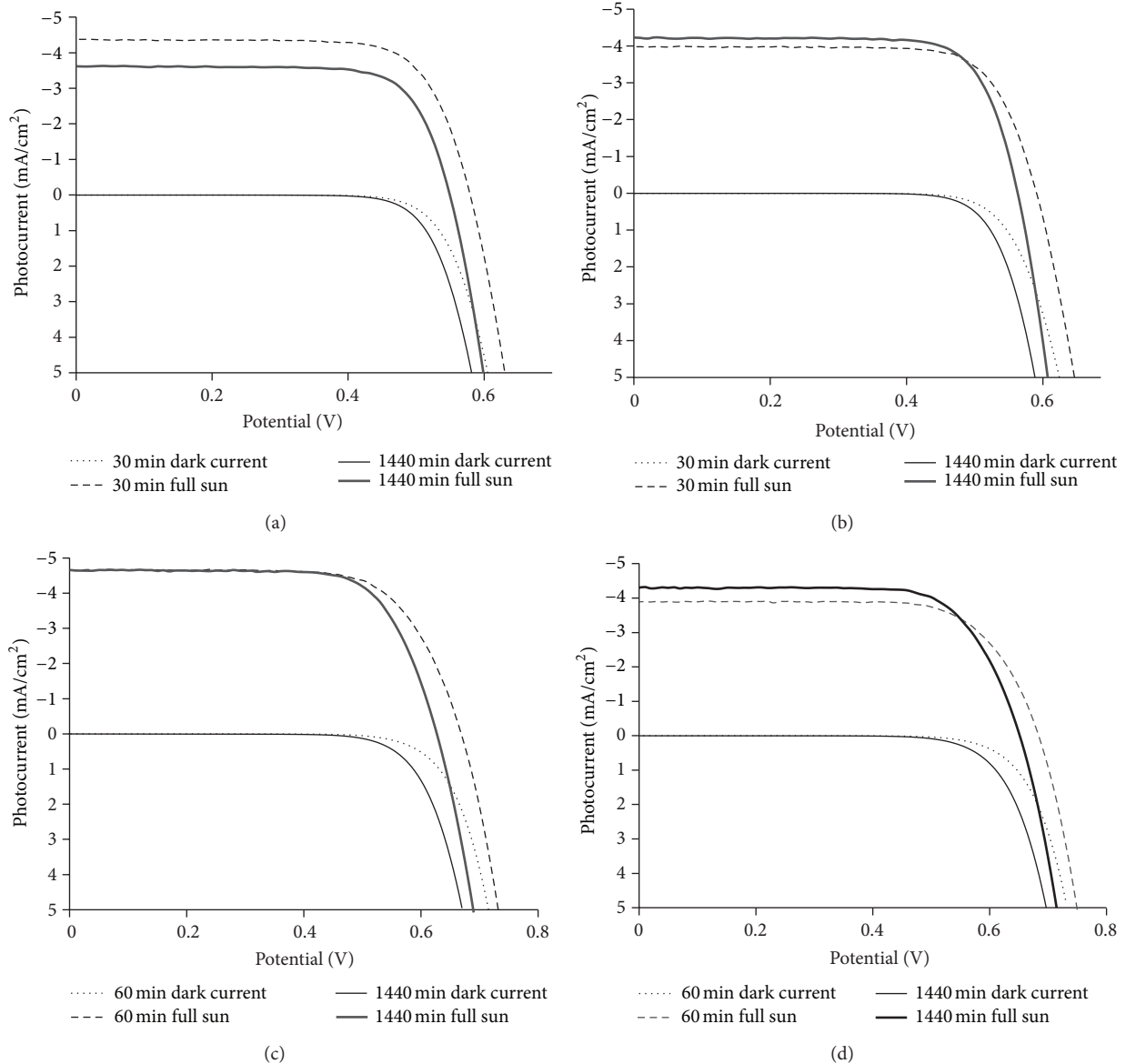


FIGURE 9: Photocurrent-voltage curves of dye-sensitized solar cells with different adsorption times for (a) CPIZn solution 3.04×10^{-4} M without CDCA, (b) CPIZn solution with CDCA 2 mM, (c) CPICu solution 3.04×10^{-4} M without CDCA, and (d) CPICu solution with CDCA 2 mM.

could be adsorbed. Knowing in fact the effective surface area of CPI-dye molecules that is approximately 1.31×10^{-14} cm^2 , it is possible to calculate the theoretical degree of covering $(DC)_T$ that can be compared with that experimental $(DC)_E$ as reported in Table 5.

From the ratio between theoretical $(DC)_T$ and experimental $(DC)_E$ values, obtained after immersion of 30 min for CPIZn and 60 min for CPI and CPICu with different CDCA concentrations, it may be deduced that the CPI-dyes form a single layer on the TiO_2 surface, in which the increase of CDCA concentration causes a competition with the dyes to the active sites on the semiconductor and consequently less dye molecules are adsorbed.

From the results obtained, since the amount of dye adsorbed on the TiO_2 film changed with time and with CDCA concentrations, it was also interesting to investigate the change of photovoltaic properties with adsorption time and coadsorbent.

Figure 9 shows the results of photocurrent-voltage curves for different experimental conditions of CPIZn and CPICu dye solutions, respectively, and the relevant photovoltaic parameters are listed in Table 6.

It is very important to consider that in the presence of CDCA 2 mM the V_{oc} values increased but, only at long adsorption times, this is translatable in an increase in efficiency.

TABLE 6: Effects of adsorption time and CDCA on the short-circuit photocurrent density (J_{sc}) open-circuit voltage, fill factor (FF), and overall conversion efficiency (η) of dye-sensitized solar cells based on CPICu and CPIZn (0.3 mM) with 2.7 μm thick monolayer TiO_2 film and using Z960 as electrolyte under an illumination of the AM 1.5G full sunlight intensity.

| | Dye | CDCA | Adsorption time (min) | J_{sc} (mA/cm^2) | Module U_{oc} (mV) | FF | η (%) |
|-----|-------|------|-----------------------|--------------------------------------|----------------------|-------|------------|
| (a) | CPIZn | — | 1440 | 3.62 | 549.12 | 73.54 | 1.48 |
| | CPIZn | — | 30 | 4.38 | 579.10 | 70.36 | 1.86 |
| (b) | CPIZn | 2 mM | 1440 | 4.23 | 562.48 | 69.88 | 1.80 |
| | CPIZn | 2 mM | 30 | 3.98 | 590.31 | 70.96 | 1.77 |
| (c) | CPICu | — | 1440 | 4.66 | 626.64 | 71.85 | 2.10 |
| | CPICu | — | 60 | 4.65 | 668.20 | 70.36 | 2.20 |
| (d) | CPICu | 2 mM | 1440 | 4.70 | 650.19 | 69.88 | 2.14 |
| | CPICu | 2 mM | 60 | 3.89 | 686.50 | 70.94 | 1.89 |

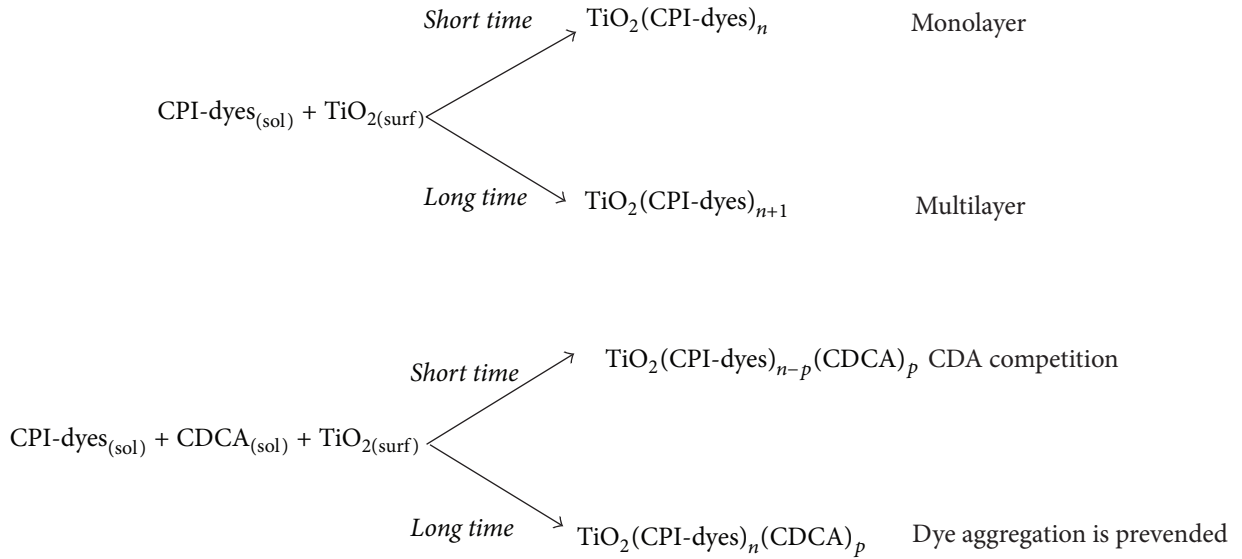


FIGURE 10

In fact, as it can be seen in Table 6, for the CPIZn dye, in the presence of CDCA 2 mM and with the adsorption time of 1440 min, the efficiency is greater than that in absence of CDCA; on the contrary when the adsorption time is of 30 min, in the presence of CDCA, the efficiency is lower with respect to that without CDCA; similar results were obtained with CPICu.

However, in the absence of CDCA, monolayer coverage is expected to be formed in 30 min for CPIZn and 60 min for CPICu, while multilayer (due to dye aggregation) is expected only after these times. Because the dye aggregates have been known to be inactive for electron injection and shield the dye molecules in direct contact with TiO_2 from absorbing light, it is thus expected that, in the absence of CDCA, long adsorption time exhibits lower photocurrent in spite of higher dye loading.

The best efficiencies are obtained at 30 min adsorption from CPIZn solution and at 60 min adsorption from CPICu, in the absence of CDCA, condition in which a single layer

of the dyes is obtained as verified from the stoichiometry of adsorption process (see Table 5).

So, for both CPIZn and CPICu the use of CDCA is negative for short immersion times because, thank of its competition with CPI-dyes, the dye coverage on TiO_2 surface decrease, while is positive only with long immersion times probably because it permits the evolution of adsorption process with reduction of dye aggregation on the TiO_2 surface. For these results the adsorption mechanisms of CPI-dyes in the presence and in the absence of CDCA can be explained as shown in Figure 10.

4. Conclusions

For the best manufacture of DSSC devices, optimum objectives are represented by very rapid and complete adsorption of single layer of dye on the semiconductor surface.

In this study we have described that the CPI-dyes concentration and adsorption times affected the dyes adsorption

on TiO₂ monolayer surfaces and consequently the DSSC performances.

The analytical study, with the equilibrium and kinetic data presented for adsorption of CPI-dyes onto TiO₂ monolayer surfaces, also in the presence of CDCA as coadsorbent, has allowed us to establish the best experimental conditions for the adsorption of these dyes and has demonstrated that the CPI-dyes, according to the Langmuir model and with pseudo-first-order kinetics, are adsorbed effectively on the TiO₂ monolayer without chemical changes. A systematic study of kinetic and equilibrium has been proposed demonstrating that the suppression of the dyes aggregation permits the optimization of selective adsorption of one layer of dyes molecules to stoichiometric ratios indicating a powerful strategy, which can be applied to other dyes, for improving performances in DSSC.

Conflict of Interests

The authors declare that there is no conflict of interests regarding the publication of this article.

Acknowledgments

The authors gratefully appreciate Professor Grätzel and Dr. Shaik M. Zakeeruddin of Ecole Polytechnique Federale of Lausanne, for allowing and facilitating Leila Alibabaei in assembling cells and on photovoltaic measurements. The authors also thanks Dr. Takeru Bessho for fabricated TiO₂ electrodes and Professor Vito Bartocci for fruitful discussions.

References

- [1] M. Grätzel, "Photoelectrochemical cells," *Nature*, vol. 414, no. 6861, pp. 338–344, 2001.
- [2] A. Hagfeldt, G. Boschloo, L. Sun, L. Kloo, and H. Pettersson, "Dye-sensitized solar cells," *Chemical Reviews*, vol. 110, no. 11, pp. 6595–6663, 2010.
- [3] K.-M. Lee, V. Suryanarayanan, and K.-C. Ho, "Influences of different TiO₂ morphologies and solvents on the photovoltaic performance of dye-sensitized solar cells," *Journal of Power Sources*, vol. 188, no. 2, pp. 635–641, 2009.
- [4] K. Fan, T. Peng, J. Chen, X. Zhang, and R. Li, "A simple preparation method for quasi-solid-state flexible dye-sensitized solar cells by using sea urchin-like anatase TiO₂ microspheres," *Journal of Power Sources*, vol. 222, pp. 38–44, 2013.
- [5] C.-R. Ke and J.-M. Ting, "Anatase TiO₂ beads having ultra-fast electron diffusion rates for use in low temperature flexible dye-sensitized solar cells," *Journal of Power Sources*, vol. 208, pp. 316–321, 2012.
- [6] X. Chen and S. S. Mao, "Titanium dioxide nanomaterials: synthesis, properties, modifications and applications," *Chemical Reviews*, vol. 107, no. 7, pp. 2891–2959, 2007.
- [7] A. Sepehrifard, S. Chen, A. Stublla, P. G. Potvin, and S. Morin, "Effects of ligand LUMO levels, anchoring groups and spacers in Ru(II)-based terpyridine and dipyrzinylypyridine complexes on adsorption and photoconversion efficiency in DSSCs," *Electrochimica Acta*, vol. 87, pp. 236–244, 2013.
- [8] A. Yella, H.-W. Lee, H. N. Tsao et al., "Porphyrin-sensitized solar cells with cobalt (II/III)-based redox electrolyte exceed 12 percent efficiency," *Science*, vol. 334, no. 6056, pp. 629–634, 2011.
- [9] S. Ramkumar and S. Anandan, "Synthesis of bioanchored metal free organic dyes for dye sensitized solar cells," *Dyes and Pigments*, vol. 97, no. 3, pp. 397–404, 2013.
- [10] R. Sirohi, D. H. Kim, S.-C. Yu, and S. H. Lee, "Novel di-anchoring dye for DSSC by bridging of two mono anchoring dye molecules: a conformational approach to reduce aggregation," *Dyes and Pigments*, vol. 92, no. 3, pp. 1132–1137, 2012.
- [11] M. K. Panda, K. Ladomenou, and A. G. Coutsolelos, "Porphyrins in bio-inspired transformations: light-harvesting to solar cell," *Coordination Chemistry Reviews*, vol. 256, no. 21–22, pp. 2601–2627, 2012.
- [12] W. M. Campbell, A. K. Burrell, D. L. Officer, and K. W. Jolley, "Porphyrins as light harvesters in the dye-sensitized TiO₂ solar cell," *Coordination Chemistry Reviews*, vol. 248, no. 13–14, pp. 1363–1379, 2004.
- [13] R. Dabestani, A. J. Bard, A. Campion et al., "Sensitization of titanium dioxide and strontium titanate electrodes by ruthenium(II) tris(2,2′-bipyridine-4,4′-dicarboxylic acid) and zinc tetrakis(4-carboxyphenyl)porphyrin: an evaluation of sensitization efficiency for component photoelectrodes in a multipanel device," *The Journal of Physical Chemistry*, vol. 92, no. 7, pp. 1872–1878, 1988.
- [14] G. K. Boschloo and A. Goossens, "Electron trapping in porphyrin-sensitized porous nanocrystalline TiO₂ electrodes," *The Journal of Physical Chemistry*, vol. 100, no. 50, pp. 19489–19494, 1996.
- [15] C. C. Wamser, H.-S. Kim, and J.-K. Lee, "Solar cells with porphyrin sensitization," *Optical Materials*, vol. 21, no. 1–3, pp. 221–224, 2003.
- [16] D. Daphnomili, G. D. Sharma, S. Biswas, K. R. J. Thomas, and A. G. Coutsolelos, "A new porphyrin bearing a pyridinylethynyl group as sensitizer for dye sensitized solar cells," *Journal of Photochemistry and Photobiology A*, vol. 253, pp. 88–96, 2013.
- [17] T. Ma, K. Inoue, K. Yao et al., "Photoelectrochemical properties of TiO₂ electrodes sensitized by porphyrin derivatives with different numbers of carboxyl groups," *Journal of Electroanalytical Chemistry*, vol. 537, no. 1–2, pp. 31–38, 2002.
- [18] Q. Wang, W. M. Campbell, E. E. Bonfantani et al., "Efficient light harvesting by using green Zn-porphyrin-sensitized nanocrystalline TiO₂ films," *The Journal of Physical Chemistry B*, vol. 109, no. 32, pp. 15397–15409, 2005.
- [19] M. K. Nazeeruddin, R. Humphry-Baker, D. L. Officer, W. M. Campbell, A. K. Burrell, and M. Grätzel, "Application of metalloporphyrins in nanocrystalline dye-sensitized solar cells for conversion of sunlight into electricity," *Langmuir*, vol. 20, no. 15, pp. 6514–6517, 2004.
- [20] W. M. Campbell, K. W. Jolley, P. Wagner et al., "Highly efficient porphyrin sensitizers for dye-sensitized solar cells," *The Journal of Physical Chemistry C*, vol. 111, no. 32, pp. 11760–11762, 2007.
- [21] M. Gervaldo, F. Fungo, E. N. Durantini, J. J. Silber, L. Sereno, and L. Otero, "Carboxyphenyl metalloporphyrins as photosensitizers of semiconductor film electrodes. A study of the effect of different central metals," *The Journal of Physical Chemistry B*, vol. 109, no. 44, pp. 20953–20962, 2005.
- [22] L. Alibabaei, M. Wang, R. Giovannetti et al., "Application of Cu(II) and Zn(II) coproporphyrins as sensitizers for thin film dye sensitized solar cells," *Energy and Environmental Science*, vol. 3, no. 7, pp. 956–961, 2010.

- [23] P. Castellero, J. R. Sánchez-Valencia, M. Cano et al., "Active and optically transparent tetracationic porphyrin/TiO₂ composite thin films," *ACS Applied Materials and Interfaces*, vol. 2, no. 3, pp. 712–721, 2010.
- [24] C.-R. Lee, H.-S. Kim, I.-H. Jang, J.-H. Im, and N.-G. Park, "Pseudo first-order adsorption kinetics of N719 dye on TiO₂ surface," *ACS Applied Materials and Interfaces*, vol. 3, no. 6, pp. 1953–1957, 2011.
- [25] P. J. Holliman, B. Vaca Velasco, I. Butler, M. Wijdekop, and D. A. Worsley, "Studies of dye sensitisation kinetics and sorption isotherms of direct red 23 on titania," *International Journal of Photoenergy*, vol. 2008, Article ID 827605, 7 pages, 2008.
- [26] P. Wang, S. M. Zakeeruddin, J.-E. Moser, and M. Grätzel, "A new ionic liquid electrolyte enhances the conversion efficiency of dye-sensitized solar cells," *The Journal of Physical Chemistry B*, vol. 107, no. 48, pp. 13280–13285, 2003.
- [27] L. Alibabaei, J.-H. Kim, M. Wang et al., "Molecular design of metal-free D- π -A substituted sensitizers for dye-sensitized solar cells," *Energy and Environmental Science*, vol. 3, no. 11, pp. 1757–1764, 2010.
- [28] M. Özacar and I. A. Şengil, "Equilibrium data and process design for adsorption of disperse dyes onto alunite," *Environmental Geology*, vol. 45, no. 6, pp. 762–768, 2004.
- [29] M. Özacar, "Equilibrium and kinetic modelling of adsorption of phosphorus on calcined alunite," *Adsorption*, vol. 9, no. 2, pp. 125–132, 2003.
- [30] A. Günay, E. Arslankaya, and I. Tosun, "Lead removal from aqueous solution by natural and pretreated clinoptilolite: adsorption equilibrium and kinetics," *Journal of Hazardous Materials*, vol. 146, no. 1-2, pp. 362–371, 2007.
- [31] J. Rochford, D. Chu, A. Hagfeldt, and E. Galoppini, "Tetra-chelate porphyrin chromophores for metal oxide semiconductor sensitization: effect of the spacer length and anchoring group position," *Journal of the American Chemical Society*, vol. 129, no. 15, pp. 4655–4665, 2007.
- [32] K. Hara, Y. Dan-Oh, C. Kasada et al., "Effect of additives on the photovoltaic performance of coumarin-dye-sensitized nanocrystalline TiO₂ solar cells," *Langmuir*, vol. 20, no. 10, pp. 4205–4210, 2004.
- [33] S. H. Kang, J.-Y. Kim, and Y.-E. Sung, "Role of surface state on the electron flow in modified TiO₂ film incorporating carbon powder for a dye-sensitized solar cell," *Electrochimica Acta*, vol. 52, no. 16, pp. 5242–5250, 2007.